Phase syntheses of Ni-Bi system using ion beam mixing

By

Vantari Siva

PHYS11201204018

National Institute of Science Education and Research, Bhubaneswar

A thesis submitted to the
Board of Studies in **Physical Sciences**

In partial fulfillment of requirements
For the Degree of
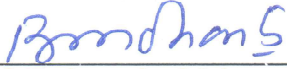
DOCTOR OF PHILOSOPHY

of
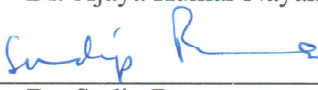
HOMI BHABHA NATIONAL INSTITUTE

March, 2018

Homi Bhabha National Institute

Recommendations of the Viva Voce Committee

As members of the Viva Voce Committee, we certify that we have read the dissertation prepared by "**Vantari Siva**" entitled "**Phase syntheses of Ni-Bi system using ion beam mixing**" and recommend that it may be accepted as fulfilling the thesis requirement for the award of Degree of Doctor of Philosophy.

Chairman - Prof. Bedangadas Mohanty	Date: 19/3/2018
Guide / Convener - Dr. Pratap Kumar Sahoo	Date: 19/03/2018
Co-Guide - Dr. Kartikeswar Senapati	Date: 19/03/2018
External Examiner - Prof. Sanjeev Kumar Srivastava	Date: 19.3.18
Member 1 - Dr. Subhankar Bedanta	Date: 19.03.2018
Member 2 - Dr. Ajaya Kumar Nayak	Date: 19/03/18
Member 3 - Dr. Sudip Barman	Date: 19/03/18

Final approval and acceptance of this thesis is contingent upon the candidate's submission of the final copies of the thesis to HBNI.

We hereby certify that we have read this thesis prepared under our direction and recommend that it may be accepted as fulfilling the thesis requirement.

Date: 19.03.2018
Place: NISER

Dr. Kartikeswar Senapati   Dr. Pratap K. Sahoo

ii

STATEMENT BY AUTHOR

This dissertation has been submitted in partial fulfillment of requirements for an advanced degree at Homi Bhabha National Institute (HBNI) and is deposited in the Library to be made available to borrowers under the rules of HBNI.

Brief quotations from this dissertation are allowable without special permission, provided that accurate acknowledgment of source is made. Requests for permission for extended quotation from or reproduction of this manuscript in whole or in part may be granted by the Competent Authority of HBNI when in his or her judgement the proposed use of the material is in the interests of scholarship. In all other instances, however, permission must be obtained from the author.

(Vantari Siva)

DECLARATION

I, hereby declare that the investigation presented in the thesis has been carried out by me. The work is original and has not been submitted earlier as a whole or in part for a degree/diploma at this or any other Institution/University.

(Vantari Siva)

List of Publications arising from the thesis

Journal:

†**1. V. Siva**, K. Senapati, B. Satpati, S. Prusty, D. K. Avasthi, D. Kanjilal, P. K. Sahoo, Spontaneous formation of superconducting $NiBi_3$ phase in Ni-Bi bilayer films, J. Appl. Phys. 117,083902 (2015).

†**2. V. Siva**, D. P. Datta, A. Singh, T. Som, P. K. Sahoo, Nanocomposite synthesis and photoluminescence properties of MeV Au-ion beam modified Ni thin films, Appl. Surf. Sci. 360, 276 (2016).

†**3. V. Siva**, P. C. Pradhan, G. S. Babu, M. Nayak, P. K. Sahoo, K. Senapati, Superconducting proximity effect in $NiBi_3$-Ni-$NiBi_3$ trilayer system with sharp superconductor-ferromagnet boundaries, J. Appl. Phys. 119, 063902 (2016).

†**4. V. Siva**, A. Chettah, B. Satpati, S. Ojha, D. Kanjilal and P. K. Sahoo, Enhanced surface and interface diffusion in NiBi bilayers by swift heavy ion irradiation, RSC Adv. 58950, 6 (2016).

†**5. V. Siva**, D. P. Datta, S. Chatterjee, S. Varma, D. Kanjilal and P. K. Sahoo, Synthesis of sponge-like hydrophobic $NiBi_3$ surface by 200 keV Ar ion implantation, Appl. Surf. Sci. 410, 519 (2017).

†**6. V. Siva**, A. Chettah, A. Tripathi, D. Kanjilal and P. K. Sahoo, Interface mediated enhanced mixing of multilayered Ni-Bi thin films by swift heavy ion irradiation, Nucl. Instrum. Methods Phys. Res. Sect. B 409, 314 (2017)

†**7. V. Siva**, A. Chettah, A. Tripathi, D. Kanjilal and P. K. Sahoo, Enhanced mixing in Ni-Bi multilayers using swift heavy ion irradiation: Application of the inelastic thermal spike model, Intermetallics (Under review).

Conferences:

[†]**1. V. Siva**, D. P. Datta, S. Prusty, and P. K. Sahoo, Solid state reaction induced phase evolution of Ni/Bi thin films, AIP conf. proc. 1832, 080021 (2017).

2. S. Prusty, **V. Siva**, S. Ojha, D. Kabiraj and P. K. Sahoo, Nanoscale Interfacial Mixing of Au/Bi Layers Using MeV Ion Beams, AIP Conf. Proc. 1832, 080026 (2017).

[†] **Related to thesis.**
Others:

1. V. Siva, S. S. Sahu, D. P. Datta, P. C. Pradhan, M. Nayak, V. Solanki, D. Topwal, K. Senapati, P. K. Sahoo, Ion irradiation induced phase transition of Co in Co/Au thin films, J. Alloys Compd., 680, 722 (2016).

2. S. Prusty[‡], **V. Siva**[‡], N. Shukla, B. Satpati, K. Senapati and P. K. Sahoo, Unusual ferromagnetic behaviour of embedded non-functionalized Au nanoparticles in Bi/Au bilayer films, RSC Adv. 6, 106584(2016). [‡]equal contribution.

3. D. P. Datta, **V. Siva**, A. Singh, S. R. Joshi, D. Kanjilal and P. K. Sahoo Ion-beam-induced nanodots formation from Au/Si thin films on quartz surface, Nucl. Instrum. Methods Phys. Res. Sect. B, 379, 48, (2016).

4. D. P. Datta, **V. Siva**, S. Varma, D. Kanjilal and P. K. Sahoo, Ion induced dewetting of Au-Si on SiO$_2$ surface- composite nanodot evolution and wettability transition, Phys.Chem. Chem. Phys. 18, 29955 (2016).

5. S. N. Sarangi, **V. Siva**, B. K. Padhi and P. K. Sahoo, Synthesis of Cu-doped ZnO nanorods for photosensitive UV detection application, Adv. Mater. Lett. 8, 524 (2017).

6. S. S. Sahu, **V. Siva**, P. C. Pradhan, M. Nayak, K. Senapati and P. K. Sahoo, Progressive magnetic softening of ferromagnetic layers in multilayer ferromagnet-nonmagnet systems and

the role of granularity, J. Appl. Phys. 121, 213905 (2017).

7. D. P. Datta, **V. Siva**, A. Singh, D. Kanjilal and P. K. Sahoo, Photoluminescent Au-Ge composite nanodots formation on SiO_2 surface by ion induced dewetting, Nucl. Instrum. Methods Phys. Res. Sect. B 407, 141 (2017).

8. D. P. Datta, A. Chettah, **V. Siva**, D. Kanjilal, and P. K. Sahoo, Dewetting induced Au-Ge composite nanodot evolution in SiO_2, Appl. Surf. Sci. 428, 676 (2018).

9. D. Suri, **V. Siva**, S. Joshi, K. Senapati, P. K. Sahoo, S. Varma, R. S. Patel, A study of electron and thermal transport in layered titanium disulphide single crystals, J. Phys.: Cond. Matt. 29, 485708 (2017).

(Vantari Siva)

To my Mother

Acknowledgement

As a matter of fact, PhD is a long journey, where one has several sweet memories as well as various hardships. Like any other PhD scholar, I also have gone through all these steps. The journey became so memorable, because of the help of plenty of lending hands to save me in hard times as well as to share the joy on the happier occasions. In the process of accomplishing the work that has been carried out for this thesis, which is a result of nearly five years of research in the group of Ion beam and nanomaterials laboratory (IBNL), School of Physical Sciences, National Institute of Science Education and Research (NISER), Bhubaneswar. It is my pleasure to get a chance to thank all of the cool and great persons who extended their help extensively at times, without whom it is not possible to accomplish the work done.

First and foremost, I would like to express my deep and sincere gratitude to my supervisor Dr. P. K. Sahoo for his enthusiasm, guidance, patience and constant support throughout the course of these five long years. He believes in knowledge sharing and gaining and hence always has encouraged me to attend several workshops, schools, and conferences. He is a person, who never hesitated to approach the faculties/ scientists in and outside NISER for experimental facilities whenever needed, without such support it was not at all possible for me to finish this work, as NISER was still establishing back then. That is how I have got a chance to meet with Dr. Chettah for theoretical support for our experiments. It was his very nature helped me to visit various labs across India and conduct experiments there, including TIFR-Mumbai, IUAC-New Delhi, UGC-DAE-CSR Indore, RRCAT-Indore, IIT Kharagpur, and IOP Bhubaneswar. He is so kind and generous to take me to the hospital when I was suffering from very bad health in his own car. The freedom and support that I have received from him are one of the best things that a PhD student can ever get. I used to call him on weekends and night times during the experiments and he never gets anger or irritation for all these things. It may clearly be understood from the number of my publications that how supportive, enthusiastic and interested in research he is. He had even allowed me to share his room when I was not having funds for accommodation during IBMM conference in Wellington, New Zealand. This PhD tenure will remain as some of the best days of my life with a lot of parties and picnics with him and his family. I am really indebted to him for being such a nice supervisor. More importantly, the moral support and joyful moments from him and his family, Seema Ma'am,

Krish and Prince is unforgettable.

Last but not the least, I will never be able to pay the price for what my family members and relatives have done for me. It is my pleasure having their immense support and encouragement at various points of life. If I am given a chance, I wish to have the same Mother in the upcoming births (if they exist). How can I simply thank her through a single sentence or paragraph, which cannot be expressed in the words. I am ever indebted to her for the uncountable love, care and support. I thank my Sister, Brother-in-Law, niece and nephew for their support. I thank my Father, Father-in-law, Mother-in-law, paternal uncle and aunt, for their unconditional love and support. I am pleased to have such a nice childhood with Rajasekhar, Revanth, Raj kumar, Malli and other relatives. I greatly acknowledge the unconditional love and support by my wife Geetha and my daughter Toshita. My Mother, Daughter, and Wife are the three persons, after looking at whose face I forget all the worries that I may have. I am lucky enough to have them in my life.

Date: **Vantari Siva**

Contents

Synopsis

Ion beam mixing (IBM) is one of the most efficient and effective methods for synthesizing stable or metastable compound phases. This technique offers distinct advantages compared to conventional mixing processes such as thermal annealing, particularly in terms of spatial selectivity, relatively low-temperature process and capability of mixing immiscible systems. IBM can be defined as an intermixing and/or alloying that can happen at the interface separating two different materials during ion matter interaction [1]. It is worth noting here that energetic ion beam, while traversing through the matter, loses their energy to the target atoms, mainly, through two different processes, which can be classified into elastic and inelastic collisions. During ion matter interaction, depending on the energy, species of the implanted ions and density of target atoms, one process dominates over the other. For example, in the low energy regime, elastic collisions are expected to dominate the inelastic ones. During this process, ion deposits most of its energy to the atomic subsystem due to lesser velocity of ions, which is widely known as nuclear energy loss (S_n). Similarly, in the high energy regime most of the energy of the ions gets deposited to the electronic subsystem and therefore named as electronic energy loss (S_e) [2]. In the Sn dominant regime, mostly ballistic effects govern the mixing and in the Se dominant regime, thermal spike effects play a key role. In the regime where both Se and Sn are comparable, synergistic effects of both ballistic and thermal spike effects are expected. In order to accomplish mixing of the layers using IBM, one can play with different parameters such as the energy, fluence and species of ions.

This IBM tool was first discovered by Van der Weg *et al.* in 1973 [3], where Pd thin films on Si substrates were lead to form palladium silicide after Ar ion irradiation. There are lots of studies on IBM of binary multilayer systems in the literature. For example, Ibrahim *et al.*, [4] studied on the synthesis of alloys of Bi-Sb system using IBM technique by varying different parameters such as ion fluence, ion energy and temperature. Manju *et al.* [5] have shown the engineering of thermo-electric properties of Co-Sb and Pb-Te systems along with the mixing. Cheng *et al.* [6] have extensively studied the IBM and the formation of amorphous alloys of various binary systems such as Au-Ag, Pt-Pd, Hf-Zr, W-Mo, Ta-Nb, Ru-Zr, Ru-Ti and so on. The study of IBM has been performed in ferromagnetic and non-ferromagnetic

metals [5], non-ferromagnetic and non-ferromagnetic metals [6], superconducting and normal metals [6] till now. In the present case, we investigate the IBM of ferromagnetic metal (Ni) and diamagnetic semimetal (Bi) at different energy regimes. It may be mentioned here that the ion beam mixing depends on several different parameters such as the energy of ion beams, ion fluence, ion species, target temperature, the number of layers and their thicknesses. Among many proposed theories, the thermal spiked model is the most successful theory to explain ion beam mixing [7, 8]. In this model, it is assumed that the heat energy generated by the incident ion first on the electronic subsystem, which will then be communicated to atomic subsystem through electron-phonon interaction. The heat energy diffuses in both radial and axial directions, whose information can be obtained by solving a set of coupled differential equations numerically. Though there are several reports of IBM on various binary systems at different energies, a systematic study which covers Se dominant, Sn dominant and intermediate ranges on a single system has not been performed till date. Thus in the present report, three different energy regimes such as low, medium and high energy ions have been chosen for the study of ion beam mixing.

In the present case, we have selected Ni-Bi system for the study of the ion beam mixing, as it offers interesting physics and applications in the field of science and technology. To start with, Ni-Bi binary system has two possible alloy phases, they are NiBi and NiBi$_3$. The crystal structure of NiBi is a NiAs type with phase group P6$_3$/mmc, while that of NiBi$_3$ it is CaLiSi$_2$ type with the space group Pnma [9, 10]. It is interesting to note that both the phases, NiBi and NiBi$_3$, are superconducting in nature with transition temperatures 4.25 K and 4.06 K respectively. The melting points of NiBi and NiBi$_3$ compounds are and 646 ^{o}C and 467 ^{o}C respectively [11]. The phase diagram of this binary system has been reported by many research groups, which was first pursued by G. Voss *et al.* [12] It was studied and modified by Feschotte *et al.* [9], Hansen *et al.* [13]. Recently, Dybkov [11] has come up with a phase diagram after compiling all the previous phase diagrams. In 2005, LeClair *et al.*, [14] have reported a phenomenon called coexistence of superconductivity and ferromagnetism (CSF) in a simple system like Ni/Bi bilayers, where the same electrons were responsible for both ferromagnetism and superconductivity. It was reported that the competition can be tailored by varying the thickness of Ni layer in Ni/Bi bilayers. More interestingly, the coexistence was observed in the Ni side of Ni/Bi layers, but not in both the layers. Later on, Herrmansdörfer *et al.*, [15] have shown this CSF in the nanostructured NiBi$_3$, one of the stable alloy phases of Ni-Bi system.

In the same year, Pineiro *et al.*, [16] have reported a possibility of the coexistence in $NiBi_3$ polycrystals. On the other hand, the same material was reported to show superconductivity alone without ferromagnetism [17]. The above contradicting results suggest that the compound $NiBi_3$ needs further investigation to conclude whether $NiBi_3$ show the coexistence or not. It is to be mentioned here that the Ni-Bi system also falls into the category of the very few materials such as UGe_2, URhGe, UCoGe, viz. [15], which show the CSF property. Apart from the above interesting aspects, $NiBi_3$ was also reported to show large field dependent magnetoresistance (MR) and thermal transport properties [18].

Till date, the phase synthesis of NiBi and $NiBi_3$ has been reported using conventional thermal annealing and chemical routes. In this thesis, we make use of ion beam mixing (IBM) for the phase synthesis of Ni-Bi system as a function of ion fluence at three different energy regimes. They are low (200 keV Ar), medium (1 MeV Ni) and very high (100-120 MeV Au ions) energetic ions. These three different regimes have been chosen in such a way that we can cover three different regions, where S_e dominates S_n, S_n dominates S_e and both are comparable. Prior to the study of IBM, we perform thermal annealing study to verify the phase synthesis of Ni-Bi system in the case of thin films [19]. In this case, the thermally deposited Ni (7 nm)/Bi (7 nm) thin bilayers were annealed at different temperatures such as 500 ^{o}C, 600 ^{o}C, 700 ^{o}C and 800 ^{o}C. We show the evolution of Ni-Bi phases as a function of annealing temperature. This evolution has been compared with the previously proposed phase diagrams for confirming the case of thin films with the bulk. The as-deposited sample shows the presence of Ni, Bi and Si peaks in the X-ray diffraction analysis. As soon as these films are annealed at 500 ^{o}C temperature, we notice the formation of both the phases of Ni and Bi along with the NiO peaks. In these phases, NiBi compound exists till the highest annealing temperature (700 ^{o}C), while the other phase $NiBi_3$ starts disappearing after a temperature of 700 ^{o}C. The trend observed in the present experiment is in agreement with the proposed phases diagram in the literature. The surface morphology of the films initially looks grainy in nature and after annealing, they start agglomerating then finally reach molten-like morphology at higher temperatures. The low melting point of Bi must have led to such morphological evolution with the temperature. Moreover, we notice that the as-deposited samples are semi-metallic nature as Bi is on top and annealed samples turn out to be metallic in nature [19]. This also supports the fact that the phases of Ni and Bi have indeed been formed. As mentioned earlier, we have studied ion beam mixing at three different energy regimes. In order to verify the mixing at very

high energy regime, where S_e is sufficiently large compared to S_n, we have irradiated Ni (35 nm)/Bi (35 nm) films with 100 MeV Au ions at different ion fluences [20, 21]. The values of S_e/S_n are 39.09 and 30.85 for Ni and Bi respectively. After the irradiation, the enhancement in the mixing of Ni and Bi at the interface with the increase in ion fluence has been observed. However, the mixing features were within 10 nm, which is less than 15% of the total thickness. From the TSM model, the temperature of the ion track is much less than the melting point of Ni and for that of Bi, it exceeds the melting point of Bi. For this reason, Ni was also called as an insensitive element for the swift heavy ions. Therefore, the observed marginal mixing has been attributed to the insensitivity of the Ni layer [20, 21]. After irradiation, an evolution of porous-like structures from a smoother surface has been observed. A possible out-diffusion of Bi, as it readily reaches the molten state after ion irradiation, must have been the reason for the observed evolution of porous structures. The thermal transport properties revealed that these films are superconducting at 3.9 K, which is very near to that of NiBi$_3$ phase. The critical fields of these layers remained almost the same with increasing ion fluence till highest fluence. This represents the robustness of the NiBi$_3$ compound to even such huge energy and higher fluences, which makes it a suitable candidate for space applications.

Prior to IBM study at medium energy, the sensitivity of Ni to that particular energy has to be verified. For this study, we have used 2.2 MeV Au ions on Ni thin films. After ion irradiation as a function of ion fluence, we have noticed that the islands of as-deposited films initially undergo volume diffusion followed by a surface diffusion. As a consequence of these processes, a drastic change in the surface morphology with increasing fluence has been observed. Depth profiles extracted from Rutherford backscattering spectrometry (RBS) spectra, revealed that this diffusion of Ni does not confine to the surface itself, but also diffuse much deep into the substrate. These findings suggest that the Ni layer is sensitive to such medium energy regime. Thermal spike model calculations also support these results, where it was noticed that the Ni layer reaches molten phase at this energy. Then, the IBM study on Ni/Bi bilayer system has been performed, where we have used 1 MeV Ni ions on Ni (5 nm)/Bi (5 nm) bilayer films. The values of Se/Sn are 0.99 and 1.21 for Ni and Bi respectively. Even this set of as-deposited samples show spontaneous diffusion, but the composition seems to be neither NiBi nor NiBi$_3$. The presence of these phases cannot be ruled out completely as their fraction might be quite less to quantify. Interestingly, the mixing features were extended almost to 6 nm, which is approximately 60% of the total thickness. The reason for such significant mixing

can be attributed to the improvement in the temperature and radii of latent ion tracks for both the layers. These effects were mainly due to comparable magnitudes of electronic and nuclear energy depositions. Therefore, as mentioned earlier, such values of S_e and S_n are believed to show synergistic effects, which may be responsible for the appreciable mixing.

In the low energy case, we have used 200 keV Ar ions for IBM of Ni (35 nm)/Bi (35 nm) bilayers as a function of ion fluence [22]. The values of S_e/S_n are 0.809 and 1.082 for Ni and Bi respectively. In the as-deposited films, we notice the presence of NiBi$_3$ phase, which was understood as a spontaneously formed layer during deposition due to reaction-diffusion mechanism [21]. No such layer formation has been observed in the previous case because the thickness of the films and as a result, the volume fraction of NiBi$_3$ may be quite less to detect. The heat of mixing or enthalpy of mixing for Ni and Bi is negative, which is responsible for the spontaneously formed NiBi$_3$ layer. After 200 keV Ar ion irradiation, the Ni layer diffuses towards Bi layer and the Bi layer diffuses into Ni layer upon increasing ion fluence. However, the observed mixing features were within 20 nm, which is less than 25% of the total thickness of the films. The mixing features were understood on the basis of thermal spike model calculations. According to the calculations, the ion beam drives the Bi layer to molten phase within the track radii of more than 3 nm around the ion path. However, the latent ion track radii for Ni layer were 1 nm only, which is the reason why there was no sufficient mixing, observed experimentally [30]. After irradiation, we observe the evolution of sponge-like morphology till certain fluence (5×10^{16} ions/cm^2), beyond which the surface becomes smoother. A competition between crystallization and amorphization of phases as a function of ion fluence has been realized. Interestingly, these features were reflected in the contact angle measurements, which show a transition of wettability from hydrophobic nature to hydrophilicity. All these findings were corroborated to the ion-induced sputtering and compositional changes of the layers.

From all the above findings, the mixing is more effective in the case of medium energy ion beam, where S_e and S_n are comparable. In the medium energy case, the mixing was almost 60% while it was less than 25% and 15% in low and swift heavy ion energy regimes respectively. The better mixing in the medium energy case must have been emanated from the equal contribution of nuclear and electronic energy losses. In the other cases, either S_e dominates over S_n or S_n dominates over S_e. Therefore, we conclude that the IBM for Ni-Bi system is much efficient for the ions, whose S_e and S_n are comparable with each other.

References:

1. M. Nastasi and J. W. Mayer, Mater. Sci. Eng., R, 12, 1 (1994).

2. J. F. Ziegler, *et al.*, Nucl. Instrum. Methods Phys. Res. Sect. B, 268, 1818 (2010).

3. Van der Weg, *et al.*, (Plenum Press, New York, 209 (1973).

4. A. Ibrahim, D. Thompson, Nucl. Instrum. Meth. in Phys. Res. Sec. B 7 566 (1985).

5. M. Bala, PhD thesis, IUAC, New Delhi (2016).

6. Y.T. Cheng, *et al.*, J. Appl. Phys. 60, 2615 (1986).

7. C. Dufour, PhD thesis, CEA-R-5638 (1993).

8. A. Chettah, PhD thesis, Universit de Skikda, Algeria, (2006).

9. P. Feschotte and J.M. Rosset, J. Less-Com. Met., 143, 31-37 (1988) (in French).

10. G. P. Vassilev, X. J. Liu, and K. Ishida, J. Phase Eq. Diff., 26, 2 (2005).

11. V. I. Dybkov, Solid State Reaction Kinetics, IMPS Publications, Kyiv, Ukraine, (2013).

12. G. Voss, Anorg. Chem. 57, 34 (1908).

13. M. Hansen. Constitution of binary alloys. 2nd ed.- New York: McGraw-Hill, (1958).

14. P. LeClair, J. S. Moodera, J. Philip and D. Heiman, Phys. Rev. Lett. 94, 037006 (2005).

15. T. Herrmannsdörfer, *et al.*, Phys. Rev. B 83, 140501(R) (2011).

16. E.L.M. Piñeiro *et al.*, Solid State Commun. 151, 425 (2011).

17. J. Kumar, *et al.*, Supercond. Sci. Technol. 24, 085002 (2011).

18. M. Sakarai, T. Ono, I. Yoshida, and S. Tanuma, Jpn. J. Appl. Phys. 39, 6366 (2000).

19. V. Siva, D. P. Datta, S. Prusty, and P. K. Sahoo, AIP conf. proc. 1832(1), 080021 (2017).

20. V. Siva, K. Senapati, B. Satpati, S. Prusty, D. K. Avasthi, D. Kanjilal, P. K. Sahoo, J. Appl. Phys. 117,083902 (2015).

21. V. Siva, A. Chettah, B. Satpati, S. Ojha, D. Kanjilal, P. K. Sahoo, RSC Adv. 58950, 6 (2016).

22. V. Siva, D. P. Datta, S. Chatterjee, S. Varma, D. Kanjilal and P. K. Sahoo, Appl. Surf. Sci. 410, 519 (2017).

Publications in Referred Journal:

a. Published

[†]1. V. Siva, K. Senapati, B. Satpati, S. Prusty, D. K. Avasthi, D. Kanjilal, P. K. Sahoo, Spontaneous formation of superconducting $NiBi_3$ phase in Ni-Bi bilayer films, J. Appl. Phys.

117,083902 (2015).

†2. V. Siva, D. P. Datta, A. Singh, T. Som, P. K. Sahoo, Nanocomposite synthesis and photoluminescence properties of MeV Au-ion beam modified Ni thin films, Appl. Surf. Sci. 360, 276 (2016).

†3. V. Siva, P. C. Pradhan, G. S. Babu, M. Nayak, P. K. Sahoo, K. Senapati, Superconducting proximity effect in $NiBi_3$-Ni-$NiBi_3$ trilayer system with sharp superconductor-ferromagnet boundaries, J. Appl. Phys. 119, 063902 (2016).

†4. V. Siva, A. Chettah, B. Satpati, S. Ojha, D. Kanjilal and P. K. Sahoo, Enhanced surface and interface diffusion in NiBi bilayers by swift heavy ion irradiation, RSC Adv. 58950, 6 (2016).

†5. V. Siva, D. P. Datta, S. Chatterjee, S. Varma, D. Kanjilal and P. K. Sahoo, Synthesis of sponge-like hydrophobic $NiBi_3$ surface by 200 keV Ar ion implantation, Appl. Surf. Sci. 410, 519 (2017).

6. V. Siva, S. S. Sahu, D. P. Datta, P. C. Pradhan, M. Nayak, V. Solanki, D. Topwal, K. Senapati, P. K. Sahoo, Ion irradiation induced phase transition of Co in Co/Au thin films, J. Alloys Compd., 680, 722 (2016).

7. S. Prusty‡, V. Siva‡, N. Shukla, B. Satpati, K. Senapati and P. K. Sahoo, Unusual ferromagnetic behaviour of embedded non-functionalized Au nanoparticles in Bi/Au bilayer films, RSC Adv. 6, 106584(2016). ‡equal contribution.

8. D. P. Datta, V. Siva, A. Singh, S. R. Joshi, D. Kanjilal and P. K. Sahoo Ion-beam-induced nanodots formation from Au/Si thin films on quartz surface, Nucl. Instrum. Methods Phys. Res. Sect. B, 379, 48, (2016).

9. D. P. Datta, V. Siva, S. Varma, D. Kanjilal and P. K. Sahoo, Ion induced dewetting of Au-Si on SiO_2 surface- composite nanodot evolution and wettability transition, Phys.Chem. Chem. Phys. 18, 29955 (2016).

10. S. N. Sarangi, V. Siva, B. K. Padhi and P. K. Sahoo, Synthesis of Cu-doped ZnO nanorods for photosensitive UV detection application, Adv. Mater. Lett. 8, 524 (2017).

11. S. S. Sahu, V. Siva, P. C. Pradhan, M. Nayak, K. Senapati and P. K. Sahoo, Progressive magnetic softening of ferromagnetic layers in multilayer ferromagnet-nonmagnet systems and the role of granularity, J. Appl. Phys. 121, 213905 (2017).

12. D. P. Datta, V. Siva, A. Singh, D. Kanjilal and P. K. Sahoo, Photoluminescent Au-Ge composite nanodots formation on SiO_2 surface by ion induced dewetting, Nucl. Instrum. Methods Phys. Res. Sect. B 407, 141 (2017).

b. Accepted:

[†]1. V. Siva, A. Chettah, A. Tripathi, D. Kanjilal and P. K. Sahoo, Interface mediated enhanced mixing of multilayered Ni-Bi thin films by swift heavy ion irradiation, Nucl. Instrum. Methods Phys. Res. Sect. B (2017) (DOI: 10.1016/j.nimb.2017.03.074)

c. Communicated:

[†]1. V. Siva, A. Chettah, A. Tripathi, D. Kanjilal and P. K. Sahoo, Enhanced mixing in Ni-Bi multilayers using swift heavy ion irradiation: Application of the inelastic thermal spike model, Intermetallics (Under review).

2. D. P. Datta, A. Chettah, V. Siva, D. Kanjilal, and P. K. Sahoo, Dewetting induced Au-Ge composite nanodot evolution in SiO_2, Appl. Surf. Sci.(Under review).

3. D. Suri, V. Siva, S. Joshi, K. Senapati, P. K. Sahoo, S. Varma, R. S. Patel, A study on electron and thermal transport in layered TiS_2 single crystals, Appl. Phys. Lett.(Communicated).

d. Other Publications (Published in Conference Proceedings):

[†]1. V. Siva, D. P. Datta, S. Prusty, and P. K. Sahoo, Solid state reaction induced phase evolution of Ni/Bi thin films, AIP conf. proc. 1832, 080021 (2017).

2. S. Prusty, V. Siva, S. Ojha, D. Kabiraj and P. K. Sahoo, Nanoscale Interfacial Mixing of Au/Bi Layers Using MeV Ion Beams, AIP Conf. Proc. 1832, 080026 (2017).

[†] Related to thesis.

List of conferences and workshops participated:

1. **Synthesis of chemically stable Phases in Ni/Bi Thin Film system by Ion Implantation and Thermal Annealing-** V. Siva, S. Prusty, A. Behera, M. Kumar, T. Som, D. Kabiraj, S. Ojha, D. Kanjilal and P. K. Sahoo in an International Conference on Nanostructuring by Ion Beams (ICNIB 2013) at the Gold Palace and Resorts, Jaipur India, from 23-25, October, 2013. (Poster presentation)

2. **Magnetic properties and phase synthesis of Ni/Bi thin film systems by swift heavy ions** -V. Siva, K. Senapati, S. Prusty, S. Ojha, D. K. Avasthi, D. Kanjilal, and P. K. Sahoo in an International conference on Swift Heavy Ions in Materials Engineering and Characterization (SHIMEC 2014) at Inter-University Accelerator Centre (IUAC), New Delhi, India from 14-17,

October, 2014. (Poster presentation)

3. **Structural modification of Ni/Bi bi-layer thin films by ion implantation and thermal annealing-** V. Siva, S. Prusty, M. Kumar, T. Som and P. K. Sahoo in an International conference on Physics at surfaces and Interfaces (PSI 2014), at Puri, Odisha, India from 24-28, February, 2014. (Poster presentation)

4. **Modification of structural and magnetic properties of Ni/Bi systems by swift heavy ions -**V. Siva, K. Senapati, B. Satpati, S. Prusty and P. K. Sahoo Indo-Japan Workshop on Magnetism at Nanoscale (IJWMN) at NISER Bhubaneswar, Odisha, India from 09-12, January, 2015. (Poster presentation)

5. **Modifications of structural and magnetic properties of Au/Co multi layers by ion irradiation -**V. Siva, K. Senapati, S. S. Sahu, A. Agrawal, P. C. Pradhan, M. Nayak, S. Mahana, D. Topwal and P. K. Sahoo Current trends on Condensed Matter Physics (CTCMP 2015) at NISER Bhubaneswar, Odisha, India from 19-22, February, 2015. (Poster presentation)

6. **MeV Ion beam induced modification of bi-metallic system -** V. Siva, P. C. Pradhan, M. Nayak, and P. K. Sahoo, in the Workshop on the Use of Low Energy Ion Beams at Institute of Physics, Bhubaneswar, Odisha, India from 7-9, November, 2015. (Oral presentation)

7. **Interface mediated enhanced mixing of multilayered Ni-Bi thin films by swift heavy ion irradiation -**V. Siva, E. Bhatia, K. Senapati, A. Tripathi, D. Kanjilal, P. K. Sahoo in an international conference Ion beam Modification of Materials (IBMM 2016) at Te Papa, Wellington, New Zealand from 30 October 04 November, 2016. (Poster presentation)

8. **Solid state reaction induced phase evolution of Ni/Bi thin films** V. Siva, D. P. Datta, S. Prusty and P. K. Sahoo in a national conference DAE Solid State Physics Symposium (DAE-SSPS 2016) at KIIT University, Bhubaneswar, Odisha, India from 26-30, 2016. (Poster presentation)

List of Figures

List of tables

List of Abbreviations

AFM	Atomic Force Microscopy
ALD	Atomic Layer Deposition
CBED	Convergent Beam Electron Diffraction
CCD	Charge Coupled Device
CSF	Coexistence of Superconductivity and Ferromagnetism
CVD	Chemical Vapour Deposition
DC	Direct Current
ECR	Electron Cyclotron Resonance
EDS	Energy Dispersive Spectroscopy
ETSM	Elastic Thermal Spike Model
FESEM	Field Emission Scanning Electron Microscope
FFLO	Fulde Ferrel Larkin Ovchinnikov
FM	Ferromagnetism
FWHM	Full Width at Half Maximum
GAXRD	Glancing Angle X- Ray Diffraction
HAADF	High Angle Annular Dark Field
HOM	Heat Of Mixing
IBM	Ion Beam Mixing
IPA	IsoPropyl Alcohol
ITSM	Inelastic Thermal Spike Model
IUAC	Inter University Accelerator Center

keV	kilo electron Volt
LEIBF	Low Energy Ion Beam Facility
MBE	Molecular Beam Epitaxy
MC-SNICS	Multi Cathode- Source of Negative Ions by Cesium Sputtering
MeV	Mega electron Volt
nm	nanometers
pnA	particle nano Ampere
PPMS	Physical Property Measurement System
PSD	Power Spectral Density
PVD	Physical Vapour Deposition
QCM	Quartz Crystal Monitor
RBS	Rutherford Backscattering Spectrometry
RED	Radiation Enhanced Diffusion
RF	Radio Frequency
RMS	Root Mean Square
SAED	Selected Area Electron Diffraction
SC	Superconductivity
SHI	Swift Heavy Ions
SQUID	Superconducting QUantum Interference Device
SRIM	Stopping and Range of Ions in Matter
STEM	Scanning Transmission Electron Microscope
TEM	Transmission Electron Microscope
TMP	Turbo Molecular Pump
TSM	Thermal Spike Model
UHV	Ultra High Vacuum
XRD	X-Ray Diffraction
XTEM	Cross-sectional Transmission Electron Microscope

Chapter 1

Introduction

1.1 Ion beam mixing

Ion beam mixing (IBM) is one of the most efficient and effective routes to synthesize stable or metastable alloy phases. IBM may be defined as an intermixing and/or alloying that can occur at the interface of two different materials during ion irradiation [1]. This technique offers several advantages over conventional techniques, particularly in terms of spatial selectivity, relatively low-temperature process, less preparation time, and capability of mixing immiscible systems. Among these advantages, spatial selectivity offers a way to synthesize the phases in a particular region of interest by irradiating the films in that specified area. Moreover, this method does not require high temperatures like the thermal annealing (several hundred to few thousands of degree Celsius), which can be performed even at the room temperature. Furthermore, the duration of the phase synthesis may considerably be reduced compared to the other conventional techniques. Among the aforementioned advantages, the capability of mixing immiscible systems is the most interesting aspect of this technique, which is only possible through this method due to the ion-induced long-range ballistic effects [2–6].

This IBM technique was first discovered by Van der Weg *et al.* in 1973 [7], where Pd thin films on Si substrates led to form palladium silicide after Ar ion irradiation. There are several studies on IBM of binary multilayer systems in the literature. For example, Ibrahim *et. al.*, have reported on the alloy phase synthesis of Bi-Sb system using this method by varying different parameters such as ion fluence, ion energy, and temperature [8]. Also, Manju *et. al.* have shown the mixing of Co-Sb and Pb-Te systems as well as engineering their thermo-electric properties upon ion irradiation [9]. Cheng *et al.* have extensively studied the IBM and the formation of amorphous alloys of various binary systems such as Au-Ag, Pt-Pd, Hf-Zr, W-Mo, Ta-Nb, Ru-

Zr, Ru-Ti and so on [10]. Apart from the IBM study of metal-metal systems, there are few more interesting studies on metal-semiconductor systems. For example, the IBM study of metal-Ge systems such as Cu-Ge, Ni-Ge, Co-Ge, and Au-Ge have been studied by various groups and also reported their phase formation [11–16]. Similar work has been carried out on ion beam mixing of the metal-Si system such as Co-Si, Ni-Si, Pt-Si, Pd-Si, Mo-Si, W-Si, Cr-Si, Mg-Si, Fe-Si, Ta-Si, Au-Si systems [17–22], where they have achieved their stable and/or meta-stable phases. Since ion beam mixing is one of the best alternatives for conventional techniques for the phase synthesis with added advantages, it has been the subject of research interest to many research groups from last few decades.

1.2 Ion-matter interaction

In order to understand the mechanism of ion beam mixing, it is essential to have a basic knowledge of ion-matter interaction, which has been discussed below. While an energetic ion traversing through the target atoms, the energy of ion dissipates via two processes, those are (i) elastic and (ii) inelastic collisions. In the former process, most of the ion loses its energy to the atomic subsystem, which is widely known as nuclear energy loss (S_n). Whereas, in the later process, the ion loses its energy mostly to the electronic subsystem and it is known as electronic energy loss (S_e). It is to be mentioned here that both these energy losses take place at all the energy regimes. However, one of them dominates over the other, depending on the energy and species of the ion beam. The total energy loss of the ion beam is simply the arithmetic summation of both nuclear and electronic energy losses. This can be described mathematically as the following:

$$\left(\frac{dE}{dx}\right)_{Total} = \left(\frac{dE}{dx}\right)_{nuclear} + \left(\frac{dE}{dx}\right)_{electronic} \qquad (1.1)$$

Depending on the energy and species of the ion beam and the target species, the ion stops at a certain depth from the surface, which is known as projected range of ions. The values of energy loss and ion range can be obtained using a software called SRIM (Stopping and Range of Ions in Matter) [28]. This software works based on a Monte Carlo simulation method, which considers the binary collision approximation with a random selection of the impact parameter of the next colliding ion. The software also gives certain other information such as ion and recoil distribution, sputtering yield, ionization, vacancies and so on. Among all of them, the energy
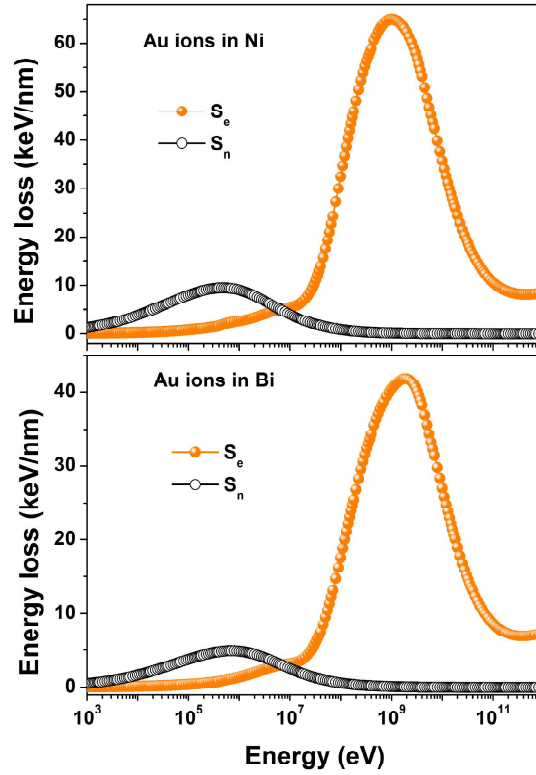
Figure 1.1: Electronic and nuclear energy losses variation for Ni and Bi targets as a function of ion energies.

losses are of primary interest in any basic study related to ion-matter interaction. Therefore, the dependence of electronic and nuclear energy losses on the energy of Au ions for Ni and Bi targets are shown in 1.1. It is discernible from the figure 1.1 that the nuclear energy loss is dominating electronic energy loss at low energy regime which follows the opposite trend at the high energy regime. This kind of behaviour is true for any material. In general, the ions with energy per nucleon is less than few keV/amu are termed as low energy ions, while the energy of ions is greater than 0.1 MeV/amu are termed as swift heavy ions (SHI). In the present study, the medium energy term is used for the ions whose electronic and nuclear energy losses are of the same order.

It is well known that the ion beam mixing depends on several parameters such as the energy of ion beam, ion fluence, ion species, target temperature, number of layers and their thicknesses. Therefore, it is essential to discuss each of these parameters before getting into the details of IBM. The energy of ion beam plays an important role as it is one of deciding factors for the

mechanism of mixing and hence it needs to be carefully selected. It also decides the penetration depth of ions where most of the ions stop inside the target, which is broadly known as projected range of ions (R_P). Ion fluence/ dose is nothing but the number of deposited ions in the target per unit area. In general, the range of these ion fluences is selected based on the energy of the ion beam. The selection of ion species is equally important, where one can choose two types of species. The ion species can be either the same species that of the target elements or the inert gas elements to avoid the presence of foreign elements and impurities in the matrix. The target temperature during the ion irradiation, which is an additional thermal energy supplied to the target atoms to enhance the mixing rates. This process is widely known as radiation enhanced diffusion (RED). The number of layers is also one of the important parameters, as the more number of layers can increase the possibility of mixing the atoms at the interface with the additional neighbouring layers. The thickness of each layer is also a matter of concern in the mixing study. If the thickness is less, then there is a high chance for the atoms to mix at the interface. Therefore, it is always preferable to have more number of layers and lesser thick films to increase the rate of mixing and thereby achieve more mixing. The main parameter in the case of IBM, which decides whether a system is miscible or not, is the heat of mixing.

The possibility of mixing of any system using ion beam mixing may be predicted using two factors, they are the heat of mixing and cohesive energy.

1.2.1 Heat of mixing

Prior to the selection of a particular system for the investigation of the ion beam mixing, there is an important factor to be taken into consideration, which is the so-called heat of mixing (ΔH_{mix}). It gives a measure of how repulsive (or attractive) the elements are to each other compared to their repulsiveness (or attractiveness) to themselves. For example, if there are two layers A and B, as shown in figure 1.2, whose ΔH_{mix} can be given by the following equation [23]:

$$\Delta H_{mix} = X_A X_B Z_c N_a \left[H_{AB} - \frac{(H_{AA} + H_{BB})}{2} \right] \tag{1.2}$$

Where X_A and X_B are the mole fractions of A and B respectively. The terms Z_c and N_a are the coordination number and Avogadro's number respectively. The parameters H_{AA}, H_{AB} and H_{BB} are the mean bonding enthalpies between the atom pairs A-A, B-B and C-C respectively. Depending on the values of ΔH_{mix}, any given binary system can be classified into

4
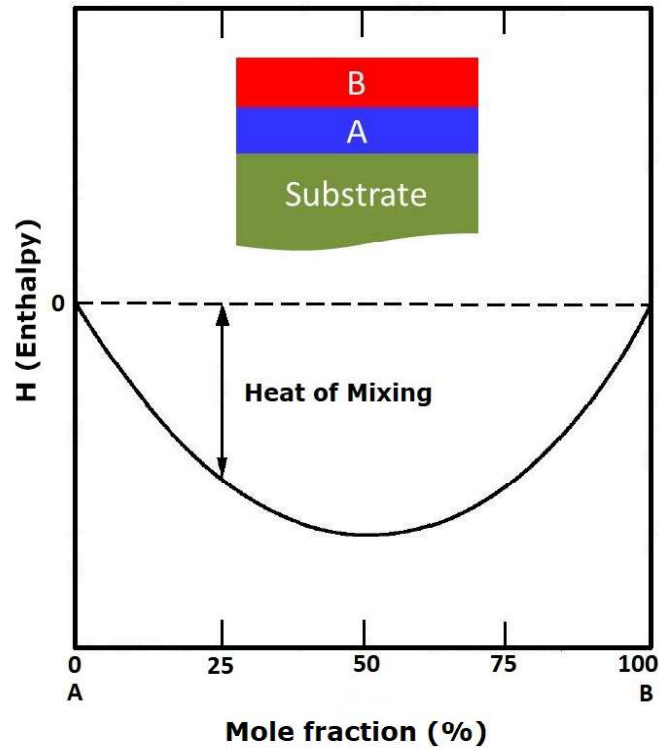
Figure 1.2: Variation of the heat of mixing with the mole fraction of A from 0 to 100% (from right to left) and B (from left to right) respectively. The inset shows the schematic diagram of the layers A and B, deposited on a substrate.

two categories i.e., miscible and immiscible systems. The ΔH_{mix} can also be understood in terms of the heat of alloy formation, which is negative for the miscible systems and it is positive for the immiscible systems. It is worth mentioning here that the more negative is the ΔH_{mix}, the greater is the possibility of alloy formation. After ion irradiation, the systems with the negative ΔH_{mix} lead to the stable phases formation while that of the systems with the positive ΔH_{mix} leads to the formation of meta-stable phases or no phases. For example, Pan *et al.* [5] have reported the formation of metastable phases in immiscible systems, like Fe-Cu system whose ΔH_{mix} is $+13kJ/mol$. A similar study on Fe/Ag system has revealed the mixing, even though the ΔH_{mix} is $+28kJ/mol$, using the ion beam mixing [6]. Therefore, it is essential to have a sufficient information about the ΔH_{mix} of the binary system to be studied. The heats of formation for both the phases NiBi and NiBi$_3$ are negative and these values were calculated to be $-4\ kJ.mol^{-1}$ and $-5\ kJ.mol^{-1}$ respectively [24]. However, there are no experimental data available for these phases till now. Therefore, it is safe to consider the Ni-Bi system as a miscible system.

1.2.2 Cohesive energy

In the previous section, two cases have been discussed where the ΔH_{mix} was either negative or positive. It means that the chemical driving forces are responsible for the alloys to be formed. If the ΔH_{mix} between two elements is zero, which means that there is no role of chemical forces in the observed mixing. In such case, the mixing phenomenon can be explained on the basis of ballistic effects that are governed by the cohesive energy of the elements. For example, a study of the ion beam mixing on several systems has already been performed such as Au-Ag, Ta-Nb, Hf-Zr, Pt-Pd, and W-Mo, whose heats of mixing are zero [1, 25]. In this case, the experimentally observed rates of mixing were explained with the help of cohesive energy. The cohesive energy (ΔH_{coh}) has been defined as the difference between the energy of the same number of free neutral atoms at infinite separation and the energy of the solid. This ΔH_{coh} can, simply, be understood in terms of an energy that holds a material together. Interestingly, it was observed that the rates of ion beam mixing of various systems were seen to vary inversely proportional to the square of the cohesive energy [26, 27]. The dependence of rates of ion beam mixing on cohesive energy was believed to be rooted in the atomic diffusion in the cascade. This cohesive energy can be expressed mathematically as the following [1]

$$\Delta H_{coh} \approx (X_A \Delta H_A^0 + X_B \Delta H_B^0) + \Delta H_{mix} \tag{1.3}$$

Where X_A, X_B are mole fractions of elements A and B respectively. The cohesive energies of individual elements A and B are represented by ΔH_A^0 and ΔH_B^0 respectively.

1.3 Configurations in the study of IBM

In general, the ion beam mixing can be carried out in various ways or configurations [18, 29]. These configurations can broadly be classified into three types, which are bilayer, multilayer, and marker layer configurations as shown in figure 1.3. In the case of bilayer configuration, there are two possibilities. The first one is taking two thin film layers, say A and B, while the other one is depositing A layer on B substrate or vice-versa. After the irradiation, the atoms of one layer at the interface mixes with the atoms in the other layer. The mixing depends on the energy loss mechanism of ion as well as on the nature of the target. In order to enhance the mixing, one can use many such alternating bilayers, the so-called, multilayers, where each layer gets to have two neighboring layers. This improves the chance of mixing compared to

6

Ion beam

A
B
Substrate

A+B
Substrate

(a) Bilayer Configuration

Ion beam

A
B
⋮
A
B
Substrate

A+B
Substrate

(b) Multilayer Configuration

Ion beam

A
C
B
Substrate

A
C
B
Substrate

(c) Marker Configuration
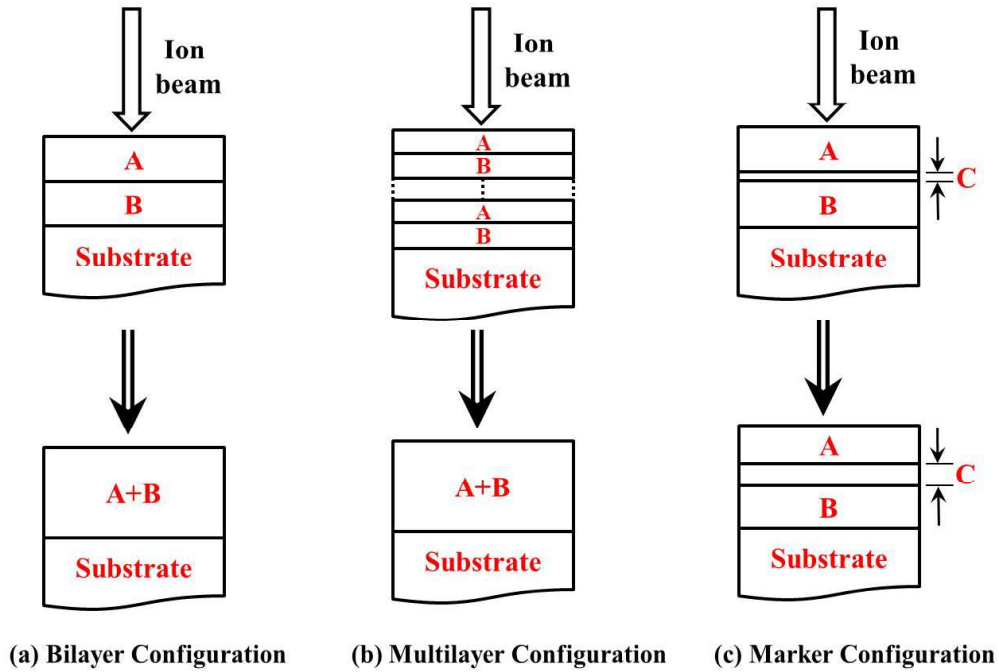
Figure 1.3: Typical configurations for the study of ion beam mixing.

bilayer configuration. In the case of marker layer configuration, a thin i.e., typically a few nm's of thick, layer separates the layers A and B. The purpose of this configuration is mainly to understand the diffusion and dynamics of the atoms upon the ion irradiation. Using the marker layer configuration, one can also determine the effective diffusive coefficient of a material. The aforesaid configurations mainly provide the basic understanding of ion beam mixing process.

1.4 Models to explain IBM

In order to explain the mechanism of ion beam mixing, several theoretical models have been proposed, which varies depending on the ions energy regime as well as on the type of target materials. A schematic representation of all the successful models to explain the ion beam mixing are shown in figure 1.4. These models can be classified into three types based on the energy loss mechanisms. In the case of dominant electronic energy loss over nuclear energy loss, coulomb explosion model and thermal spike model are two successful models to explain the mixing in this energy regime and both the models are explained below in detail. On the other hand, in the energy regime, where the S_n dominates over S_e, elastic thermal spike model and ballistic models can explain the mixing. Finally, in the energy regime where both the

IBM Models

$S_e \gg S_n$	$S_e \ll S_n$	$S_e \approx S_n$

Coulomb explosion model **Inelastic TSM**	**Ballistic model** **Elastic TSM**	**Ballistic model** **Unified TSM**
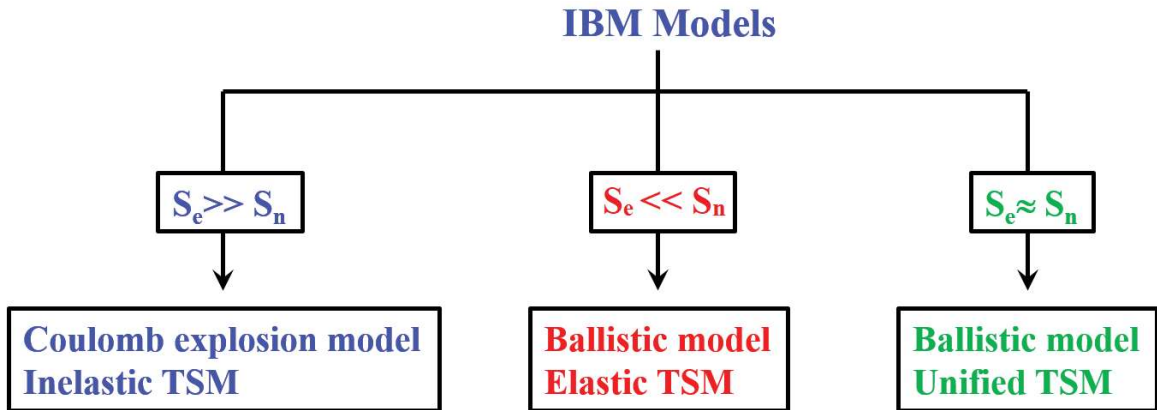
Figure 1.4: Models to explain the ion beam mixing at different energy regimes.

magnitudes of S_e and S_n are of the same order, then the unified thermal spike model and ballistic model are used in explaining the mixing. To understand the mixing phenomenon in Ni-Bi system, the IBM study has been performed at three different energy regimes, where the underlying mechanisms are different. They are:

1. Swift heavy ion beam mixing

2. Medium energy ion beam mixing

3. Low energy ion beam mixing

1.4.1 Swift heavy ion beam mixing

Swift heavy ions are those ions, whose energy per nucleon is more than 0.1 MeV/amu. In this energy regime, the magnitude of the electronic energy loss (S_e) is much higher compared to that of nuclear energy loss (S_n). The most successful models among the proposed models to explain the mixing phenomenon in this energy regime are Coulomb explosion model and thermal spike model.

Coulomb explosion model

According to this model, the ion beam ionizes the atoms around its path while passing through the target as shown in figure 1.5. These ions form a cylindrical track along their path, where most of the target atoms are ionized. Since these are likely charged ions and are subjected to experience the coulomb repulsive force. This repulsive force can drive these ionized atoms

8
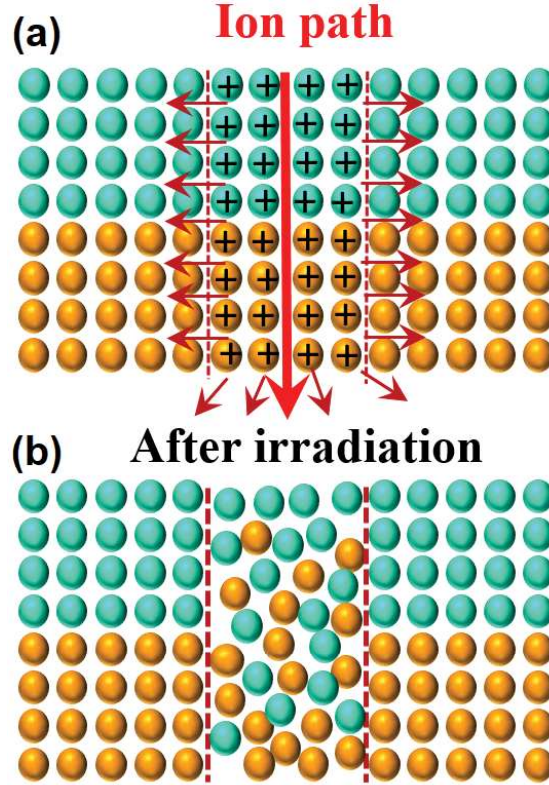
Figure 1.5: Schematic representation of ion beam mixing in a single bilayer through coulomb explosion model, before (a) and after (b) ion irradiation.

away from the ion's path. These positive ions can modify the chemical bonds and crystalline nature and may result in phase transition [30–32]. The coulomb explosion is expected to take place, when the charge neutralization time is greater than 10^{-14} s and coulomb repulsive force is greater than the binding forces between the lattice atoms. The coulomb repulsive forces are sufficient enough to break the bonds of lattice atoms in terms of a local electrostatic stress being more than the strength of those bonds. If two ions having charge e, dielectric constant (ϵ), average atomic spacing (a) and the number (n) of times the ion has undergone ionization, then the electrostatic stress (σ) between the ions can be given by [33]

$$\sigma = \frac{n^2 e^2}{\epsilon a^4} \tag{1.4}$$

For the coulomb explosion to takes place during the ion-matter interaction, the magnitude of σ should be at least ten times more than Young's modulus of that material. Therefore, the formation of such ion tracks is possible in only those materials, whose mechanical strength and dielectric constants are low as well as the average inter-atomic spacing is small. To provide
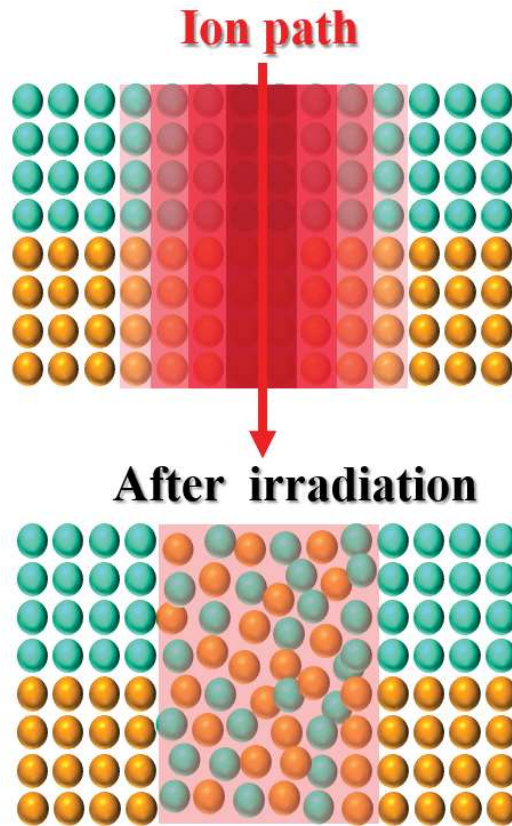
Figure 1.6: Schematic representation of thermal spike model, where (a) shows the latent track formation around the ion path in the atomic lattice of single bilayer films and (b) shows the ion-induced mixing around the ion path.

a clear picture in mind about the coulomb spike model, it has been shown using a schematic diagram in figure 1.5. An atomic arrangement in a lattice and ionization of those atoms around the ion track are shown in this figure. The movement of target atoms away from the ion's path after the ion irradiation has also been shown. This model does not explain the formation of ion track in the case of metals because of the availability of abundant amount of electrons in metals, which can immediately neutralize the ionized target atoms [34]. Therefore, this model cannot explain the mixing in the case of metallic systems, which has been addressed by a model called thermal spike model.

Thermal spike model

Thermal spike model assumes the target as two different subsystems, namely electronic and atomic subsystems, which are coupled together through an electron-phonon coupling constant. The thermal spike is often defined as a limited volume, where the majority of target atoms are

temporarily in motion. In order to explain the thermal spike diffusion, various models have been proposed by different groups. This model was initially proposed by Dessauser [35], which was developed by G. H. Vineyard [36]. It was further developed by M. Toulemonde *et al.* [36–39], which was widely known as inelastic thermal spike model (ITSM). This model was named so, because it does not include the contribution of nuclear energy loss term in the calculations. In 2011, Toulemonde *et al.* have further improved the model by including the contribution of nuclear energy loss in the calculations, which is now known as unified thermal spike model (UTSM). This model is the most successful one among all the other proposed models, which explains the mixing starting from low to very high energy regimes. A schematic representation of the thermal spike model has been shown in figure 1.6. An arrangement of the lattice atoms and rise in temperature of the atoms after the irradiation has been also shown in this figure. The latent track formation around the ion path and the temperature gradience (highlighted in red color) away from the ion-path radially have also been higlighted in the figure. Further details of the thermal spike models are provided in the chapter-6.

It is to be mentioned here that the mechanism of ion beam mixing differs depending on the dominant energy loss in that particular system. While Scanning over the energy dependence on the ion-induced mechanism based models may be described as the following:

$$S_e + S_n(\approx 0) \; = \; Inelastic\,Thermal\,Spike\,Model \tag{1.5}$$

$$S_e(\approx 0) + S_n \; = \; Elastic\,Thermal\,Spike\,Model \tag{1.6}$$

$$S_e + S_n \; = \; Unified\,Thermal\,Spike\,Model \tag{1.7}$$

1.4.2   Low energy ion beam mixing

If the energy of the ion per nucleon is less than or equal to few keV/amu, then those ions are known as low energy ions. In this energy regime, most of the energy of the ions would be spent in collisions with the target atoms. In the collision process, the target atoms may get displaced from their lattice sites and gradually form a collision cascade. These displaced atoms from one layer at the interface may mix with the atoms in the next neighbouring layer. Depending on

the interaction duration, one can divide the effect of these collisions into two regimes. Those are namely, prompt and delayed regimes, which happens in few picoseconds and nanoseconds respectively. In the former regime, mostly ballistic effects take place, whereas in the later one thermal spike and radiation enhanced diffusion are expected take place.

Ballistic effects

In the ballistic processes, both cascade and recoil effects are believed to be responsible for the mixing. During the passage of an ion into a solid, it transfers part of its kinetic energy to the target atoms through the so-called primary collisions. These atoms get recoiled and collide with the other target atoms, which were termed as secondary collisions. The later generated collisions yield several such low energy recoils, which lead to smaller displacements in arbitrary directions. The observed mixing in this process is often known as cascade mixing. If the atomic relocation or mixing happens due to the recoils that are generated during the primary collision process, that process is known as recoil mixing. However, the contribution of recoil mixing to overall mixing is almost negligible. These processes during the interaction of low energy ions with the matter are shown in figure 1.7. The ballistic effects take place typically within the time frame of 10^{-11} s, which is also called as the prompt regime. There can be two types of collisions, namely head-on and side-wise collisions. The head-on collision can take the atoms to much farther distances from their actual positions compared to the collision process and hence can improve the mixing considerably.

Radiation Enhanced Diffusion (RED)

It is known that the ion bombardment with the matter can create several types of defects such as Frenkel defects, point defects, vacancies, displacements, interstitials and replacement collisions. These are the defects produced in the prompt regime at ambient temperature, which may thermally be activated by providing certain temperatures. If the ion irradiation experiments are carried out at elevated temperatures, then this process is known as Radiation enhanced diffusion (RED). In this process, the defects created during ion irradiation can become highly mobile due to additionally supplied thermal energy, which leads to more and more diffusion and hence can improve the mixing. Following are the assumptions that were made in the development of this model [40]:

1. Recombination of vacancy and interstitials determines the RED process mostly
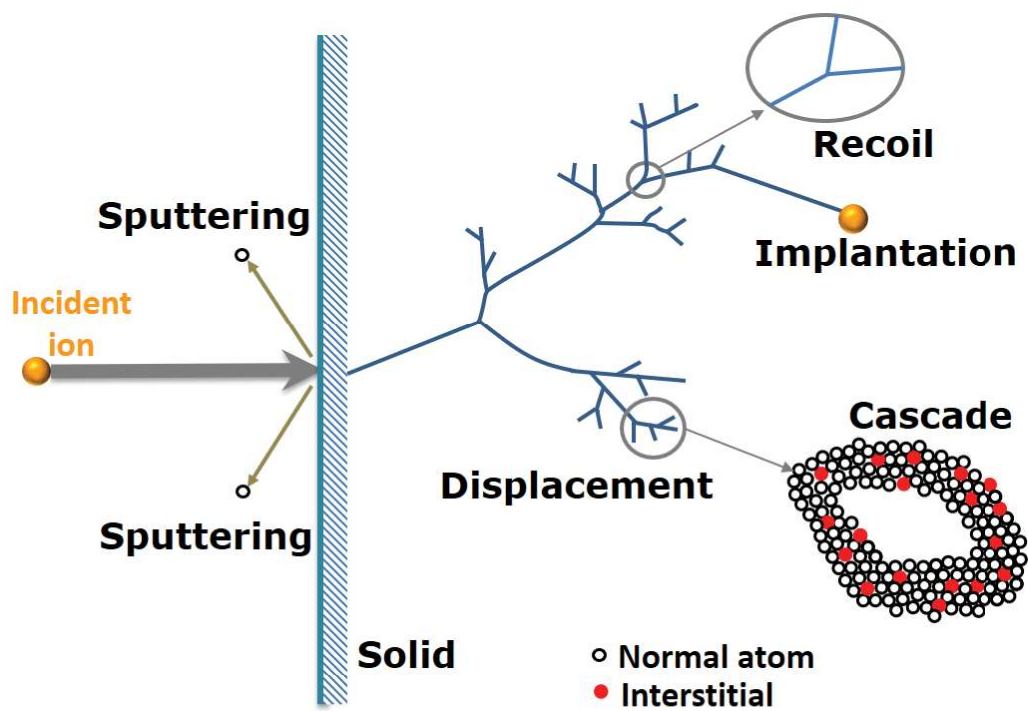
Figure 1.7: Schematic representation of ballistic processes during the ion-matter interaction. The main effects such as sputtering, implantation, recoils, displacement, and cascades are shown in figure.

2. Ion irradiation does not affect the activation energy for defect migration

3. Production and annihilation of defects are balanced and thereby causing stationary vacancy and interstitial concentrations.

It may be noticed here that the ballistic mixing is temperature independent, but the RED is temperature dependent. The required temperature to make the defects mobile was named as transition temperature (T_c), which depends on the cohesive energy ($\triangle H_{coh}$) of the system [40] .

$$T_c = 95.2 \times \triangle H_{coh}(ev/atom) \tag{1.8}$$

It was shown by Rauschenbach *et al.*, that the vacancy migration enthalpy depends linearly on T_c [41]. It was further confirmed by Cheng *et al.*, through their experimental findings [10,42]. In the present study, the temperature has not been supplied to the target atoms during the ion irradiation.

Thermal spike effects

The thermal spike effects in the low energy regime can also be explained on the basis of the same nonlinear coupled differential equations. In the case of ideal low energy case, the contribution of electronic energy loss is almost neglected compared to the nuclear energy loss. Therefore, the energy deposition happens to the atomic subsystem directly, unlike the case of SHI regime, where the energy deposition happens to the electronic subsystem and then it is transferred to the atomic subsystem of the target. Since the energy deposition happens to the atomic subsystem through elastic collisions, this model is also known as elastic thermal spike model (ETSM).

1.4.3   Medium energy ion beam mixing

The medium energy of ion beams, in the present case, has been defined as the ions, having nearly equal magnitudes or same order of magnitudes of electronic and nuclear energy losses. In the case of high energy ions, where the S_e dominates over S_n, which is the other way around in the case of low energy ions. In this energy regime, since the S_e and S_n are in the same order of magnitude, the synergistic effects of both electronic and nuclear energy losses are expected to be responsible for the mixing.

Table 1.1: Electronic, nuclear energy losses and their ratio as well as projected ranges of different energetic ions in Ni and Bi targets

Species and energy of ion beam	Target elements	S_e (keV/nm)	S_n (keV/nm)	S_e/S_n	Projected Range (nm)
200 keV Ar ions	Ni	0.826	1.02	0.809	78.4
	Bi	0.435	0.402	1.082	112.8
1 MeV Ni ions	Ni	1.234	1.239	0.99	314.5
	Bi	0.74	0.61	1.21	419
2.2 MeV Au ions	Ni	3.45	7.63	0.45	181
100 MeV Au ions	Ni	32.45	0.83	39.09	6010
	Bi	17.59	0.57	30.85	9840
120 MeV Au ions	Ni	36.7	0.72	50.65	6570
	Bi	20	0.5	39.74	1084
150 MeV Au ions	Ni	41.95	0.61	68.73	7310
	Bi	23	0.42	54.14	1218
200 MeV Au ions	Ni	48.13	0.49	98.95	8400
	Bi	26.8	0.34	78.63	1412

1.5 Parameters in the present IBM study

In the present thesis, three different energy regimes have been used as mentioned above. In the low energy regime, 200 keV Ar ions and the fluence range of $5 \times 10^{14} - 1 \times 10^{17}$ ions/cm^2 have been used. In the case of medium energy regime, 1 MeV Ni and the fluence range of $1 \times 10^{15} - 1 \times 10^{16}$ ions/cm^2 have been used. In the case of swift heavy ion energy regime, 100 and 120 MeV Au ions have been used within the fluence range of $1 \times 10^{12} - 1 \times 10^{14}$ ions/cm^2. The values of electronic (S_e), nuclear energy losses (S_n), their ratios and the projected ranges of all the ions in the Ni and Bi targets are shown in the table 1.1. In the Ni layer or target, it may be observed from the table 1.1 that the ratio of S_e over S_n is almost 1 in the case of medium energy (1 MeV Ni) ions, whereas it is much higher than 1 and lesser than 1 in the case of Swift heavy (100 MeV Au, 120 MeV Au, 150 MeV Au and 200 MeV Au) ions and low energy (200 keV Ar) ions respectively. However, it may be noticed that the ratio of S_e and S_n i.e., S_e/S_n in the case of Bi target is more than 1 in all the used energy regimes. Since, the Bi target is sensitive to the ion beams and reaches the molten phase in all the given energy regimes, it does not affect the mixing of the present system much. Therefore, the S_e/S_n ratio for Ni target is crucial in the present case. Accordingly, the aforementioned energy regimes have been chosen.

1.6 Importance of Ni-Bi system

In the present thesis, we have chosen Ni-Bi system for the study of the ion beam mixing, as it offers several interesting physics issues along with its applications in the field of science and technology. It needs to be mentioned here that the Ni-Bi binary system has two possible alloy phases, those are NiBi and NiBi$_3$. The crystal structure of NiBi is identical to NiAs structure with a phase group of P6$_3$/mmc, whereas the crystal structure of NiBi$_3$ is similar to that of CaLiSi$_2$ structure with the space group Pnma [44, 47]. Schematics of crystal structures of NiBi$_3$ and NiBi are shown in figure 1.8(a) and (b) respectively. Interestingly, both these phases, NiBi and NiBi$_3$, are superconducting in nature with the transition temperatures 4.25 K and 4.06 K respectively. The melting points of NiBi and NiBi$_3$ compounds are 646 ^{o}C and 467 ^{o}C respectively [45]. The phase diagram of this binary system has been reported by many research groups, which was first proposed by G. Voss *et al.* [46]. It was further studied by Feschotte *et al.* [47] and Hansen *et al.* [48], where they have proposed a modified phase diagram. The latest phase diagram of Ni-Bi system is shown in figure 1.9, which was reported
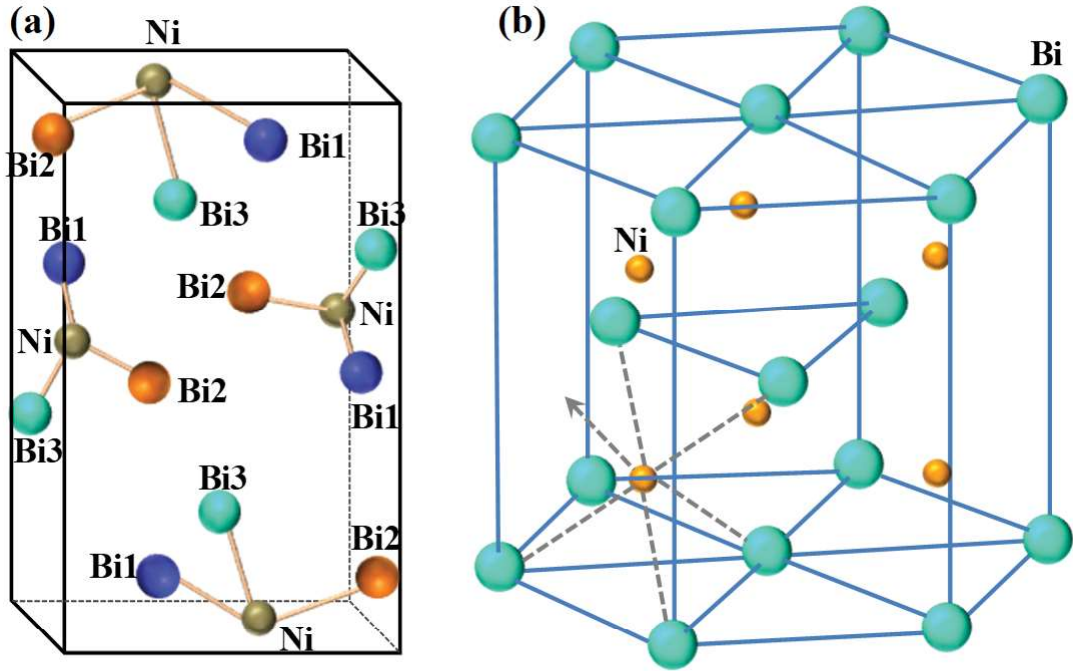
Figure 1.8: Schematics of crystal structures of (a) $NiBi_3$ and (b) NiBi compounds.

by Okamoto *et al.* [43]. It has been suggested that the composition of NiBi phase is 51.0 ± 0.3 at %, whose range of homogeneity was found to be quite narrow, while the other intermetallic compound ($NiBi_3$) was reported to be stoichiometric [43, 45]. This binary system has got one eutectic point and two peritectic points. The eutectic temperature is $\approx271^oC$, above which, the Ni and Bi atoms start forming $NiBi_3$ phase. Depending on the ratio or the composition of Ni and Bi, they form NiBi and $NiBi_3$. The peritectic temperature is something at which one of the existing phases would start disappearing. The first peritectic temperature (P1) of this system is $\approx471^oC$, above this temperature $NiBi_3$ phase would slowly decompose into NiBi compound and two Bi atoms. On the other hand, the second peritectic temperature (P2) is $\approx654\ ^oC$ in this case. Beyond this temperature, NiBi would decompose into individual Ni and Bi atoms.

For the first time in Ni-Bi system, LeClair *et al.*, [49] have reported a phenomenon called coexistence of superconductivity and ferromagnetism (CSF), where the same electrons are responsible for both ferromagnetism and superconductivity. It was mentioned that the competition can be tailored by varying the thickness of Ni layer in Ni/Bi bilayers. More interestingly, the coexistence was observed in the Ni side of Ni/Bi layers, but not in both the layers. Before, getting into the details of other properties of Ni-Bi system, It is worth noting here that the details of the CSF in brief. It is well known that the Superconductivity (SC) and Ferromagnetism

17

(FM) are two fundamental phenomena of a condensed matter. It is to be mentioned here that the FM favours all spins parallel, while in the other one spins align themselves in an antiparallel configuration as soon as the carriers condense in the form of cooper pairs. These cooper pairs can easily be broken, if there exists any small concentration of magnetic impurities, which is widely known as the pair-breaking effect. Therefore, it was anticipated that both these phases cannot coexist together in a single material, till the prediction of FFLO theory(Fulde, Ferrel, Larkin and Ovchinnikov) [50, 51]. They proposed, for the first time, that these phases can coexist together, when an exchange or Zeeman splitting of carrier bands occur. As a consequence of which, the minority and majority Fermi surfaces will no longer be identical and time-reversed pairs with zero net momentum cannot form [49]. Therefore, the realization of such coexistence experimentally becomes quite difficult as the competition between the exchange energy and superconducting condensation energy is extremely delicate. However, there are few compounds where the coexistence of Superconductivity and Ferromagnetism (CSF) has been accomplished. Till date, there are few compounds which shows the CSF property, some of them are Uranium based compounds such as UGe_2 [52], URhGe [53], UCoGe [54]. This phenomena has also been observed in other compounds like $ErRh_4B_4$ [55], $ErNi_2B_2C$ [56] and few more complex compounds. Ni-Bi system is one of the very few compounds/phases to show the CSF.

Later on, Herrmansdörfer *et al.*, [57] have shown this coexistence in the case of submicrometer and quasi-one-dimensional $NiBi_3$ nanostructures, which had been attributed to the structural confinement of the compound. In the same year, Pineiro *et al.*, [58] have reported a possibility of the coexistence in the polycrystals of $NiBi_3$. In the same compound of flux-grown single crystals, Silva *et al.*, [59] have shown superconductivity at 4 K, where it has been mentioned that the ferromagnetism stems from amorphous Ni impurities, but not from $NiBi_3$ itself. Another study by Kumar *et al.,* has revealed that $NiBi_3$ phase show superconducting transition at 4.1 K, with no signature of ferromagnetism [60]. The above contradicting results of $NiBi_3$ compound suggest that this compound needs further investigation to arrive at a conclusion whether this compound show the coexistence or not. Moreover, polycrystal $NiBi_3$ phase was reported to show large field dependent thermal transport properties and magnetoresistance, as described by Sakurai *et al.* [61]. Apart from these interesting aspects of this compound along with the other stable phase, NiBi compound, of Ni-Bi system offer many other applications in the field of science and technology as well. Furthermore, the binary alloys of Ni-Bi are also
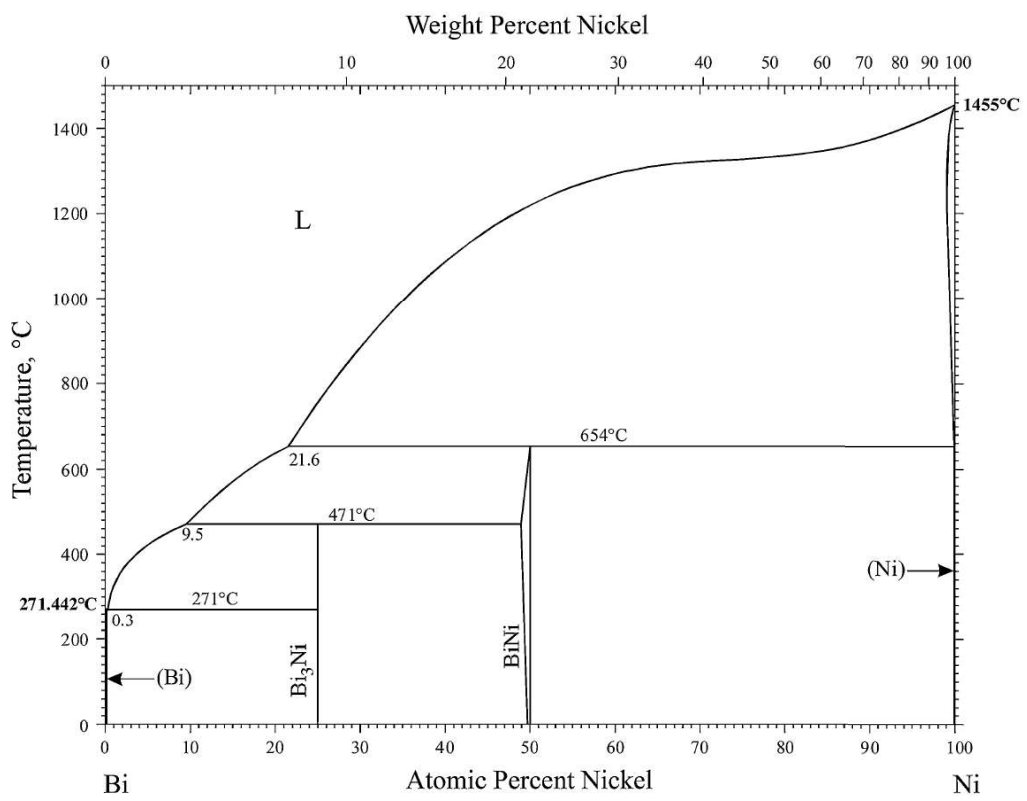
Figure 1.9: Phase Diagram of Ni-Bi system reported by Okamoto [43].

technologically important for control of coating thickness in the process of galvanization of silicon-containing steels [62]. The Ni-Bi system also has found its potential applications in lead-free soldering technology, where the alloys of Ni-Bi was shown to improve the thermal fatigue and drop impact resistant considerably simultaneously. [63]

The phase synthesis of Ni-Bi system has been carried out using various techniques till now. Sakurai *et al.* have prepared the poly-crystalline $NiBi_3$ compound by initial co-melting of high purity Ni (99.99%) and Bi (99.9999%) at 900 ^oC for 1 hour under a vacuum of $\approx 10^{-5}$ Torr. It was then followed by a subsequent annealing at 480 ^oC for 12 hours and at 460 ^oC for 12 hours successively [61]. Zhu *et al.* [64]have prepared single crystals of $NiBi_3$ using self-flux method, where they have taken the ratio of Ni and Bi as 1:10 and evacuated in a quartz tube. It was then heated to a temperature of 1150 ^oC for 2 hours and was cooled down very slowly with a rate of 5 ^oC/min tube to get the single crystalline $NiBi_3$ phase. An advantage of using this method is to avoid the possibility of the presence of other phases like magnetic Ni, NiBi and Bi phases.

The single crystals of $NiBi_3$ were synthesized by Silva *et al.*using slightly different parameters by taking 90% of Bi (purity 99.99%) and 10% of Ni (purity 99.99%) in quartz tube sealed under inert gas atmosphere. These tubes were heated for 4 hours to reach a temperature of 1100 ^oC, which was kept in that condition for 100 hours. The tube was then cooled down to 300 ^oC in 300 hours, which was kept at that temperature for 100 hours [59]. Seo *et al.* have synthesized $NiBi_3$ phase by taking Ni and Bi shots in the ratio of 1:3 in a quartz tube and it was then annealed at 450 ^oC for almost 168 hours [65]. Yoshida *et al.* have prepared the NiBi phase using arc melting in He gas, where heat treatment was performed at a temperature range of 570-900 K in a vacuum. NiBi nanoparticles were synthesized by Park *et al.* using a chemical route known as hydrothermal reduction method, where the reaction temperatures of 150 ^oC and a duration of 18 hours have been employed. In few reports, Dybkov et al. [45, 66, 67] have extensively investigated the growth kinetics of $NiBi_3$ layer at Ni-Bi interface as a function of temperature (150 ^oC-250 ^oC) and time (1-300 hours). The dependence of grown-layer thickness on time and temperature has been reported.

As discussed above, the Ni-Bi system has received sufficient attention in both the fundamental physics as well as in technological point of view. It may also be noticed that, till now, the phase synthesis of Ni-Bi system has been studied in the case of bulk and the ion beam mixing of this interesting system has also not been explored yet. Therefore, we perform the ion beam mixing in all the three different energy regimes, where the mechanisms responsible

20

for mixing are different. Moreover, the ion beam mixing of several binary systems such as metal-metal, metal-semiconductor, and semiconductor-semiconductor has been carried out extensively. However, the present study of ion beam mixing of Ni-Bi system is novel as it is a rare combination of ferromagnetic metal and semi-metal, where such studies are scarcely available in the literature. In the present study, energy of ion beams has been scanned from 0.2 MeV to 120 MeV so that the mixing and corresponding phenomenon in all the three different energy regimes can be realized.

1.7 Theme and organization of thesis

The representative theme of the present thesis has been shown in figure 1.10, which describes certain important aspects of the thesis. The single and five bilayer Ni/Bi films have been prepared by using thermal and electron beam evapouration techniques. These films were irradiated using ion beams of different energy to study the ion beam mixing. According to the thermal spike model, the ion beam creates a latent track around the ion path and the atoms across the interface along the latent track mix with each other. This mixing process due to ion irradiation is known as ion beam mixing. The dependence of the mixing percentages on the energy of ion beam and number of bilayers has been shown in the figure 1.10. The maximum ion-induced mixing has been observed in the case of 120 MeV Au ions irradiated on five bilayer Ni/Bi films. The magnetization measurements at 2.5 K and 5 K has revealed that these films are ferromagnetic in nature, which is due to Ni impurities and/or $NiBi_3$ phase. The dip around 100 Oe in the M-H loop at 2.5 K is the signature of superconductivity, which must be due to NiBi and/or $NiBi_3$ phases. The contact angle measurements on the low energy ion irradiated samples have shown a transition of the films surface from hydrophobic to hydrophilic in nature. The hydrophobic nature of the films at the lower fluences was due to the presence of $NiBi_3$ on the surface, which gets sputtered out at the higher fluences to form hydrophilic surface.

The thesis has been organized into seven chapters as described below.

Chapter 1 provides a general idea about the ion beam mixing (IBM) and their theoretical models, ion-matter interaction. This chapter also explains the interesting aspects of Ni-Bi system and the importance of IBM study of this system.

Chapter 2 presents the various fabrication and characterisation tools, which have been used during the present study. In this chapter, various fabrication techniques that are used in the
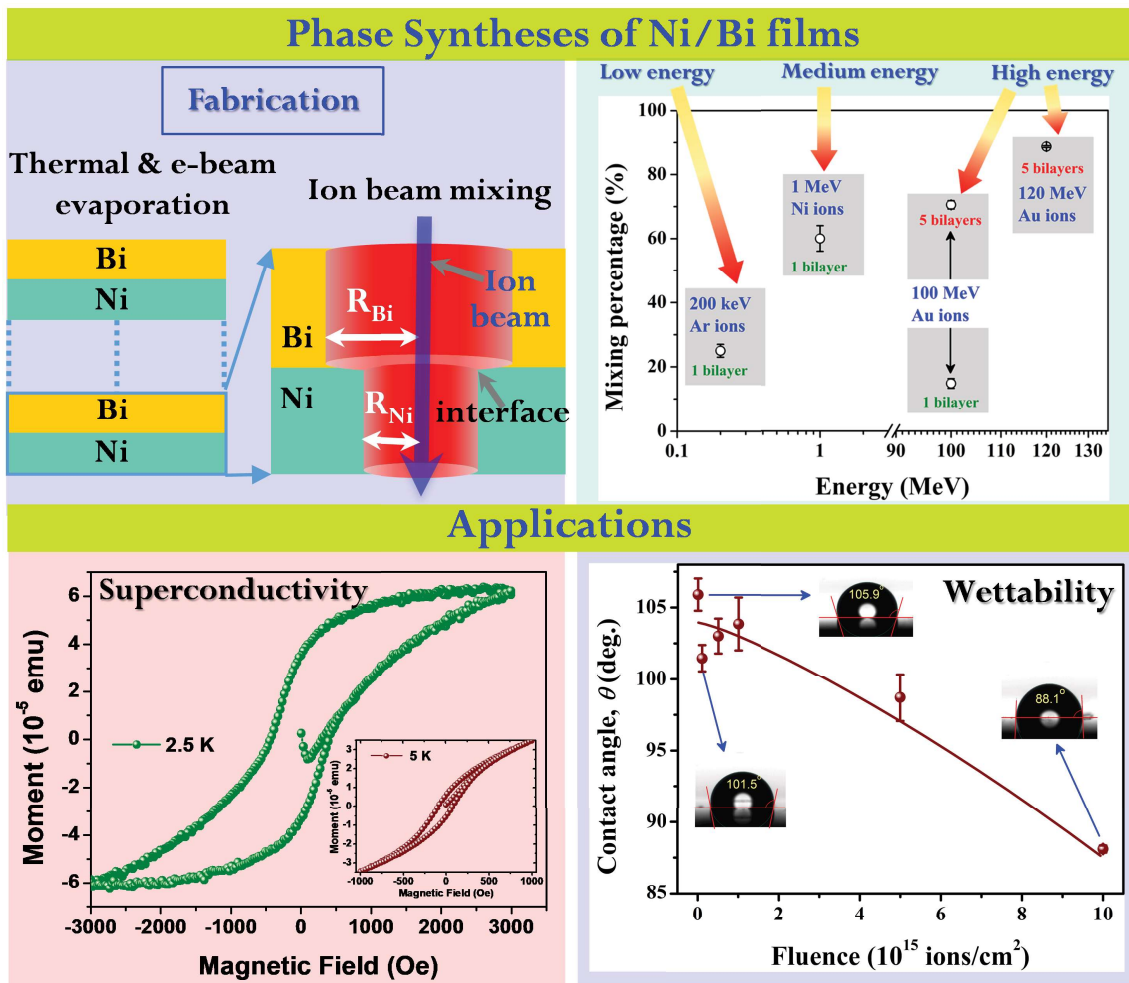
Figure 1.10: Theme of the thesis.

present study will be explained, such as thermal and electron beam evapouration. Further techniques that are used in the treatment of this films such as thermal annealing and ion irradiation techniques are discussed. Also, the details of characterisation techniques such as Rutherford Backscattering Spectrometry (RBS), X-ray diffraction (XRD), Scanning Electron Microscope (SEM) and Atomic Force Microscopy (AFM) will be discussed.

The experimental results and discussion of the present work are explained from chapter 3 onwards. The work has been projected in the order of high energy to low energy regime from chapter 3 to 5. Chapter 3 deals with the study of ion beam mixing of Ni-Bi system using swift heavy (100 -120 MeV Au) ions. Before getting into the details of ion beam mixing, the spontaneous formation of stable phases of Ni-Bi films at their interface during the deposition will be introduced. The ion-induced effects on these films, such as mixing, surface morphological evolution as a function of irradiation fluence will be discussed. The experimental results are explained in the framework of thermal spike model calculations (chapter-6).

Chapter 4 describes the effect of medium energy (few MeV) ions on Ni films as well as Ni/Bi films. First of all, we examine the insensitive nature of Ni film at this energy regime as the Ni layer was the reason less mixing in the previous case. Then, we investigate the ion beam mixing of Ni-Bi system as a function of fluence. In both these cases, the results will be explained on the grounds of thermal spike model calculations (chapter-6).

Chapter 5 discusses the study of ion beam mixing as well as other ion-induced modifications on Ni-Bi films using low energy (200 keV Ar) ions as a function of ion fluence. The ion-induced effects on the structure, surface morphology and mixing will be discussed. These experimental observations will be validated on the basis of theoretical model calculations (chapter-6). The thermal annealing study of the Ni-Bi films is also discussed in this chapter.

Chapter 6 describes the details of thermal spike model at various energy regimes. The experimentally observed ion induced modifications, as well as mixing, will be explained on the basis of this model. The underlying mechanisms in each case of different energies are explained. A discussion on comparing the mixing features at all the energy regimes will be presented along with the schematic and graphical representation.

Chapter 7 summarises the experimental observations and their theoretical understandings of the work done. This chapter also discusses the future scope of the present thesis.

Bibliography

[1] M. Nastasi and J. W. Mayer, Mater. Sci. Eng., R, 12, 1 (1994).

[2] R. S. Averback, D. Peak, and L. J. Thompson, Appl. Phys. A, 39, 59 (1986).

[3] M. Neubauer, K. P. Lieb, P. Schaaf, and M. Uhrmacher, Phys. Rev. B, 53, 10237 (1996).

[4] A. C.-Sosa, P. Schaaf, W. Bolse, K.-P. Lieb, M. Gimbel, U. Geyer, C. Tosello, Phys. Rev. B, 53, 14795 (1996).

[5] P. Pan, T. Yang, K. Tao and B. X. Liu, Phys. Status Solidi a 135, 199 (1993).

[6] F. Pan and B. X. Liu., J. Phys.: Condens. Matter 5, L315 (1993).

[7] W. F. Van der Weg, D. Sigurd, and J. W. Mayer, Applications of ion beams to metals, edited by S.T. Picraux, E. P. EerNiss and F. L. Vook (Plenum Press, New York, p. 209 (1973).

[8] A. Ibrahim, D. Thompson, Nucl. Instrum. Meth. Phys. Res. Sec. B, 7, 566 (1985).

[9] Manju bala, PhD Thesis, Jawaharlal Nehru University, New Delhi, India (2016).

[10] Y. T. Cheng, Mat. Sci. Rep., 5, 45 (1990).

[11] S. Dhar, PhD Thesis, Department of physics, IIT Kanpur (1996).

[12] S. Dhar, T. Som, Y. N. Mohapatra, and V. N. Kulkarni, Appl. Phys. Lett. 67, 1700 (1995).

[13] S. Dhar, Y. N. Mohapatra, and V. N. Kulkarni, Phys. Rev. B 54, 5769 (1996).

[14] S. Dhar, and V. N. Kulkarni, Thin solid films 333, 20 (1998).

[15] T. Som, B. Satpati, P. V. Satyam, D. Kabiraj, A. Gupta, and N. C. Mishra, J. Appl. Phys., 96, 7141 (2004).

[16] D. P. Datta, V. Siva, A. Singh, D. Kanjilal, and P. K. Sahoo, Nucl. Instrum. Meth. Phys. Res. Sec. B, 407, 141 (2017).

[17] W. Xia, C. A. Hewett, M. Fernandes, S. S Lau, and D. B Poker, J. Appl. Phys., 65, 2300 (1989).

[18] W. Xia, M. Fernandes, C. A. Hewett, S. S. Lau, D. B. Poker, and J. P. Biersack, Nucl. Instr. and Meth. B 37/38, 408 (1989).

[19] S. Dhar, M. Milosavljevic, N. Bibic, and K. P. Lieb, Phys. Rev. B 65, 024109 (2002).

[20] S. Dhar, P. Schaaf, N. Bibic, E. Hooker, M. Milosavljevic, and K. P. Lieb, Appl. Phys A 76, 773 (2003).

[21] D. P. Datta, V. Siva, A. Singh, S. R. Joshi, D. Kanjilal, and P. K. Sahoo, Nucl. Instrum. Meth. Phys. Res. Sec. B, 379, 48 (2016).

[22] D. P. Datta, V. Siva, S. Varma, D. Kanjilal, and P. K. Sahoo, Phys. Chem. Chem. Phys., 18, 29955 (2016).

[23] R. A. Swalin, Thermodynamics of Solids, 2nd ed., Wiley Interscience, New York (1972).

[24] W. Jiang, M. F. gui , L. L. bin , J. Z. peng, Trans. Nonferrous Met. Soc. China, 21, 139 (2011).

[25] F. W. Saris, in C. J. McHargue, R. Kossowsky and W. O. Hofer (eds.), Structure-Property Relationships in Surface-Modified Ceramics, Kluwer Academic, Dordrecht, p. 103, (1989).

[26] L. Zhang, M. J. Demkowicz, Acta Mater. 76, 135 (2014).

[27] H. Gades and H. M. Urbassek, Phys. Rev. B 51, 14559 (1995).

[28] J. F. Ziegler, M.D. Ziegler, and J.P. Biersack, Nucl. Instrum. Methods Phys. Res. Sect. B, 268, 1818 (2010).

[29] B. M. Paine and R. S. Averback, Nucl. Instrum. Meth. Phys. Res. Sec. B, 7-8, 666 (1985).

[30] L. T. Chadderton, S. A. Cruz and D. W. Fink, Nucl. Tracs Rad. Meas., 22, 29 (1993).

[31] E. H. Lee, Nucl. Instrum. Meth. Phys. Res. Sec. B, 151, 29 (1999).

[32] R. L. Fleischer, P. B. Price, and R. M. Walker, Nuclear tracks in solids: principles and applications, Univ. of California Press, (1975).

[33] R. L. Fleischer, P. Price, and R. Walker, J. Appl. Phys. 36, 3645 (1965).

[34] S. Klaumünzer, M. Hou, and G. Schumacher, Phys. Rev. Lett., 57, 850 (1986).

[35] F. Dessauer, I. Z Physik., 12, 38 (1923).

[36] G. H. Vineyard, Rad. Effects, 29, 245, (1976).

[37] M. Toulemonde, C. Dufour, and E. Paumier, Phys. Rev. B., 46, 14362 (1992).

[38] M. Toulemonde, E. Paumier, and C. Dufour, Rad. Effects, 126, 201 (1993).

[39] M. Toulemonde, C. Dufour, A. Meftah, and E. Paumier, Nucl. Instrum. Meth. Phys. Res. B, 166, 903 (2000).

[40] W. Bolse, Materials Science and Engineering: R: Reports 12, 53 (1994) vii.

[41] B. Rauschenbach, Phys. Stat. Sol., 102a, 645 (1987).

[42] Y. T. Cheng, M. van Rossum, M.A. Nicolet and W.L. Johnson, Appl. Phys. Lett., 45, 185 (1984).

[43] H. Okamoto, J. Phase Equilibria Diff., 33, 6 (2012).

[44] G. P. Vassilev, X. J. Liu, and K. Ishida, J. Phase Eq. Diff., 26, 2 (2005).

[45] V. I. Dybkov, in Solid State Reaction Kinetics, IMPS Publications, Kyiv, Ukraine, (2013).

[46] G. Voss and D. Legierungen, Z. anorg. Chemie. 57, 34 (1908).

[47] P. Feschotte and J.-M. Rosset, J. Less-Common Metals. 143, 31, (1988).

[48] M. Hansen. Constitution of binary alloys. 2nd ed.- New York: McGraw-Hill, (1958).

[49] P. LeClair, J. S. Moodera, and J. Philip, D. Heiman, Phys. Rev. Lett. 94, 037006 (2005).

[50] P. Fulde and R. A. Ferrel, Phys. Rev. 135, A550 (1964).

[51] A. I. Larkin and Y. N. Ovchinnikov, Sov. Phys. JETP 20, 762 (1965).

[52] S. S. Saxena, P. Agarwal, K. Ahilan, F. M. Grosche, R. K. W. Haselwimmer, M. J. Steiner, E. Pugh, I. R. Walker, S. R. Julian, P. Monthoux, G. G. Lonzarich, A. Huxley, I. Sheikin, D. Braithwaite, and J. Flouquet, Nature (London) 406, 587 (2000).

[53] D. Aoki, A. Huxley, E. Ressouche, D. Braithwaite, J. Flouquet, J.-P. Brison, E. Lhotel, and C. Paulsen, Nature (London) 413, 613 (2001).

[54] N. T. Huy, A. Gasparini, D. E. de Nijs, Y. Huang, J. C. P. Klaasse, T. Gortenmulder, A. de Visser, A. Hamann, T. Gorlach, and H. v. Löhneysen, Phys. Rev. Lett. 99, 067006 (2007).

[55] W. A. Fertig, D. C. Johnston, L. E. DeLong, R. W. McCallum, M. B. Maple, and B. T. Matthias, Phys. Rev. Lett. 38, 987 (1977).

[56] B. K. Cho, P. C. Canfield, L. L. Miller, D. C. Johnston, W. P. Beyermann, and A. Yatskar, Phys. Rev. B 52, 3684 (1995).

[57] T. Herrmannsdörfer, R. Skrotzki, J. Wosnitza, D. Köhler, R. Boldt, and M. Ruck, Phys. Rev. B 83, 140501(R) (2011).

[58] E. L. M. Piñeiro a, B. L. R. Herrera, R. Escudero, and L. Bucio, Solid State Commun.151, 425 (2011).

[59] B. Silva, R. F. Luccas, N. M. Nemes, J. Hanko, M. R. Osorio, P. Kulkarni, F. Mompean, M. Garcìa-Hernàndez, M. A. Ramos, S. Vieira, and H. Suderow, Phys. Rev. B, 88, 184508 (2013).

[60] J. Kumar, A. Kumar, A. Vajpayee, B. Gahtori, D. Sharma, P. K. Ahluwalia, S. Auluck, and V. P. S. Awana, Supercond. Sci. Technol. 24, 085002 (2011).

[61] M. Sakurai, T. Ono, I. Yoshida, and S. Tanuma, Jpn. J. Appl. Phys. 39, 6366 (2000).

[62] R. Fratesi, N. Ruffini, M. Malavolta, and T. Bellezze, Surf. Coating Technol., 157, 34 (2002).

[63] J. H. Lee, S. Kumar, H. J. Kim, Y. W. Lee, J. T. Moon, High Thermo-Mechanical Fatigue and Drop Impact Resistant Ni-Bi Doped Lead Free Solder, Proceedings of the 64th Electronic Components and Technology Conference, 712, (2014).

[64] X. Zhu, H. Lei, C. Petrovic, and Y. Zhang, Phys. Rev. B 86, 024527 (2012).

[65] S. Seo, M. G. Cho, and H. M. Lee, J. Electr. Mater., 36, 1536 (2007).

[66] O. V. Duchenko and V. I. Dybkov, J. Mat. Sci. Lett. 14, 1725 (1995).

[67] V. I. Dybkov and O. V. Duchenko, J. Alloy. Compd. 234, 295 (1996).

Chapter 2

Experimental Techniques

The present chapter discusses the detailed explanation of the experimental and characterisation techniques that are being used in this thesis. The chapter would cover the techniques of synthesis of Ni-Bi thin films, ion irradiation, and the characterisation. The synthesis techniques include thermal and electron beam evapouration. The ions of three different energy regimes have been used for irradiating the films and hence, three different ion accelerator systems were used. The details of these systems and other details such as ion fluence, charge states have been discussed below. The study of annealing has been performed at different temperatures using vacuum tubular furnace. The characterisation techniques include Rutherford Backscattering spectrometry (RBS), X-ray Diffraction (XRD), Field Emission Scanning Electron Microscopy (FESEM), Transmission Electron Microscopy (TEM), Physical property measurement system (PPMS) and Atomic Force Microscopy (AFM).

2.1 Thin film deposition

It is well known that the thin films can be prepared by a number of deposition methods. These deposition methods can be broadly classified into two types, those are Chemical vapour deposition (CVD) and Physical vapour deposition (PVD). Chemical vapour deposition is a process, where chemical reactions take place during the deposition. On the other hand, in the PVD process, no chemical reaction will take place during the deposition. In the case of PVD category also, there are many deposition methods such as thermal evapouration, electron beam evapouration, radio frequency (RF) Sputtering, direct current (DC) sputtering, pulsed laser deposition (PLD), molecular beam epitaxy (MBE) and atomic layer deposition (ALD). In the present case, the Ni and Bi layers have been deposited using thermal and electron beam evap-
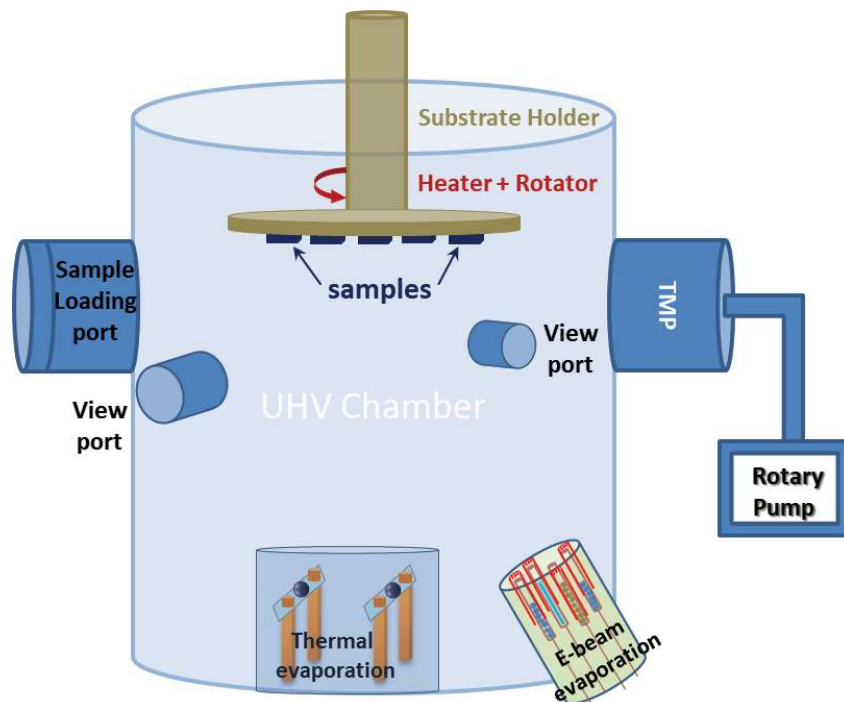
Figure 2.1: Schematic of thermal and electron beam evapouration systems in ion beam and nanomaterials laboratory.

ouration techniques. In our deposition system, both thermal and electron beam evapouration techniques have been integrated into a single UHV chamber as shown in figure 2.1. In this system, a base vacuum of less than 2×10^{-7} mbar is being achieved through the combination of rotary and turbo molecular pumps. There is a provision to rotate the substrate holder in the range of 0 to 24 rotations per minute, during the deposition. It is used mostly to ensure the uniformity of the films throughout the surface. A set of heater and thermocouple are attached to the substrate holder to supply and measure the temperatures in the range of 30-300 ^{o}C through a PID controller. A quartz crystal monitor (QCM) is placed just at the level of substrate holder to monitor the rate of deposition and thickness of the films. By looking at the QCM, one can control the rate of deposition and the thickness of the films manually by adjusting the power supply knobs of thermal and e-beam evapouration sources. There are two view ports in the system, one of them is used to watch inside the chamber, especially when the chamber is in the vacuum, and a lamp is located at the other port. Moreover, there is a port to load and remove the samples as well as the target materials.

2.1.1 Thermal evapouration:

Thermal evapouration is one of the most widely used and cost-effective techniques, which is a simple and convenient one among all the PVD processes. It requires a vacuum environment in which a sufficient amount of heat through resistive heating is provided to the target material or evapourant to attain the sufficient vapour pressure to evapourate the material [1, 2]. In this method, the heat is supplied to the so-called boats. Depending on the shape/geometry, these are of several types like filament, wire, crucible, spirals, and basket. Mostly the boats are made up of Tungsten (W), Molybdenum (Mo) or Tantalum (Ta). In general, any thermal boat should have high melting point, lower vapour pressure, and high tensile strengths. The thermal evapouration process may be explained in 3 different steps. They are:

1. Transition of evapourant from solid or liquid state into the gaseous phase.

2. Transporting the vapour to substrate from the source.

3. Depositing these evapourated species onto the substrate.

Thermal evapouration works on the principle of Joule effect, where the evapouration of desired material occurs after passing sufficient current through the boat. In this process, the target material to be evapourated is mounted on a boat. The schematic of the thermal evapouration system is shown in figure 2.1, where two independent ports can be seen. The substrate holder is situated almost 15 cm distance away and exactly on the topside from both the thermal boats. For the better quality films, the slow rate of deposition and lower substrate rotation were always maintained during the deposition. There is a shutter employed downside of the substrate holder which helps us to start the deposition after reaching the desired rate of deposition as well as to stop immediately whenever required. The typical values of voltage and current used for the deposition of Bi were ≈ 1 V and ≈ 60 A and these values for Ni were ≈ 5.5 V and ≈ 65 A respectively.

2.1.2 Electron beam evapouration:

The present e-beam geometry is slightly different from the typical e-beam evapourator. The schematic of this technique is shown in figure 2.2. The evapourant material is either mounted as a rod or loaded on a pocket or using alumina liner. The electron filaments are placed just beside the pocket or rod. In this process, the electrons are generated from a filament due to thermionic
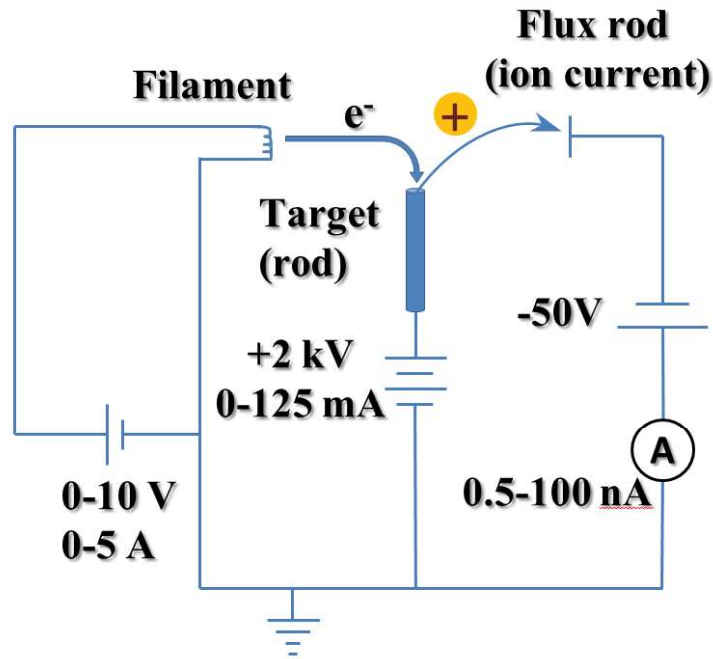
Figure 2.2: Schematic representation of working principle of electron beam evapourator.

emission, when sufficient current is passed through the filament. After providing sufficient power to the electron filament, the electrons will be ejected. These ejected electrons are directed towards the target rod/pocket by keeping at a bias of +2000 V so that the negatively charged electron flux gets attracted towards the rod. The stream of electrons hit the rod/pocket with very high energy and causes heating which will, in turn, lead to evapouration. The deposition system is basically a four pocket mini e-beam evapourator. Electron beam evapourator is also situated 15 cm away from the substrate holder, but with an angle of around 30°, in the same UHV chamber. Therefore, the deposition conditions of this technique are almost similar to that of the thermal evapourator. The typical values of flux, power, and filament current to evapourate Bi were $\approx$ 3 nA, $\approx$20 W, and $\approx$ 0.6 A and these values for Ni were $\approx$5 nA, $\approx$125 W and $\approx$1 A respectively.

2.1.3   Thermal annealing

The thermal annealing study was performed in a tubular vacuum furnace system, which is shown in the figure 2.3. Annealing was performed in Ar ambience and the flow of argon gas was ensured through bubbles coming out from silicone oil. The silicone oil was filled in "W" shaped tube so that the back flow of air molecules does not happen, in the case of completion
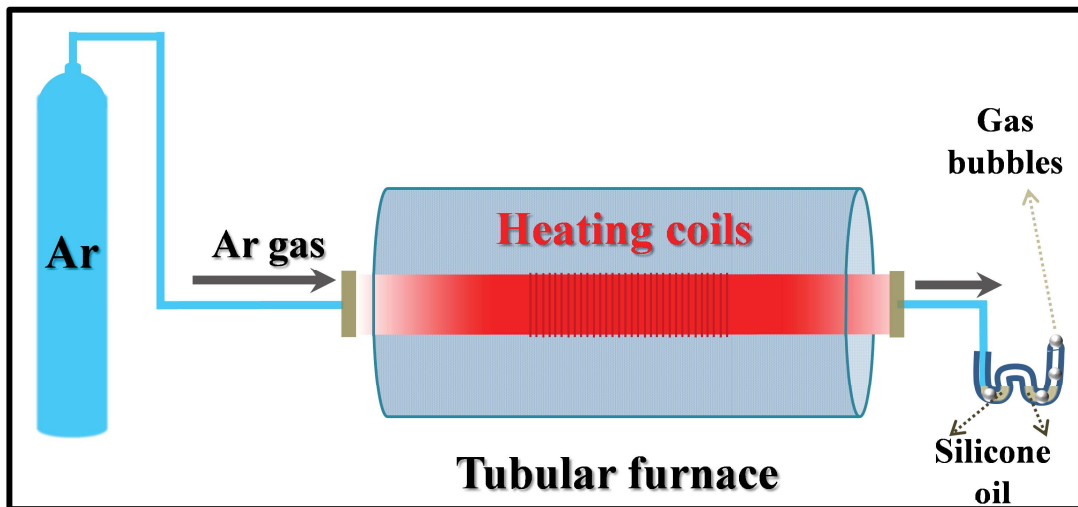
Figure 2.3: Vacuum tubular furnace system for the study of thermal annealing.

of Ar gas in the cylinder. The accessible temperatures using this system are up to 1200 ^{o}C from the room temperature.

In the process of thermal annealing, the samples were loaded in the middle of the furnace, where the temperature is uniform. Then the argon gas was purged into the vacuum tube for some time. After that, heating coils were used to ramp up the temperatures till the required temperatures were reached and then was kept on hold for 1 hour in the case of all samples. Thereafter, the samples were allowed to cool down to the room temperature naturally. The gas flow was maintained till the temperature reaches down to room temperature, after the required annealing time.

2.2 Ion irradiation

2.2.1 100 and 120 MeV Au ion irradiation

These experiments were performed using 15 UD pelletron accelerator, at Inter University Accelerator Center (IUAC), New Delhi, India [3]. The schematic representation of this facility has been shown in figure 2.4. In general, any ion beam facility possesses three major components such as ion source, accelerating column and irradiation chamber. The ion source in this facility is the so-called Multi-Cathode Source of Negative Ion by Cesium Sputtering (MC-SNICS). In this case, firstly, negative ions are generated from a source of solid cathodes, by sputtering of the target with the help of Cesium ions. These ions are pre-accelerated to an energy of 250

33

keV. These energetic negative ions are then injected into the accelerating column using injector magnets. In the accelerating column, the negative ions are accelerated towards the positive central terminal and acquire the energy of terminal potential. Thereafter, these negative ions will be transformed as the positive ions with the help of stripper gas. The stripper gas essentially removes the electrons from those negative ions and form the positive ions. These positive ions are then repelled from the positive terminal and get further accelerated towards the other end of the tank. The energy (E) of the out-coming ions can be estimated using the following formula

$$E(MeV) = E_i + (1 + q) \times V_T \tag{2.1}$$

Where E_i, q, and V_T are pre-accelerated energy, electron charge, and terminal voltage. The selection of desired energy and charge state of the ion beam can be made with the help of analyser magnet. The current of ions can be measured using Faraday cup. These ions with the desired energy and charge state can be raster-scanned in XY directions uniformly using a magnetic scanner. The ions are then used to irradiate the samples that are loaded into the irradiation chamber.

In this thesis work, using the IUAC facility, Au ions of 100 MeV and 120 MeV energy were used for irradiation, whose charge states were 8^+ and 9^+ respectively. Ion fluences in the range of 1×10^{12} - 1×10^{14} ions/cm² were used. The current of ion beam was 100 pnA (particle nano Ampere) in both the cases.

2.2.2   2.2 MeV Au and 1.1 MeV Ni ion irradiation

These set of irradiation experiments were conducted using 3 MV tandem pelletron accelerator at Institute of Physics, Bhubaneswar, India. The ion source and working principle of this accelerator are the same as the previous one. In the case of 2.2 MeV Au²⁺ ions, the irradiation fluences were from 5×10^{14} to 1×10^{16} ions/cm². In the case of 1 MeV Ni⁺ ions, the ion fluence ranges from 1×10^{15} to 1×10^{16} ions/cm².

2.2.3   200 keV Ar ion irradiation

200 keV Ar irradiation experiments were carried out using Low Energy Ion Beam Facility (LEIBF) at IUAC, New Delhi, India [4, 5]. In this system, ions are produced from a nanogun type Electron Cyclotron Resonance (ECR) ion source. An ECR ion source is a kind of plasma reservoir for ions, electrons and neutral atoms. Using this source, one can produce highly
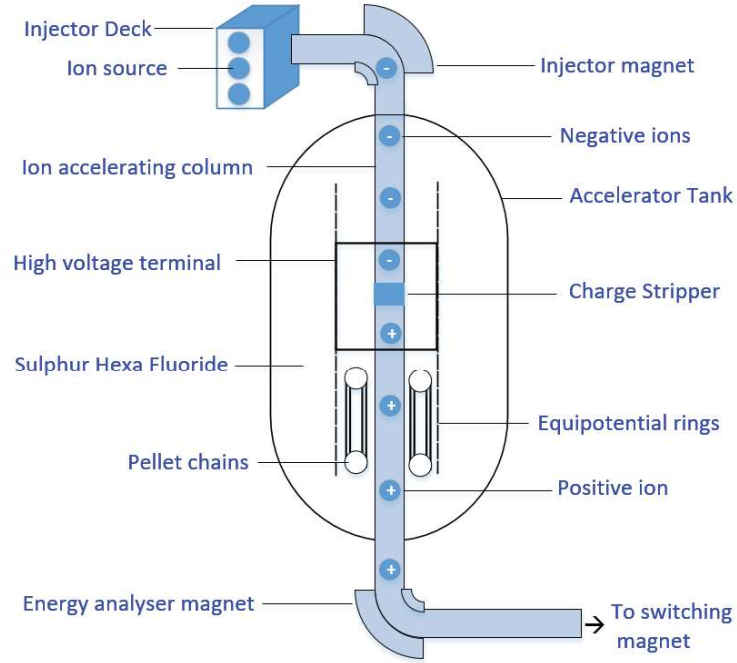
Figure 2.4: A schematic of 15 UD pelletron tandem accelerator at IUAC, New Delhi.

charged ions of various elements, including the noble gases. In an ECR ion source, an electron moves in a spiral orbit due to Lorentz force, if a static and uniform magnetic field (B) is applied. The frequency of gyration (ω_g) of these electrons may be expressed as

$$\omega_g = \frac{e.B}{m_e} \tag{2.2}$$

Where e and m_e are the charge and mass of electron respectively.

If microwave of the frequency that is equal to ω_g of electrons is injected from an external ultra-high frequency travelling wave tube amplifier into a volume of low-pressure gas. Depending on the phase of their transverse velocity component with respect to the electric field, the electrons are either resonantly accelerated or decelerated. This ECR condition is being used to heat the plasma. The injected microwaves heat the free electrons in the gas which in turn collide with the atoms or molecules of the gas in the volume and cause ionization. The ions are confined by the ECR ion source for sufficiently longer durations so that multiple numbers of collisions and ionizations take place and thereby produce highly charged ions. The low gas pressure in the source is maintained deliberately to avoid any possibility of recombination. These ions from the ECR ion source are extracted by using a suitable extraction electrode.

In this thesis, Ar ions of 200 keV energy and 2+ charge state were used for irradiation. The

35

irradiation fluences were from 5×10^{14} to 1×10^{17} ions/cm^2. The typical current of the ion beam was 1.5 μA.

2.3 Characterisation Techniques :

2.3.1 X-ray diffraction (XRD):

X-ray diffraction (XRD) is a powerful and non-destructive technique for phase analyses, identification of crystalline nature of the material, crystallite or grain size, stress in the materials etc [6]. The technique is based on the Bragg's law [7], which can be mathematically represented as following:

$$2dsin\theta = n\lambda \tag{2.3}$$
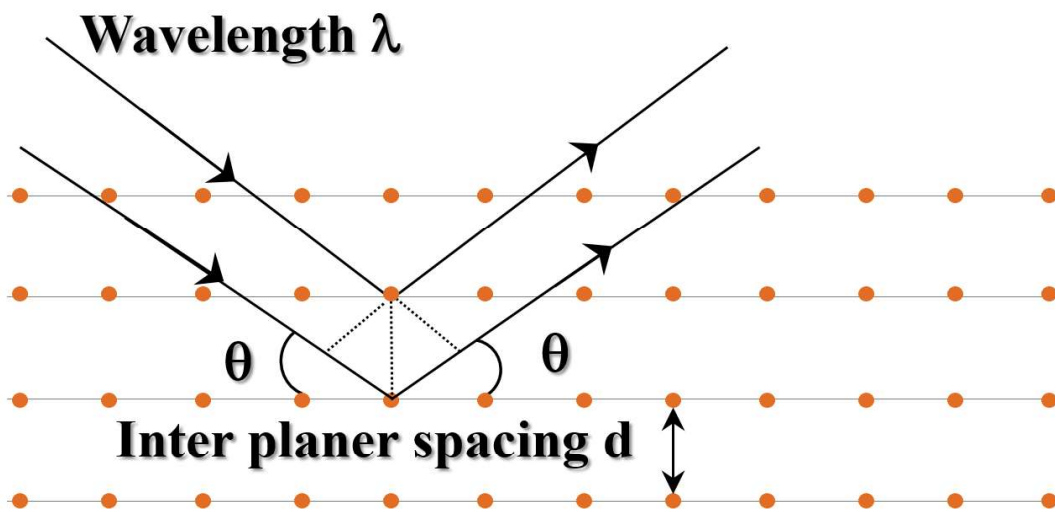
Figure 2.5: Schematic representation of Bragg's reflection from a single crystal.

Where λ is the wavelength of the incident X-rays, θ is the incident angle as shown figure 2.5 ,d is the inter planer spacing and n is an integer. A typical geometry of XRD set up is shown in figure 2.6. In general, the X-ray radiation interacts with the matter, it penetrates much deeper into the material, which would provide the best information of the matter in the case of bulk. While in the case of the thin films, the diffracted intensities from the layered materials are very low compared to the substrate and background. In order to get rid of this issue, we performed Glancing angle X-ray diffraction (GAXRD) on our samples. Another notable advantage of the

36

GAXRD measurement is that it is a depth-sensitive technique through which one can obtain the information of any layer at a particular depth by probing the X-rays using the incident angle θ. In this geometry, the X-ray source (the angle of incident X-ray beam) is fixed at a particular small angle, which increases the path length of X-rays in the film and thereby increasing the diffraction intensity from thin films and reducing the intensity of background and substrate considerably [8].
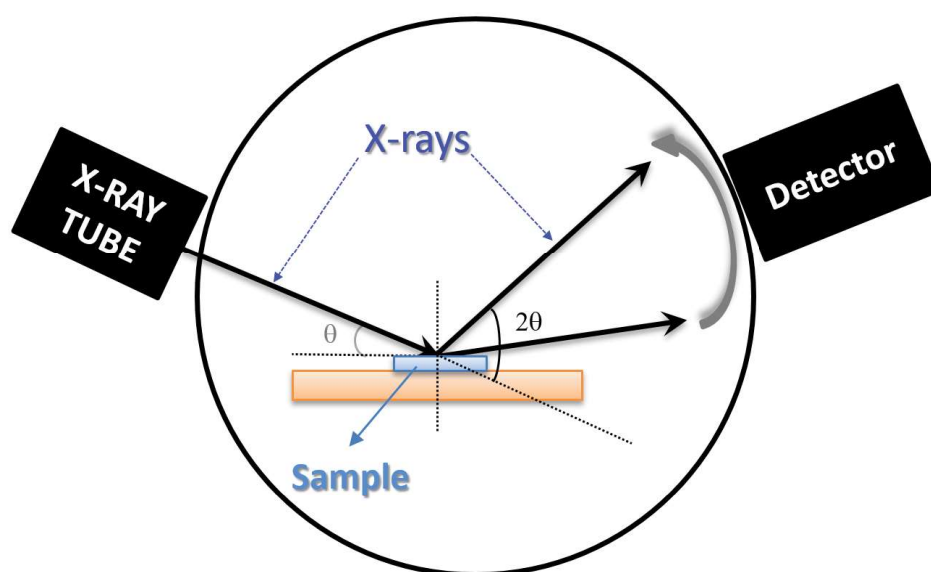
Figure 2.6: Geometrical representation of X-ray diffraction set up.

In this thesis, Bruker D8 advance diffractometer has been used for the GAXRD measurements. There are basically three main parts in the X-ray diffractometer, they are the X-ray source, a goniometer, and an X-ray detector. In the present case, the Cu $K\alpha$ (λ = 1.5418 $\mathring{A}$) source has been used. These X-rays fall on the sample, which is mounted on 5-axis goniometer. The detector part would rotate around within the given range to collect the data.

2.3.2 Rutherford Backscattering Spectrometry (RBS)

Rutherford Backscattering Spectrometry (RBS) is one of the well known and non-destructive techniques for analysing the thickness, composition of the bulk and thin films [9–11]. In this technique, a beam of α particles with few MeV energy is probed on the samples and the backscattered α particles are collected using surface barrier detector at around 165°. Among the many incident α particles, some of them get backscattered from the target material and fall on the detector area within a solid angle, where they produce an electrical signal. This

signal is further amplified and processed to obtain the spectrum by using the multi-channel analyzer. The experimental set up that has been used in the present case is shown figure 2.7. The schematic representation of working principle of RBS has been shown in figure 2.8. In the RBS facility that we have used, the angle between the incident and backscattered ions are decided based on the IBM geometry. As the incident ion passes through the target atoms, they lose a certain amount of energy and hence the energy of backscattered ions will no longer be the same as incident ones. If a projectile with energy E_0 and mass M_1 collides with a stationary target atoms of mass M_2 elastically (where $M_2 > M_1$) and backscatter at an angle θ with an energy of E_1 [12]. The relation of the energy of the backscattered and incident ions can be given by

$$E_1 = K.E_0 \tag{2.4}$$

Where K is the kinematic factor, which is nothing but the ratio of energies of backscattered and incident ions and it can be mathematically expressed as:

$$K = \frac{E_1}{E_0} = \left[\frac{(M_2^2 - M_1^2 sin^2\theta)^{1/2} + M_1 cos\theta}{M_2 + M_1} \right]^2 \tag{2.5}$$

An important factor that plays a key role to observe backscattering of projectiles is that the scattering cross-section. It is based on the coulomb interaction potential and can be understood as the probability with which a projectile is scattered elastically from the target atoms [13]. If the ions with energy E_0 and atomic number Z_1 gets backscattered with an angle θ from the target atom with atomic number Z_2, then the scattering cross section can be expressed as

$$\frac{d\sigma}{d\Omega_s} = \left[\frac{Z_1 Z_2 e^2}{4E_0} \right]^2 \frac{4}{sin^4\theta} \frac{\left([1 - ((M_1/M_2)sin\theta)^2]^{1/2} + cos\theta \right)^2}{[1 - ((M_1/M_2)sin\theta)^2]^{1/2}} \tag{2.6}$$

This scattering cross section can be used for quantifying the atomic concentration of target, which can be expressed in terms of backscattering yield as the following:

$$Y = \frac{d\sigma}{d\Omega_s} \left(\frac{N_p t\Omega N}{t sin\alpha} \right) \tag{2.7}$$

Where $\frac{d\sigma}{d\Omega_s}$ is the scattering cross section, N_p is the number of incident ions, t is the thickness, α is the sample surface tilt angle, Ω is the solid angle of the detector.

Figure 2.7: Rutherford Backscattering Spectrometry facility at IUAC, New Delhi.
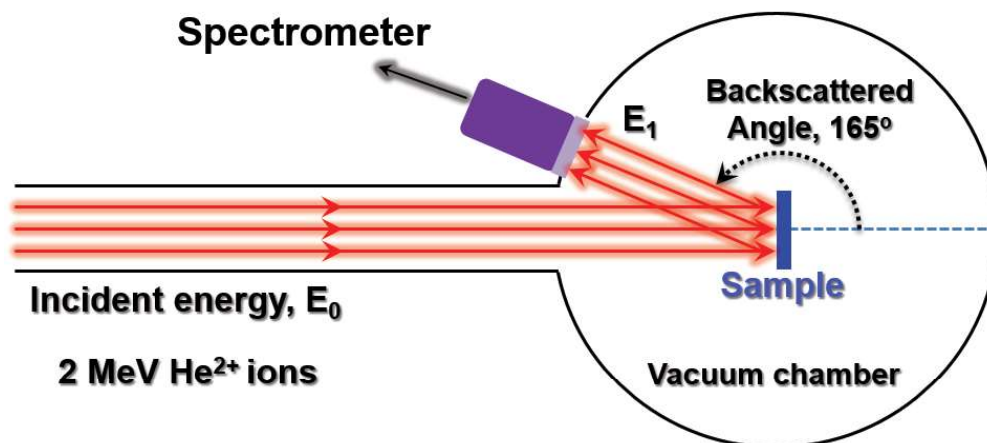
Figure 2.8: Schematic representation of Rutherford Backscattering Spectrometry.

Depth profiling

Depth profiling is one of the well-known applications of RBS spectra, where one can use the energy of backscattered ions and obtain the depth profile of the sample [10, 12]. A schematic

illustration of the depth profiling is shown in figure 2.9(a). The incident ion from the sample surface will be backscattered with an energy of $E_1 = K.E_0$ and the corresponding signal appears at the position, E_1, in the spectrum. The position of a signal from the atoms sitting below the surface is expected to shift by an amount of the energy lost by the projectile while it is passing through the sample in both inward ($\triangle E_{in}$) and outward direction ($\triangle E_{out}$) as shown in figure 2.9(a). A typical RBS spectra for such target has been shown in figure 2.9(b).

The energy of the backscattered ion from an atom sitting at a depth of x from the surface of the sample can be written as:

$$E_1 = (K \times E_0) - \left[\frac{K}{cos\theta_{in}} \frac{dE}{dx}|_{in} + \frac{1}{cos\theta_{out}} \frac{dE}{dx}|_{out} \right] \times x \qquad (2.8)$$

Where the first term on the right-hand side, $K \times E_0$, represents the energy of scattered particles from the atoms at the surface of the sample or target. The difference in the energies of the backscattered ions from the atoms at the surface and at a depth, x, plays a key role in constructing the depth profile of any target. The energy difference can be expressed as [10]:

$$\triangle E_1 = (K \times E_0) - E_1 = \left[\frac{K}{cos\theta_{in}} \left(\frac{dE}{dx} \right)_{in} + \frac{1}{cos\theta_{out}} \left(\frac{dE}{dx} \right)_{out} \right] \times x \qquad (2.9)$$

It may be noticed from the above equation that the energy difference $\triangle E_1$ is directly proportional to the depth (x), for the constant for the stopping powers. Therefore, the depth profile corresponding to a given target can be obtained using the energy of the backscattered particles.

In order to get the information of the target such as thickness, composition, interface diffusion and depth profiles, the RBS data was analysed using RUMP simulations package [14].

2.3.3 Field emission scanning electron microscopy (FESEM)

Scanning electron microscopy (SEM) is one of the powerful techniques to analyse the surface morphology, the topography of the specimen [15]. It may be noted here that when a beam of primary electrons impinge on the specimen and interact with the matter to produce secondary electrons, backscattered electrons, X-rays, Auger electrons, transmitted electrons etc. Depending on the collected signal, one can obtain the required information about the specimen. In conventional SEM, electrons are produced by electrical heating of electron filament via thermionic emission. Most used thermionic electron guns are tungsten (W) and Lanthanum hexaboride (LaB_6). Such electrons have the limitations in terms of spatial resolution. How-
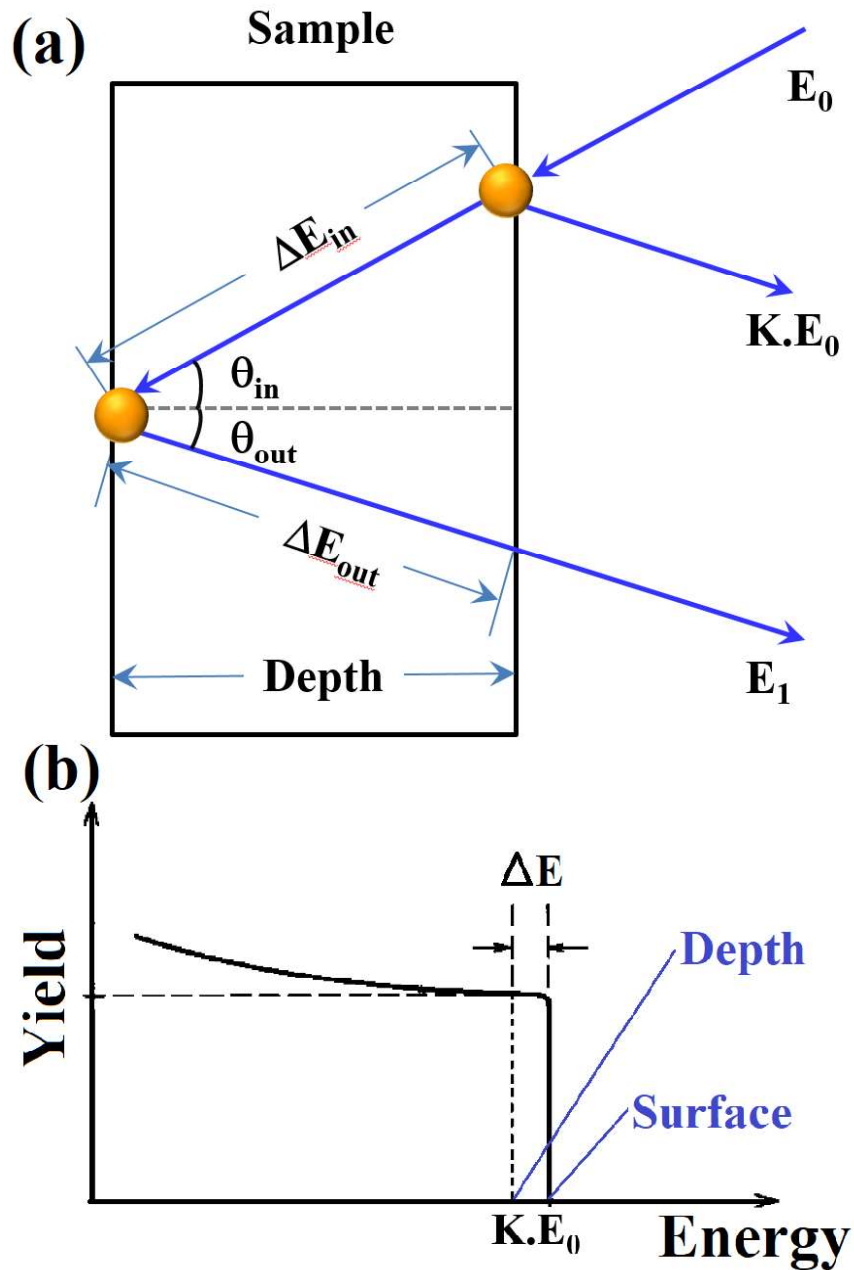
Figure 2.9: Schematic representation of (a) depth profiling using RBS and (b) corresponding typical RBS spectra.

ever, Field emission gun has several advantages such as less spot diameter, energy spread, and crossover diameter along with more coherent and bright electron beam, all of which increases the resolution. The notable advantage of FESEM is that the electrons are emitted from a source of Schottky field emitter in which emission occurs at or near the work function barrier. The primary electron beam with an energy of few keV to 30 keV gets focussed by an electromagnetic

lens system before interacting with the specimen. The schematic of typical FESEM is shown in figure 2.10. The electron beam is focussed using a combination of various components such as condenser lens, condenser aperture, and the objective lens. The scan coil is used to scan the electron beam on the sample surface.
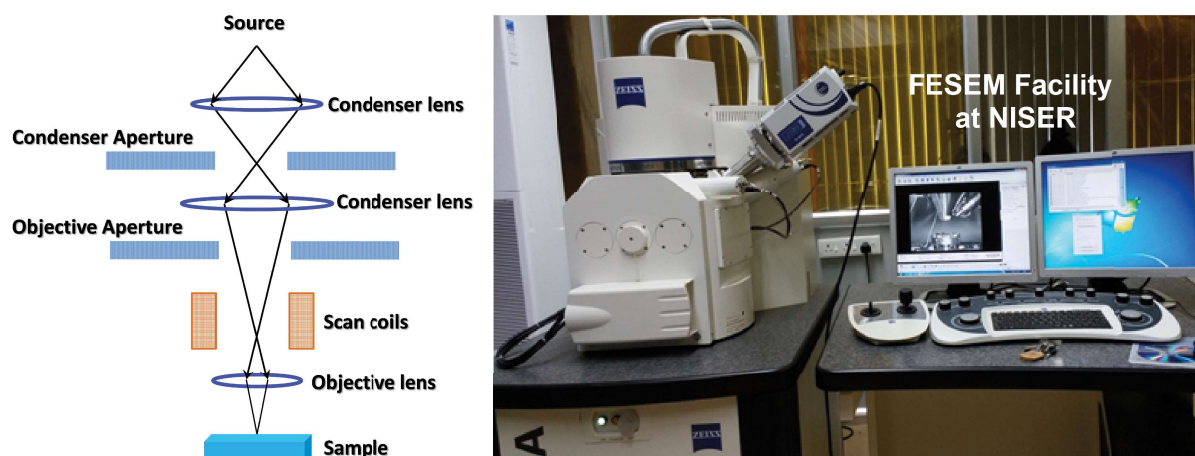
Figure 2.10: Schematic representation of working principle of Scanning electron microscope.

In the present study, FESEM (SIGMA model, Carl-Zeiss made) was used to investigate the ion-induced surface morphological modifications. It was also used to demonstrate the evolution of surface morphology upon ion irradiation as a function of fluence. The system has 3 different detectors, they are In-lens detector, Backscattered electron detector, Secondary electron detector, EDS detector. The system has a provision to move the stage in 5 different directions using 5-axis movement stage, which has a freedom to move from 0 to 125 mm, 125 mm and 50 mm in X, Y and Z directions respectively along with a possibility of tilt from -10 ^{o} to 90 ^{o} and rotation of 360 ^{o}. FESEM system requires the vacuum, typically in the range of 1×10^{-9}-3×10^{-9} mbar, for gun operation and to prevent collision of electrons with gas molecules.

2.3.4 Transmission electron microscopy (TEM)

Transmission electron microscopy is very powerful technique among many available characterisation tools. In the TEM, a beam of primary electrons interact with the sample and it generates various types of signals. After processing of these signals, one can attain atomic resolution, elemental composition, diffraction patterns and other useful information about the specimen [16–19]. A schematic diagram of typical TEM system is presented in figure 2.11. It illuminates the role of various components in transferring the energetic electrons from the

electron source to the specimen. There are two principle modes of the TEM operation and they are using parallel and convergent beams. The parallel beam is used in obtaining selected area electron diffraction (SAED) pattern, while the convergent beam can provide the convergent beam electron diffraction (CBED) pattern.
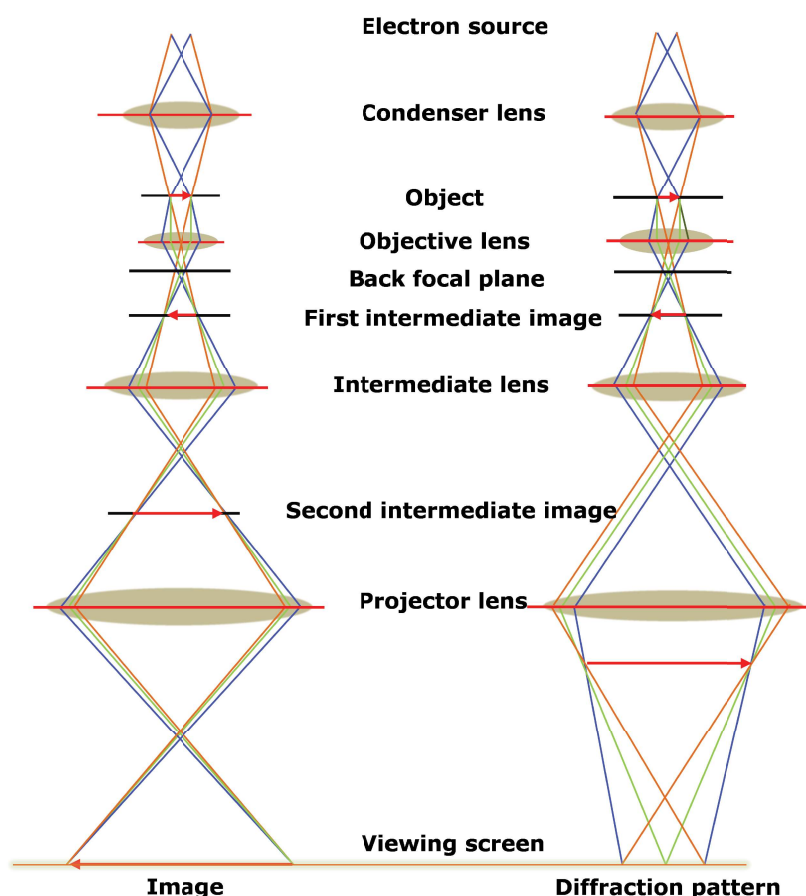
Figure 2.11: Schematic diagram of working principle of TEM for the formation of image and electron diffraction pattern.

For the TEM measurement, since the electrons have to transmit from the specimen, it should be sufficiently thin (typically in the range of 50-100 nm). These transmitted electrons are collected and focussed using various objective lenses. These electrons are then projected by the projector lens and form a magnified real image of the specimen with the help of florescent screen or CCD (charge coupled device) camera. The whole column needs to be maintained under high vacuum so that the electron does not get scattered or absorbed upon interacting with the air molecules. The main important issue in the cross-sectional TEM measurements is that the sample preparation. In the present case, the sample was cut into two slides of 2.5 mm

size and they were glued face-to-face with the help of epoxy glue. These glued samples were further glued using a dummy Si substrate at the rear side of the sample. This whole structure was inserted in a metallic tube of 3 mm diameter and was sliced-off sufficiently using a diamond wheel saw to get a thin disc. This disc was further thinned by double dimpling followed by a final thinning using a precision-ion- polishing system. The ion polishing was carried out at 3.0 keV energy without liquid nitrogen cooling, followed by a 1.2 keV cleaning process.

In this thesis, selected area electron diffraction (SAED) has been used to confirm the phase synthesis. The inter-layer diffusion and mixing phenomena were understood using the elemental line profiles, which were extracted from Energy dispersive analysis of X-rays.

2.3.5 Atomic force microscopy (AFM)

Atomic force microscopy (AFM) is one of the most powerful and non-destructive techniques, which is capable of providing the surface morphology of all kind of material films (including metals, semiconductors, and insulators). Using AFM, one can obtain surface roughness and growth mechanism (from power spectral density spectra). AFM makes use of a sharp tip that is mounted at the end of a cantilever to obtain the topographic information. In general, the AFM tips are made up of silicon or silicon nitride, whose radius is within 10-50 nm. There are three modes that the AFM operates, depending on the nature of the interaction between the atoms of the sample surface and tip, they are: (1). contact mode, (2). non-contact mode and (3). tapping mode. These modes are indicated in figure 2.12, where the force between the atoms of specimen surface and the tip is shown as a function of the distance between the surface and tip. When the probe is in contact with the sample surface, it experiences a predominant repulsive force, which is known as contact mode. When the probe starts moving away from the surface, the attractive forces become dominant and this mode is known as a non-contact mode. In the tapping mode, the cantilever oscillates up and down from the sample surface. In this case, while scanning the surface, there is no mechanical contact between the surface and tip. In this thesis, the information of surface morphology and their growth mechanism has been gathered from the AFM measurements. The AFM data was analysed using WSXM software package [21].

2.3.6 Physical property measurement system (PPMS)

A homemade Physical property measurement system (PPMS) at UGC-DAE-CSR, Indore was used for the electrical transport measurements. The electrical resistivity as a function of temper-
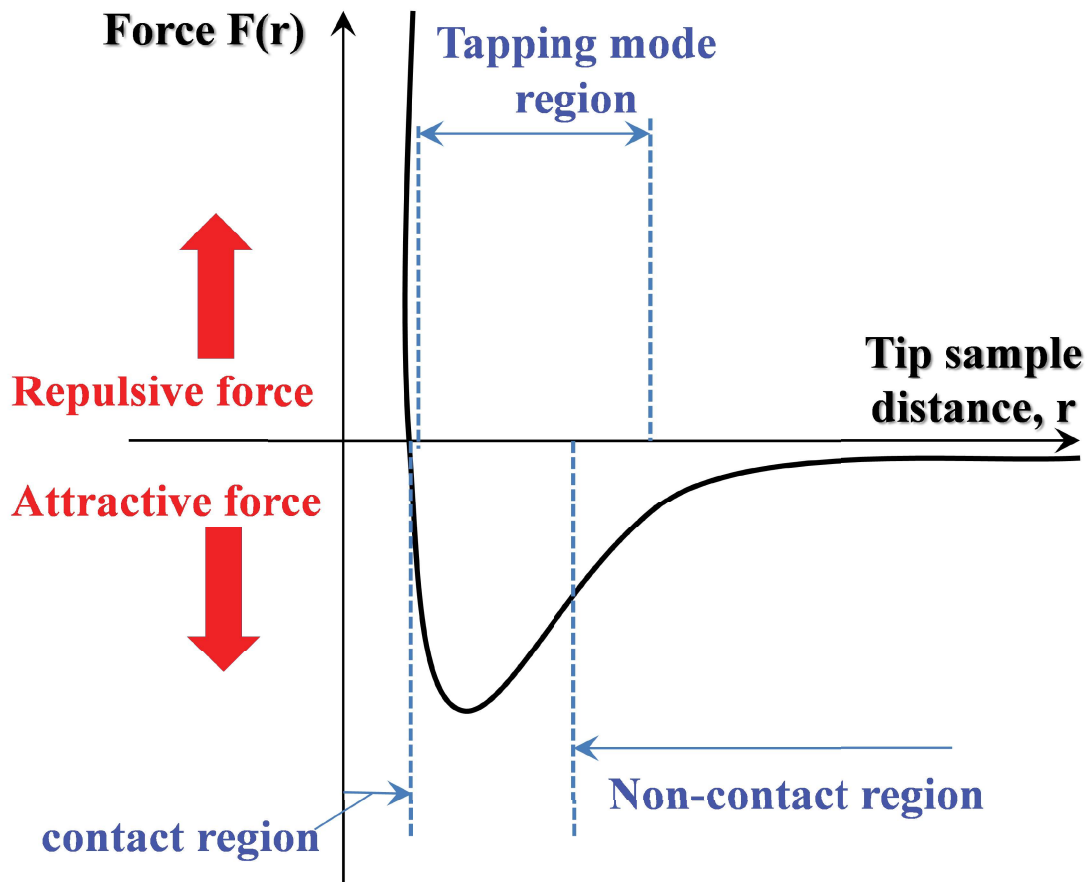
Figure 2.12: Force between the atoms of surface and tip as a function of the tip-sample distance.

ature and magnetic fields was measured to obtain the information related to the superconducting properties. This set up has a provision to load 16 samples at a time and it is capable of measuring 8 samples simultaneously. The system can measure a maximum of 1 $M\Omega$ resistance. The accessible temperatures are from 1.5 to 300 K, where liquid nitrogen and liquid helium were used for the cooling of samples. It has a magnet of 8 Tesla, with a sensitivity of 0.001%. The magnetic field can be applied parallel to the current direction. Bar-shaped samples of 15 mm $\times$ 2 mm $\times$ 1 mm are required for the measurements. All the four contacts were made using Indium soldering along the length of the sample. The measurements were performed by supplying the current and by measuring the voltage.

Bibliography

[1] J. George, Preparation of thin films, CRC Press, (1992).

[2] J. E. Mahan, Physical vapour Deposition of Thin Films, Wiley-VCH, January 336 (2000).

[3] D. Kanjilal, S. Chopra, M. Narayanan, I. S. Iyer, V. Jha, R. Joshi, S. Datta, Nucl. Instrum. Meth. Phys. Res. Sec. A, 328, 97 (1993).

[4] D. Kanjilal, G. O. Rodrigues, U. K. Rao, C. P. Safvan, and A. Roy, Ind. Jour. Pure Appl. Phys. 39, 25 (2001).

[5] P. Kumar, G. O. Rodrigues, U. K. Rao, C. P. Safvan, D. Kanjilal, A. Roy, Pramana 59, 805 (2002).

[6] H. P. Klug, L. E. Alexander, X-ray Diffraction Procedures, Wiley New York, (1954).

[7] W. L. Bragg, Nature 90, 410 (1912).

[8] M. Birkholz, Thin Film Analysis by X-Ray Scattering. Wiley, Weinheim, 378 (2006).

[9] E. Rutherford, Phil. Mag. 21, 669 (1911).

[10] W. K. Chu, Backscattering Spectrometry, Elsevier, (2012).

[11] W. K. Chu, J. W. Mayer, M. A. Nicolet, Backscattering spectrometry, Academic Press, New York, (1978).

[12] J. O'Connor, B. Sexton, R. St. C. Smart, Surface Analysis Methods in Materials Science, Springer Series in Surface Sciences, (2003).

[13] J. C. Vickerman, I.S. Gilmore, Surface Analysis: the principal techniques, Wiley Online Library, (1997).

[14] L. R. Doolittle, Nucl. Instrum. Methods B 9, 344 (1985).

[15] J. I. Goldstein, D. E. Newbury, P. Echlin, D.C. Joy, C. E. Lyman, E. Lifshin, L. Sawyer, J. R. Michael, Scanning Electron Microscopy and X-ray Microanalysis, Springer, 453 (2003).

[16] D. B. Williams, C. B. Carter, Transmission electron microscopy, Springer, 3 (1996).

[17] L. Reimer, Transmission Electron Microscopy: Physics of Image Formation and Micro-analysis, Springer, (2013).

[18] J. C. H. Spence, High-resolution Electron Microscopy, Oxford University Press, 3rd Ed. (2003).

[19] B. Fultz and J. Howe, Transmission Electron Microscopy and Diffractometry of Materials, Springer, 2nd Ed. (2005).

[20] G. Binnig, C. F. Quate, and C. Gerber, Phys. Rev. Lett. 56, 930 (1986).

[21] I. Horcas, R. Fernández, J. M. Gómez-Rodríguez, J. Colchero, J. Gómez-Herrero, A. M. Baro, Rev. Sci. Instrum. 78, 013705 (2007).

Chapter 3

Phase synthesis of Ni-Bi bilayers and effect of swift heavy ions

3.1   Introduction:

As mentioned in the chapter 1 that the stable phases of Ni and Bi ($NiBi$ and $NiBi_3$) are interesting for both fundamental physics and several applications. The synthesis of these phases has been carried out using various conventional techniques [1–15]. In this chapter, the phase synthesis is carried out by swift heavy ion beam mixing using 100 MeV Au ions [16, 17]. Prior to this study, an interesting aspect of this Ni-Bi system is discussed that is the spontaneous formation of stable phases during the deposition of Bi layer on top of Ni layer and vice versa [16, 18]. It is necessary to understand the origin of such fascinating phenomenon of spontaneous phase formation. Therefore, the confirmation studies of the formation of stable phases are carried out using various analysis techniques. This chapter also explains about an enhancement in the mixing due to 100 MeV Au ions upon increasing ion fluence using Rutherford backscattering spectrometry and transmission electron microscopy measurements. The dependence of the superconducting order parameters on the fluence of swift heavy ion irradiation is also discussed. As it has been mentioned above in chapter 1 that the ion beam mixing has several advantages compared to conventional phase synthesis techniques. A set of single bilayer samples of Ni and Bi were deposited on Si substrate using thermal evapouration technique. These films were irradiated using 100 MeV Au ions in the fluence range of 1×10^{12}-1×10^{14} ions/cm^2. The ion beam mixing is further extended for five bilayers of Ni/Bi films so that each Ni layer gets two adjacent Bi layers and vice versa as the number of bilayers increases, which is expected to enhance the mixing compared to single bilayers. These ion beam mixing has been performed using 100 and 120 MeV Au ions. The fluence ranges in both the cases were kept as same as

Species and energy of ion beam	Target elements	S_e (keV/nm)	S_n (keV/nm)	$\frac{S_e}{S_n}$	Range (nm)
100 MeV Au ions	Ni	32.45	0.835	38.86	6010
	Bi	17.59	0.58	30.45	9840
	NiBi	25.29	0.76	33.05	7120
	NiBi$_3$	21.26	0.67	31.54	8280
120 MeV Au ions	Ni	36.77	0.73	50.64	6570
	Bi	20.04	0.5	39.74	10840
	NiBi	28.76	0.67	43.1	7830
	NiBi$_3$	24.2	0.59	41.15	9110

Table 3.1: The electronic, nuclear energy losses and their ratio as well as range of 100 MeV Au ions in Ni and Bi layers.

the above study (1×10^{12}-1×10^{14} ions/cm^2).

The estimated nuclear energy loss, electronic energy loss and their ratios along with the range of 100 MeV Au ions in individual Ni, Bi, NiBi and NiBi$_3$ targets, calculated from SRIM [19], were shown in the table 3.1. It may be observed that the electronic energy loss dominates over nuclear energy loss by two orders of magnitude. Therefore, the mixing features are expected to be mostly from electronic energy loss. The ranges of these ions are more than 6 μm and 9 μm in Ni and Bi layers respectively, which means that the irradiated Au ions stop much deeper in the Si substrate.

3.2   Experimental:

A set of Ni and Bi films of thickness $\sim$ 35 nm each were prepared on Si (100) substrates using in-situ thermal evapouration by evapourating highly pure Ni and Bi materials. Prior to the deposition, the Si substrates were cleaned by ultrasonication in acetone and followed by isopropyl alcohol and then dried carefully to prevent the external contamination. A constant deposition rate of $0.1 \mathring{A}/s$ and substrate rotation of 20 revolutions per minute were maintained throughout the deposition. The vacuum during the deposition was less than 5×10^{-7} mbar. The substrates were supplied with no external temperature during the deposition. These samples were irradiated using 100 MeV Au ions were used for irradiating the films and the irradiated fluences were 1×10^{12}, 3×10^{12}, 1×10^{13} and 1×10^{14} ions/cm^2. GAXRD measurements were

performed in all the samples using Bruker D8 Advance diffractometer with Cu Kα radiation (λ=1.514Å). Rutherford backscattering spectrometry (RBS) measurements were performed on both the irradiated and as-deposited films, to obtain the thickness of the films, composition and the mixing information after irradiation. With the help of field emission scanning electron microscope (FESEM), ion-induced surface morphological modifications were observed. In order to observe these modifications microscopically, transmission electron microscopy along the cross section of the sample was performed using a TEM (FEI, Tecnai F30) equipped with a GATAN Orius CCD camera and energy dispersive x-ray spectroscopy instruments. Electrical transport measurements were carried out to investigate the superconducting nature of the films using the standard linear four probe method on a bar-shaped sample. In order to confirm the superconductivity from the transport measurements, M-H loops were recorded using a SQUID magnetometer.

A set of 5 bilayer Ni (15 nm) and Bi (15 nm) films were prepared using thermal evapouration at a base pressure less than 5×10^{-7} mbar. The films were prepared in the similar way as mentioned above. These films were also irradiated using 100 MeV and 120 MeV Au ions in a fluence range of 1×10^{12} ions/cm^2 - 1×10^{14} ions/cm^2 at room temperature. The phase analysis of the films before and after ion irradiation was performed using GAXRD. The ion-induced surface modifications of all the films were investigated using FESEM. The effect of ion irradiation in terms of mixing and sputtering was understood by means of RBS using 2 MeV He-ions.

3.3 Results and discussion:

3.3.1 Spontaneous formation of stable phases

A set of Ni/Bi bilayer films of thickness 35 nm each were deposited on Si substrate. The glancing angle X-ray diffraction pattern of this sample is shown in figure 3.1. The XRD patterns show the presence of NiBi$_3$ phase along with the elemental Ni and Bi in the as-deposited Ni/Bi bilayer films, which is strange and was not observed in the case of an untreated Ni/Bi bilayers. The 2θ position of Ni peaks are found at 44.5^o, 51.9^o and that of Bi are 28.6^o, 31°, and 58.9^o. The peaks corresponding to NiBi$_3$ are found to be at 2θ positions of 25.4^o, 29.7^o, 32°, 34.12^o, 37.33^o, 38.33^o, 40.6^o, 43.6^o, 55.39^o, 57°, 58.9^o, 60.16^o, and 60.85^o.

For the better understanding of spontaneous formation, we perform GAXRD measurements at various incident angles from 0.05^o to 0.8 ^{o}. These values of incident angles can be converted
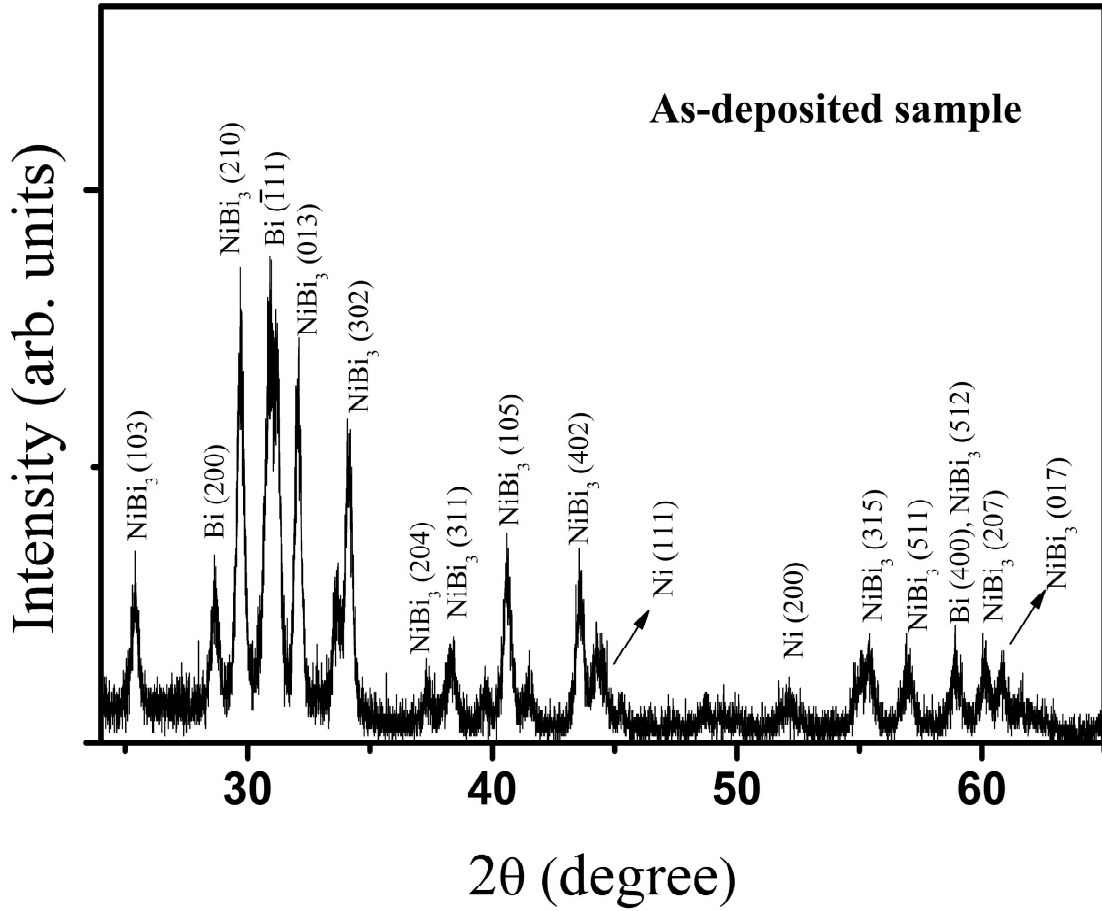
Figure 3.1: GAXRD pattern of the as-deposited sample.

into penetration depths (d) of X-rays inside the samples using the following formula: [23]

$$d = sin\theta/\mu \tag{3.1}$$

Where θ is the incident angle and μ is absorption coefficient at X-ray wavelength. The integral intensities of the strongest peaks of Bi ($\bar{1}$11) and NiBi$_3$((210) and (013)) of the as-deposited sample are plotted as a function of the penetration depth of X-rays in figure 3.2. In this figure, a finite signature of NiBi$_3$ can be noticed till the depth of 5 nm from the film surface. The peak intensities of both NiBi$_3$ and Bi are increasing with increasing the penetration depth and get saturated after a depth $\approx$ 32 nm, which is nearly equal to the thickness of the Bi film. It can be inferred that the NiBi$_3$ compound has been formed throughout the top layer, which can be understood in terms of reaction-diffusion mechanism. The spontaneous formation of NiBi$_3$ during the deposition can be shown using the following equation:

51

$$Ni + 3Bi \rightarrow NiBi_3 \tag{3.2}$$
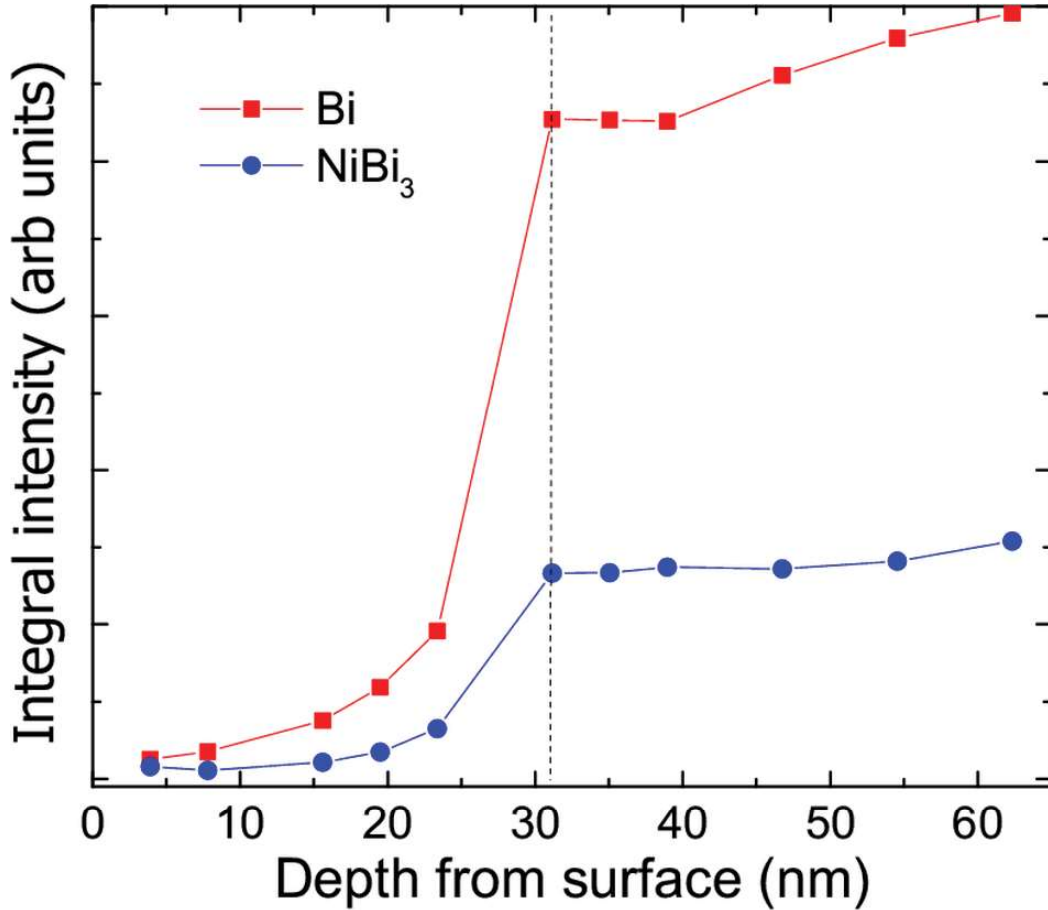
Figure 3.2: Integral intensities of NiBi$_3$ (average of (013) and (210)) and Bi ($\bar{1}11$) peaks of as-deposited sample as a function of X-ray penetration depth from the surface

The spontaneous formation of NiBi$_3$ has been further illustrated using a cross-sectional transmission electron micrograph of the as-deposited sample, as shown in figure 3.3. The spontaneously formed NiBi$_3$ grains can be noticed in the figure 3.3. Along with the existence of NiBi$_3$ phase, one can also notice the presence of elemental Ni, Bi, SiO$_x$ (native silicon oxide layer), and Si (from the substrate) in the TEM image corresponding to as-deposited Ni/Bi films. Dybkov *et al.*, has reported that the NiBi$_3$ would form at the Ni-Bi interface initially, if a temperature is supplied that is similar to the melting point of Bi [2]. The thickness of such NiBi$_3$ layer would increase by the diffusion of Bi atoms into the Ni side through the already existing NiBi$_3$ layer. Such diffusion is counter-intuitive as the radius of Bi atoms is larger compared to that of Ni atoms. However, it was explained by Dybkov [2] in terms of the

difference in their melting points, which is ≈ 544 K in the case of Bi and is ≈ 1728 K in the case of Ni. Due to this fact, Bi atoms are much more mobile compared to the Ni atoms. It was also found by Dybkov and co-workers that the keeping a solid Ni in contact with the molten Bi can result in the formation of $NiBi_3$ layer with the thickness of more than 1 μm within a minute duration. In the present case, the deposition rate of Bi was 0.6 nm per minute on the Ni layer. Such substantial amount of time may allow energetic Bi atoms to migrate and form the initial $NiBi_3$ grains through the reaction-diffusion process.
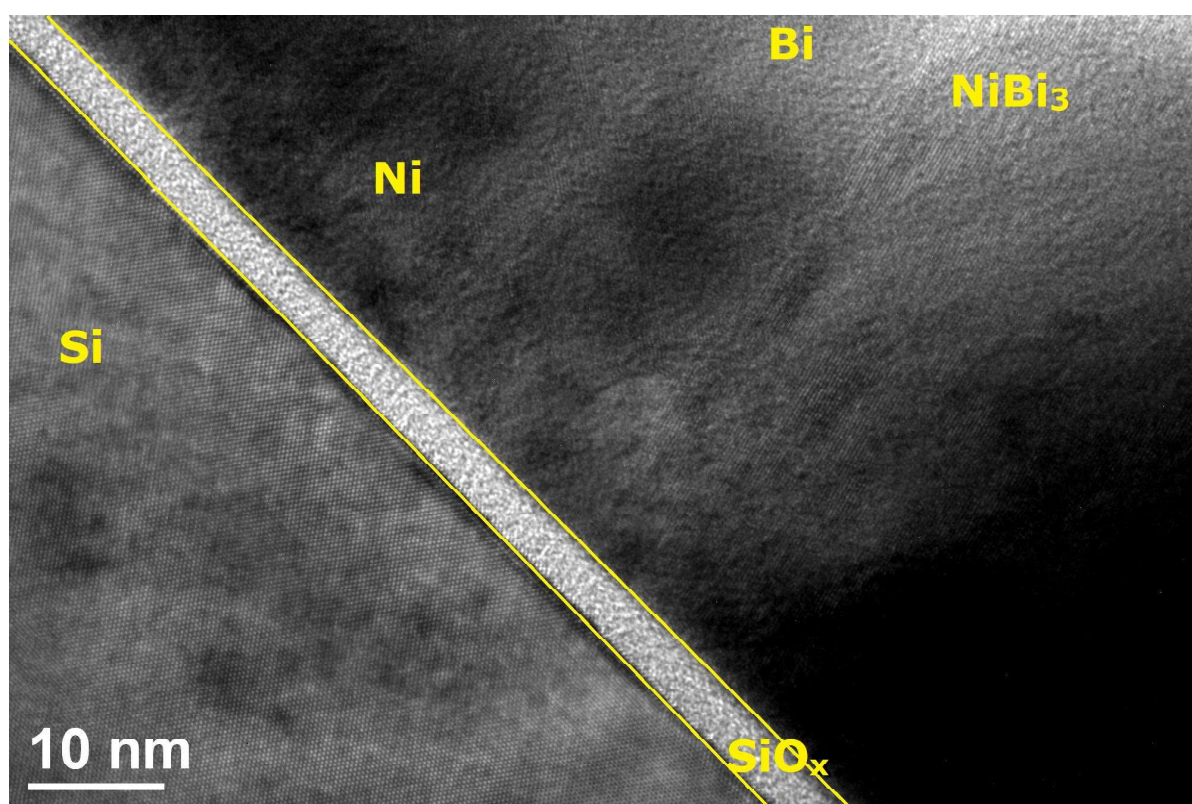
Figure 3.3: Cross sectional TEM image of as-deposited sample

3.3.2 Effect of 100 MeV Au ions on Ni/Bi single bilayer films

Figure 3.4 shows the GAXRD patterns of the as-deposited and swift heavy ion irradiated films. As mentioned above, the as-deposited sample shows the presence of Ni, Bi, and $NiBi_3$ peaks, whose existence is still present in the case of all the irradiated samples as well. It may be inferred that the ion irradiation has not affected the already existing phases in the as-deposited bilayers. In the inset, full width at half maximum (FWHM) of the strongest $NiBi_3$ (210) peak as a function of fluence has been shown. It shows an initial drop and rises with increasing ion
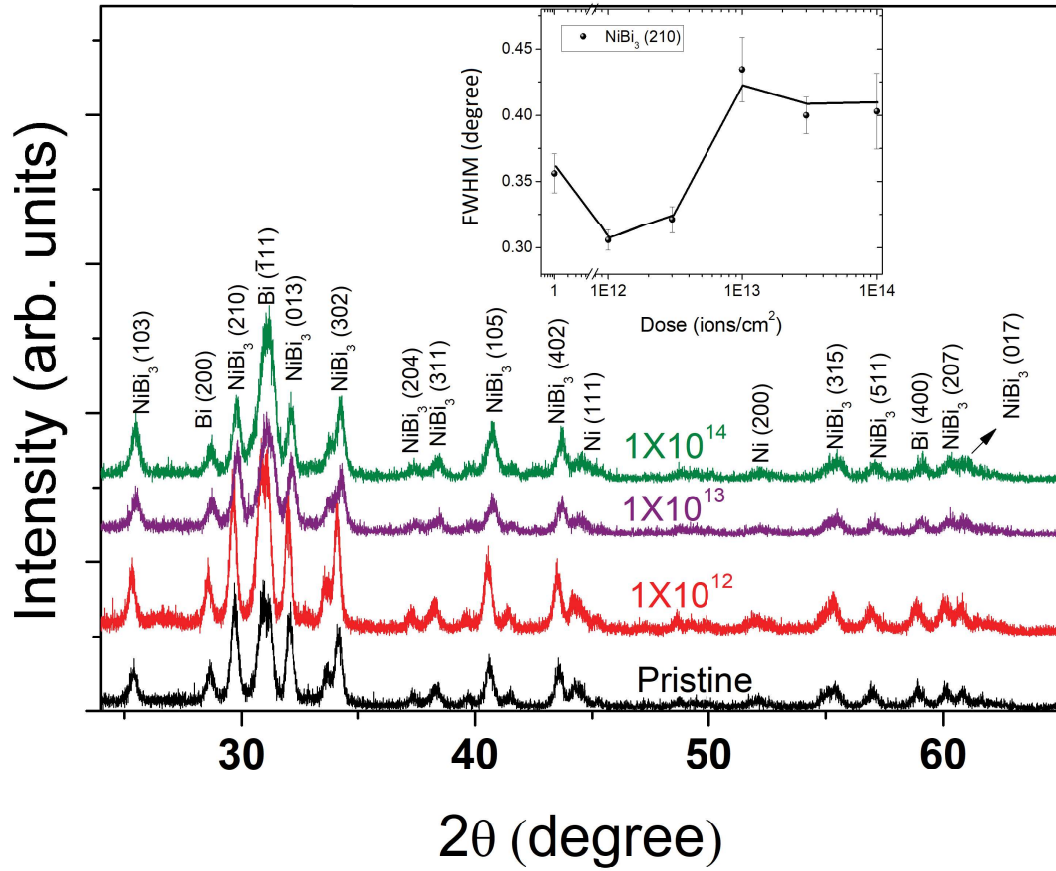
Figure 3.4: GAXRD patterns of the as-deposited and all the irradiated films. FWHM of $NiBi_3(210)$ peak as a function of ion fluences is shown in the inset.

fluence and finally saturates at higher fluences. The initial drop in FWHM is an indication of annealing effect [20] in the films due to ion-induced thermal energy deposition. However, at higher fluences, the increasing FWHM indicates an increasing degree of random disorderedness (amorphization) of $NiBi_3$ phases due to rapid quenching of high temperatures and heavy ion-beam induced ballistic effects. The quenching rate of the latent track is typically in the order of 10^{14} K/s [21], which can induce the degree of amorphization. The SHI induced nuclear energy loss (though less in magnitude) can lead to ballistic effects in the system [22], whose role cannot be excluded in the enhanced degree of amorphization.

A high-resolution cross-sectional transmission electron microscopy image of the sample irradiated at a fluence of 1×10^{14} ions/cm^2 is shown in figure 3.5(a). It also shows the presence of Ni, Bi, $NiBi_3$ and Si, like in the case of as-deposited sample. However, the thickness of the native silicon oxide (SiO_x) was noticed to be reduced, which is due to the ion irradiation. A
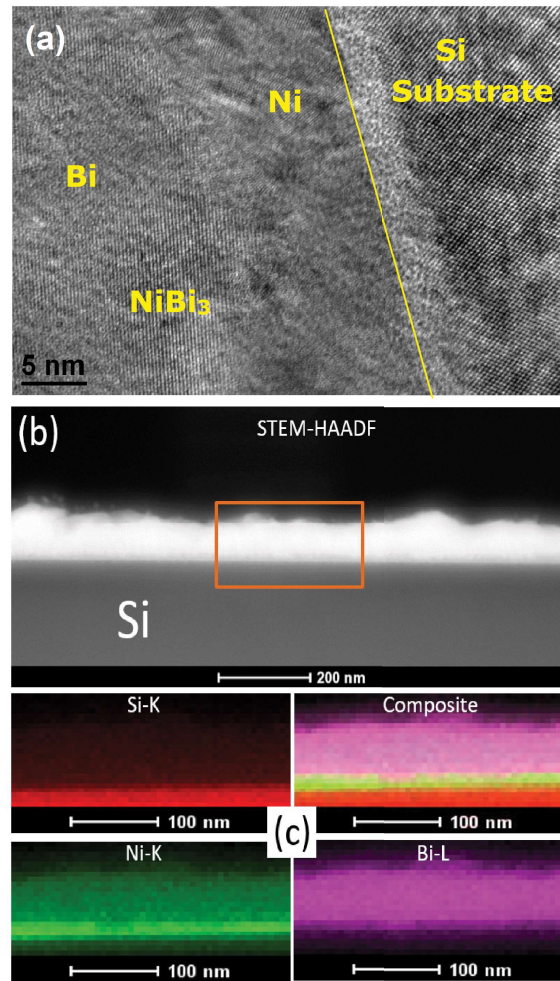
Figure 3.5: (a). High resolution Cross-sectional transmission electron micrograph of the sample irradiated at the fluence of 1×10^{14} ions/cm^2, (b). STEM-HAADF pattern of the sample irradiated at 1×10^{14} ions/cm^2, (c). Individual elemental (Si-K, Ni-K and Bi-L) maps and their composite map.

high angle annular dark field (HAADF) scanning transmission electron microscopy (STEM) image of the sample irradiated at highest fluence is shown in figure 3.5(b). Elemental mapping of Ni, Bi, Si and their composites are shown in 3.5(c), which were obtained from the Energy dispersive spectroscopy (EDS) in the orange region marked in panel (b). A significant diffusion of Ni throughout the thickness of the Bi layer can be clearly noticed in figure 3.5(c). This is an interesting observation, as the incident energy of the ion beam was not sufficient to cause thermal mixing of Ni and Bi, according to Wang and co-workers [24]. It was suggested that the electronic energy loss should be more than 49 keV/nm to drive the Ni into molten phase [24]. Swift heavy ion-induced ballistic effects are expected to drive the Ni atoms in the direction of

Si substrate. However, figure 3.5(c) shows a predominant diffusion of Ni towards the surface, which is in opposite direction. Moreover, the GAXRD pattern shows that there is hardly any Ni signal, which is an indication that most of the Ni that can be seen in figure3.5(c) is coming from $NiBi_3$ grains.
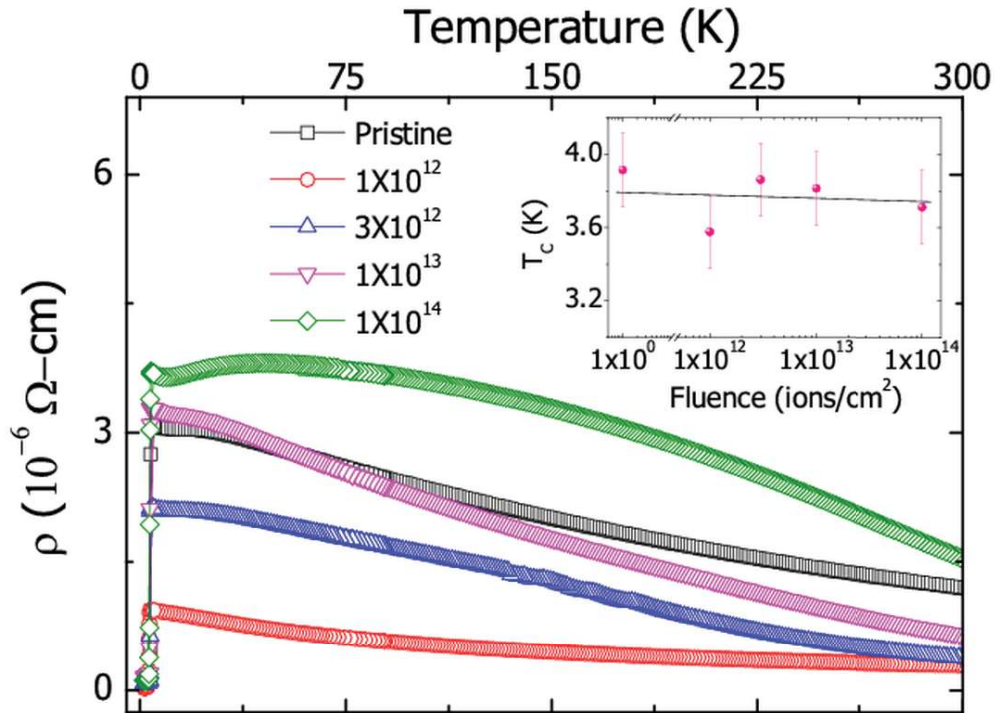
Figure 3.6: Resistivity as a function of temperature for irradiated and as-deposited samples. Variation of T_c with irradiation fluence is shown in the inset.

Further confirmation of $NiBi_3$ layer formation will be discussed using the electrical transport measurements. The temperature dependent resistivity for the as-deposited and irradiated samples is shown in figure 3.6. A semi-metallic nature can be noticed in the normal state resistivity, which was due to the contact leads were made on the top semi-metallic Bi layer. All the samples show superconducting transition below a temperature of ≈ 3.9 K. The temperature at which the resistance drops to about 90 % of the normal state has been defined as the superconducting transition (T_c). The values of transition temperatures in the present case are somewhat less than the reported T_c of $NiBi_3$ [5–7, 10]. The reason for the reduced T_c may be due to the existence of Ni and Bi impurities in the $NiBi_3$ grains. It may be observed in the inset of figure 3.6 that there is barely any change in T_c as a function of irradiation fluence, within experimental errors. It is interesting to note that the nature of normal state resistivity for all the samples as

a function of fluence is in congruence with the variation of FWHM of $NiBi_3$ peaks as shown in the inset of figure 3.4. After irradiation, the overall resistivity in normal state decreases at the lowest fluence (1×10^{12} ions/cm^2) compared to the as-deposited sample. However, with increasing the irradiation fluence, the overall resistance increases systematically.
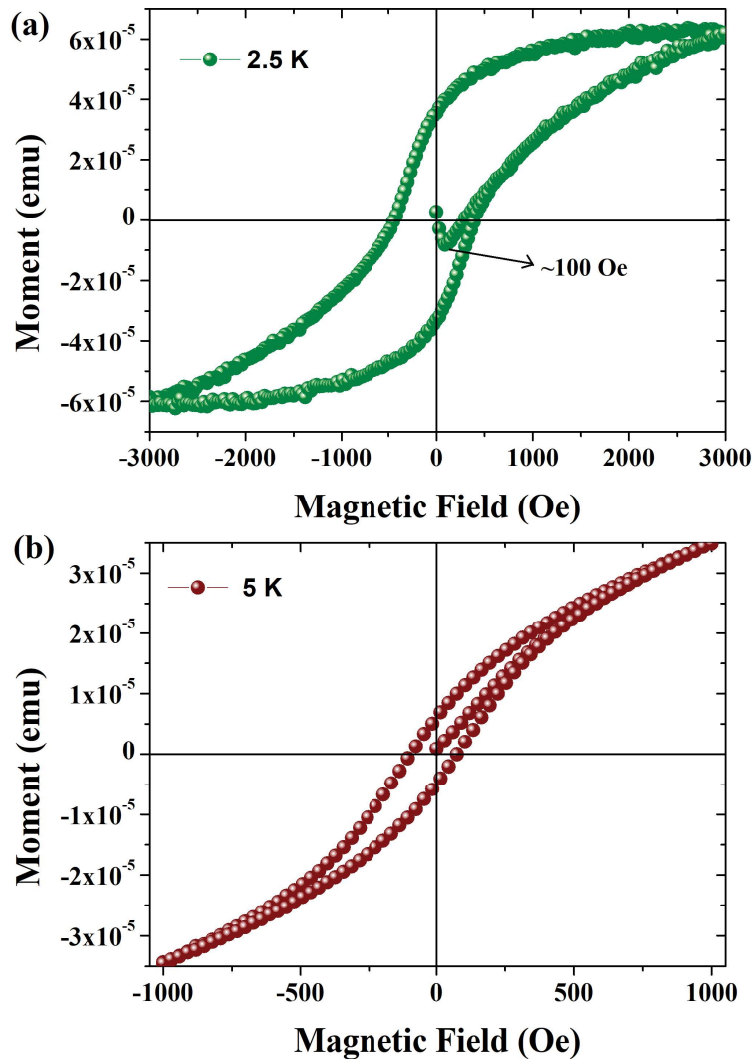
Figure 3.7: Zero-field in-plane magnetization as function of applied magnetic field at 2.5 K (a) and 5 K (b) in the sample irradiated at highest fluence.

The sample irradiated at lowest fluence (1×10^{12} ions/cm^2) shows an initial decrease in resistivity compared to the as-deposited sample, and then increases for the higher irradiation fluences. This finding is in good agreement with our previous argument related to ion-induced thermal annealing of the films as explained in the context of the inset of figure 3.4. The relative

insensitivity of T_c in these films towards ion irradiation has suggested us to rule out the other possible origins of superconductivity. The bismuth films were reported to be superconducting below 7 K under particular conditions [25]. This possibility has been excluded, as there was no superconducting transition down to 2 K in plain Bi films of similar thickness and was prepared in the same conditions. The indium that was used contacts may also be the other possibility, which was excluded by measuring the magnetization as a function of applied magnetic field at constant temperatures. Figures 3.7(a) and (b) show the M-H loop that is measured at 2.5 K and 5 K respectively, which were the temperatures slightly below and above the superconducting transition temperatures. Figure 3.7(a) shows a clear diamagnetic behaviour at low field, whereas the figure 3.7(b) shows no diamagnetic behaviour in the M-H loop. From the panel (a) of figure 3.7, the lower critical field (H_{c1}) of NiBi$_3$ was found to be $\approx$100 Oe, which is consistent with the previously reported values for bulk NiBi$_3$ [7]. However, estimating the actual critical current density from these measurements is difficult due to the presence of Ni layer, which has a strong ferromagnetic contribution to the magnetic moment. The slope of this hysteresis loop in the Meissner state, which is a state of the superconductor below the superconducting transition, confirms the existence of a finite critical current density and hence bulk superconductivity.

Surface morphology of the films before and after ion irradiation are shown in figure 3.8, where the FESEM images of (a). as-deposited films, (b). 1×10^{12} ions/cm^2 (c). 3×10^{12} ions/cm^2 and (d). 1×10^{14} ions/cm^2 are illustrated. A plain morphology throughout the film surface has been noticed in the case of as-deposited films, whereas after ion irradiation, porous like structures were observed. Interestingly, with increasing ion fluence, the average size of these porous structures was found to be increased. However, the grain sizes in nanometer scale are noticed to be almost the same, which is evident from the insets of figure 3.8. The increment in the average size of pores can be assigned to the ion-induced local melting. As mentioned in the table 3.1, 100 MeV Au ions lose their energy predominantly to electronic subsystem compared to the atomic subsystem and hence have dominant S_e over S_n [19]. In such case, most of the energy utilized in the electron excitation process initially and then transfers the energy to lattice atoms through electron-phonon coupling [26]. According to thermal spike model, high temperatures are expected to produce during this process. As a consequence, mixing, alloys formation, dewetting, phase transition and other physical processes take place. Likewise in the present case, the Bi temperature can readily reach its melting point at this
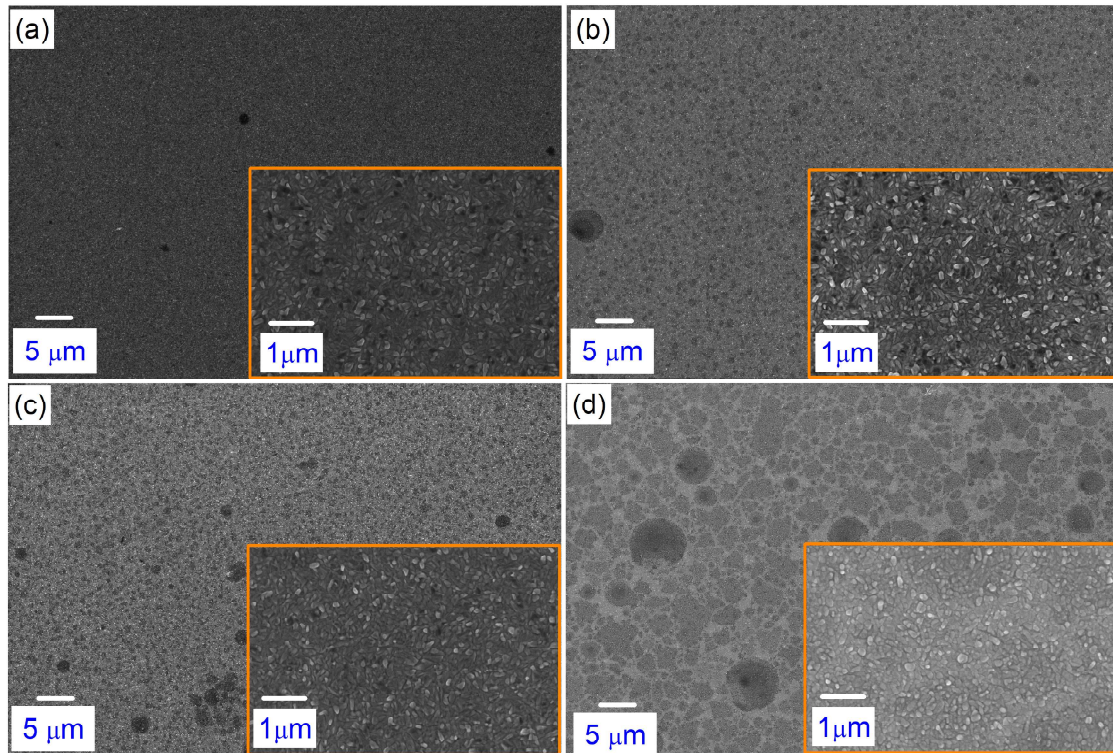
Figure 3.8: Scanning electron micrographs of as-deposited (a), 1×10^{12} ions/cm^2 (b), 3×10^{12} ions/cm^2 (c) and 1×10^{14} ions/cm^2 (d). The corresponding magnified images are shown in the inset.

energy regime [27]. This porous morphology after ion irradiation has been attributed to the out-diffusion of Bi along the ion-induced molten zones.

In order to observe the mixing microscopically, cross-sectional TEM-EDX measurements on as-deposited and irradiated samples have been performed. Figure 3.9 (a), (b) and (c) shows the cross-sectional view of as-deposited and irradiated films at the fluences of 1×10^{12} and 1×10^{14} ions/cm^2 respectively. The corresponding elemental depth profiles of Ni, Bi and Si are shown in panels (d), (e) and (f) of figure 3.9, which were extracted along the orange lines drawn across the cross section of the films. A green coloured window of cross lines is shown in the panels (d), (e) and (f), to emphasize the effect of mixing in all the samples. In the left sided region of this window, the ratio of Ni and Bi are almost 1:3, which is the spontaneously formed NiBi$_3$ layer. It is interesting to note that the width of this window gradually increases with increasing the ion fluence. It also confirms the improvement in the mixing of Ni and Bi with increasing ion fluence. The enhancement in the mixing can be seen more clearly in the high resolution cross sectional TEM images 3.10(a), (b) and (c) of the as-deposited

59
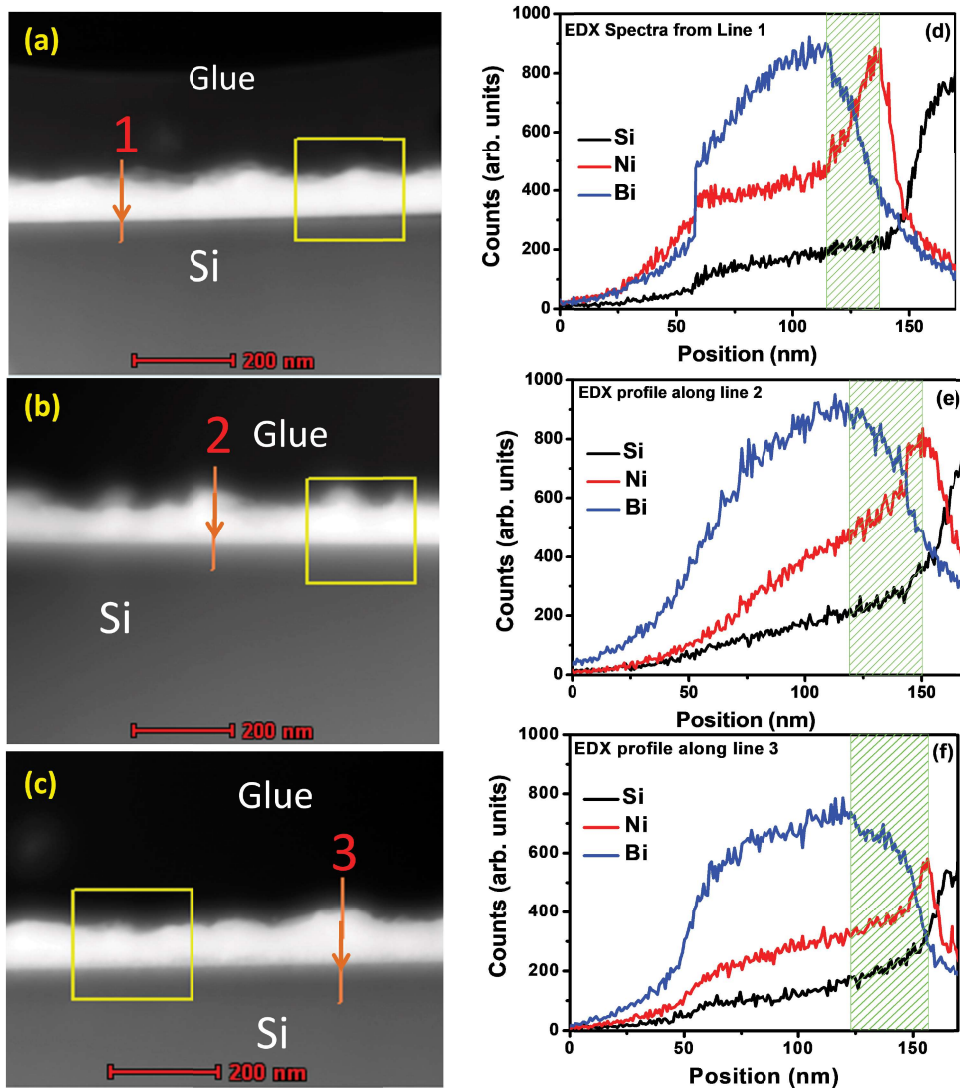
Figure 3.9: cross sectional TEM images of the as-deposited (a) and irradiated samples at the fluences of 1×10^{12} (b) and 1×10^{14} (c) ions/cm^2 respectively. The panels (d), (e) and (f) show elemental line profiles.

and the irradiated samples at the lowest and highest fluences. Since the as-deposited films (figure 3.10(a)) were polycrystalline in nature, the individual Ni and Bi layers could not be clearly identified. However, after ion irradiation at the highest fluence, the phases and layers can be clearly identified (figure3.10(b) and (c)) due to the ion-induced annealing effect. In figure 3.10(c), the Ni and NiBi$_3$ phases are determined with the help of inter planar spacing (d-spacing) values and those are 2.08 Å and 2.98 Å for (111) and (210) respectively. The average thickness of the Ni layer in the lowest irradiated sample was around 20 nm, which reduces to

almost 10 nm at the highest fluence. It indicates that the Ni layer of $\approx$ 10 nm is being utilized in the intermixing of Ni and Bi, which is a signature of enhancement in the mixing.
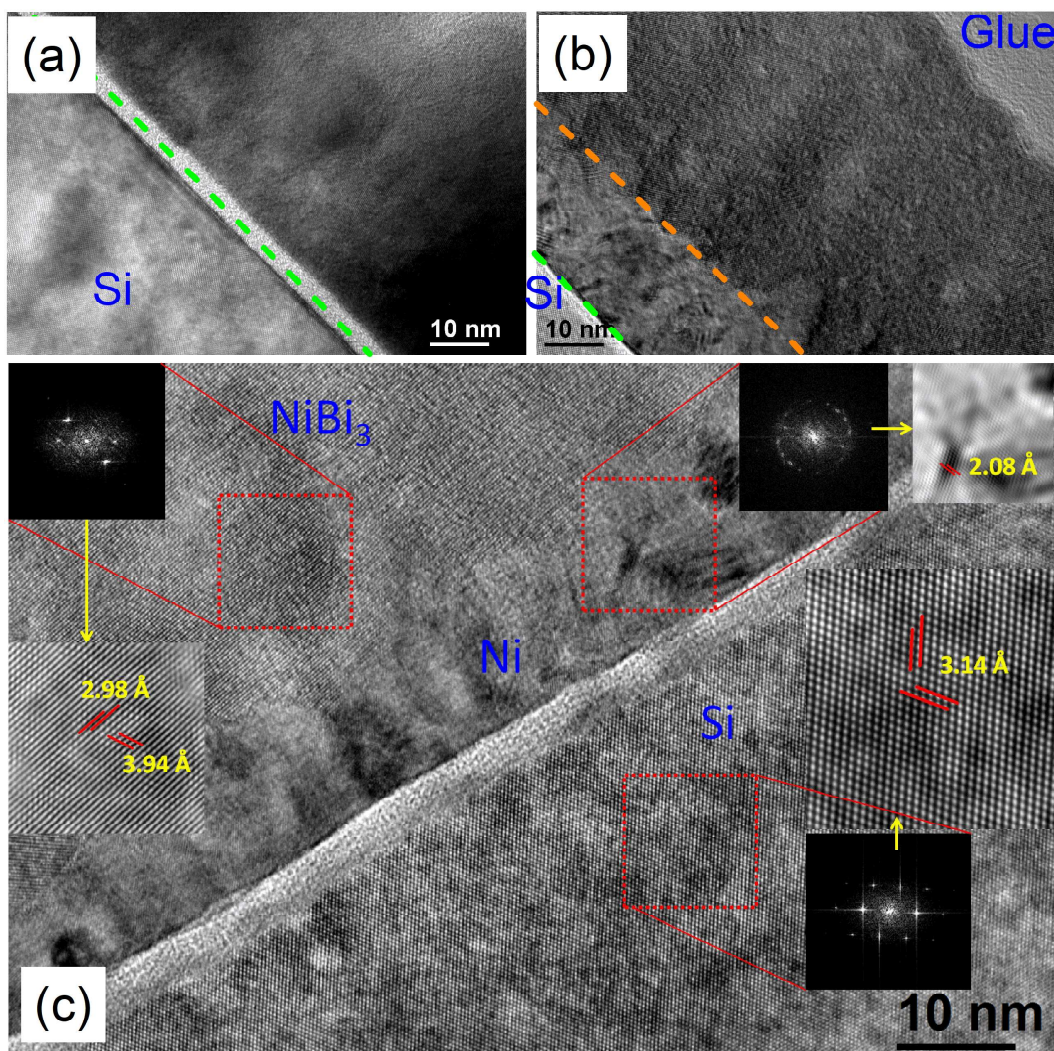
Figure 3.10: The panels (a), (b) and (c) represent the cross sectional view of the HRTEM images of as-deposited and irradiated samples at 1×10^{12} and 1×10^{14} ions/cm^2. The SAED patterns are shown in the insets.

Although the transmission electron microscope provides clear information of mixing, it is quite local. Therefore, the Rutherford backscattering spectrometry (RBS) measurements were performed to obtain the mixing information macroscopically. The RBS spectra of the as-deposited and ion irradiated samples are shown in figure 3.11. The magnified regions of Ni and Bi peaks are shown in the insets of figure 3.11, to emphasize the ion-induced modifications. One can notice a tailing effect at the high energy side of Ni peak in all the samples, which is an evidence of the spontaneous phase formation. As mentioned in the second paragraph of

this section that the temperature of Ni does not reach its melting point at the present energy, because the value of S_e is much less than the reported threshold value (77 keV/nm) [24, 28]. The integral intensities of both Ni and Bi peaks are slightly reducing with increasing the ion fluence, which is due to the out-diffusion of Bi as well as both Ni and Bi from NiBi$_3$ grains at the surface from the ion-induced molten zones (as explained above in the context of surface morphology).
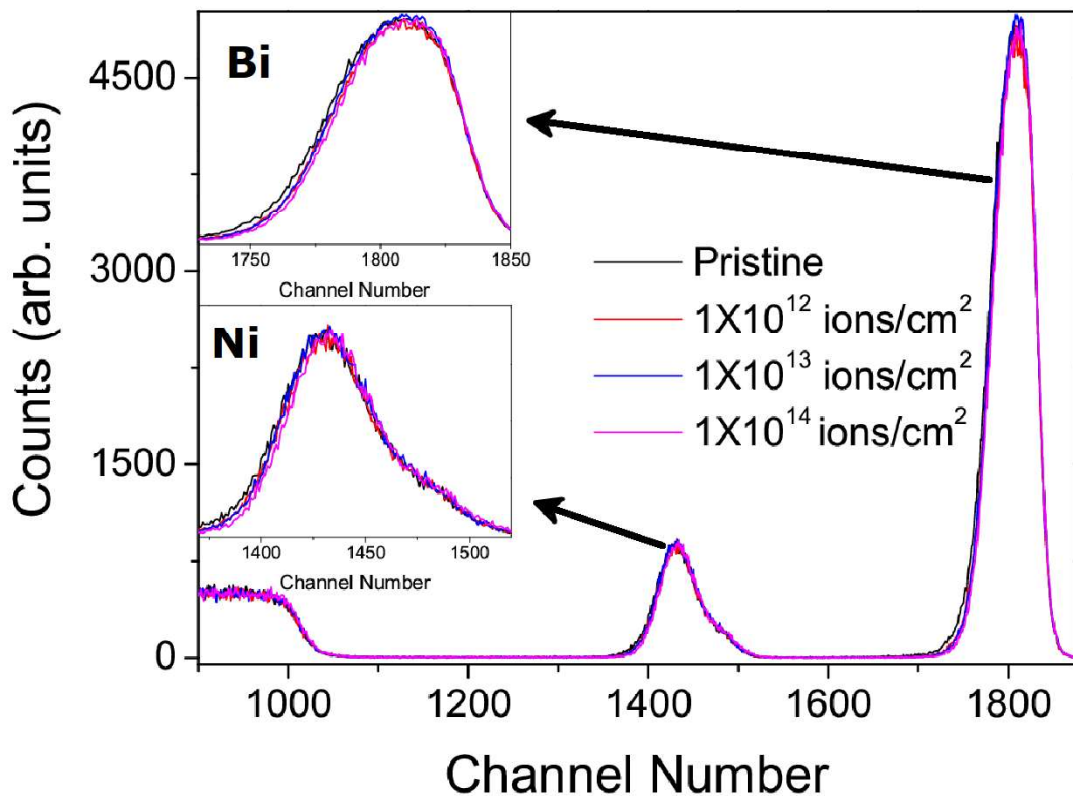
Figure 3.11: RBS spectra of as-deposited and all the irradiated samples. The inset shows the magnified peaks of Ni and Bi.

The RBS spectra were fitted using RUMP simulation package [29] and the depth profiles were extracted from the fits. The atomic fraction of Ni and Bi as a function of depth from the surface are plotted in figure 3.12. The region of Ni-Bi interface is magnified and shown in figure 3.12(b). From the surface to the depth of $\approx$50 nm, a constant distribution of Ni and Bi can be seen as 0.77 and 0.23 atomic fractions respectively. It indicates that the top layer consists of the NiBi$_3$ grains along with elemental Bi inside the top Bi layer. After this depth till $\approx$ 68 nm, the atomic fractions of both Ni and Bi are nearly equal, which can be due to the

presence of NiBi grains or elemental Ni and Bi atoms. Beyond this depth, the layer consists a small fraction of Bi and the remaining faction is Ni. Two grey coloured boxes are used to highlight the enhanced mixing features in figure 3.12(b). Sum of the thickness values of these two regions can be defined as the enhancement in the mixing due to ion irradiation. It is almost 10 nm, the summation of 3 nm and 7 nm, as shown in figure 3.12(b). The enhanced mixing has been defined by using the following equation:

$$Percentage \ of \ enhanced \ mixing = \frac{thickness \ of \ ion \ induced \ mixing}{total \ thickness \ of \ the \ films} \times 100 \quad (3.3)$$

The enhanced mixing due to 100 MeV Au ions is $\approx$15% ($\frac{10}{70} \times 100$) of the total thickness of the films. The temperatures during ion-matter interaction reach more than 1000 K, which is much greater than the melting points of Bi and NiBi$_3$. These athermal effects can lead to mobilization of atoms of Ni and Bi during the ions passage, which can eventually cause more and more mixing. Though less in quantity, the contribution from the swift heavy ion-induced ballistic effects cannot be ruled out. Hence, the reason for such enhanced mixing has been attributed to athermal and ballistic effects. The limited mixing in the present case is due to the insensitivity of Ni to 100 MeV Au ions as the S_e is much less than threshold electronic energy loss (S_{eth}), which is the main criteria for the melting at this energy regime [28, 30]. The details of thermal spike model calculations are provided in the chapter-6.

3.3.3 Effect of 100 MeV Au ions on Ni/Bi five bilayer films

It has been observed that the number of interfaces plays a key role in the mixing by ion irradiation. Therefore, number of Ni/Bi bilayers has been increased from one to five in the present case, where the effect of the ions at the same energy and fluence on five bilayers of Ni/Bi films is studied. The advantage of this study can be realized in terms of more interfaces of Ni and Bi, and thereby maximize the possibility of mixing compared to single Ni/Bi bilayers, where only one interface of Ni and Bi would exist. The GAXRD patterns of as-deposited and irradiated samples are shown in figure 3.13. The presence of NiBi and NiBi$_3$ phases along with elemental Ni and Bi is noticed in all the samples. As in the previous case, the as-deposited samples in the present study also indicate the formation of the stable phases due to the diffusion-reaction mechanism. Moreover, the presence of Bi$_2$O$_4$ is also observed in the as-deposited films, which may be on the surface of the samples. The intensity of this peak reduces considerably with
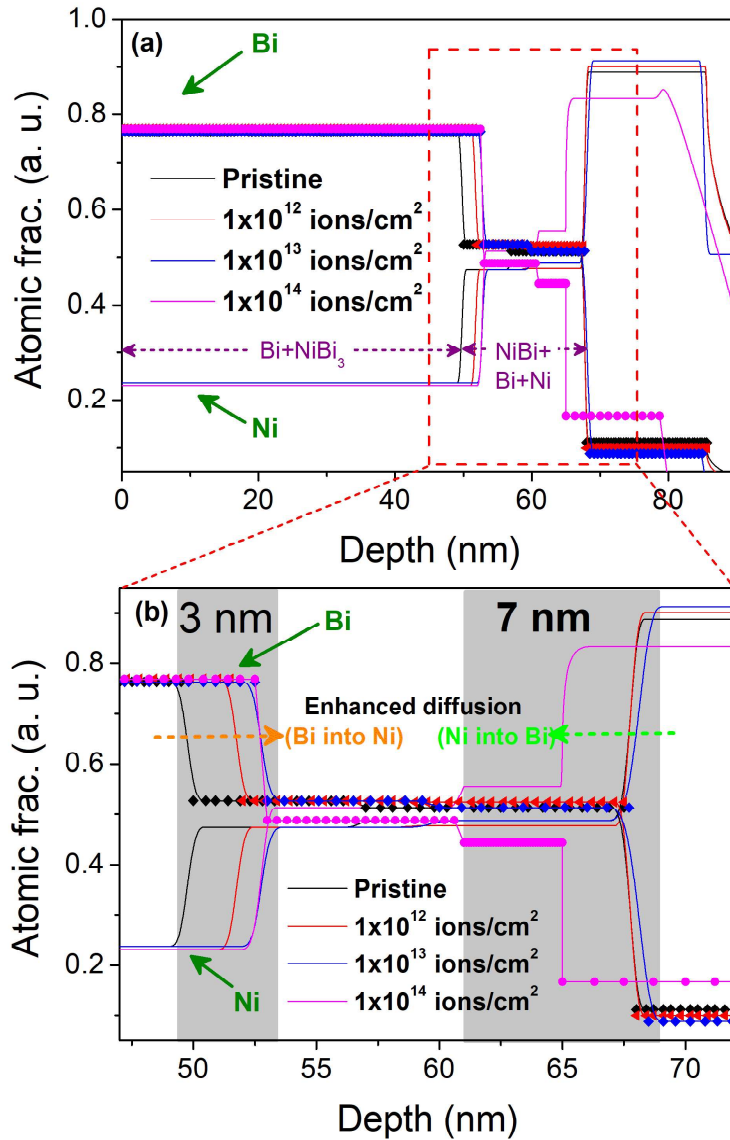
Figure 3.12: Panel (a) shows the depth profiles of Bi (solid lines with symbols) and Ni (solid lines) for the as-deposited and irradiated samples. Panel (b) shows magnified version of panel (a).

increasing ion fluence, which is due to the decomposition or sputtering of oxygen atoms from bismuth oxide on the surface. The FWHM of all the peaks is seen to be increased with the increase in fluence. The ion-induced temperatures are expected to reach much higher than its melting point (M. P. $\approx$544 K), which is discussed in chapter -6. It is well known that these ion-induced temperatures are proposed to quench very rapidly within $\approx 10^{12}$ K/s [31], which can certainly induce random amorphization in the existing phases. The fraction of these phases

64
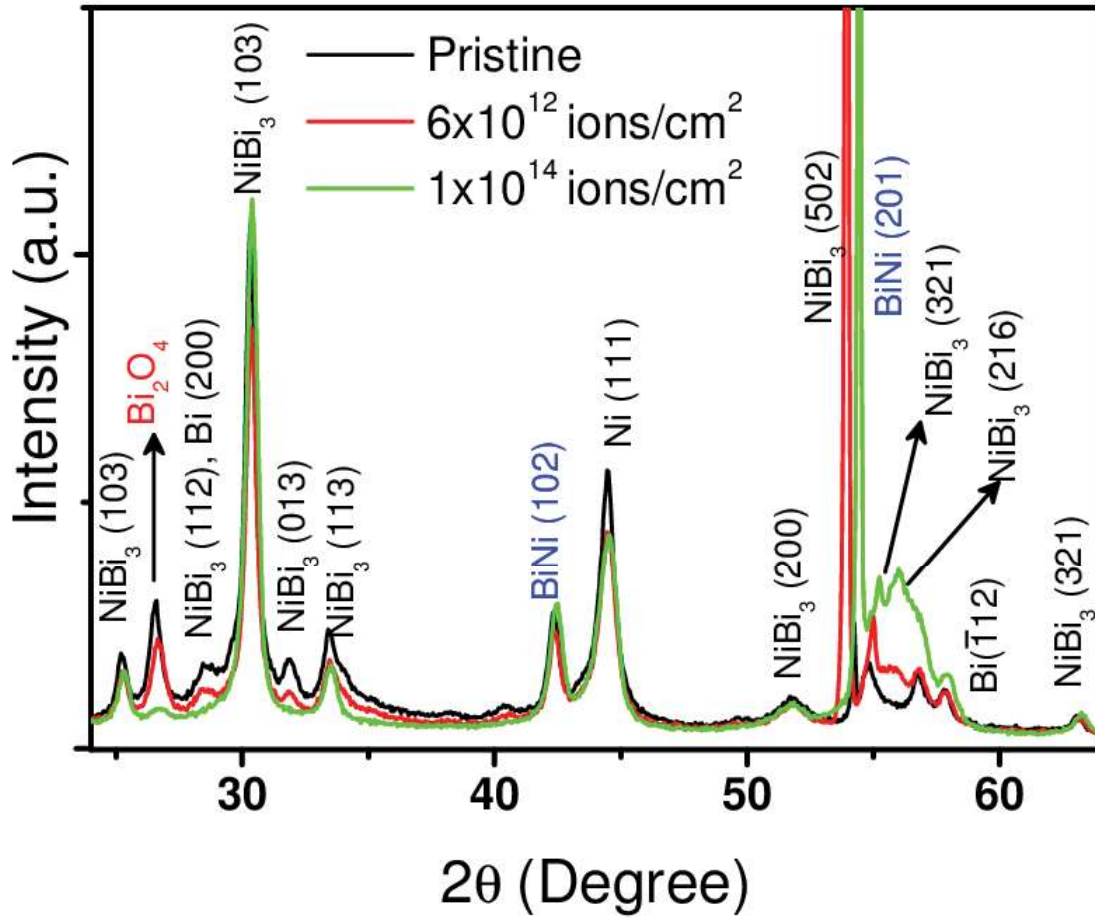
Figure 3.13: Glancing angle (0.5^o) XRD patterns of as-deposited and 100 MeV Au ion irradiated samples

is quantified by estimating the integral intensities of the highest intense peaks of $NiBi_3$, $NiBi$ and Ni, whose values and their ratios are presented in table 3.2. The specified uncertainties corresponding to each quantity are the standard errors obtained from the fits. The uncertainties corresponding to the ratios i.e., $NiBi_3/Ni$ and $NiBi/Ni$ are deduced using error propagation calculations. The incremental rise in the magnitude of these ratios with increasing ion fluences is a clear indication of the ion-induced mixing of Ni and Bi.

The ion-induced surface morphological modifications as a function of ion fluence have been investigated using FESEM and corresponding images are shown in figure 3.14. As-deposited samples show a granular surface morphology, which becomes more grainy after 100 MeV Au ion irradiation at initial fluences (till 1×10^{13} ions/cm^2). Interestingly, an evolution of molten like surface morphology at higher fluences may be noticed. The above features clearly indicate the ion-induced temperature evolution, which is further discussed in chapter 6. The surfaces in

Table 3.2: Peak integral intensities of $NiBi_3$, NiBi, Ni, $NiBi_3$/Ni and NiBi/Ni

Fluence (ion/cm^2)	$NiBi_3$	NiBi	Ni	$NiBi_3$/Ni	NiBi/Ni
as-deposited	6809±135	1698±128	4584±147	1.48±0.06	0.37±0.03
6×10^{12}	6135±107	1560±129	4152±173	1.48±0.07	0.38±0.04
1×10^{14}	9244±290	2699±128	4824±322	1.91±0.14	0.56±0.05
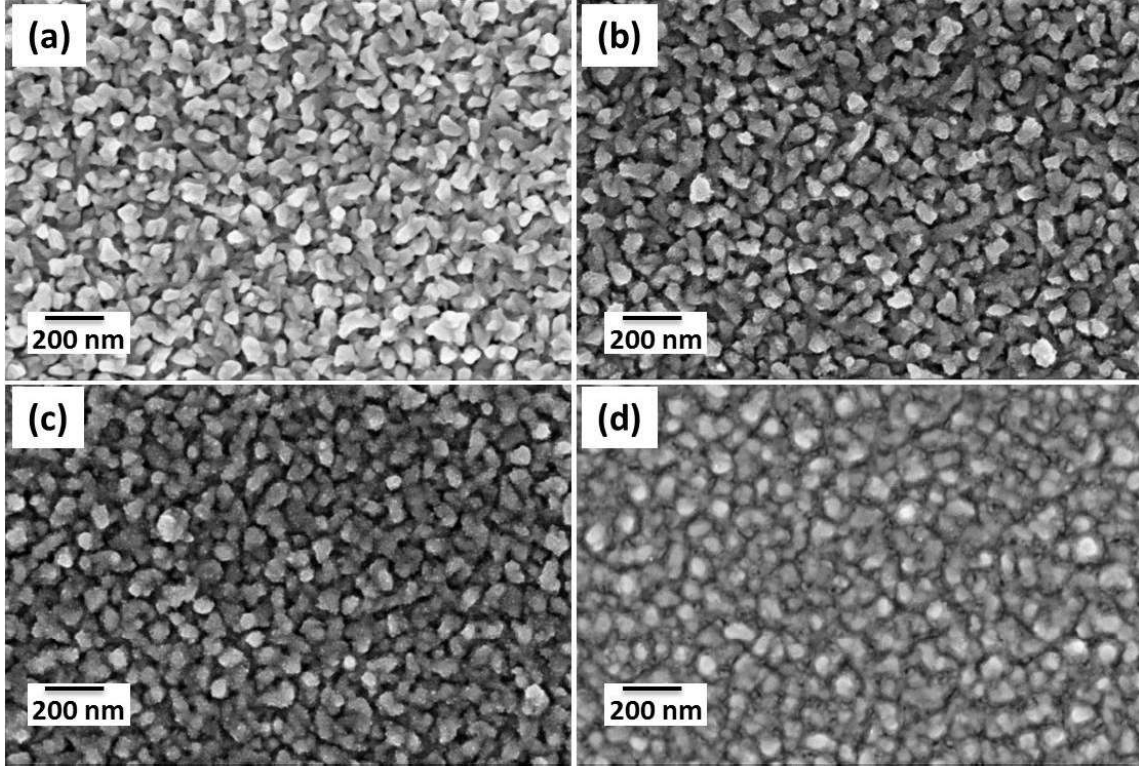
Figure 3.14: SEM images of (a) as-deposited and 100 MeV Au ion irradiated samples to a fluences of (b) 1×10^{12} ions/cm^2, (c) 1×10^{13} ions/cm^2 and (d) 1×10^{14} ions/cm^2.

figure 3.14(a)-(c) may look similar in terms of distribution of grain sizes. A closer examination of these images, however, reveals that there is an emergence of smaller nanostructures of few nanometres on the morphology, along with the existing bigger grains, with the increase in ion fluence. These structures are expected to form as a consequence of the large temperature evolution followed by a sudden quenching in the thermal spikes at higher fluences. It may be noted here that all such latent spikes are believed to merge with one another and as a result can lead to such molten morphology.

The RBS spectra corresponding to as-deposited and representative irradiated samples are illustrated in figure 3.15, where the Bi peaks are zoomed and shown in 4.3. It may be noticed that there are five distinguishable peaks related to Bi, while the peaks corresponding to Ni
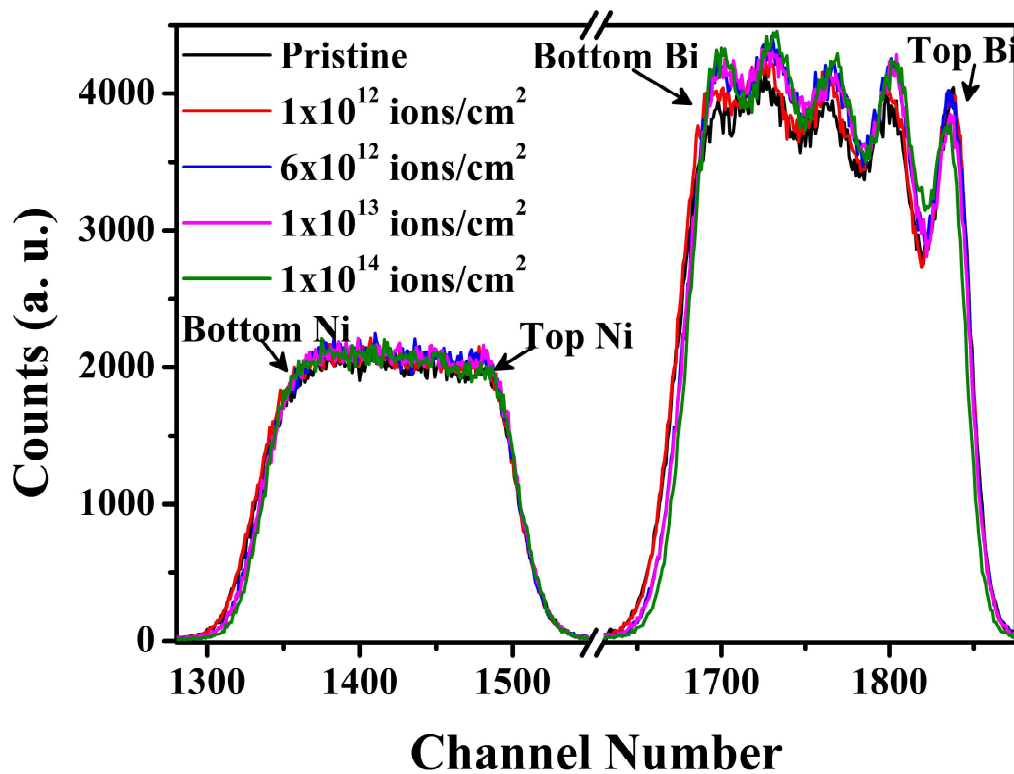
Figure 3.15: RBS spectra for the as-deposited and all the irradiated samples.

seem merged with each other. The difference in distribution is due to a fact that the resolution of RBS becomes better for high atomic number elements. The spectra related to the samples after 100 MeV Au irradiation reveal that these Bi peaks tend to merge with the other Bi layers as a function of the ion fluence. This is an evidence for the enhancement in mixing due to 100 MeV Au ions.

In order to confirm the above prediction of enhanced mixing, these spectra have been fitted and the corresponding depth profiles were extracted. The depth profiles of Ni, Bi, O, and Si corresponding to the as-deposited samples and irradiated one at the highest fluence are shown in figure 3.16. The depth profiles of as-deposited samples are shown using dotted lines, whereas the irradiated ones are indicated using solid lines with symbols. Both the depth profiles related to as-deposited and irradiated samples indicate the existence of 5 bilayers. In the case of as-deposited films, one can notice the signature of spontaneous diffusion of Ni and Bi in all the layers as observed in the previous cases. Unlike the other layers, the top layer alone contains oxygen in its composition along with the Ni and Bi, which is due to bismuth oxide, as discussed in the XRD section above. The oxygen quantity is found to be reduced in the irradiated sample, which is in good agreement with the XRD data. The highlighted grey regions are the ones in
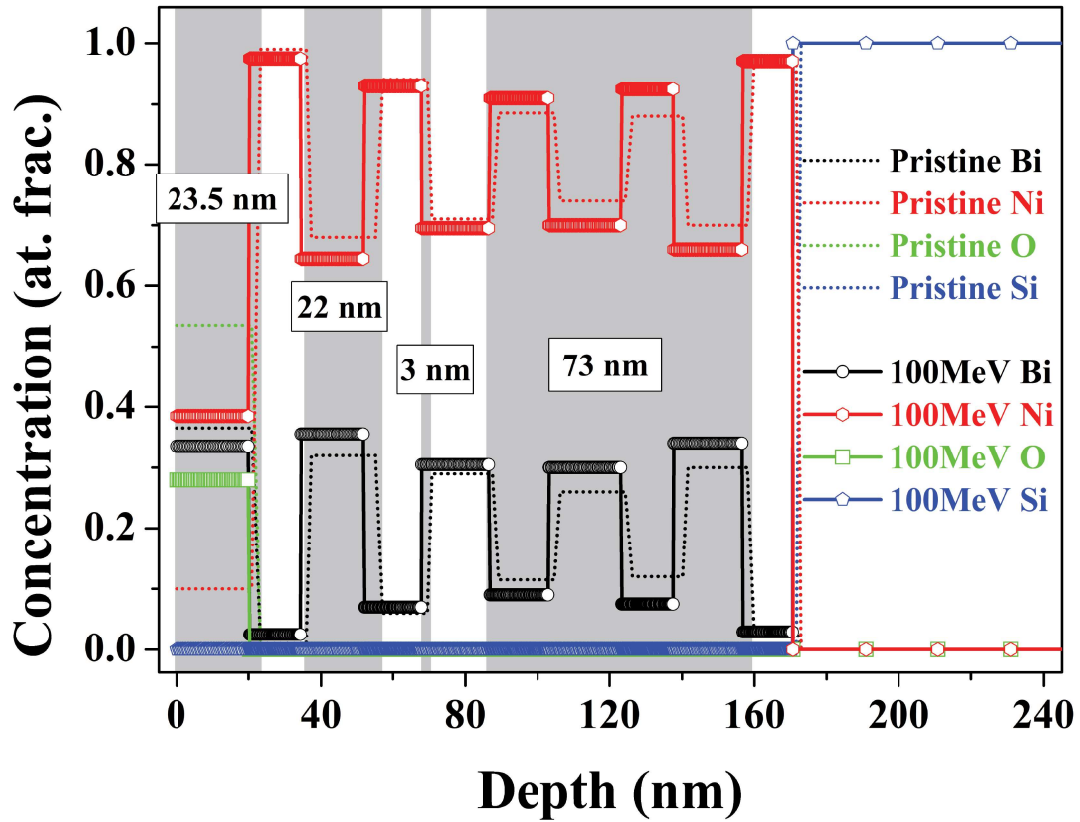
Figure 3.16: Depth profiles of Ni, Bi, O and Si in the as-deposited and 100 MeV Au ion irradiated (1×10^{14} ions/cm^2) Ni/Bi five bilayers samples. The profiles of as-deposited and irradiated samples are shown using dotted lines alone and solid lines with symbols respectively.

which the composition of elements differ and has been marked as the ion-induced mixing. The enhanced mixing after 100 MeV Au ion irradiation was estimated to be around 120 nm, which is $\approx70\%$ of the total thickness of the films. The mixing in the present case is more than 4 times than the mixing observed in the single bilayer Ni/Bi films with the same energy and ions. Such an enhancement in the mixing can be attributed to two reasons, apart from the reasons explained in the single bilayer case. One is being the more number of layers, which means more number of interfaces of Ni and Bi. The thicknesses of both the Ni and Bi layers, in this case, are nearly half compared to that of the single bilayer films, which is the other possible reason. Both these reasons can effectively increase the availability of Ni atoms to react with Bi and vice-versa, which can enhance the mixing.
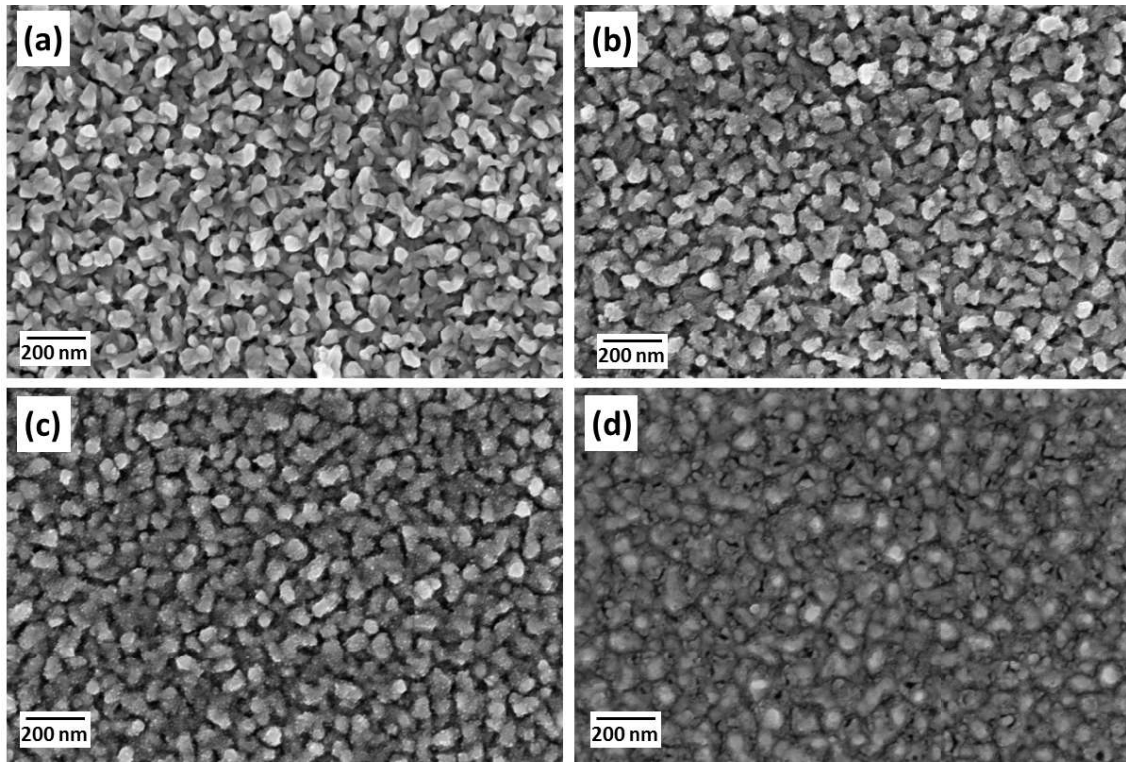
Figure 3.17: SEM images of (a). as-deposited and 120 MeV Au ion irradiated samples to a fluences of (b). 1×10^{12} ions/cm^2, (c). 1×10^{13} ions/cm^2 and (d). 1×10^{14} ions/cm^2.

3.3.4 Effect of 120 MeV Au ions on Ni/Bi five bilayer films

Surface morphology of as-deposited and representative 120 MeV Au ion irradiated samples shown in figure 3.17. The surface morphology of the as-deposited sample show grainy structured morphology, whereas these structures evolve into molten like morphology at the highest fluence (1×10^{14} ions/cm^2), which is clearly visible in Fig.3.17 (d) (as observed in the previous case). Such morphological evolution takes place in stages as soon as the ion fluence increases which is discernible in Fig. 3.17 (b) and (c). In the lower fluences, 1×10^{12} ions/cm^2 and 1×10^{13} ions/cm^2, one can notice the effect of local temperature rise along the ion track due to which small nano structures develop on the surface. At the highest fluence, 1×10^{14} ions/cm^2, such small molten zones merge with each other to form molten like surface as shown in Fig. 3.17(d). The evolution of this morphology after ion irradiation may be explained in terms of temperature generation along the ion track during the ion-matter interaction (the details are discussed in chapter 6).

Figure 3.18 shows the XRD patterns of as-deposited and irradiated samples as a function
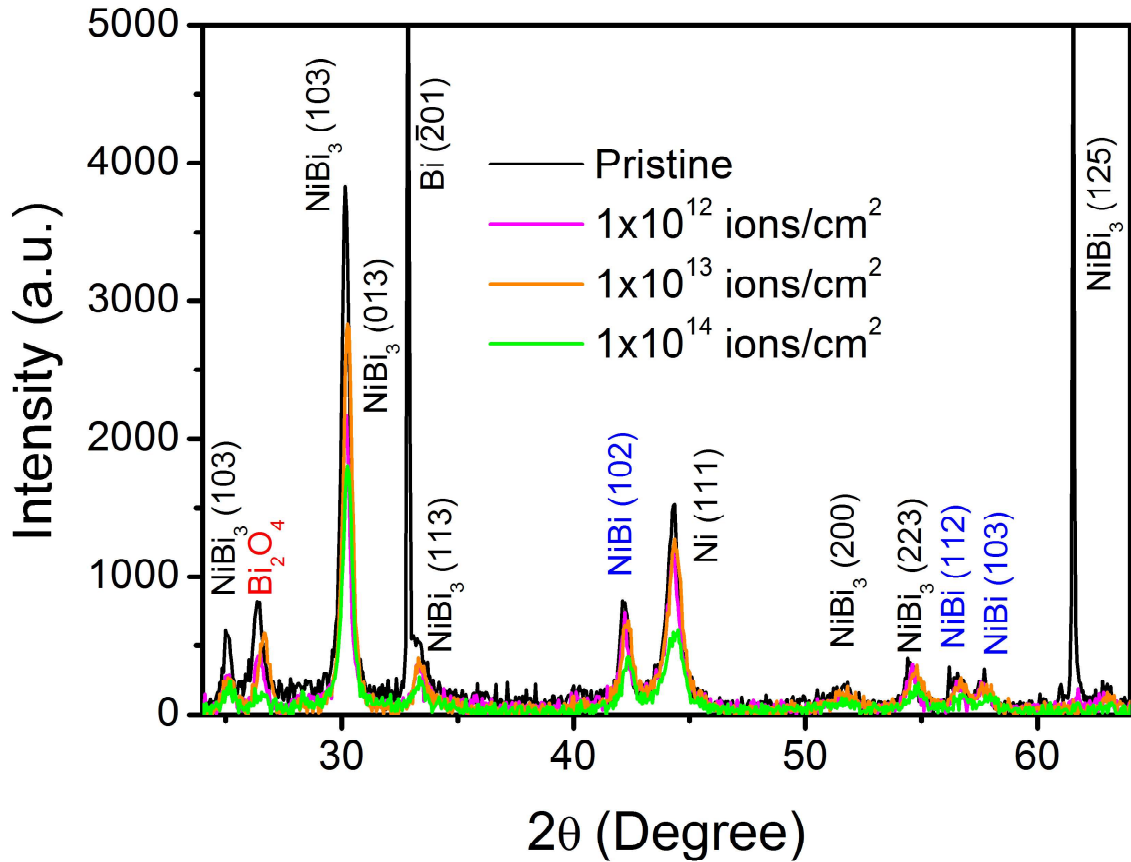
Figure 3.18: X-ray diffraction patterns of as-deposited and 120 MeV Au ion irradiated samples

of ion fluence. It can be noticed that the peaks of Ni, Bi along with the stable phases of Ni-Bi system (NiBi and NiBi$_3$) in all the samples. These stable phases in the as-deposited samples have been formed due to reaction-diffusion mechanism [16]. Apart from these phases, there is another peak corresponding to Bismuth oxide as shown Fig. 3.18, which gradually gets suppressed with increasing ion fluence (as in the previous case). The Full Width at Half Maximum (FWHM) values of Ni, NiBi, and NiBi$_3$ have been tabulated in table 3.3. It shows that these values are gradually increasing with ion fluence, which indicates an increase in the degree of amorphization of these phases after ion irradiation. Such an increase can also be attributed to the high quenching rates of the thermal spikes and S_n induced ballistic effects (as explained in the section 3.3.2).

As discussed in the previous section, after looking at the molten-like morphological evolution of the irradiated films, the ion-induced mixing at the Ni-Bi interfaces has been investigated using RBS measurements on all the samples. The spectra for the as-deposited and irradiated

Table 3.3: The FWHM values of $NiBi_3$ (103), NiBi (102) and Ni (111) for as-deposited and irradiated samples.

Fluence (ions/cm^2)	$NiBi_3$ (103)	NiBi (102)	Ni (111)
As-deposited	0.375±0.007	0.425±0.036	0.545±0.019
1×10^{12}	0.378±0.008	0.387±0.027	0.570±0.018
1×10^{13}	0.440±0.009	0.520±0.054	0.678±0.027
1×10^{14}	0.467±0.011	0.588±0.062	0.888±0.062
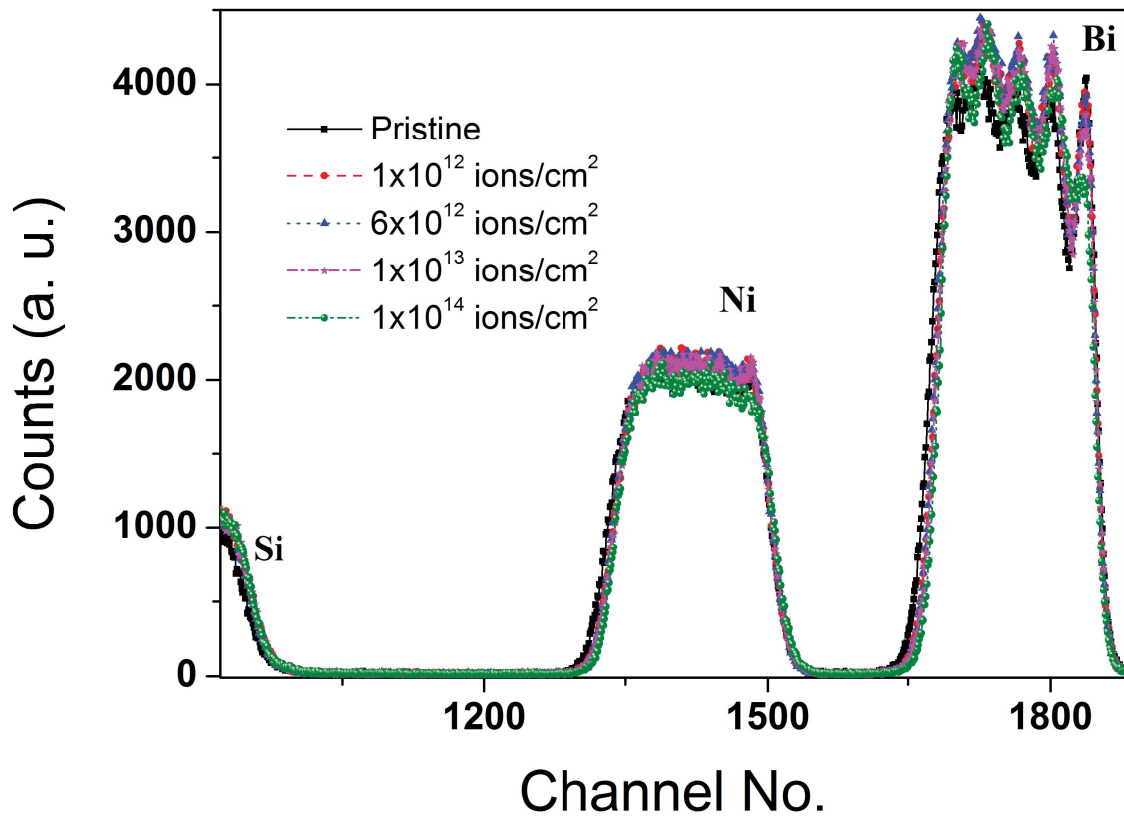
Figure 3.19: RBS spectra of the as-deposited and 120 MeV Au ion irradiated samples at different fluences.

samples are shown in figure 3.19. After 120 MeV Au ion irradiation, one can notice an improvement in the already existing mixing of Ni and Bi with increasing ion fluence. It may be noted here that the surface morphological evolution and improved mixing with increasing ion fluence are in good agreement with each other.

The depth profiles of Ni, Bi, O, and Si were extracted from the above RBS spectra in order to quantify the ion-induced mixing. These depth profiles are shown in figure 3.20(a) and the depth profiles corresponding to top two layers of the 5 bilayers are shown in panel (b). The dotted lines represent the profiles of as-deposited and the solid lines with symbols represent the
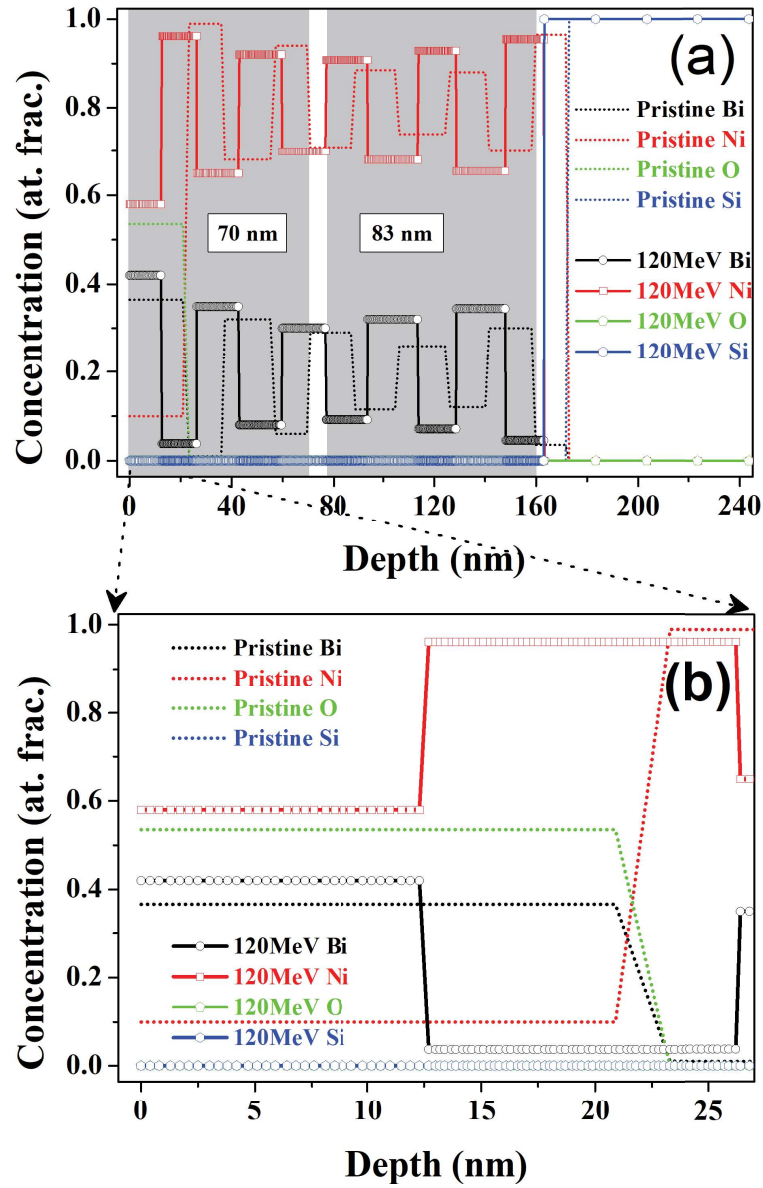
Figure 3.20: Depth profiles of Ni, Bi, O and Si in the as-deposited and 120 MeV Au ion irradiated (1×10^{14} ions/cm^2) Ni/Bi five bilayers samples. The profiles of as-deposited and irradiated samples are shown using dotted lines alone and solid lines with symbols respectively.

profiles of the irradiated sample at the maximum fluence (1×10^{14} ions/cm^2). The ion-induced mixing has been marked with the grey color. In this case, the mixing due to 120 MeV Au ion irradiation was found to be almost 153 nm, which is $\approx$ 89% of the total thickness of all the deposited layers. The figure 3.20(b) shows the spontaneous diffusion in the case of both the as-deposited and irradiated samples. Apart from the mixing enhancement, 120 MeV Au ion irradiation also helped in removing the oxygen from the top layer considerably. The mechanism

behind these ion-induced modifications is explained on the basis of the TSM calculations in chapter 6.

3.4 Conclusion:

In this chapter, initially, the spontaneous formation of stable phases during the deposition of Ni and Bi layers has been explained with the help of GAXRD, XTEM measurements. It was further confirmed by the superconducting properties using electrical transport and magnetic measurements. Interestingly, most of the $NiBi_3$ grains are embedded in the top layer and this spontaneous formation has been assigned to the reaction-diffusion mechanism. The superconducting transition in the as-deposited and irradiated samples are ≈ 3.9 K, which is marginally lesser compared to the reported values. An evolution of porous like structures with increasing swift heavy ion fluence has revealed the out-diffusion of Bi from the top layer. The clear pre-mixing features and their enhancement after the ion irradiation was observed microscopically through high resolution transmission electron microscope and energy dispersive analysis of X-rays measurements. In order to confirm the mixing in the larger area, RBS measurements were performed. The enhanced mixing features after the irradiation are almost 10 nm, which is around 15% of the total thickness of the as-deposited films. Such enhanced mixing was attributed to swift heavy ion-induced athermal and ballistic effects. However, the observed mixing is limited, which is due to the insensitivity of Ni to the present energy regime.

In the case of 5 bilayer Ni/Bi films, ion beam mixing was performed in two different energy regimes (using 100 and 120 MeV Au ions). In both the cases, the surface of the samples shows molten-like morphology with increasing ion fluence and this effect is more apparent in the case of 120 MeV Au ions. Moreover, the phase analysis from the XRD measurements reveals an enhancement in the fraction of alloy phases as a function of fluence. Furthermore, the mixing enhancement due to 100 and 120 MeV Au ions from the RBS measurements was noticed to be $\approx 70\%$ and $\approx 89\%$ respectively. More number of Ni-Bi interfaces and less thickness of the layers were the possible reasons in both the cases. The mixing is more in the case of 120 MeV Au ions compared to 100 MeV case in Ni/Bi five bilayers, which is due to the larger radius of latent track in Bi. The underlying mechanisms of the observed mixing features are further explained on the basis of TSM results in the section 6.3.1 of chapter 6.

Bibliography

[1] G. P. Vassilev, X. J. Liu, and K. Ishida, J. Phase Eq. Diff., 26, 2 (2005).

[2] V. I. Dybkov, in Solid State Reaction Kinetics, IMPS Publications, Kyiv, Ukraine, (2013).

[3] G. Voss and D. Legierungen, Z. anorg. Chemie. 57, 34 (1908).

[4] P. Feschotte and J.-M. Rosset, J. Less-Common Metals. 143, 31, (1988).

[5] T. Herrmannsdörfer, R. Skrotzki, J. Wosnitza, D. Köhler, R. Boldt, and M. Ruck, Phys. Rev. B 83, 140501(R) (2011).

[6] E. L. M. Pineiro, B. L. R. Herrera, R. Escudero, and L. Bucio, Solid State Commun. 151, 425 (2011).

[7] B. Silva, R. F. Luccas, N. M. Nemes, J. Hanko, M. R. Osorio, P. Kulkarni, F. Mompean, M. Garcìa-Hernàndez, M. A. Ramos, S. Vieira, and H. Suderow, Phys. Rev. B 88, 184508 (2013)

[8] J. Kumar, A. Kumar, A. Vajpayee, B. Gahtori, D. Sharma, P. K. Ahluwalia, S. Auluck, and V. P. S. Awana, Supercond. Sci. Technol. 24, 085002 (2011).

[9] M. Sakurai, T. Ono, I. Yoshida, and S. Tanuma, Jpn. J. Appl. Phys. 39, 6366 (2000).

[10] X. Zhu, H. Lei, C. Petrovic, and Y. Zhang, Phys. Rev. B 86, 024527 (2012).

[11] R. Fratesi, N. Ruffini, M. Malavolta, and T. Bellezze, Surf. Coat. Technol., 157, 34, (2002).

[12] J. H. Lee, S. Kumar, H. J. Kim, Y. W. Lee, J. T. Moon, High Thermo-Mechanical Fatigue and Drop Impact Resistant Ni-Bi Doped Lead Free Solder, Proceedings of the 64th Electronic Components and Technology Conference, 712, (2014).

[13] S. Seo, M. G. Cho, and H. M. Lee, J. Electr. Mater., 36, 1536 (2007).

[14] O. V. Duchenko and V. I. Dybkov, J. Mat. Sci. Lett. 14, 1725 (1995).

[15] V. I. Dybkov and O. V. Duchenko, J. Alloy. Compd. 234, 295 (1996).

[16] V. Siva, K. Senapati, B. Satpati, S. Prusty, D. K. Avasthi, D. Kanjilal and P. K. Sahoo, J. Appl. Phys., 117, 083902 (2015).

[17] V. Siva, A. Chettah, B. Satpati, S. Ojha, D. Kanjilal and P. K. Sahoo, RSC Adv., 6, 58950 (2016).

[18] V. Siva, P. C. Pradhan, G. S. Babu, M. Nayak, P. K. Sahoo and K. Senapati, J. Appl. Phys., 119, 063902 (2016).

[19] J. F. Ziegler, M. D. Ziegler and J. P. Biersack, Nucl. Instrum. Meth. Phys. Res., Sect. B, 268, 1818 (2010).

[20] P. K. Sahoo, S. Gsiorek, and K. P. Lieb, Appl. Phys. Lett. 87, 021105 (2005).

[21] M. Toulemonde, M. Costantini, Ch. Dufour A. Meftah, E. Paumier, and F. Studer, Nucl. Instrum. Meth. Phys. Res., Sect. B, 116, 37 (1996).

[22] W. Bolse, Surf. Coat. Technol. 158, 1 (2002).

[23] M. Bouroushian and T. Kosanovic, Crystal Structure Theory and Applications 1, 35 (2012).

[24] Z. G. Wang, Ch. Dufour, E. Paumier, and M. Toulemoude, J. Phys.: Condens. Matter 6, 6733 (1994).

[25] M. Tian, J. Wang, N. Kumar, T. Han, Y. Kobayashi, Y. Liu, T. E. Mallouk, and M. H. W. Chan, Nano Lett. 6(12), 2773 (2006).

[26] D. K. Avasthi, W. Assmann, A. Tripathi, S. K. Srivastava, S. Ghosh, F. Gruner and M. Toulemonde, Phys. Rev. B, 68, 153106 (2003).

[27] T. Diana, D. C. Agarwal, P. K. Kulriya, S. K. Tripathi and H. N. Sarma, Adv. Mater. Lett., 5, 223 (2014).

[28] S. Kraft, B. Schattat, W. Bolse, S. Klaumunzer, F. Harbsmeier, A. Kulinska, A. Löffl, J. Appl. Phys. 91, 1129 (2002).

[29] L. R. Doolittle, Nucl. Instrum. Methods Phys. Res., Sect. B, 9, 344 (1985).

[30] B. Schattat, W. Bolse, Nucl. Instrum. Methods Phys. Res., Sect. B: 225, 105 (2004).

[31] M. Nastasi, J. Mayer, J. K. Hirvonen, Ion-solid interactions: fundamentals and applications, Cambridge University Press, (1996).

Chapter 4

Effect of medium energy ions on Ni and Ni/Bi films

4.1 Introduction:

It may be inferred from the chapter 3 that the swift heavy ions with the dominant electronic energy loss over nuclear energy loss makes Ni insensitive, below certain threshold electronic energy loss [1, 2], and thereby limits the possibility of mixing. To address this issue, medium energy ion beam is used for the ion beam mixing, whose electronic and nuclear energy losses are comparable in magnitude. This chapter has two parts, in the first part, the sensitivity of Ni to the medium energy ion beam will be investigated to address the response of Ni at this energy regime prior to the study of IBM of Ni-Bi system. In the second part, the ion beam mixing study of Ni/Bi bilayers will be performed in the medium energy regime.

In the first part of this chapter, 2.2 MeV Au ions have been used for the study of the sensitivity of Ni at this energy regime. The Ni films of 5 nm thick were irradiated as a function of ion fluence at room temperature. The estimated values of electronic energy loss (S_e), nuclear energy loss (S_n) and projected ranges for Ni target from SRIM simulations [3] are shown in table 4.1. It may be noticed that the values of S_e and S_n are in the same order of magnitude and it is expected to have synergistic effects of both S_e and S_n. The characterisation of these films after irradiation was carried out using atomic force microscope (AFM) and Rutherford backscattering spectrometry (RBS) measurements. The study of surface morphology and power spectral density (PSD) analysis would reveal the information about the sensitivity of Ni. It may be further confirmed by noticing the diffusion or mass flow of Ni atoms through RBS measurements.

In the second part, the ion beam mixing of Ni-Bi system will be studied using 1 MeV

77

Species and energy of ion beam	Target elements	S_e (keV/nm)	S_n (keV/nm)	$\frac{S_e}{S_n}$	Range (nm)
2.2 MeV Au ions	Ni	3.45	7.63	0.45	181
1 MeV Ni ions	Ni	1.234	1.239	0.995	315
	Bi	0.74	0.612	1.209	420
	NiBi	0.884	0.75	1.17	364
	NiBi$_3$	1.03	0.91	1.13	326

Table 4.1: The values of S_e, S_e, ratio of S_e and S_n, and R_p in the case of 2.2 MeV Au ion irradiated Ni target and 1 MeV Ni ion irradiated Ni/Bi target

Ni ions as a function of ion fluence. The thickness of the Ni and Bi layers were $\approx$ 5 nm each. The rate of deposition of Ni and Bi were 0.1 Å/s and 0.2 Å/s respectively. The values of S_e and S_n are almost the same in the Ni target and for the Bi, they are in the same order of magnitude. The projected ranges of these ions in Ni, Bi, NiBi and NiBi$_3$ are approximately 315 nm, 420 nm, 364 nm and 326 nm respectively, which are much higher than the thickness of the films. The structural modifications were understood with the help of GAXRD measurements. The mixing information was obtained by analysing the RBS spectra of the as-deposited and irradiated samples.

4.2   Experimental:

The Ni films of 5 nm thickness were deposited using e-beam evapouration method on cleaned fused silica substrates. Before deposition, these substrates were cleaned using ultrasonication in acetone and then in IPA, followed by a rigorous drying. These films were deposited at a base pressure of $\approx 2 \times 10^{-7}$ mbar. Constant rate of deposition and substrate rotation were ensured throughout the deposition, for the better quality films. These films were irradiated using 2.2 MeV Au ions at different fluences from 5×10^{14} to 1×10^{16} ions/cm^2. The irradiation experiments were performed at IOP Bhubaneswar using 3 MV pelletron accelerator. Rutherford backscattering spectrometry (RBS) measurements on the films were carried out using 2 MeV He^{2+} ions, to avail the information related to the thickness of the as-deposited films as well as the ion-induced modifications. The surface topography and roughness of the as-deposited and irradiated samples were obtained using atomic force microscopy (AFM).

The Ni and Bi layers were deposited on cleaned Si substrates using thermal evapouration

for the ion beam mixing study, where the thickness of each layer is as same as 7 nm. Both the Ni and Bi films were deposited at a base pressure less than $\approx 5 \times 10^{-7}$ mbar. A set of these Ni/Bi films were irradiated using 1 MeV Ni ions at various ion fluences. A constant sample rotation of 14 revolutions per minute was maintained throughout the deposition. The rate of deposition for Ni and Bi were maintained as 0.1 and 0.2 Å/s respectively. X-ray diffraction was performed using Bruker D8 advance diffractometer. The surface morphological information was obtained using Carl-Zeiss made (Sigma model) Field emission scanning electron microscopy (FESEM). The RBS was performed using the same parameters as mentioned in the case of Ni film above.

The energy per nucleon is 0.017 MeV/amu and 0.011 MeV/amu for 1 MeV Ni and 2.2 MeV Au ions, whose magnitudes are almost the same. The selection of the ions and their energy in both these cases was done based on the above-mentioned fact.

4.3 Results and discussion:

4.3.1 Effect of medium energy ions on Ni films

In order to obtain the surface topography and roughness of the films, AFM measurements have been performed. The AFM images of as-deposited and irradiated films are shown in figure 4.1. The as-deposited films has uniformly distributed Ni grains on the surface (shown in figure 4.1(a)). One can notice various stages of evolution as a function of fluence in figure 4.1(b)-(f). In the case of lower fluences, 5×10^{14} ions/cm^2 and 1×10^{15} ions/cm^2, the ion beam seems to induce a coalescence of distinct grains and leads to smoother surfaces as shown in figure 4.1(b) and (c). In addition, at a fluence of 2×10^{15} ions/cm^2, the formation of nano sized hillocks may be noticed on the surface, which develops further upon increasing the fluence. In the case of highest fluence, i.e., 1×10^{16} ions/cm^2, one can notice large hillocks with the lateral size distributed from 500 to 1000 nm. The evolution of surface morphology as a function of fluence can be quantified using root mean square (RMS) roughness (σ_{rms}), which can be defined as [4]:

$$\sigma_{rms} = \left(\langle h^2(r) \rangle - \langle h(r) \rangle^2 \right)^{1/2} \tag{4.1}$$

Where $r = (x, y)$ represents any point on the surface and h is the height of the surface at r. The RMS roughness values for all the samples were extracted using WSXM software package [5]. These values of surface roughness and η_0 against the ion fluences are tabulated in table 4.2. The value of σ_{RMS} is 2.55 nm for the as-deposited film. Intially, at the lower fluences,
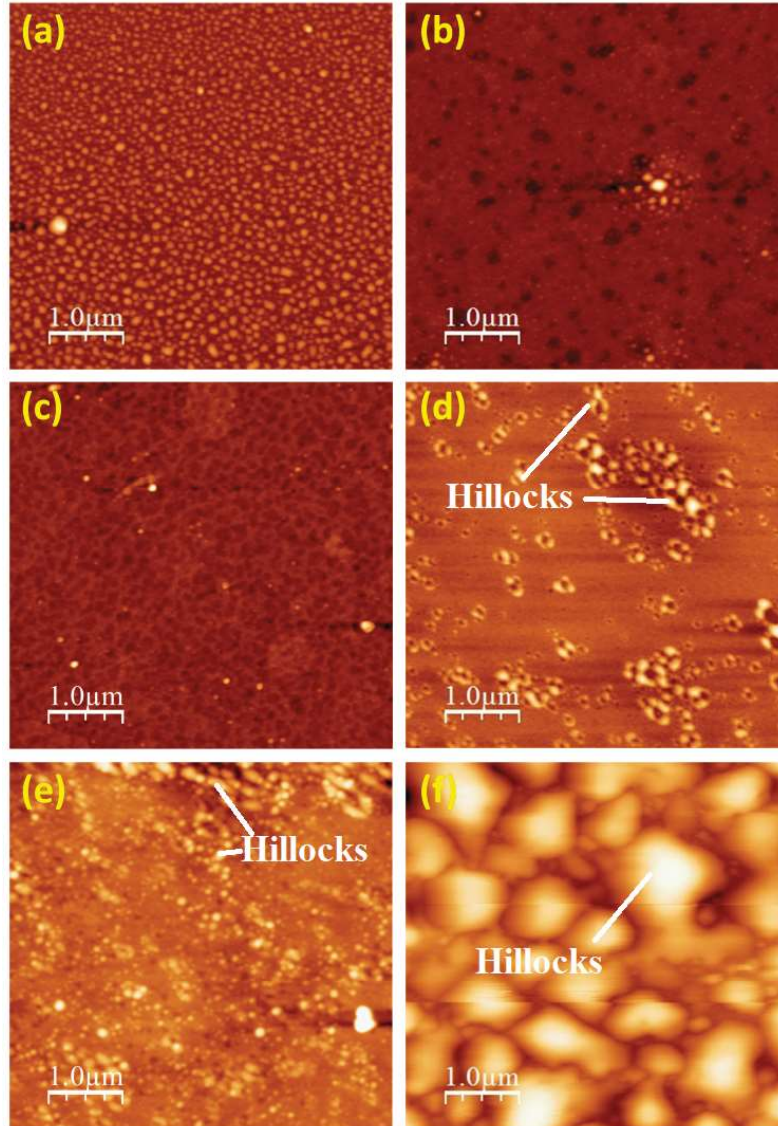
Figure 4.1: AFM images of (a) as-deposited, (b) 5×10^{14} ions/cm^2, (c) 1×10^{15} ions/cm^2, (d) 2×10^{15} ions/cm^2, (e) 5×10^{15} ions/cm^2 and (f) 1×10^{16} ions/cm^2.

the values of RMS roughness decreases, which increases gradually with the ion fluence. A substantial rise in the value of RMS roughness at the highest fluence confirms the formation large hillocks (as discussed above). The formation of such large hillocks is believed to be triggered from ion-induced local melting near the surface, which can cause the flow of material to the surface [6, 7]. The material flow to the surface is due to the stress developed in the ion-induced molten zone. It was proposed by Averback and Ghaly [8], the magnitude of the parameter $(F_d/\epsilon)^2$ is the deciding factor to find out whether melting and consecutive mass or viscous flow of material to surface is possible. Where F_d is the damage energy deposited per

Ion fluence	Surface roughness σ_{RMS}(nm)	η_0
as-deposited	2.55	122
5×10^{14} ions/cm^2	1.25	153
1×10^{15} ions/cm^2	1.27	194
2×10^{15} ions/cm^2	2.87	204
5×10^{15} ions/cm^2	4.86	312
1×10^{16} ions/cm^2	38.62	1000

Table 4.2: The values of RMS roughness and η_0 for Ni films as a function of ion fluence.

unit length and ϵ_m is the average energy per atom at the melting point [8]. The value of F_d is nearly 7.5 keV/nm at the surface for the 2.2 MeV Au ions (in the present case). The value of ϵ_m can be found to 0.44 eV by taking 1728 K as the melting point of Ni. In this case, the value of $(F_d/\epsilon)^2$ comes out to be $(17,050)^2$ nm^{-1}. In the study of Averback and Ghaly [8], they observed melting along ion track and viscous flow of material to surface in molecular dynamics simulations and also in the case of Au irradiation of Au material, where the value of $(F_d/\epsilon)^2$ was found out to be $(2978)^2$ nm^{-1}, for the values of ϵ_m and F_d as 0.47 eV and 1.4 keV/nm respectively. As the value of F_d is more in the present case and the value of ϵ_m is comparable for Ni and Au, the local melting is expected to take place.

Fluctuations in the height of the surface are characterised by the rms roughness, σ_{RMS}. PSD was used to quantify the lateral variations in surface morphology and surface growth dynamics. The PSD can be expressed mathematically as [4]:

$$C(q) = \frac{1}{area} \left| \int \int \frac{d^2r}{2\pi} e^{-iq \cdot r} \langle h(r) \rangle_t \right|^2 \tag{4.2}$$

with q ($= 2\pi/l$) being the spatial frequency for the wavelength l. The PSD function of a given surface may be obtained by averaging the squared magnitudes of the coefficients of the two dimensional Fourier transform of the digitised surface profile (C(q)). This information was obtained by using the WSXM software package [5].

The PSD functions calculated using this procedure are shown as a function of ion fluence in figure 4.2. Surface corrugation, defined as the slope of a line joining two surface points [4, 9], can be used as a criteria to divide the PSD function into two categories. When the surface corrugation is small, the PSD is independent of the spatial frequency q, and this happens when the length scale is larger than a certain value η_0 ($= 1/q_0$), which depends on the lateral

dimension of the surface features, leading to a plateau in the PSD function [4,9]. Alternatively, if the length scale is smaller than η_0 ($q < q_0$), PSD would decrease [4,9], which explains the behaviour of the functions in figure 4.2. The positions of q_0 are indicated by vertical arrows where PSD functions are observed to decrease sharply. The corresponding values of η_0 are given in table 4.2 where the increase in η_0 with fluence is correlated with coalescence of distinct grains as seen in the AFM images of the as-deposited samples (figure 4.1(a)) at lower fluences (5×10^{14} and 1×10^{15} ions/cm^2) followed by formation of hillocks having lateral dimension of 1 μm at the fluence of 1×10^{16} ions/cm^2. Furthermore, figure 4.2 also exhibits smoothening of the surfaces at lower fluences. Since the integral of the PSD over the entire range of q is proportional to the RMS roughness of the surface, the PSD curve corresponding to a higher roughness in figure 4.2 has a higher ordinate compared to that with a lower roughness. In figure 4.2, the PSD curve corresponding to the fluences of 5×10^{14} and 1×10^{15} is lower than that in case of the as-deposited sample, except for the case of q < 3×10^{-3} nm^{-1}. The integrated value of the PSD should hence be lower for these two fluences as compared to that for the as-deposited sample. This is the reason behind the clear reduction in the RMS roughness (smoothening) of the surface as seen from the AFM study (Table 4.2). Moreover, for ion fluence more than 1×10^{15} ions/cm^2, the PSD function gets higher and higher, until it attains it's highest value at the fluence of 1×10^{16} ions/cm^2. This implies that the roughness is getting higher and higher, which can be confirmed again from table 4.2.

When q>q$_0$, the variation in the PSD can be expressed by Eklund *et al.* and mayr *et al.* [9,10]:

$$C(q) \sim \left(\sum_{\gamma=1}^{4} a_\gamma q^\gamma \right)^{-1} \tag{4.3}$$

From a linear dimensional analysis, it can be observed that various modes of q with values of 1, 2, 3 and 4, correspond to viscous/mass flow, evapouration-condensation, volume diffusion, and surface diffusion, respectively [10,11]. In the present case, the evolution of surface morphology by Au ion irradiation is the result of competing processes of roughening and smoothening. The roughening process arises predominantly from ion sputtering that comes from the ions arriving randomly, while the smoothening happens due to contributions from the viscous flow, volume diffusion, redeposition of sputtered atoms, and shadowing of the ion beams on the surface [9]. In order to distinguish the dominant mechanism behind the observed
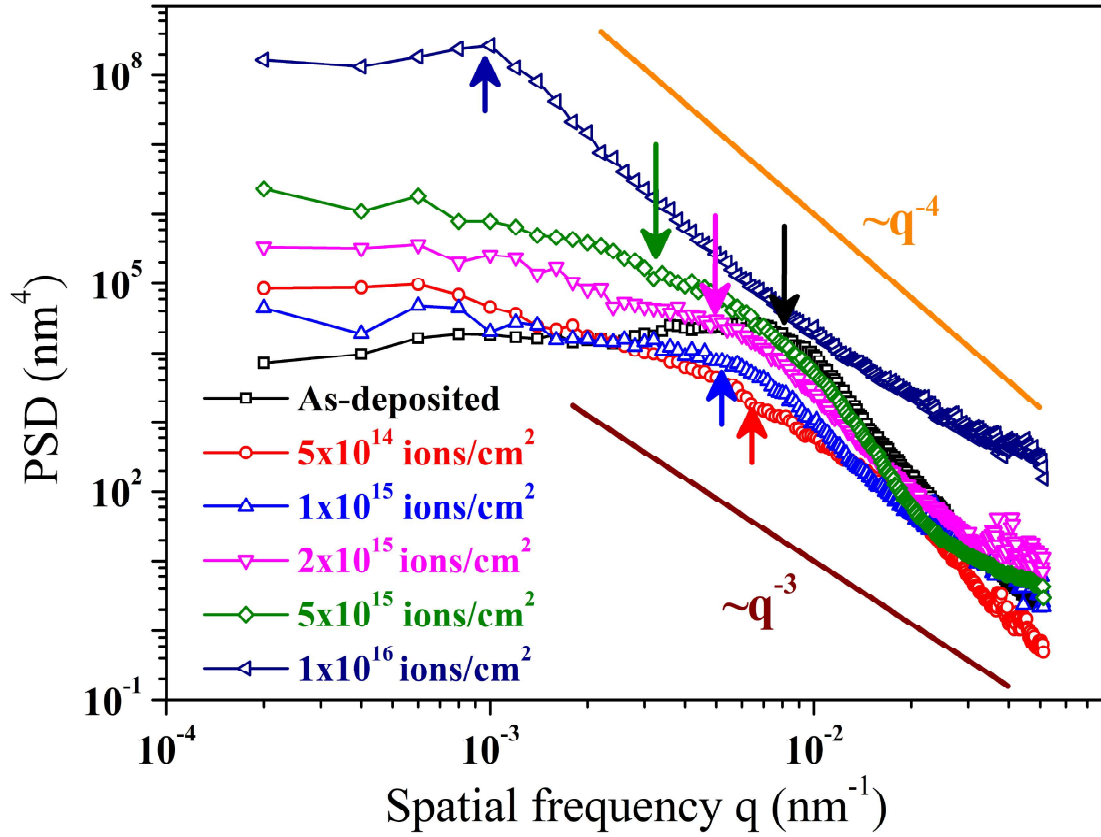
Figure 4.2: Power spectral density (PSD) of as-deposited and all the irradiated samples. The position of q_0 at respective fluences are indicated by the vertical arrows. The dependences of q^4 and q^3 are shown to compare them with the variation of PSD.

surface evolution of the Ni surface under ion irradiation, two straight lines are shown in figure 4.2, which point to the q^{-3} and q^{-4} dependencies respectively, for comparison of variations of q with PSD [4, 9, 10]. A comparison of various PSD functions reveals that for samples irradiated with fluence $> 1 \times 10^{15}$ ions/cm^2, it varies like q^{-3} for q $> 2\times10^{-2}$ nm^{-1}, which points towards volume diffusion. On the other hand, a variation in PSD as q^{-4} is also present in the PSD function corresponding to the fluence 1×10^{16} ions/cm^2, in the regime of 10^{-3} to 10^{-2} nm^{-1}, which indicates a role of surface diffusion in the morphological evolution.

The mechanism of the mass transport into the silica matrix and formation of nano-composites is explained in the following manner: the thermal spike in collision cascades and recoil implantation cause the Ni atoms to be driven from the film into the substrates. To further shed light on this, simulations using SRIM [13] have been performed, for the Ni and Au distribution, using the appropriate experimental conditions of 5 nm Ni layer on SiO$_2$. The consequent distributions of Ni and Au in SiO$_2$ are shown in figure 4.3(a) for the lowest fluence (5×10^{14} ions/cm^2) used
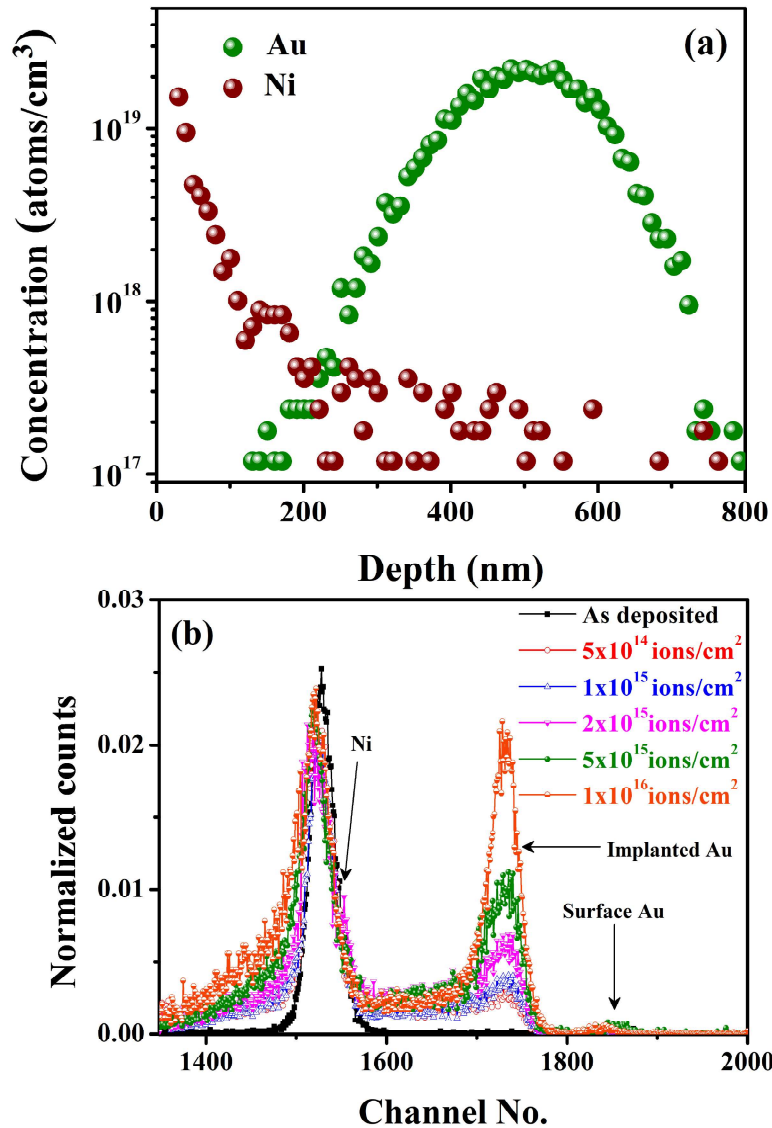
Figure 4.3: (a) Density distribution of Ni and Au due to 2.2 MeV Au irradiation on a Ni (5 nm) film on SiO_2 for ion fluence is 5×10^{14} ions/cm², (b) RBS spectra of as-deposited and the samples irradiated at different fluences.

in the experiment. While the density of Ni decreases from the surface, that of Au is seen to follow a Gaussian distribution. It is further observed from figure 4.3(a) that densities of both Au and Ni in SiO_2 remain above $\sim 10^{17}$ ions/cm³ upto a depth of ~ 500 nm from the surface. This result demonstrates that the formation of Au-Ni related composite in SiO_2 is possible during ion irradiation. However, a considerable diffusion of Ni and Au due to ion irradiation is found from RBS study, which shows that there is an increase in Ni concentration in SiO_2 along with

the formation of the nanocomposite, as explained in the following.

RBS spectra of as-deposited and representative irradiated samples are shown in figure 4.3(b). A tail in the peaks related to Ni at the lower energy side with increasing ion fluence can be noticed. Such tailing effect is a clear indication of Ni diffusion into the SiO_2 substrate. Initially, in the case of as-deposited sample, one may notice that the absence of Au peak and with increasing fluence it comes up gradually. As a function of irradiation fleunce, an increasing asymmetry in the case of Au peaks can be observed. which represents the diffusion of these Au atoms.

These RBS spectra were analysed using RUMP simulation package [12] and corresponding depth profiles were extracted from these simulations. The depth profiles of Ni and Au as a function of ion fluence are shown in figure 4.4(a) and (b) respectively. The normalized atomic concentration of Ni related to as-deposited sample is 100 at.% till a depth of 8 nm from the surface. However, the thickness of the Ni layer seems to be reduced systematically with increasing fluence and these Ni atoms are diffused into the SiO_2 substrate as shown in figure 4.4(a). From the depth profiles of Au, it may be understood that the Au atoms are distributed on the surface and also at a depth of 250-500 nm. The diffused Ni atoms are distributed till a depth of ≈ 400 nm, which is an indication of coexistence of both Ni and Au to this region. These Au and Ni atoms, which are distributed on the surface as well as inside the matrix may mix with each other and leads to the formation of Ni-Au nanocomposites. Ion-induced transient temperature rise, the rate of defect production and diffusion results in the formation of such large hillocks on the surface of the sample irradiated at the highest fluence as seen in the figure 4.1. Such morphology may be attributed to the mass transport due to 2.2 MeV Au ion irradiation. It can be inferred that the Ni is sensitive to the present energy from the above findings.

4.3.2 Effect of medium energy ions in Ni/Bi bilayer films

Since, it is clear from the above section that Ni is sensitive to medium energy ions and it would be interesting to study the ion beam mixing of Ni-Bi system using medium energy ions. The X-ray diffraction patterns of as-deposited and irradiated Ni/Bi bilayer films are shown in figure 4.5. It may be noticed that the X-ray diffraction peaks corresponding to NiBi and $NiBi_3$ along with the peaks of Ni, Bi, and Si. The formation of both these stable phases of Ni-Bi system in the as-deposited sample is believed to take place due to the reaction-diffusion mechanism, as discussed in our previous work [16–20]. One may observe that the formation of both the phases
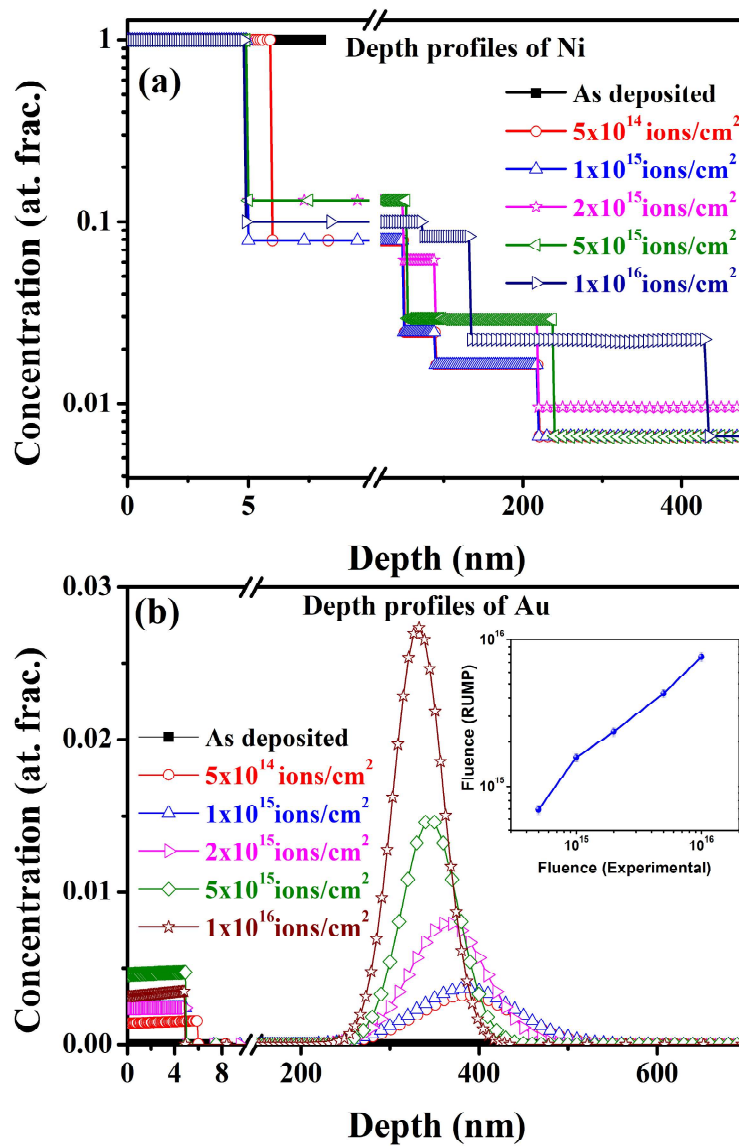
Figure 4.4: Depth profiles of Ni (a) and Au (b) at various fluences. The irradiation fluence obtained from RUMP simulation as a function of experimental fluence is shown in the inset of panel (b).

in the present case and only $NiBi_3$ phase in the previous chapter is an inconsistency. Such an inconsistency may be understood as the dominance of $NiBi_3$ peak intensities over NiBi peaks in the earlier case. After the irradiation at the lowest fluence (1×10^{15} ions/cm^2), one can notice only $NiBi_3$ phase and all the peaks corresponding to these phases disappear above this fluence. Moreover, the peaks of Ni and Bi also seemed to be broadened with increasing ion fluence. The observation of disappearance of stable phases and broadening of Ni, Bi peaks can be attributed

to the ion-induced amorphization of the phases with increasing ion fluence.
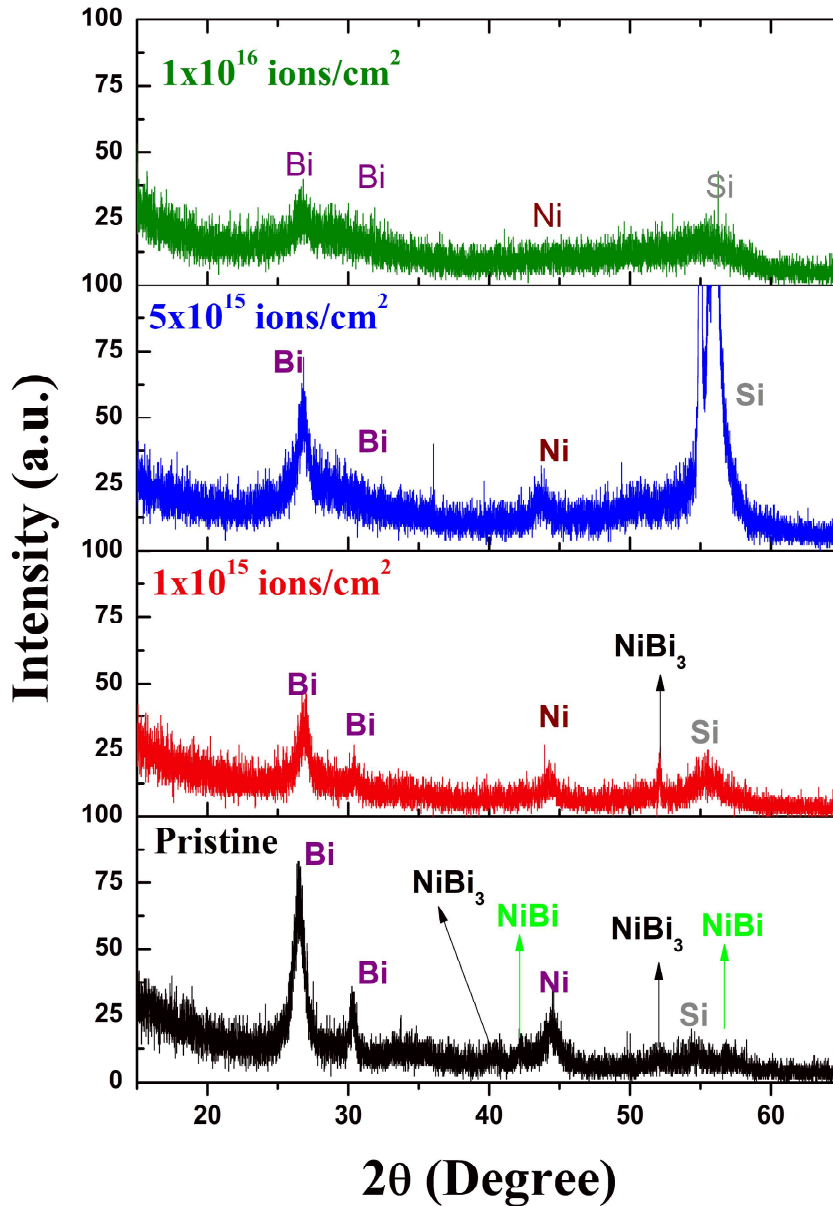
Figure 4.5: The X-ray diffraction patterns of as-deposited and irradiated samples at fluences of 1×10^{15} ions/cm^2, 5×10^{15} ions/cm^2 and 1×10^{16} ions/cm^2.

Figure 4.6 shows the surface morphology of the as-deposited and irradiated samples as a function of ion fluence. All these images were recorded using the same parameters (200 nm scale and 100 kx magnification). The as-deposited sample shows the distribution of grains on the sample surface. After 1 MeV Ni ion irradiation, these grains become smaller and small with increasing ion fluence till 5×10^{15} ions/cm^2. Beyond this fluence, the surface of the films evolves into a molten-like morphology. These observed changes can be attributed to the

ion-induced local melting, where the lattice temperatures of both Ni and Bi goes beyond their respective melting temperatures (details are explained in chapter-6). It is well known that the ion-induced temperatures quench very rapidly [14] and such a high rapid quenching of lattice temperatures can leave the surface in the molten-like morphology.
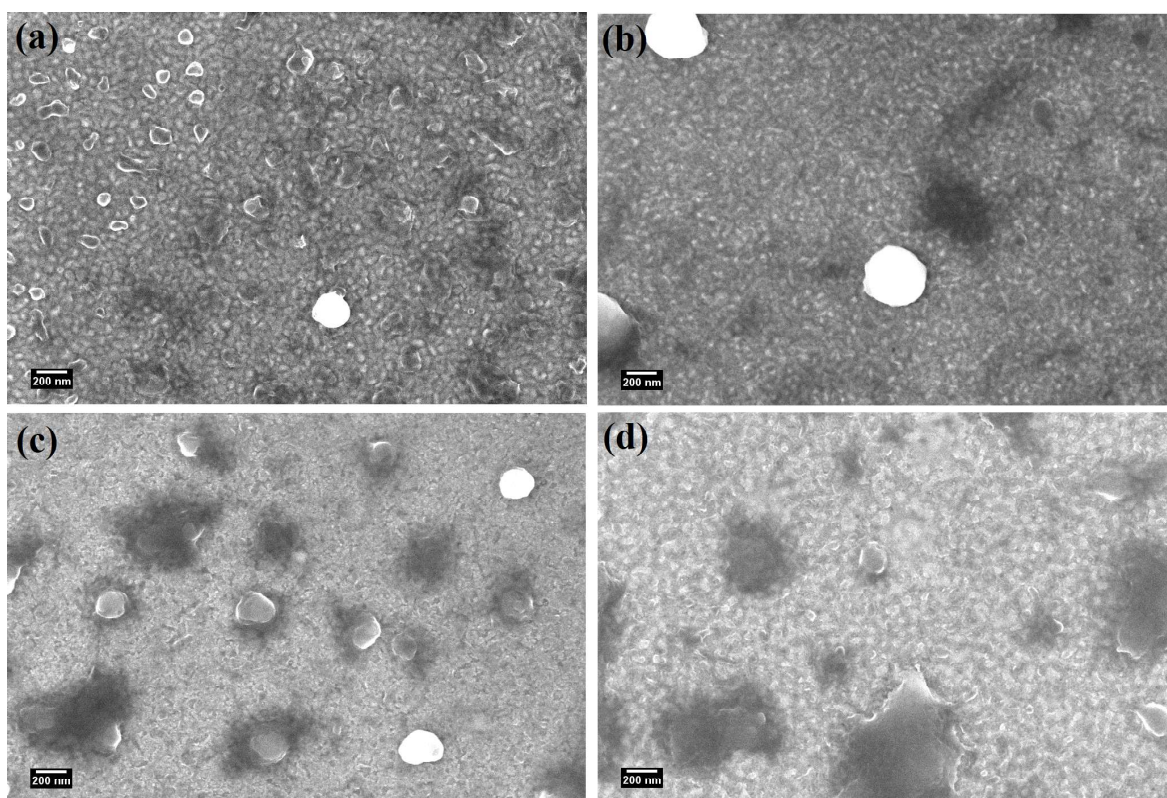
Figure 4.6: Scanning electron micrographs of as-deposited and irradiated samples at fluences of 1×10^{15} ions/cm^2, 5×10^{15} ions/cm^2 and 1×10^{16} ions/cm^2.

The Rutherford backscattering spectrometry (RBS) spectra are shown for as-deposited as well as irradiated samples in figure 4.7. It may be noticed that the presence of Ni and Bi peaks in all the cases. The integral intensity of peaks corresponding to Bi is gradually reducing with the increasing fluence, which is due to ion-induced sputtering of Bi atoms. This feature can also be observed in the case of Ni peaks as well. However, The sputtering of Ni is not as much as Bi, which is expected as the sputtering is the surface phenomenon and hence it should be more in the case of Bi as it is the top layer. Moreover, in the case of the as-deposited sample, there is a small tailing of Bi at low energy side. It is due to the spontaneous diffusion of Bi atoms into the Ni layer during the deposition. With increasing ion fluence, such diffusion seems to become prominent regardless of ion-induced sputtering. In order to obtain more reliable

information about the diffusion and mixing, simulations were performed for all these spectra and are discussed below.
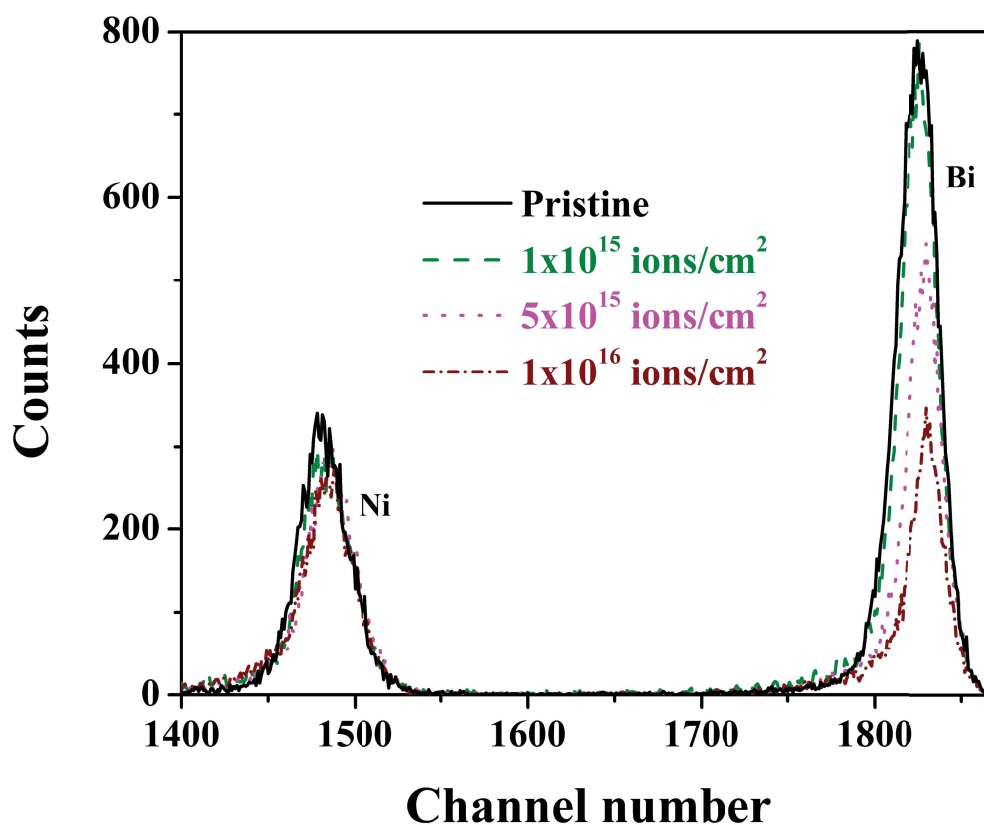
Figure 4.7: The Rutherford backscattering spectrometry spectra of as-deposited and 1 MeV Ni ion irradiated samples at different fluences.

To understand the sputtering of Ni and Bi, as observed from RBS spectra, the sputtering yields were obtained using TRIDYN simulations [15]. Variation of the sputtering yield of Bi, Ni and Si as a function of ion fluence is shown in figure 4.8. The sputtering yield of Bi was found to be reduced continuously with increasing ion fluence till a fluence of 7×10^{15} ions/cm^2 and beyond this fluence it slightly increases. On the other hand, the sputtering yield of Ni increases initially with increasing ion fluence and then it decreases at a fluence of 7×10^{15} ions/cm^2 followed by a rise in its value again. The nature of Sputtering yields of Bi and Ni till the above-mentioned fluence is due to the dominant sputtering of Bi at the lower fluences, whose nature gets altered as soon as the underneath Ni layer gets exposed to the ion beam at the higher fluences. Moreover, the sputtering yield of Si was observed to be constant (which is nearly zero) at the lower fluences whereas it increases slowly at the higher fluences. It was due

to the fact that the ion gets to interact with the Si substrate at the higher fluences only as the Si comes after both the Ni and Bi in the path of the ion beam.
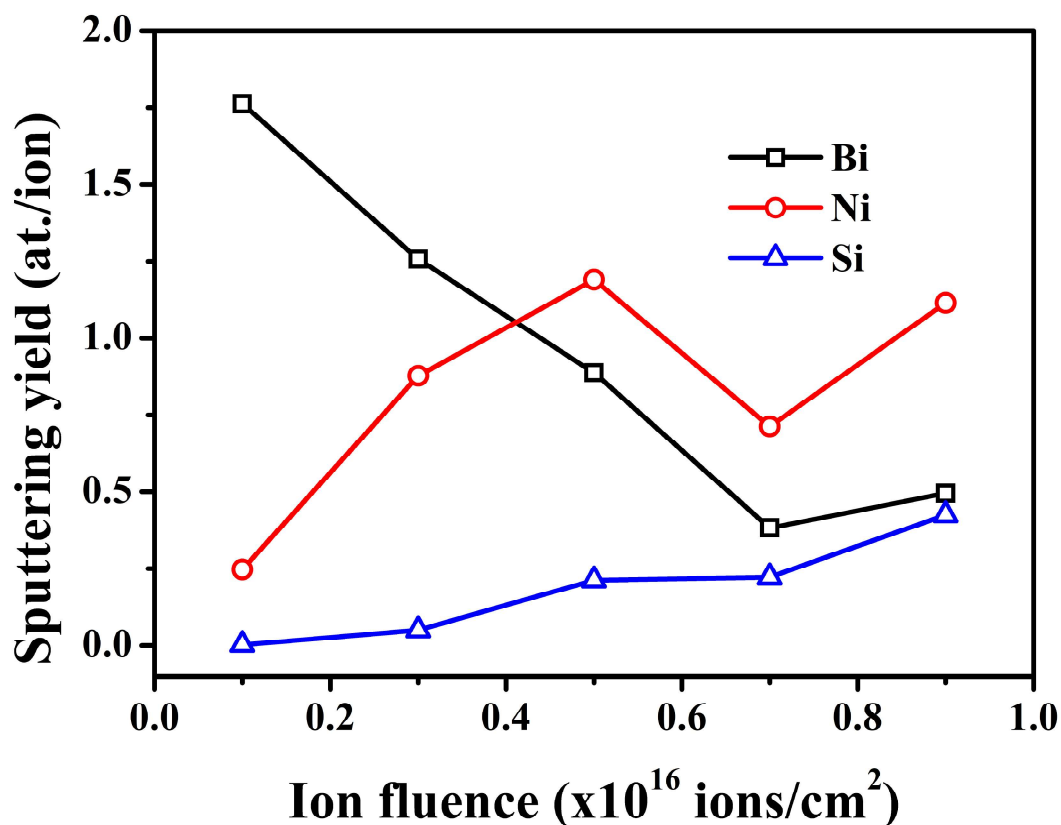
Figure 4.8: Variation of sputtering yield of Ni, Bi and Si due to 1 MeV Ni ions.

These spectra were analyzed using RUMP simulations package [12] and depth profiles of all the samples were extracted and plotted in figure 4.9. The profiles of Bi are shown with solid symbols and that of Ni ones are shown with lines. In the case of the as-deposited sample, from the surface to depth of 5 nm, the atomic fractions of Bi and Ni are 0.992 and 0.008 respectively. Beyond this depth, these atomic fractions of 0.06 and 0.94 for Bi and Ni respectively. This is a signature of the spontaneous diffusion during the deposition as discussed above. The quantity of such diffusion, in this case, is quite less compared to the diffusion in the case of the Ni/Bi films with the thickness of $\approx$ 35 nm each (as shown in the previous chapter) [16,18]. The higher duration and substrate temperature rise during the deposition can be the possible reasons for the difference in the quantity of spontaneous diffusion. After the irradiation, it may be observed the fraction of Ni, in the layer extended from surface to 5 nm, is increasing gradually with the increase in ion fluence. Similarly, after the depth of 5 nm, the fraction of Bi is noticed to

increase with ion fluence. The noticeable modifications in these depth profiles after the ion irradiation are highlighted using grey color background. This highlighted region describes the ion-induced mixing and it is almost 6 nm, which is nearly 60% of the total thickness of the deposited films. It is interesting to note that the improvement in the mixing is almost four times that of the mixing observed in the case of swift heavy ions.
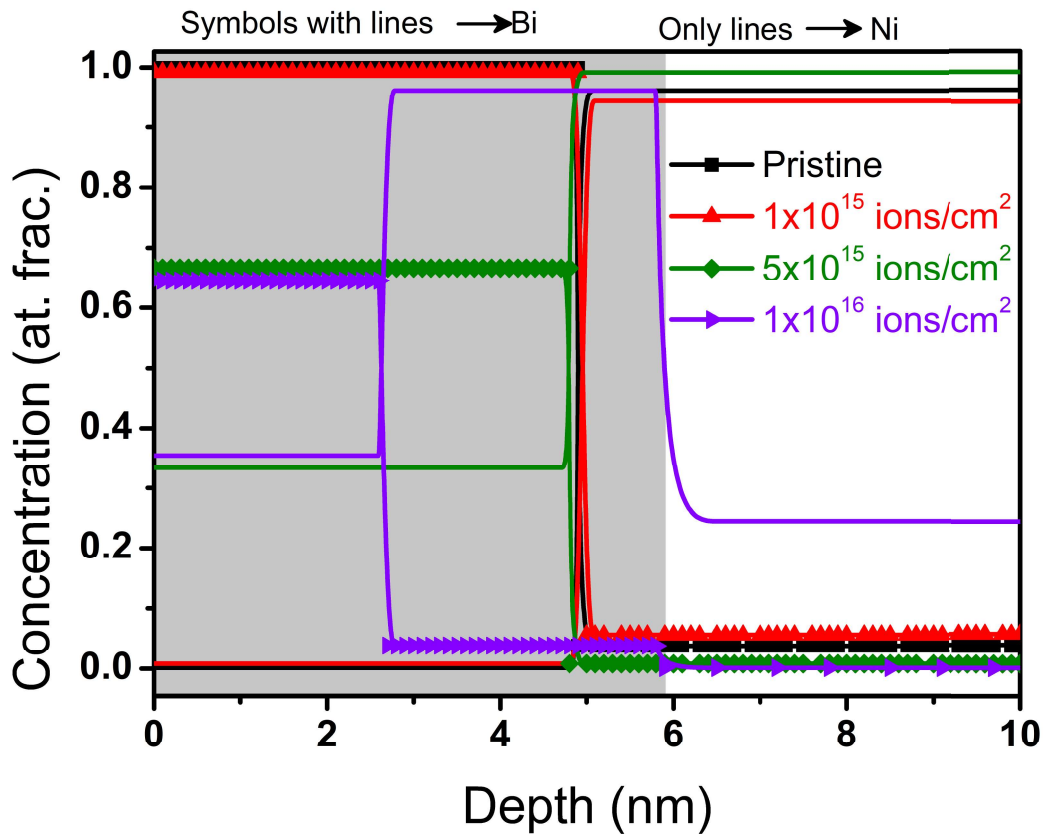
Figure 4.9: The depth profiles of Ni (only lines) and Bi (lines with solid symbols) as a function of ion fluence.

4.4 Conclusion:

In the first part of this chapter, an investigation of Ni sensitivity towards the medium energy ion beam has been carried out. The morphology of the films as a function of ion fluence has revealed different stages of evolution, from nanodots to hillocks formation. A mass flow of material on the surface has been confirmed from the Power spectral density analysis. A large diffusion of Ni atoms from the surface to much deeper in the substrate with increasing ion fluence. From all the above information, it may be inferred that the Ni is sensitive to the present

energy regime. The thermal spike model supports the fact that the Ni at this energy regime goes beyond its melting temperature, whose details are further discussed in section 6.3.2 of chapter 6. Thereafter, the study of ion beam mixing of Ni-Bi system at medium energy regime, using 1 MeV Ni ions, has been performed. The spontaneous diffusion of Ni and Bi has been observed, in the present case as well, though less in content. It has lead to the formation of NiBi and $NiBi_3$ phases in the as-deposited films. After the ion irradiation, this mixing improves considerably as a function of ion fluence. The enhancement in the mixing due to ion irradiation is almost 60% of the total thickness. Such enhancement is due to the ability of medium energy ion beam to drive both the Ni and Bi layers to molten phase as per the TSM calculations, whose details are further discussed in section 6.3.2 of chapter 6.

Bibliography

[1] S. Kraft, B. Schattat, W. Bolse, S. Klaumunzer, F. Harbsmeier, A. Kulinska, A. Löffl, J. Appl. Phys. 91, 1129 (2002).

[2] B. Schattat, W. Bolse, Nucl. Instrum. Methods Phys. Res., Sect. B: 225, 105 (2004).

[3] J. F. Ziegler, M. D. Ziegler and J. P. Biersack, Nucl. Instrum. Methods Phys. Res., Sect. B, 268, 1818 (2010).

[4] R. Pétri, P. Brault, O. Vatel, D. Henry, E. André, P. Dumas, F. Salvan, J. Appl. Phys. 75, 7498 (1994).

[5] I. Horcas, R. Fernández, J.M. Gómez-Rodrǵuez, J. Colchero, J. Gómez-Herrero,A.M. Baro, Rev. Sci. Instrum. 78, 013705 (2007).

[6] K. Nordlund, J. Keinonen, M. Ghaly, R.S. Averback, Nature (London) 398, 49 (1999).

[7] R. C. Birtcher, S. E. Donnelly, Phys. Rev. Lett. 77, 4374 (1996).

[8] R. S. Averback, M. Ghaly, J. Appl. Phys. 76, 3908 (1994).

[9] E. A. Eklund, E. J. Snyder, R. S. Williams, Surf. Sci. 285, 157 (1993).

[10] S. G. Mayr, R. S. Averback, Phys. Rev. B, 68, 075419 (2003).

[11] C. Herring, J. Appl. Phys. 21, 301 (1950).

[12] L. R. Doolittle, Nucl. Instrum. Methods B 9, 344 (1985).

[13] J. P. Biersack, L. Haggmark, Nucl. Instrum. Methods 174, 257 (1980), Also refer to www.srim.org.

[14] M. Toulemonde, M. Costantini, Ch. Dufour A. Meftah, E. Paumier, and F. Studer, Nucl. Instrum. Meth. Phys. Res., Sect. B, 116, 37 (1996).

[15] W. Möller, W. Eckstein, Nucl. Instrum. Methods Phys. Res. Sect. B, 2, 814 (1984).

[16] V. Siva, K. Senapati, B. Satpati, S. Prusty, D. K. Avasthi, D. Kanjilal, P. K. Sahoo, J. Appl. Phys. 117, 083902 (2015).

[17] V. Siva, P. C. Pradhan, G. S. Babu, M. Nayak, P. K. Sahoo and K. Senapati, J. Appl. Phys., 119, 063902 (2016).

[18] V. Siva, A. Chettah, B. Satpati, S. Ojha, D. Kanjilal, P. K. Sahoo, RSC Adv. 6, 58950 (2016).

[19] V. I. Dybkov and O. V. Duchenko, J. Alloy. Compd. 234, 295 (1996).

[20] V. I. Dybkov, in Solid State Reaction Kinetics, IMPS Publications, Kyiv, Ukraine, (2013).

Chapter 5

Effect of 200 keV Ar ions and thermal annealing on Ni-Bi bilayers

5.1 Introduction:

Phase synthesis of Ni-Bi system was studied by several groups using conventional techniques [1–7]. We have investigated the phase synthesis of Ni-Bi system through ion beam mixing by using 100 MeV Au ions, 120 MeV ions, and 1 MeV Ni ions, which has been discussed in the previous chapters [8–10]. It is clear from the previous chapters that the mixing is prominent in the case of medium energy ions (comparable magnitudes of S_e and S_n) compared to the swift heavy ions (Dominant S_e over S_n). The more mixing in the medium energy regime was attributed to the synergistic effects of both the electronic and nuclear energy losses. In general, one may expect the mixing to be much more at the high energy regimes as the energy deposition to be more, which is not true (as evident from the previous chapters). Therefore, it is necessary to investigate the ion beam mixing at the low energy regime as well, where the nuclear energy loss dominates over the electronic energy loss. In the present case, 200 keV Ar ions were chosen to irradiate the Ni ($\approx$ 35 nm)/Bi ($\approx$ 35 nm) bilayer films as a function of ion fluence. The estimated values of nuclear (S_n) and electronic (S_e) energy losses for Ni and Bi from SRIM simulations [11] are shown in table 5.1. It may be noticed that the value of S_n is more compared to S_e in the case of Ni target, which explains the effect of S_n dominance over S_e. However, the values of S_n and S_e are comparable in the case of the Bi, NiBi, NiBi$_3$ targets, which does not affect much in the present study as the Bi is sensitive at all the energy regimes. The projected ranges of 200 keV Ar ions are 78.4 nm, 113 nm, 85.6 nm and 97 nm in Ni, Bi, NiBi and NiBi$_3$ targets respectively. The ion induced mixing and structural modifications of Ni/Bi bilayer films were studied using GAXRD, FESEM, RBS techniques.

Species and energy of ion beam	Target elements	S_e (keV/nm)	S_n (keV/nm)	$\frac{S_e}{S_n}$	Range (nm)
200 keV Ar ions	Ni	0.826	1.02	0.809	78.4
	Bi	0.435	0.402	1.082	113
	NiBi	0.632	0.66	0.962	85.6
	NiBi$_3$	0.528	0.515	1.026	97

Table 5.1: The estimated values of S_e, S_n, ratio of S_e and S_n, and R_p of 200 keV Ar ions in Ni, Bi, NiBi, and NiBi$_3$ targets obatined from SRIM simulations.

Till now in this thesis, the effect of ion beams of various energies on Ni/Bi bilayers has been discussed for the phase synthesis of Ni-Bi system. The thermal annealing study of Ni-Bi system is equally important to compare both the complimentary techniques of phase synthesis. In this study, the Ni and Bi films with the thickness of 7 nm each were used and they were annealed at temperatures (500 ^{o}C - 800 ^{o}C) above the eutectic point of Ni-Bi system. The annealing was performed in argon ambience, to avoid the reaction of the films with the atmospheric gases. The annealing-induced modifications were also analysed by using various characterisation techniques.

5.2   Experimental:

A single bilayer of Ni and Bi films of the thickness of $\sim$ 35 nm each has been deposited using thermal evapouration at a vacuum of less than 5 $\times$ 10^{-7} mbar. The Si (100) substrates were cleaned carefully using ultrasonication in acetone followed by isopropyl alcohol for five minutes each and then dried with an air drier rigorously. The substrate holder was kept in rotation at a speed of 14 revolutions per minute, to make sure of the uniformity of the films. 200 keV Ar ions have been used for irradiation using the LEIBF facility of IUAC, New Delhi. The films were irradiated in the fluence range of 1×10^{15}-1×10^{17} ions/cm^2. In order to obtain the information of existing phases and to verify the crystalline nature of the films, GAXRD was carried out. Ion-induced compositional and other modifications of these films were studied by RBS measurements. The surface morphological evolution was observed using FESEM.

Ni and Bi thin films of thickness 7 nm were deposited on cleaned Si (100) substrate by the thermal evapouration method, in a high vacuum chamber at a base pressure less than 5 $\times$ 10^{-7} mbar. A constant rate of deposition of 0.1 Å/s and substrate rotation of 20 RPM were

maintained throughout the deposition. After deposition, samples were thermally annealed at different temperatures in the range of 500 ^oC to 800 ^oC for 1 hour in Ar atmosphere. These annealing temperatures were chosen in such a way that their values are above the eutectic point of Ni-Bi system. The structure and composition of the samples were studied using FESEM with EDS, GAXRD measurements.

5.3 Results and discussion:

5.3.1 IBM study using 200 keV Ar ions

GAXRD patterns of all the samples are shown in figure 5.1. The peaks at 2θ angles, $\sim 26.6^o$, 32.05^o, 60° in all the samples have been observed corresponding to monoclinic phase of Bi with space group P2$_1$/n [12]. The peaks at 2θ values 44.5^o, 51.85 ^{o} indicate (111) and (200) planes of Ni cubic phase [13]. Further, the peaks along with their miller indices corresponding to orthorhombic NiBi$_3$ phase [14], are shown in figure 5.1. These peaks in the case of as-deposited samples confirm the formation of NiBi$_3$ phase (as found from RBS measurements). On the other hand, peaks related to NiBi were not observed from GAXRD, the existence of the same can not be excluded for two reasons. Firstly, the penetration depth of X-rays at the incident angle 0.5^o is much less than the depth ($\approx$50 nm) at which the Ni-Bi (composition 1:1) layer exists. The second reason can be its existence in the amorphous phase. The values of FWHM of the highest intense X-ray peaks of Bi (020) and NiBi$_3$ ((203) and (105)) as a function of fluence are plotted in figure 5.2. The error bars of FWHM were extracted from the fitting of XRD peaks. After the ion irradiation, the values of FWHM of diffraction peaks reduce at lower fluences and they increase at the higher fluences. It can be understood in terms of crystallization at lower fluences, followed by a random amorphization of the phases.

The ion-induced surface morphological modifications were observed using FESEM and the corresponding images are shown in figure 5.3. In the as-deposited samples, the surface has a sponge-like morphology as shown in figure 5.3(a). Interestingly, with increasing ion fluence, an increase in porous nature can be observed in panels (b-e) of the figure 5.3. The evolution of such morphology as a function of ion fluence can be understood as a consequence of the removal of the surface atoms, which is also known as sputtering. However, a smoother surface may be noticed at the highest irradiated fluence (1×10^{17} ions/cm^2), which is due to the sputtering of most of the top layer (as discussed below).
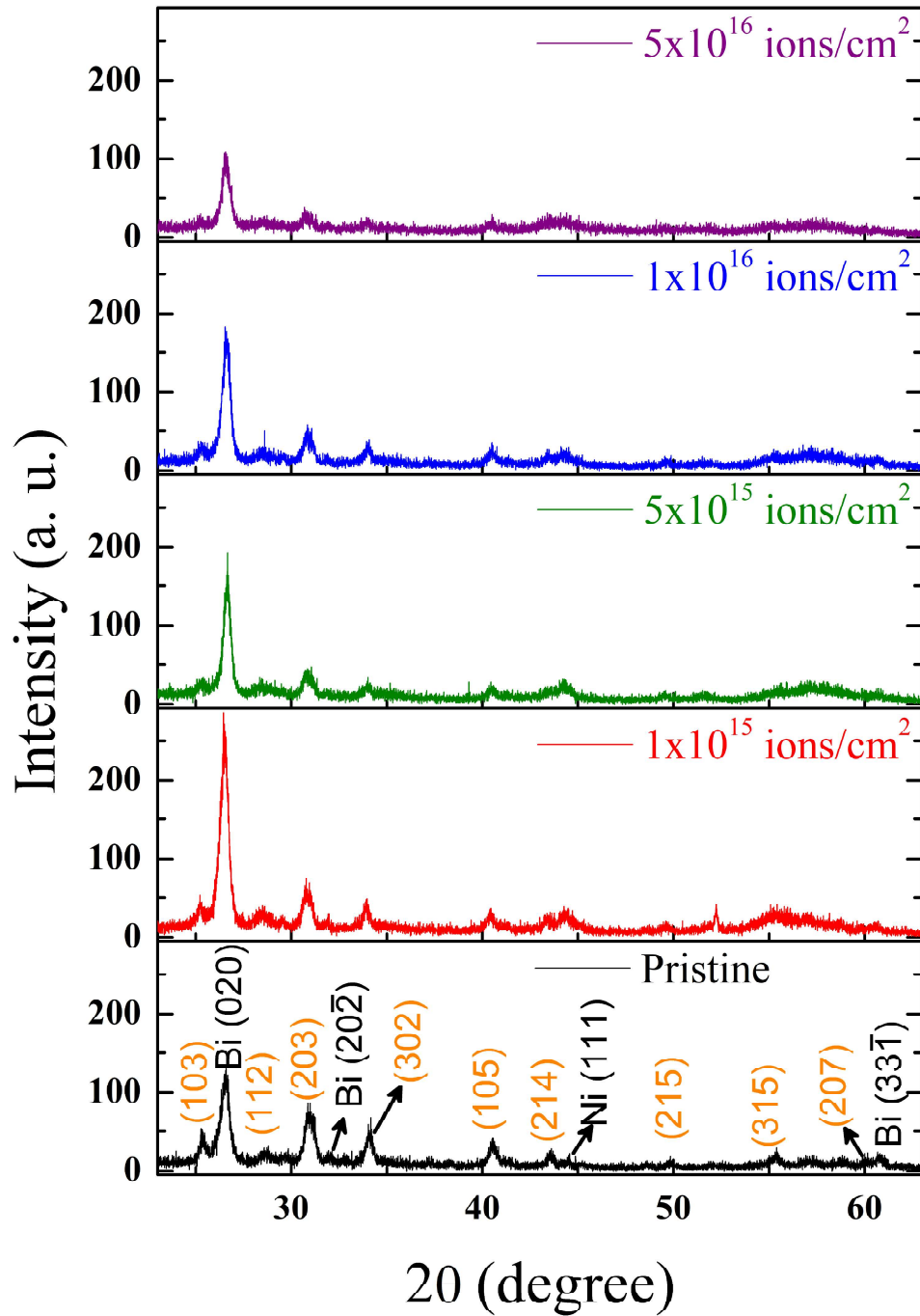
Figure 5.1: Glancing angle X-ray diffraction patterns of the as-deposited and irradiated samples at different fluences. The Ni and Bi peaks are indexed and unspecified peaks are related to $NiBi_3$.

Sputtering yield calculations were performed using TRIDYN simulations [15] to confirm the aforementioned sputtering phenomenon at higher irradiation fluences. The plots of estimated sputtering yields of Ni and Bi are shown in figure 5.4. The value of Bi sputtering yield is
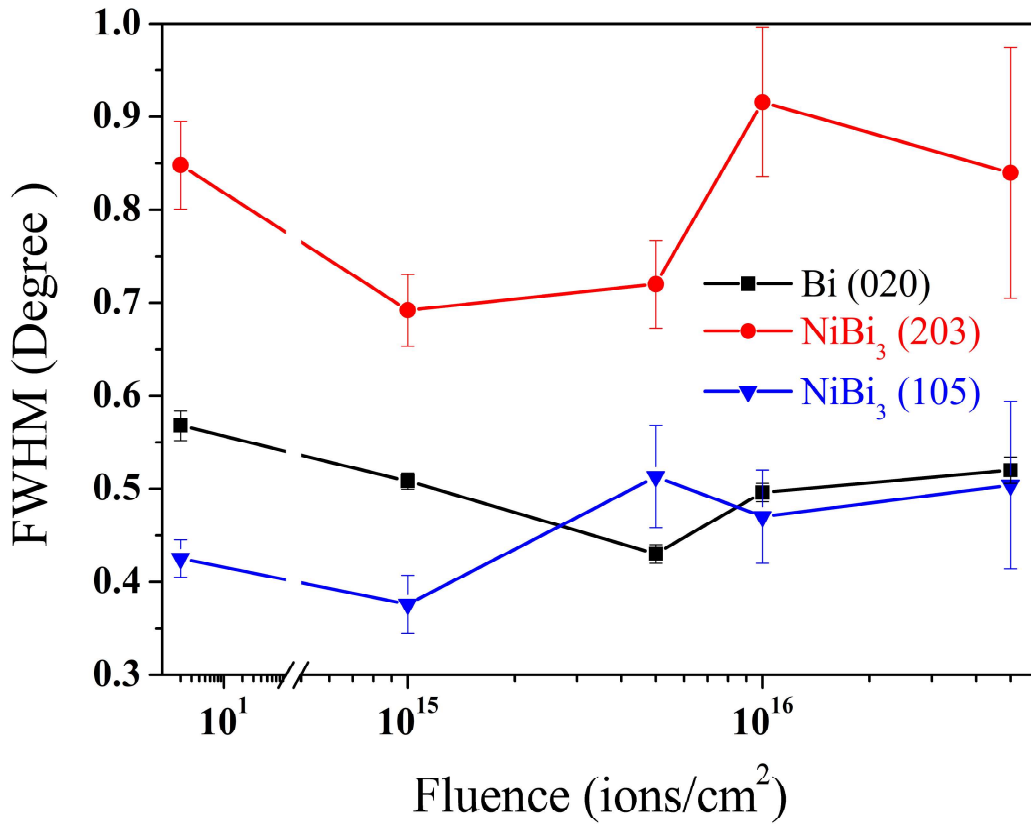
Figure 5.2: The variation of FWHM values of the highest intense (Bi (020) and NiBi$_3$ (203) and (105)) peaks as a function of ion fluence.

approximately an order of magnitude higher than the value of Ni in the fluence range of 1×10^{15} to 1×10^{16} ions/cm^2. Above this fluence, the sputtering yield of Bi tends to decrease, which arrives at a value of 0.23 atoms/ion at a fluence of 1×10^{17} ions/cm^2. On the other hand, Ni has an increasing trend of sputtering yield at this range of ion fluence. At lower fluences, the dominance of Bi sputtering yield over Ni can be understood as a gradual sputtering of top Bi atoms until the underneath Ni layer gets exposed to the ion beam. It may be inferred that the most of the top layer gets sputtered out at the highest fluence, which can be the reason for the observed smoother surface (figure 5.3(f)). It is to be mentioned here that the spontaneous formation NiBi$_3$ phase has not been taken into consideration in the TRIDYN simulations. However, such dominant sputtering yield of Bi over Ni is expected to be the same, because the quantity of Bi is sufficiently high irrespective of the presence of Bi grains and/or NiBi$_3$ grains on the surface.

RBS measurements were performed to obtain the thickness and composition of the films before and after 200 keV Ar ion irradiation. The RBS spectra of as-deposited and irradiated
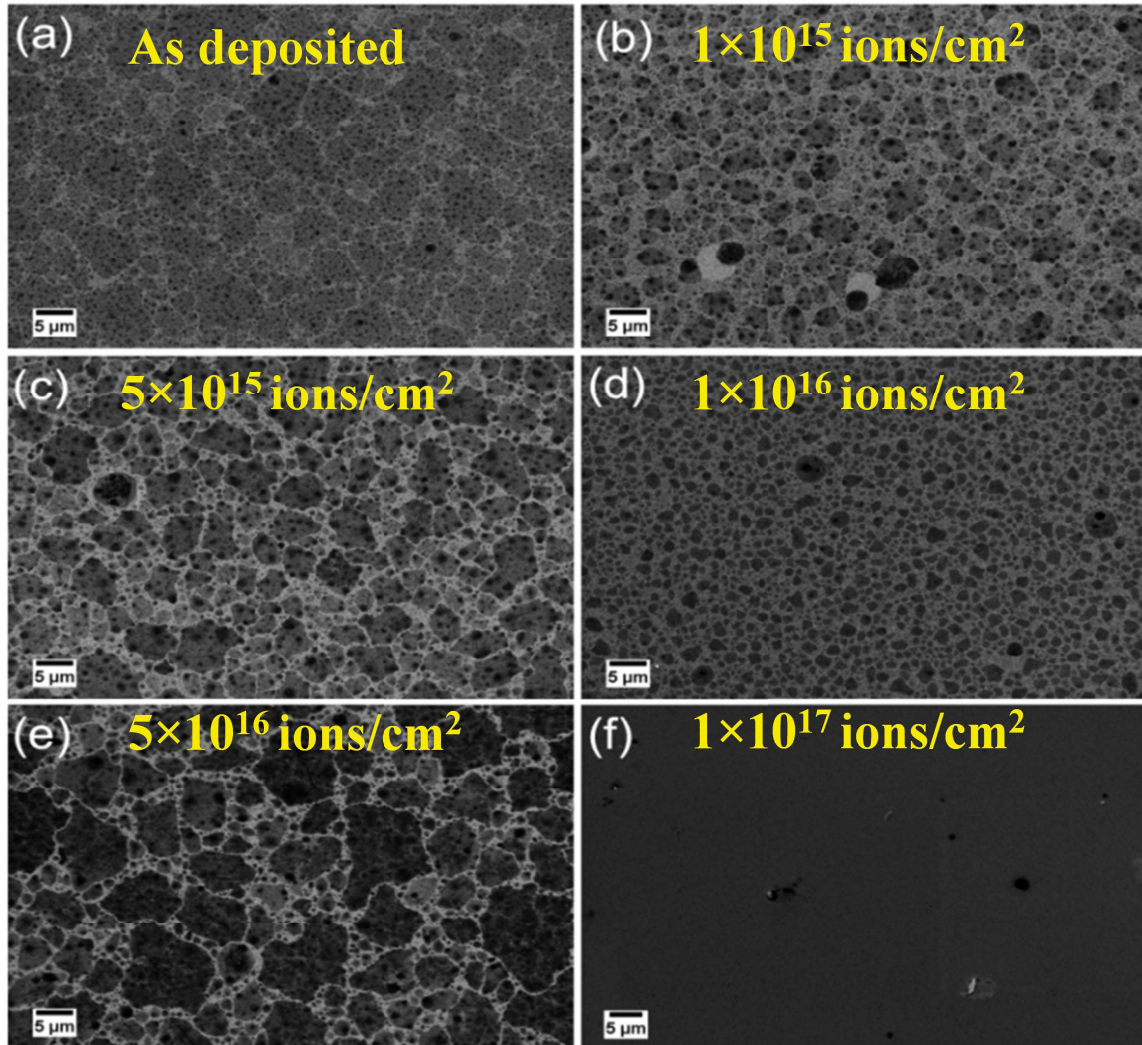
Figure 5.3: Scanning electron micrographs of (a). as-deposited, implanted to a fluence of (b). 1×10^{15} ions/cm^2, (c). 5×10^{15} ions/cm^2, (d). 1×10^{16} ions/cm^2, (e). 5×10^{16} ions/cm^2 and (f). 1×10^{17} ions/cm^2.

samples are shown in figure 5.5. One can observe the peaks corresponding to Bi and Ni layers along Si substrate edge in figure 5.5. At the higher irradiation fluences, a peak related to the irradiated Ar ions can be noticed. It may be noticed that the Ni peak, shifts towards higher energy side with increasing ion fluence, which is the indication of diffusion of Ni towards the surface. Moreover, the integral intensity corresponding to Ni layer reduces at higher fluences, which is due to the ion-induced sputtering of Ni atoms. In the case of Bi, such reduction in the integral intensity (which is sputtering) with ion fluence is much prominent. This can be attributed to sputtering of Bi, since the sputtering is a surface phenomenon. Furthermore, a tail can be noticed at the low energy side of the Bi peak with increasing ion fluence. The tailing
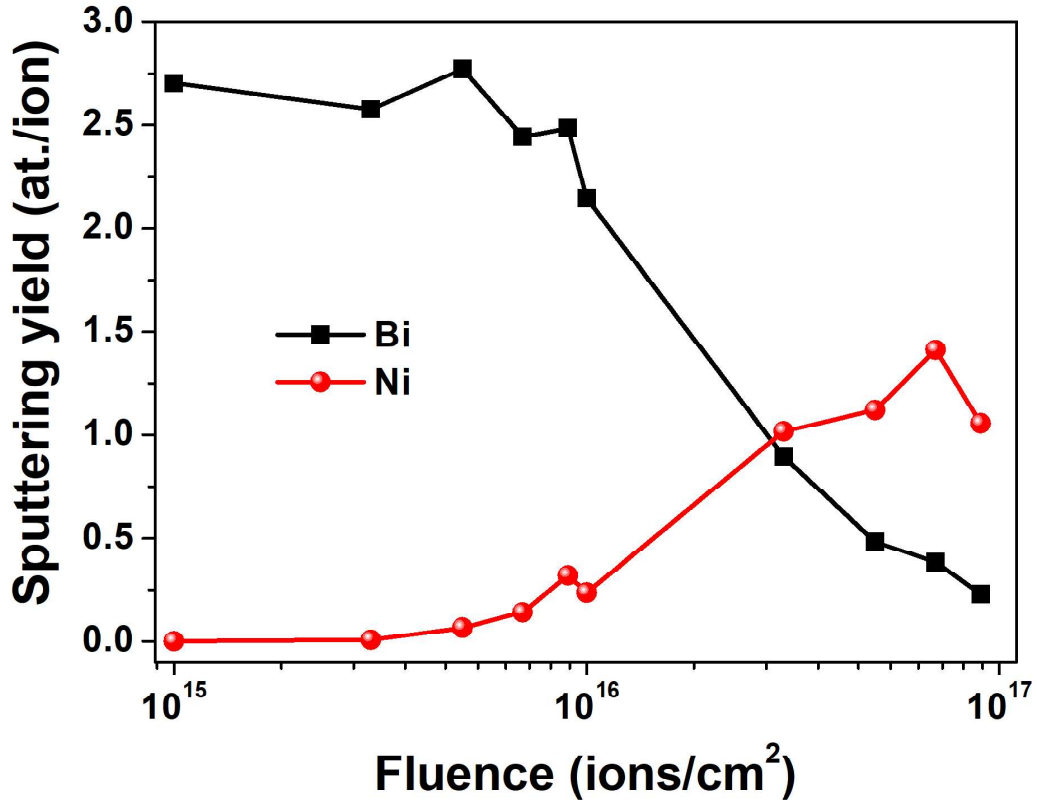
Figure 5.4: The sputtering yields of Bi and Ni as a function of ion fluence.

effect of Ni at its high energy side and that of Bi at its low energy side is the clear signature of ion-induced mixing of Ni and Bi.

The extracted depth profiles from RUMP simulations [16] corresponding to Ni and Bi layers are shown in fig. 5.6. To differentiate the depth profiles of Ni and Bi, the Ni profiles are shown using solid lines with symbols whereas the profiles of Bi are drawn using dashed lines (with no symbols). In the case of the as-deposited sample, one may notice that both the Ni and Bi elements are distributed throughout the film, whose composition varies as a function of the depth. Such distribution of Ni and Bi is counter-intuitive in the as-deposited films, which is due to the spontaneous formation of stable phases as a consequence of reaction-diffusion mechanism during the deposition [8]. From the surface till a depth of ≈ 30 nm, the ratio of Ni and Bi is noticed to be nearly 1:3, which reveals the formation of $NiBi_3$ inside the top layer. In the layer extended from ~ 30 to ~ 52 nm from the surface, the ratio of Ni and Bi are almost 1:1. Such ratio may be due to the formation of NiBi phase or presence of elemental Ni in
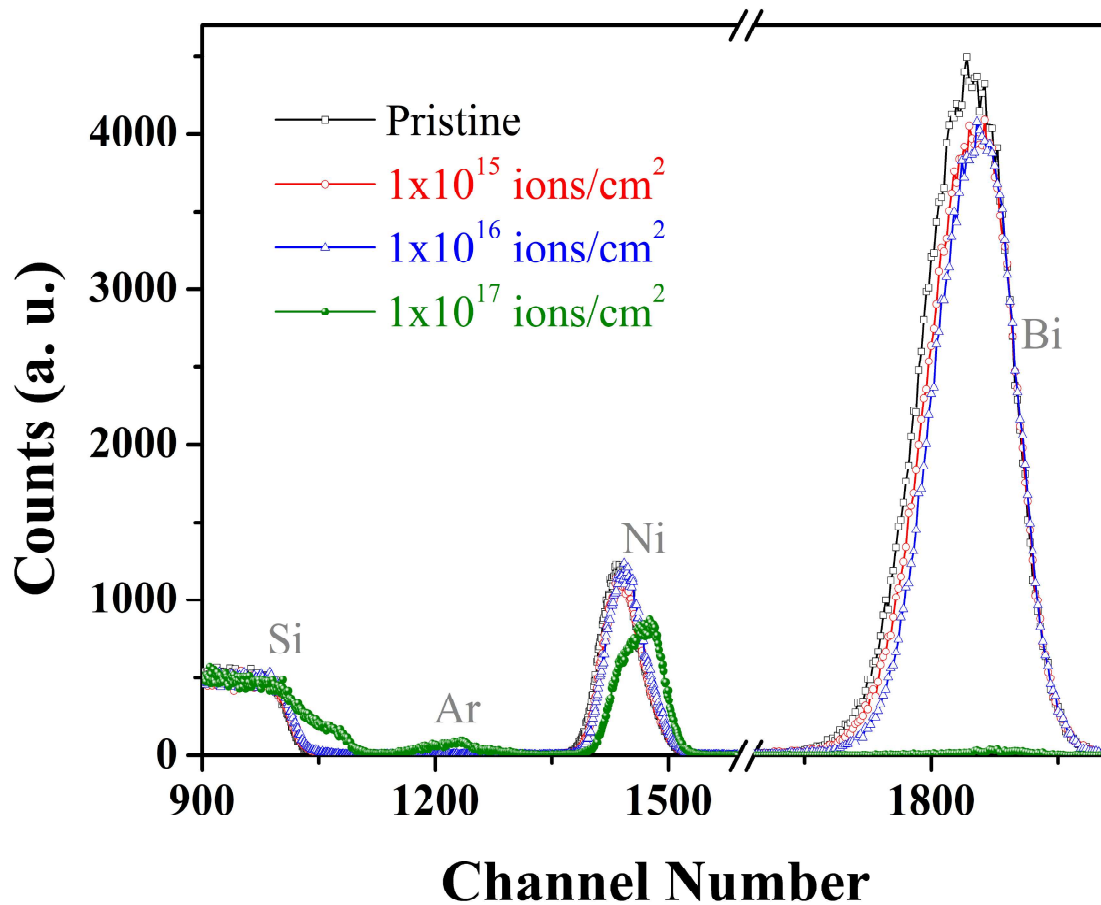
Figure 5.5: RBS spectra of as-deposited and irradiated samples at different fluences. The positions corresponding to Ni, Bi, Si and Ar are marked.

equal amount. Beyond this depth (52 nm), it is predominantly Ni with a small amount of Bi (almost 0.03 atomic fractions). It may be observed that both the Ni and Bi profiles appear to move towards the surface after irradiation. This can be understood in terms of the sputtering of Ni and Bi, which is apparent from fig. 5.6. Apart from this sputtering effect, there is also an observable improvement in intermediate layer (NiBi or Ni+Bi region), which is the ion-induced enhancement in the mixing. The mixing enhanced regions are highlighted using grey coloured backgrounds. The overall ion-induced enhancement is ≈ 20 nm (the summation of 12 nm, 6 nm, and 2 nm), which is almost 25% of the total thickness of the as-deposited samples. The enhancement in the present case is little more than the one observed in the case of SHI irradiation and it is much less compared to the medium energy ions case.

Considering all the experimental findings obtained from RBS, XRD and SEM measurements, we summarize the observed phenomenon using a schematic model as shown in figure
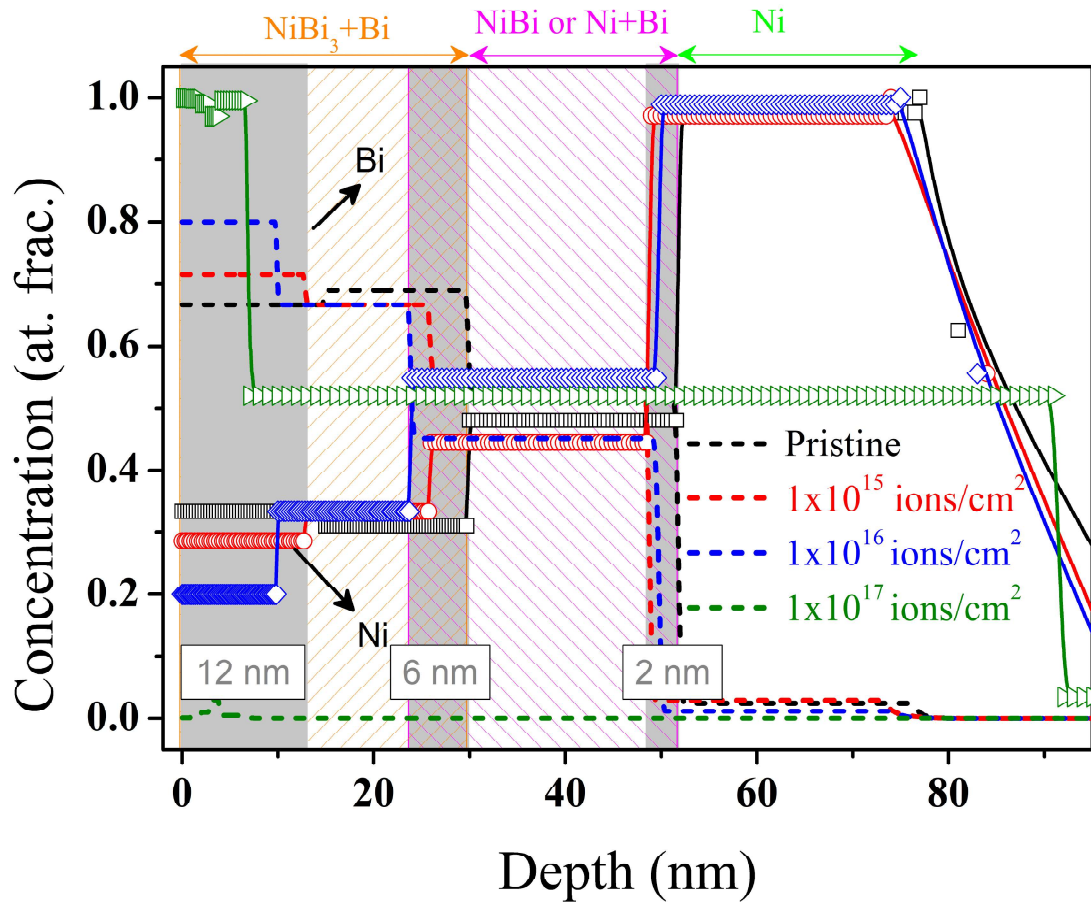
Figure 5.6: Depth profiles of Ni (solid lines with symbols) and Bi (dashed lines) for the as-deposited and implanted samples at different fluences from 1×10^{12} to 1×10^{14} ions/cm^2. Orange and magenta colored cross lines are showing the NiBi$_3$+Bi regime and NiBi or elemental Ni+Bi regime respectively.

5.7. Figure 5.7(a) represents the as-deposited film, where we indicate Ni, Bi and NiBi$_3$ phases in maroon, cyan and mix coloured (1:3-maroon:cyan) spheres. When Bi is deposited over Ni, the formation of NiBi$_3$ phase up to the surface takes place through a reaction-diffusion mechanism between Bi and Ni at the interface. Upon increasing the ion fluence, the thickness of the NiBi$_3$ layer gets reduced due to sputtering, which is evident from fig. 5.6. As it is evident from the TRIDYN simulations that the sputtering yield of Bi and Ni differs by an order of magnitude, which may cause an increase in surface roughness. This increasing roughness has actually been reflected in the observed increasing porous-like nature seen in the SEM images of fig. 5.3. It can be inferred from the GAXRD and RBS that the NiBi$_3$ exists on the surface and hence it may be concluded that the sponge-like surfaces comprise of NiBi$_3$.
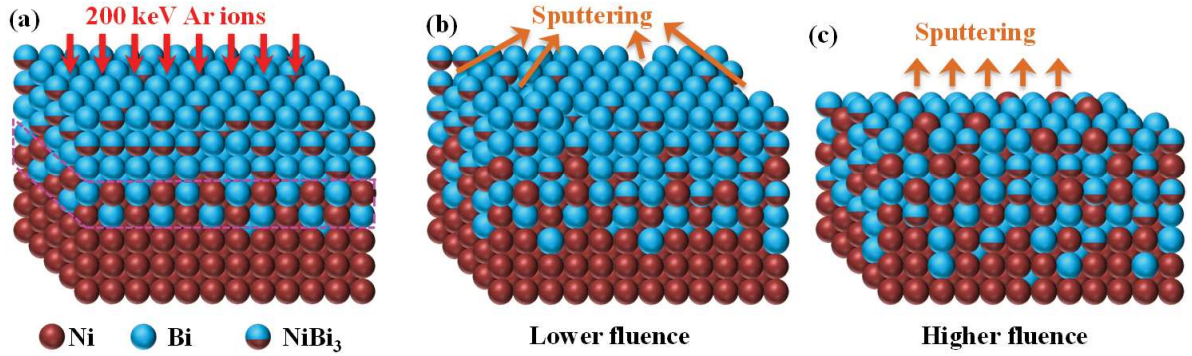
Figure 5.7: Schematic representation of (a) as-deposited, implanted films at (b) lower and (c) higher fluences.

wettability study:

The wettability study has been performed to understand the variation in the contact angle measurements in all the samples, which has been plotted in figure 5.8. In the insets of this figure, the water droplets and their contact angles are shown for the as-deposited and representative irradiated (at lowest and highest fluences) samples. The contact of the as-deposited samples is 105.9^o, which indicates that the surface is hydrophobic in nature. The error bars are the deviations from average contact angle, which were extracted from four different contact angle measurements. After 200 keV Ar ion irradiation, the contact angles are observed to be reduced with increasing ion fluence, but their magnitudes are more than 90° till a fluence of 5×10^{16} ions/cm^2. It implies that the surface remains hydrophobic till the above-mentioned fluence. On the other hand, the sample irradiated at a fluence of 1×10^{17} ions/cm^2 shows a contact angle of 88.1^o, which is the signature of hydrophilicity of the surface at this fluence. Interestingly, the transition of the surfaces from hydrophobic to hydrophilic nature takes place as soon as the NiBi$_3$ disappears from the surface (from the depth profiles). Therefore, the hydrophobic nature of the films has been attributed to the existing NiBi$_3$ phase on the surface. The contact angle of a liquid drop on the surface can be related to the surface roughness of the samples by using the following equation [17].

$$cos\theta_W = rcos\theta \tag{5.1}$$

Where θ_W and θ are the contact angles of the water drop on the rough surface and flat surface respectively. The other factor in this equation is the roughness, r, which has been

104

defined as the ratio of the area under the water drop and the flat projection of the area onto the surface. It may be observed from the above equation that the contact angle of water drop with flat surface (θ) should decrease with increasing roughness of the surface, whereas the value of the contact angle between water drop and rough surface (θ_W) should increase with the increase in roughness. Therefore, the observed decreasing trend of contact angle in the present case cannot be explained with the help of the Wenzel's law. Furthermore, it has been considered that the contact angle of water drop on a surface depends on free energy and roughness of the sample surface [18, 19]. The free energy of the surface depends on the composition of the sample surface and thereby affect the contact angle of the surface. Therefore, the observed contact angle variation in the present study can be associated with the ion-induced variation in surface free energy of the samples. These porous like structures on the surface are believed to have potential applications in the enzyme catalysis [20] and biomedical fields [21].
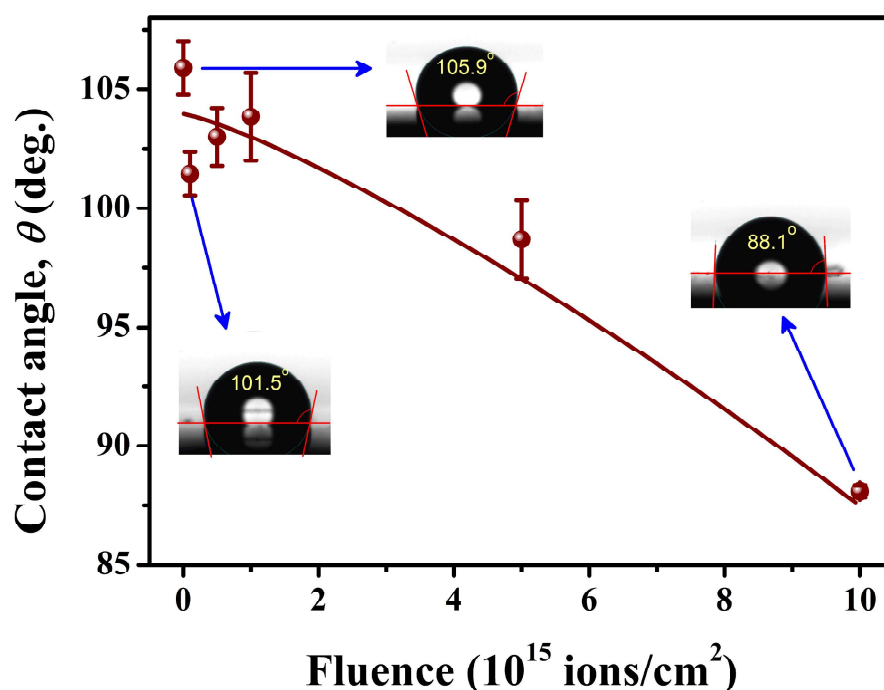
Figure 5.8: Contact angles for all the samples as a function of ion fluence.

5.3.2 Thermal annealing study of Ni/Bi bilayers

The surface morphology of as-deposited and thermally annealed samples at 500 ^{o}C, 600 ^{o}C, 700 ^{o}C and 800 ^{o}C are shown in figures 5.9(a)-(e). The structural evolution of the as-deposited films as a function of annealing temperature may be observed from these micrographs. An ag-

glomeration of the deposited Ni and Bi layers has been observed upon increasing the annealing temperature, which occurs to reduce their free energy. The figures 5.9(c)-(e) show distribution of islands on the surface with a lateral dimension of more than 400 nm due to annealing at temperatures of 600 ^oC, 700 ^oC, and 800 ^oC respectively. Moreover, on the annealed surfaces from 500 to 700 ^oC, one can notice distinguishable grains figure5.9(b)-(d), which disappear on the surface annealed at 800 ^oC (figure5.9(e)). The surface morphology seems to be formed after reaching a molten phase and this is expected as the annealing temperature is more than the peritectic point (653 ^oC) of Ni-Bi system. An EDS spectra corresponding to the sample annealed at 800 ^oC is shown in figure 5.9(f). It reveals the presence of Ni, Bi, Si as well as O, which indicates the possibility of oxide phases after the annealing of Ni-Bi layers.
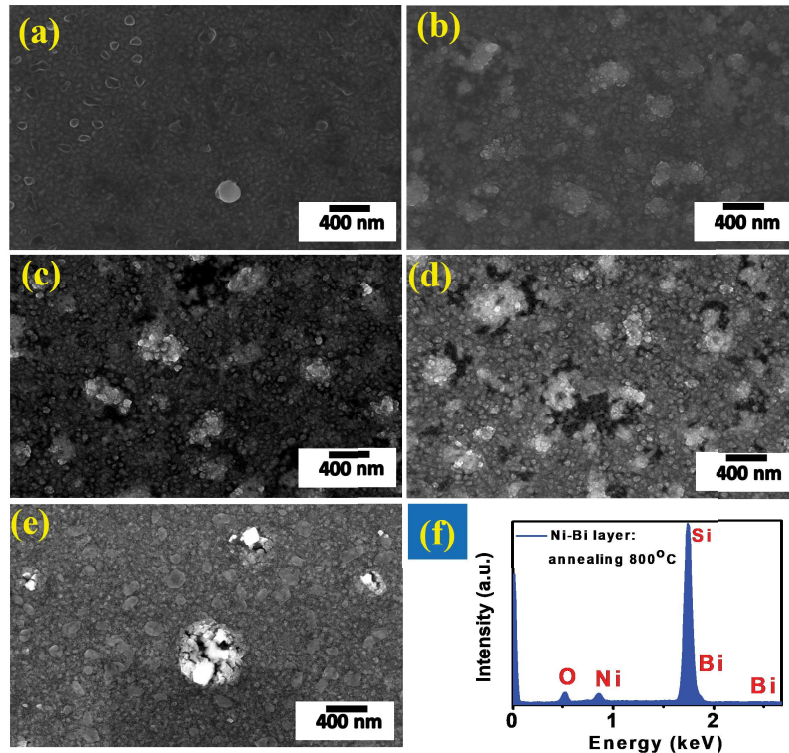
Figure 5.9: Scanning electron micrographs of (a) as-deposited films, and annealed at (b) 500 ^oC, (b) 600 ^oC, (d) 700 ^oC and (e) 800 ^oC. Panel (f) shows the EDS spectra of the sample annealed at 800 ^oC.

GAXRD patterns of as-deposited and all the annealed samples are shown in figure 5.10, which show polycrystalline nature of the films. It is observed that the Ni and Bi are in cubic and rhombohedral phases in the as-deposited sample respectively. However, the spontaneous formation of stable phases (NiBi and NiBi$_3$) in this case has not been observed. It could be

due to the existence of these phases in lesser quantity as the thickness of the films is less, which can hinder these peaks compared to the other peaks. The formation of both the stable phases of Ni-Bi system after the annealing temperature of 500 ^{o}C. The NiBi$_3$ phase, is noticed to disappear in the films annealed at a temperature of more than 700°C. The crystalline nature of the deposited films was noticed to improve with increasing annealing temperature, which is evident from the XRD peaks. Apart from these phases, all the annealed samples also show the existence of Nickel oxide peaks. The possibility of bismuth oxides cannot be ruled out completely because the formation of such phases is very likely to happen. Even if the bismuth oxide exists, they might have ended up in their amorphous phases.
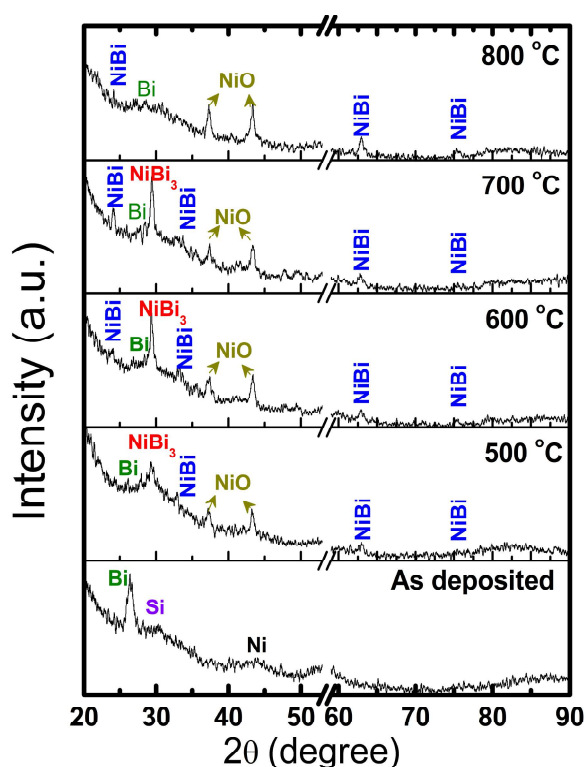
Figure 5.10: GAXRD patterns for as-deposited and all the annealed samples.

The electrical transport measurements in the as-deposited and annealed (500 ^{o}C) samples are shown in figure 5.11. These measurements were performed in four-probe method, where all the four contacts were made on the surface and in-line of the samples. The resistivity of the as-deposited sample is noticed to be increasing upon lowering the temperature, which is indicating the negative temperature coefficient of resistance just like in the case of insulators. The resistivity values are seen to saturate at very low temperatures, which is a signature of
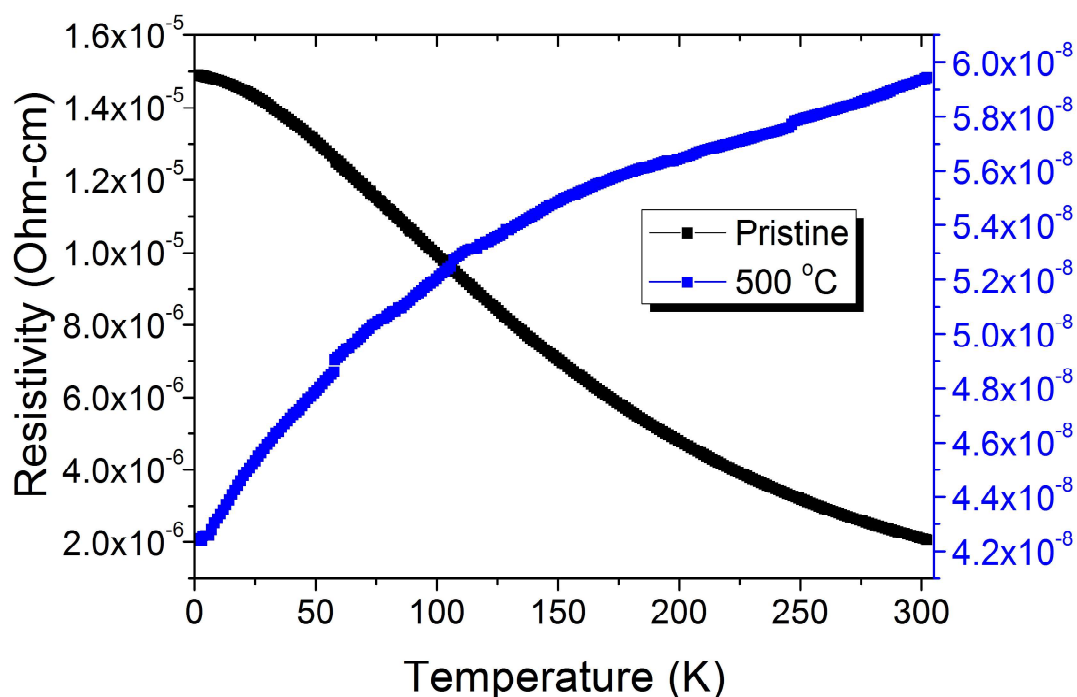
Figure 5.11: Resistivity as a function of temperature measurements on as-deposited and annealed sample at 500 ^{o}C.

semi-metal [22]. This kind of electrical behaviour is due to the semi-metallic Bi on the surface as the contacts were on the top layer. More interestingly, the annealed sample at 500 ^{o}C show a decreasing trend of resistivity with lowering temperatures i.e., positive temperature coefficient of resistance and it is a signature of metallic nature of the films. It is an indication of transition of the layers from the semi-metallic to metallic nature after the annealing. The metallic nature, in this case, is due to the formation of NiBi and NiBi$_3$. It is to be mentioned here that both the stable phases (NiBi and NiBi$_3$) are superconductors with the superconducting transition temperatures of 4.25 K and 4.05 K respectively, [23–25]. However, there was no signature of the superconductivity in the present case, till a temperature down to 2 K. These transport measurements were not performed as the resistances of the samples annealed above 500 ^{o}C were more than 1 $M\Omega$, which is beyond the capacity of the measurement system. Such high resistance corresponding to these films must have arose from the surface oxidation of the films as well as their increase in roughness due to agglomeration.

All the observed experimental findings may be visualized from the schematic diagram as shown in figure5.12. In this figure, the atomic fraction of Ni and Bi are shown as a function of
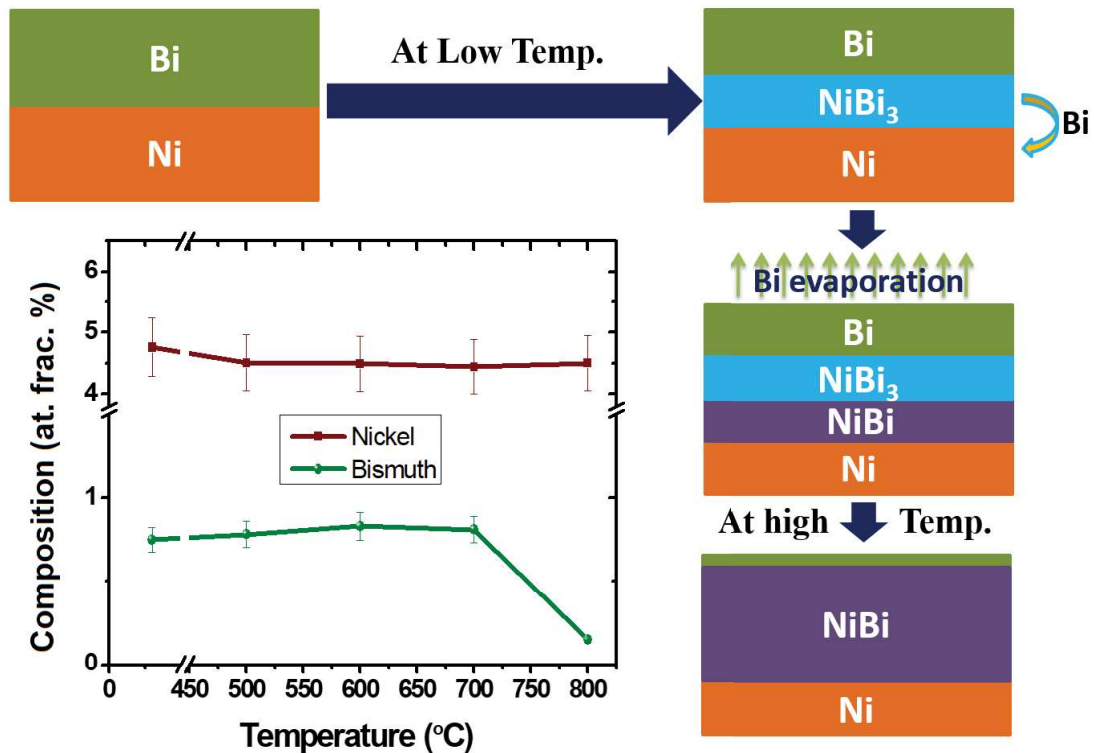
Figure 5.12: Compositional changes of the films with increasing annealing temperature. It also shows the schematic representation of the experimental findings.

annealing temperatures, which were obtained from EDS measurements. The atomic fraction of Ni is more or less constant within the error fraction of $\sim 1\%$ upon increasing the annealing temperature, while this quantity for the Bi drops off at the higher temperatures. This is expected in the case of Bi as the annealing temperature is much higher than its melting point (544 K). According to Dybkov *et al.* [26], the formation of $NiBi_3$ phase is quite expected for the range of annealing temperatures of $150\ ^oC - 250\ ^oC$, where Bi was found to be the main diffusing element. Furthermore, the annealing of $NiBi_3$ on Ni can lead to the formation of NiBi phase at their interface, due to the diffusion of Bi into Ni layer from the $NiBi_3$ layer [27]. It is also reported that the thickness of such NiBi layer increases with the rise in the annealing temperature. Since, it is known that the Bi is diffusing element during the annealing process, the formation of $NiBi_3$ would take place first as it has more negative heat formation compared to NiBi phase. In the case of $500\ ^oC$ annealing temperature, the presence of both the phases has been observed as it is the above the eutectic temperature of Ni-Bi system. Upon, further increasing the annealing temperatures, the fraction of $NiBi_3$ reduces compared to that NiBi phase. It is an indication that the $NiBi_3$ is probably dissociating into NiBi phase and two Bi

109

atoms at higher temperatures. The observed findings related to the formation of alloy phases of Ni-Bi system are in good agreement with the existing literature.

5.4   Conclusion:

In this chapter, the ion beam mixing study of Ni-Bi system using 200 keV Ar ions has been carried out. The GAXRD results reveal the $NiBi_3$ phase along with Ni and Bi peaks in the as-deposited samples. These phases have been crystallized at lower fluences after 200 keV Ar ion irradiation and followed by a random amorphization of these phases at higher fluences. The SEM images show the evolution of porous-like morphology of the films as a function of ion fluence. The RBS measurements revealed that the low energy ion beam enhances the mixing of Ni and Bi as well as sputters out the surface atoms. The enhancement in the mixing of Ni and Bi with increasing ion fluence was $\approx$20 nm, which is nearly equal to the 25% of the total thickness of the as-deposited films. The mechanism for this enhanced mixing has been attributed to the ion-induced molten phases in both Ni and Bi layers. The details of the mixing are further discussed in section 6.3.3 of chapter 6.

The thermal annealing of the Ni/Bi bilayer films were studied as a function of temperature. Formation of the stable phases of Ni-Bi system has been achieved successfully. An evolution of granular morphology followed by molten-like surface has been observed with increasing annealing temperatures. GAXRD measurements revealed the formation of NiBi, $NiBi_3$ phases along with a certain fraction of Ni, Bi, Si, and Nickel oxide phases. A transition of semi-metallic to metallic nature of the films further confirmed the formation of stable Ni-Bi alloy phases. The formation of both $NiBi_3$ and NiBi alloys at lower temperatures and conversion of $NiBi_3$ into individual NiBi and Bi phases at higher temperatures were also observed, which is in good agreement with the Ni-Bi phase diagram.

There are certain notable advantages of using the ion beam mixing for phase synthesis compared to the thermal annealing. The advantages of IBM over thermal annealing are the (1) thermal budget, (2) reducing the time of preparation, (3) spatial selectivity, and (4) ability to mix immiscible systems. The first two advantages, thermal budget and reducing the time of preparation, are apparent from the present study. The thermal budget would mean that the study of thermal annealing needed higher temperatures (more than 500 ^{o}C) compared to ion beam mixing, which has been performed at room temperature. The preparation time can

considerably be reduced using ion beam mixing. However, the irradiation time varies with the ion-current and energy. The other two advantages of IBM can be used depending on the requirement. Therefore, the study of ion beam mixing can be considered as more useful for phase synthesis over thermal annealing.

Bibliography

[1] T. Herrmannsdörfer, R. Skrotzki, J. Wosnitza, D. Köhler, R. Boldt, and M. Ruck, Phys. Rev. B, 83, 140501(R) (2011).

[2] B. Silva, R. F. Luccas, N. M. Nemes, J. Hanko, M. R. Osorio, P. Kulkarni, F. Mompean, M. García-Hernández, M. A. Ramos, S. Vieira, and H. Suderow, Phys. Rev. B 88, 184508 (2013).

[3] E. L. M. Piñeiro, B. L. R. Herrera, R. Escudero, and L. Bucio, Solid State Commun., 151, 425 (2011).

[4] Y. Fujimori, S. Kan, B. Shinozaki and T. Kawaguti, J. Phys. Soc. Jpn., 69, 3017 (2000).

[5] X. Zhu, H. Lei, C. Petrovic, and Y. Zhang, Phys. Rev. B, 86, 024527 (2012).

[6] J. Kumar, A. Kumar, A. Vajpayee, B. Gahtori, D. Sharma, P. K. Ahluwalia, S. Auluck and V. P. S. Awana, Supercond. Sci. Technol. 24, 08500 (2011).

[7] V. I. Dybkov, O. V. Duchenko, J. Alloys and Compnd. 234, 295 (1996).

[8] V. Siva, K. Senapati, B. Satpati, S. Prusty, D. K. Avasthi, D. Kanjilal, and P. K. Sahoo, J. Appl. Phys. 117, 083902 (2015).

[9] V. Siva, A. Chettah, B. Satpati, S. Ojha, D. Kanjilal and P. K. Sahoo, RSC Adv., 6, 58950 (2016).

[10] V. Siva, A. Chettah, A. Tripathi, D. Kanjilal, P. K. Sahoo, Nucl. Instrum. Methods Phys. Res. Sect. B, 409, 314 (2017).

[11] J. F. Ziegler, M. D. Ziegler, J. P. Biersack, Nucl. Instrum. Methods Phys. Res. Sect. B, 268, 1818 (2010).

[12] J. Chen, H. Iwasaki, T. Kikegawa, J. Phys. Chem. Solids, 58, 247 (1997).

[13] Swanson, Tatge, Natl. Bur. Stand. (U.S.), Circ, 539, I, 13 (1953).

[14] H. Fjellvag and S. Furuseth, J. Less-Common Met., 128, 177 (1987).

[15] W. Möller, W. Eckstein, Nucl. Instrum. Methods Phys. Res. Sect. B, 2, 814 (1984).

[16] L. R. Doolittle, Nucl. Instrum. Meth. Phys. Res. Sect. B, 9, 344 (1985).

[17] R. N. Wenzel, Ind. Eng. Chem., 28, 988 (1936).

[18] S. K. Garg, D. P. Datta, J. Ghatak, I. Thakur, K. Khare, D. Kanjilal, and T. Som, RSC Adv., 6, 48550 (2016).

[19] D. P. Datta, S. K. Garg, I. Thakur, B. Satpati, P. K. Sahoo, D. Kanjilal, and T. Som, RSC Adv., 6, 48919 (2016).

[20] D. Zang, H. Yi, Z. Gu, L. Chen, D. Han, X. Guo, S. Wang, M. Liu, and L. Jiang, Adv. Mater. 29, 1602869 (2017).

[21] Y. Fan, X. Cao, T. Hu, X. Lin, H. Dong, and X. Zou, J. Phys. Chem. C, 120, 3955 (2016).

[22] X. Du, S. Tsai, D. L. Maslov, and A. F. Hebard, Phys. Rev. Lett. 94, 166601 (2005).

[23] N. E. Alekseevskii, N. B. Brandt and T. I. Kostina, Bull. Acad. Sci. U. R. S. S. 16, 233 (1952); J. Exp. Theor. Phys. 21, 951 (1951).

[24] B. T. Matthias and J. K. Hulm, Phys. Rev. 87, 799 (1952).

[25] B. T. Matthias, Phys. Rev. 92, 874 (1953).

[26] V. I. Dybkov and O. V. Duchenko, J. Alloys. Compnd., 234, 295 (1996).

[27] S. Seo, M. G. Cho, and H. M. Lee, J. Electron. Mater. 36, 1536 (2007).

Chapter 6

Thermal spike model calculations for Ni-Bi system

6.1 Introduction:

The theoretical background is very much essential to understand the mechanism of the experimentally observed results. In the present study also, there are several frameworks to explain the underlying physics of ion beam mixing like ballistic effects, radiation enhanced diffusion, coulomb spikes, and thermal spikes. Among them, the thermal spike model is the most acceptable and successful one to explain the mixing in the case of metals, semiconductors, and insulators. This model is also capable of predicting the mixing of metal-metal, metal-semiconductor, semiconductor-semiconductor, metal-insulator, semiconductor-insulator and insulator-insulator systems. The present system of our interest is Ni and Bi, which is a metal/semi-metal system and thermal spike model has been used to explain the observed mixing. It is to be mentioned here that there are three different types in the thermal spike model, based on the energy of ions. They are elastic collision spike model [1], inelastic thermal spike model [2–4] and unified thermal spike model [4]. Among these models, the first one takes the nuclear energy loss alone into the consideration, while the second model considers electronic energy loss only. However, in the case of unified thermal spike model the total (nuclear+electronic) energy loss has been taken into account for the calculations.

In the present chapter, the details of the thermal spike model (TSM) have been described. The results of these calculations for the Ni-Bi films for all the energy regimes are discussed, whose experimental results are shown in chapter 3, 4, and 5. In this chapter, the calculations were performed for high energy (100, 120, 150, and 200 MeV Au) ions, medium energy (1 MeV Ni ions), and low energy (200 keV Ar) ions. The underlying mechanism of the experi-

mental observations is also discussed towards the end of this chapter.

6.2   The details of thermal spike model calculations:

According to this model [3,5–12], the energetic ion transfers its energy along the path resulting in a local temperature rise. Due to the temperature gradient between the surroundings and ions path, heat diffusion would take place along the cylindrical track in the radial direction as well as along the ion path. This process can be described by the following two non linear coupled differential equations [3,5–12]:

$$C_e(T_e)\frac{\partial T_e}{\partial t} = \frac{1}{r}\frac{\partial}{\partial r}\left(r\kappa_e(T_e)\frac{\partial T_e}{\partial r}\right) - g(T_e - T_a) + A(r,t) \tag{6.1}$$

$$C_a(T_a)\frac{\partial T_a}{\partial t} = \frac{1}{r}\frac{\partial}{\partial r}\left(r\kappa_a(T_a)\frac{\partial T_a}{\partial r}\right) + g(T_e - T_a) + B(r,t) \tag{6.2}$$

Where the suffixes a and e represent the atomic and electronic subsystems. The parameters C, κ, T and g are the specific heat, thermal conductivity, temperature and the electron-phonon coupling constants respectively. The functions $A(r,t)$ and $B(r,t)$ represent the electronic and nuclear energy densities deposited by the incident ions at time t and radial distance r. The evolution of electronic and atomic temperatures of a target as a function of time and space are deduced from the numerical solution of the above set of equations. According to the above equations, the diffusion of heat takes place in the radially outward direction from the ion's path. However, these equations are no more valid in the case of multilayers, where the materials are different along the length (x-direction) of the ion path. Therefore, in the case of multilayered films, an extra term has been added to include the interface of two different materials in both the equations. The modified equations can be rewritten as the following:

$$C_e(T_e)\frac{\partial T_e}{\partial t} = \frac{1}{r}\frac{\partial}{\partial r}\left(rK_e(T_e)\frac{\partial T_e}{\partial r}\right) + \frac{\partial}{\partial x}\left(K_e(T_e)\frac{\partial T_e}{\partial x}\right) - g(T_e - T_a) + A(r,t) \tag{6.3}$$

$$C_a(T_a)\frac{\partial T_a}{\partial t} = \frac{1}{r}\frac{\partial}{\partial r}\left(rK_a(T_a)\frac{\partial T_a}{\partial r}\right) + \frac{\partial}{\partial x}\left(K_a(T_a)\frac{\partial T_a}{\partial x}\right) + g(T_e - T_a) + B(r,t) \tag{6.4}$$

The variable x represents the distance traversed by the ion into the solid. While traversing through the matter, the ion may create a thermal spike around its path, i.e., a limited volume

Figure 6.1: (a) Gaussian distribution of energy as a function of time in electronic subsystem and (b) radial distribution of Waligorski function.

around the ion path in which the majority of atoms are in motion. The duration of such thermal spikes would typically be around few picoseconds and their track radius will be few nanometres. The main usage of TSM is to explain diffusion in molten phase as the diffusion coefficient in liquid phase becomes several orders of magnitude greater than that in the solid phase. If there are two such layers in the target and the temperature of lattice atoms along the ion track goes sufficiently high, then the atoms of both the layers at the interface mix with each other. Upon increasing the ion fluence, one can have many such inter-mixed regions and thereby achieve more and more mixing.

Electronic subsystem:

The term $A(r, t)$ in equations (6.1) and (6.3) is the energy deposition density per unit time, which is supplied to the electronic subsystem by the incident ions at time t and radius r. This term can mathematically be written as [13]:

$$A(r, t) = c.S_e.G_e(t).D_e(r) \tag{6.5}$$

Where c is a normalization constant, S_e is electronic energy loss. The functions $G_e(t)$ and $D_e(r)$ describe the energy deposition to electronic subsystem in time and space respectively. The energy deposition in time follows a Gaussian distribution ($G_e(t)$), which can be given by

$$G_e(t) = \frac{1}{\sigma\sqrt{2\pi}} \exp\left(-\frac{(t - t_0)}{2\sigma^2}\right) \tag{6.6}$$

Where, σ is the half-width of the Gaussian distribution, t_0 is the required time for the electrons to reach the equilibrium distribution and both these quantities are assumed to be equal (typically of the order of 10^{-15} s). A typical plot of Gaussian distribution for an electronic subsystem can be noticed in figure 6.1(a).

The other function $D_e(r)$, which takes care of the energy deposition in space, was estimated by Waligorski and co-workers [14] and it has been defined as the following:

$$D_e(r) = \frac{1}{r}\left(\frac{\left(1 - \frac{r+\theta}{T+\theta}\right)^{1/\alpha}}{r + \theta}\right) \tag{6.7}$$

Where r is the distance from the ion path or radial distance, θ is the range of delta electrons of energy equal to the ionization potential and α is a constant. The variation of Waligorski function with the radius can be observed in figure 6.1(b).
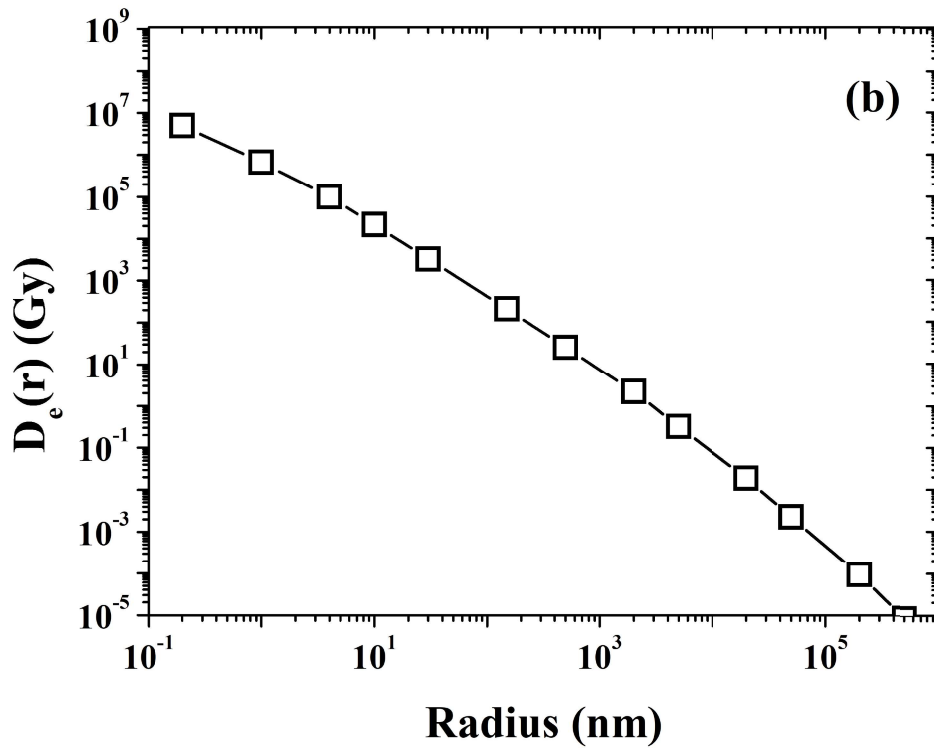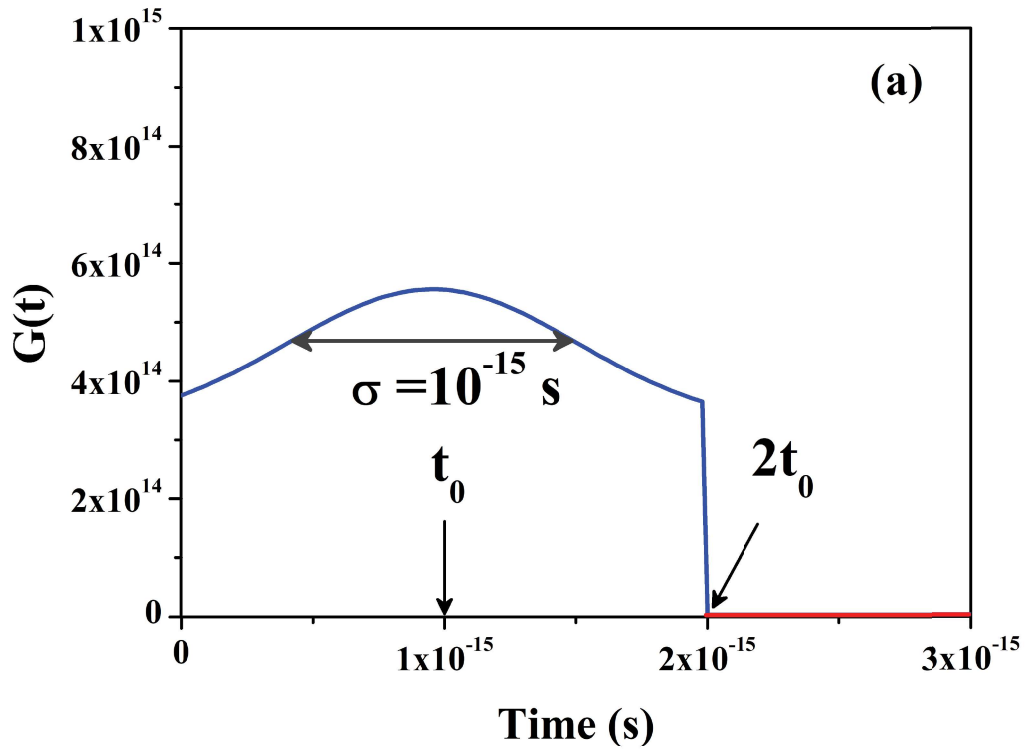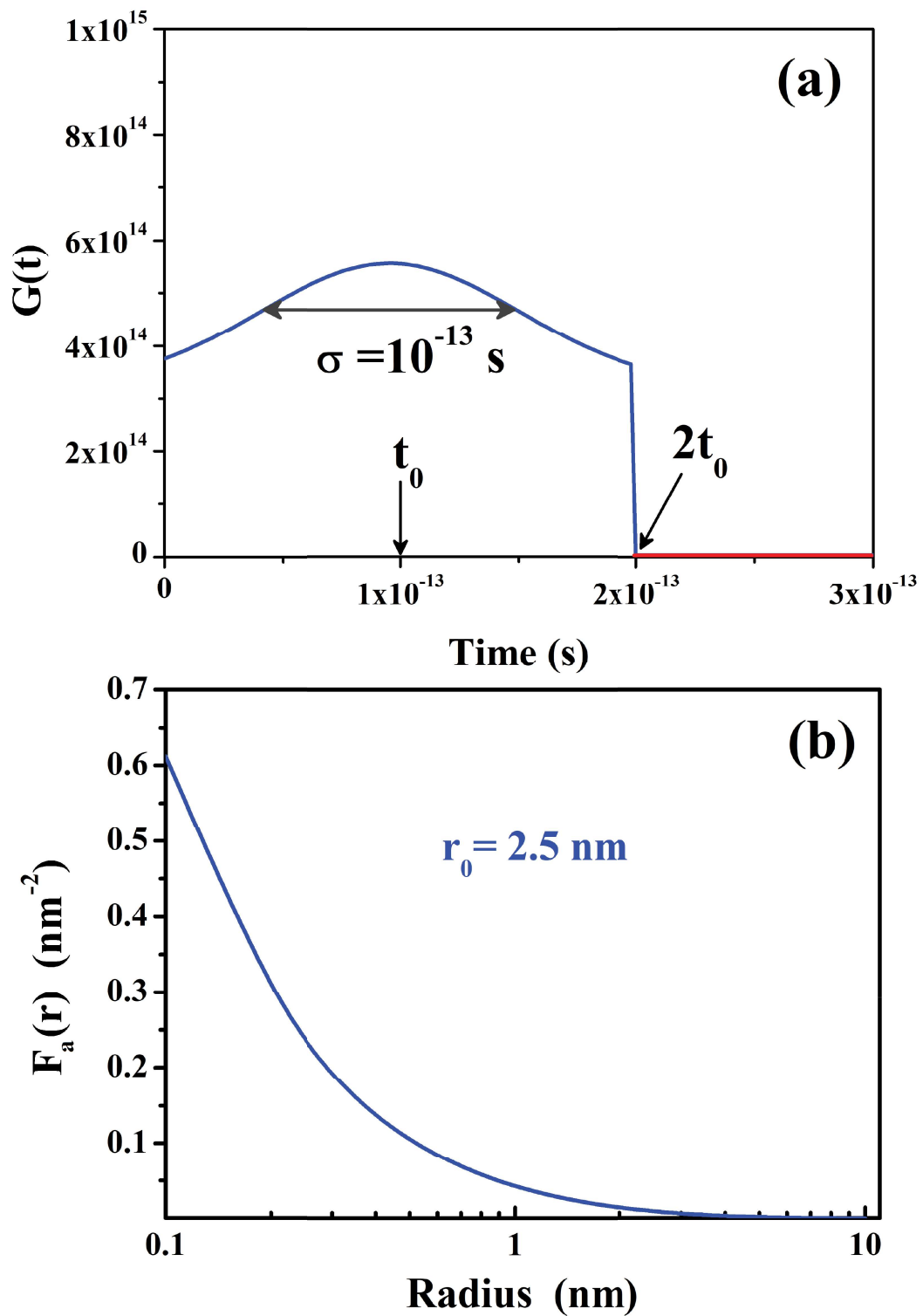
Figure 6.2: (a) Gaussian distribution of energy as a function of time in atomic subsystem and (b) The spatial distribution function $F_a(r)$ of energy.

Atomic subsystem:

The energy deposition on the atomic subsystem depends on the term $B(r, t)$ in equations (6.2) and (6.4), which represents the nuclear energy deposition density and the following expression can be used to simulate it [4, 15].

$$B(r, t) = b_n \times S_n \times G_a(t) \times F_a(r) \tag{6.8}$$

Where b_n is a normalization constant, which can be considered as an integration over time and space to yield the total S_n (nuclear energy loss). $G_a(t)$ is Gaussian function as a function of time t, which can be given by:

$$G_a(t) = \frac{1}{\sigma\sqrt{2\pi}} \exp\left(-\frac{(t - t_0)}{2\sigma^2}\right) \tag{6.9}$$

The parameter t_0 is the deposition time, and it is assumed to have a typical value of 1×10^{-13} s. Variation of the Gaussian function with the time has been shown in figure 6.2(a). In the equation of $B(r, t)$, the term $F_a(r)$ describes the energy deposition in space, which can be expressed mathematically as:

$$F_a(r) = \frac{1}{r} \exp\left(-\frac{r}{r_0}\right) \tag{6.10}$$

Where r_0 is the radius of a cylinder, where the nuclear energy is deposited. The function $F_e(r)$ drops drastically with the increasing latent track radius, as shown in figure 6.2(b). It is known that most of the energy deposition happens along the ion path and the ion loses its energy in each interaction with the target elements. These are the reasons for such a sharp fall in the function $F_e(r)$ with the radii. The values of r_0 were estimated as reported in the work by Mieskes *et al.* [15] and Toulemonde *et al.* [4]. The values of r_0 for Ni and Bi are shown in table 6.1. The table also consists of the parameters S_e, S_n, and r_0. The observed track radii at each energy are also shown. In order to drive the targets to molten phase, the maximum energy transfer per atom should be more than E_m and these values for Ni and Bi are 0.66 eV/at and 0.2 eV/at respectively. The observed values from the TSM calculations in each case are also indicated in this table.

One of the most important parameters in thermal spike model is the electron-phonon coupling factor g. The importance of the strength of this factor (g) has been discussed by Lin *et al.* [16] for different metals. This term was initially analyzed by Kaganov *et al.* [17] using

Table 6.1: Parameters used in thermal spike model calculations

Ion beam species (Energy per nucleon)	Target elements	S_e/S_n (keV/nm)	r_0 nm	Track radius (nm)	E_m (eV/at)	E_{am} (eV/at) at radial distance 1 nm
200 keV Ar ions	Ni	0.826/1.02	1.5	1.1	0.66	0.7
(0.005 MeV/amu)	Bi	0.435/0.402	3.3	3.5	0.2	0.69
1 MeV Ni ions	Ni	1.234/1.239	1.8	1.7	0.66	0.9
(0.017 MeV/amu)	Bi	0.74/0.61	2.9	4.5	0.2	1.28
2.2 MeV Au ions (0.011 MeV/amu)	Ni	3.45/7.63	3.4	3	0.66	2
100 MeV Au ions	Bi	32.45/0.83	–	0	0.66	0.4
(0.508 MeV/amu)	Ni	17.59/0.57	–	7	0.2	0.3
120 MeV Au ions	Ni	36.7/0.72	–	0	0.66	0.42
(0.609 MeV/amu)	Bi	20/0.5	–	9	0.2	0.35
150 MeV Au ions	Ni	0.826/1.02	–	0	0.66	0.53
(0.76 MeV/amu)	Bi	0.435/0.402	–	10	0.2	0.38
200 MeV Au ions	Ni	1.234/1.239	–	0	0.66	0.58
(1.015 MeV/amu)	Bi	0.74/0.61	–	12	0.2	0.42

the free electron gas model. The electron-phonon coupling factor g can mathematically be represented as:

$$g = \frac{\pi^2}{6} \frac{m_e C_s^2 n_e}{\tau(T_e) T_e}$$ (6.11)

Where m_e and n_e are the effective mass and number density of electrons respectively. C_s and $\tau(T_e)$ are the speed of sound and electron relaxation time respectively. It may be inferred from the coupled equations that the g-factor plays a key role in communicating the heat between the electronic and atomic subsystems.

Solid to liquid transformation or melting of material takes place, when the energy transfer per atom exceeds the required value of energy per atom (E_m) for melting. It can be mathematically defined as:

$$E_m = \int_{T_{initial}}^{T_{melting}} C_s(T) dT + L_m$$ (6.12)

Where the first term on the right-hand side of this equation is corresponding to the energy required to bring the material to its melting temperature. The term, $C_s(T)$ is the specific heat of lattice, which was taken from the experimental measurements as a function of temperature. The second term, L_m, corresponds to the latent heat of fusion. The energy transfer per atom i.e., E_m is the most appropriate measure to assess whether the material has undergone solid to

liquid (melting) phase transition or not. For the case of Ni and Bi, the values of E_m are 0.66 eV/at and 0.20 eV/at respectively, beyond which these materials melt. The lattice temperature calculations were performed in superheating scenario, which has been described by Chettah *et al.* [7].

6.3 Calculation results:

6.3.1 Effect of swift heavy ions in Ni/Bi thin films

Effect of 100 MeV Au ions in Ni/Bi single bilayer films:
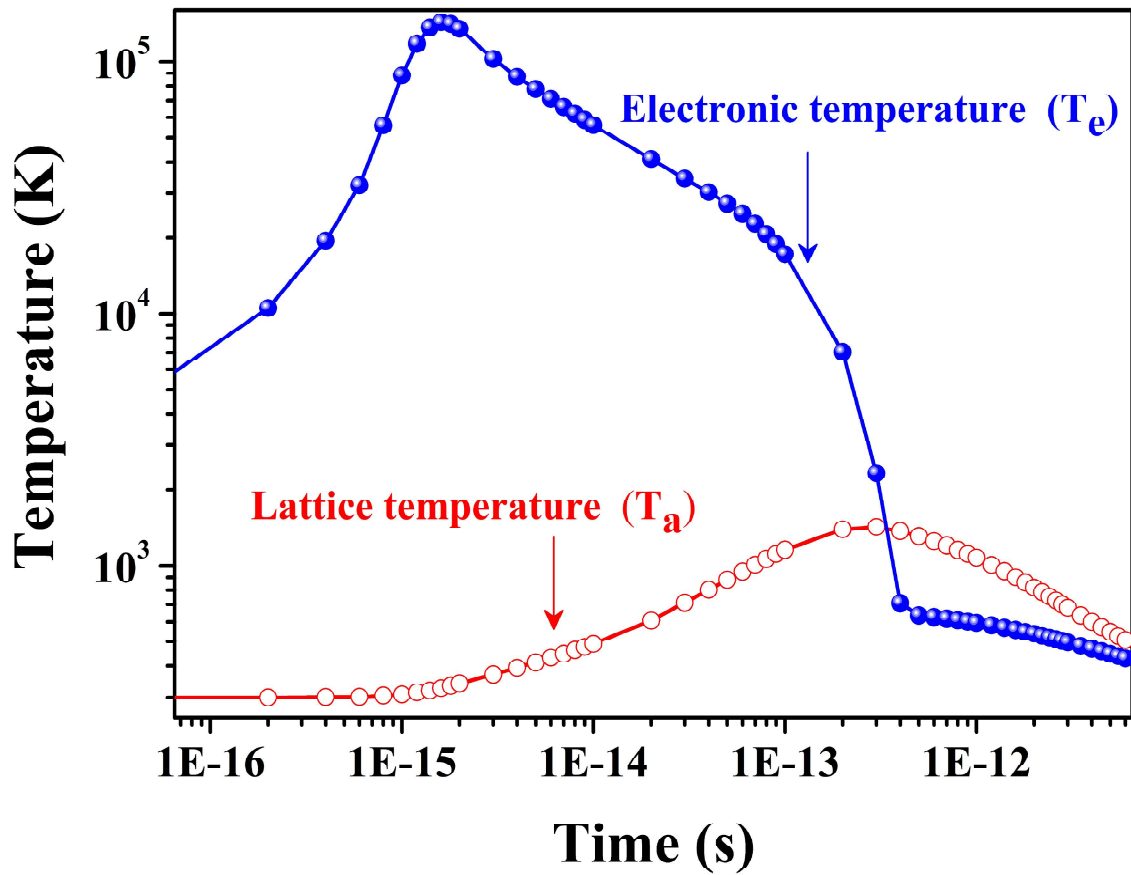
Figure 6.3: Evolution of electronic and lattice temperatures of Ni at a radial distance of 1 nm as a function of time due to 100 MeV Au ion irradiation.

As mentioned in the previous sections that the evolution of lattice and electronic temperatures as a function of time (t) and space (r, x) can be obtained by solving the coupled non-linear differential equations numerically. It is worth noting here that, in the case of swift heavy ions, the value of S_n is very small compared to S_e and hence the term $B(r,t)$ is neglected in the

present calculations. Evolution of electronic and lattice temperatures as a function of time would provide a better understanding about the thermal spike model. For example, the temperature evolution in Ni target at a radial distance of 1 nm due to 100 MeV Au ions is shown in figure 6.3. Interestingly, the temperature of the electronic subsystem in Ni target reaches more than 10^5 K within few picoseconds. Beyond this time, such large temperature gets communicated to the atomic subsystem through the electron-phonon coupling factor (g). During the transfer of heat from electronic to atomic subsystem, a sharp drop in the electronic temperature may be observed. Simultaneously, a rise in lattice temperature within the duration of 10^{-13} to 10^{-12} seconds can also be noticed, due to the energy transfer happens from electronic to atomic subsystem during this time. It is to be noted here that the electronic temperatures are almost two orders of magnitude higher compared to the lattice temperatures, which is true in most of the metals.

The calculated lattice temperatures as a function of time for Bi bulk and Bi at the interface are shown in figure 6.4 (a) and (b) respectively. Various parameters [20] that are used in these calculations are shown in table 6.2. It may be noticed from the panel (a) that the lattice temperature ($\approx$544 K) of Bi in the case of bulk reaches the melting temperature of Bi with the track radii of more than 17 nm. These ion induced lattice temperatures reach the melting point of Bi within $\approx 10^{-13}$ seconds and then remain at that temperatures for more than few picoseconds. On the other hand, the lattice temperatures in the case of Bi at the interface reaches almost two times higher than the melting temperature of Bi (as shown in figure 6.4(b)) with the similar latent track size that of the bulk. However, in this case, the temperature peaks up within few 10^{-13} seconds and drops sharply after few picoseconds unlike the case of bulk.

The evolution of lattice temperatures of Ni bulk and interface are shown in figure 6.5(a) and (b) respectively. The lattice temperatures of Ni, in the case of bulk, reach more than 1350 K within few 10^{-13} seconds and falls off rapidly. It may be noticed that these temperatures are much less than the melting temperature of Ni (1728 K). On the other hand, in the case of Ni at the interface, the observed lattice temperatures are even lesser compared to that of the bulk ones. The reduction in these temperatures can be understood in terms of the heat transfer from the Ni layer (high temperature) to the Bi layer (low temperature) due to the existing temperature gradient at the interface of Ni and Bi. Due to the same reason, the lattice temperatures of Bi at the interface (shown in figure 6.4(b)) rises considerably. Although the temperatures are more than 1000 K due to 100 MeV Au ions, but it is much lesser than the melting temperature of
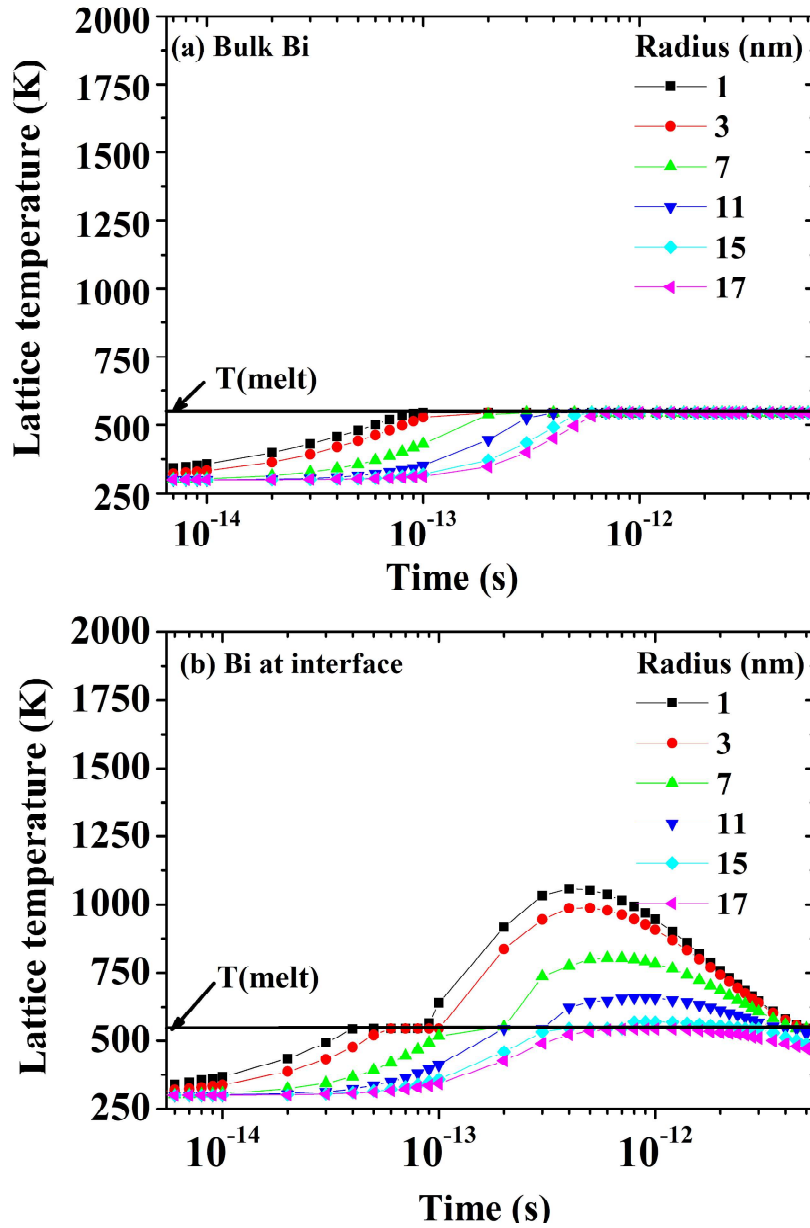
Figure 6.4: An evolution of lattice temperatures as a function of time in the case of Bi bulk (a) and Bi at interface (b) in the case of 100 MeV Au ion irradiation.

Ni. According to Kraft *et al.* [18] and Schattat *et al.* [19], Ni is insensitive to the swift heavy ions below certain value of S_e, which is known as threshold electronic energy loss S_{eth} [20]. The value of S_e for 100 MeV Au ions in Ni is 32.45 keV/nm and value of S_{eth} is 77 keV/nm according to Kraft *et al.* [18], where the value of S_e is sufficiently less compared to S_{eth}.

As mentioned in the previous section that the maximum energy per atom is the direct mea-
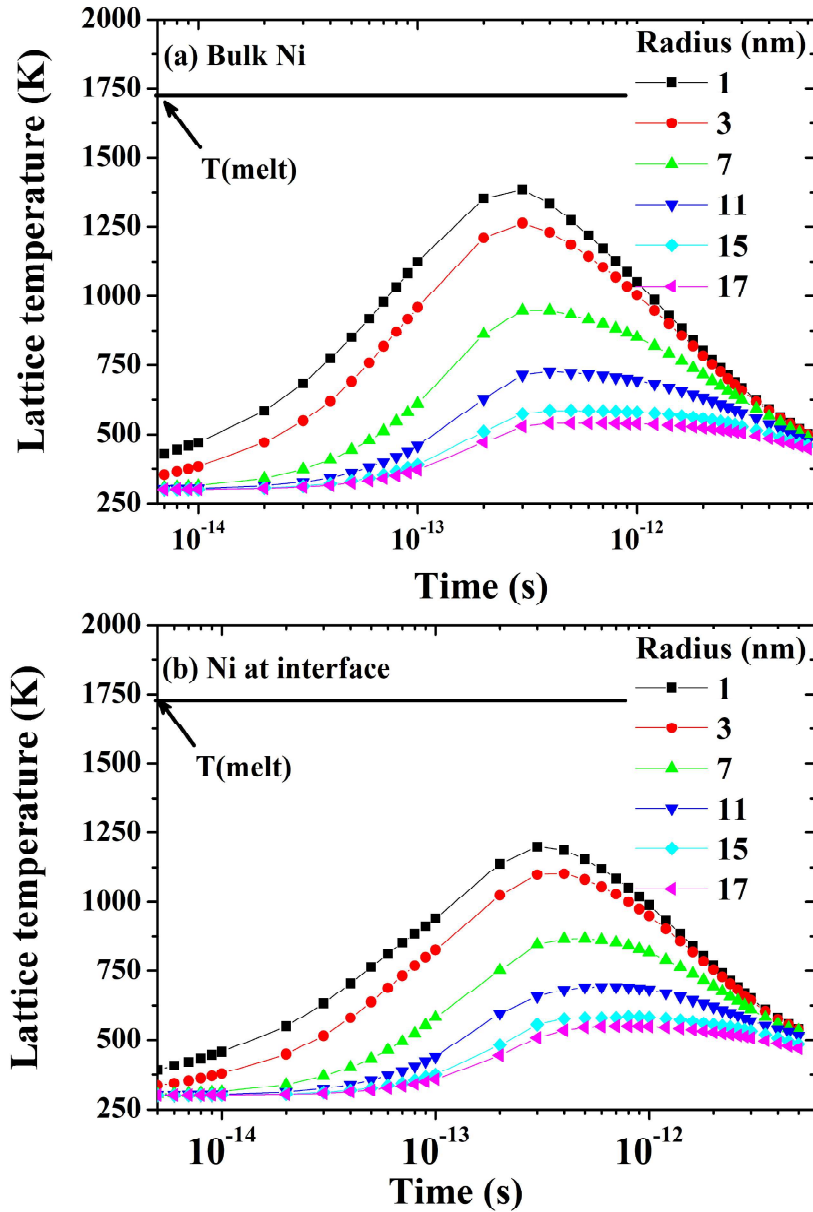
Figure 6.5: An evolution of lattice temperatures for Ni bulk and Ni at interface as a function of time, due to 100 MeV Au ion irradiation.

sure to confirm if the material reaches molten phase or not. The variation of maximum energy per atom at the interface of Ni and Bi, due to 100 MeV Au ions, for different radial distances are shown in the figure 6.6. It may be noticed that the maximum energy per atom (E_{am}) for the Bi layer in the present case is marginally less compared to the required E_m value. However, it reaches more than the value of E_m at the interface. On the other hand, these values

Table 6.2: Various parameters used in the current TSM calculations [20]

Parameter	Ni	Bi
e^--phonon coupling (g)	$1\times10^{12}\ W.cm^3\ K^{-1}$	$1.35\times10^{11}\ W.cm^3\ K^{-1}$
Electronic diffusivity D_e at 300 K	$150\ cm^2$/s	$38\ cm^2$/s
Electronic energy loss	$32.4\ keV/nm$	$17.6\ keV/nm$
Melting temperature	$1726\ K$	$544\ K$
Latent heat of fusion	$297\ J/g$	$54\ J/g$
Boiling temperature	$3003\ K$	$1837\ K$
Latent heat of boiling	$6309\ J/g$	$491\ J/g$
Solid density	$8.9\ g/cm^3$	$9.81\ g/cm^3$
Liquid density	$7.9\ g/cm^3$	$10.02\ g/cm^3$

corresponding to Ni layer in the present case are much less than the required E_m values of Ni, which suggests that the Ni layer does not reach molten phase. It may be mentioned here that the experimentally observed mixing due to 100 MeV Au ions was $\approx 15\%$ of total thickness of the deposited films. The observed mixing is limited, which is due to the insensitive nature of Ni at this energy regime. Although one of the layers (Ni) does not reach molten phase, there is a finite mixing, which can be understood as the following. The ion induced lattice temperatures are almost 1000 K, at which both Bi and NiBi$_3$ reaches the molten phase certainly. Since the Ni is in constant contact with the molten Bi and NiBi$_3$, athermal effects are expected to drive the mixing. Another possibility which cannot be ruled out is that the ballistic effects [22] that are driven by nuclear energy loss (though less in quantity). Therefore the mixing observed in the present case can be attributed to the combination of both athermal (driven by molten Bi and NiBi$_3$ phases) and ballistic (caused by nuclear energy loss) effects [20].

Effect of 100 MeV Au ions on Ni/Bi five bilayer films:

In the TSM calculations, the parameters, specific heat (C) and thermal conductivity(κ) were obtained from the experimental work of Wang *et al.* [3] for Ni and Dufour *et al.* [10] for Bi respectively. The value of electron-phonon coupling constant (g) at 300 K for Ni were found to be $1.0 \times 10^{12}\ Wcm^{-3}K^{-1}$, from defect annealing [6] and in the case of Bi, it is $1.35 \times 10^{11}\ Wcm^{-3}K^{-1}$, from damage efficiency measurements [6]. The parameters C, κ
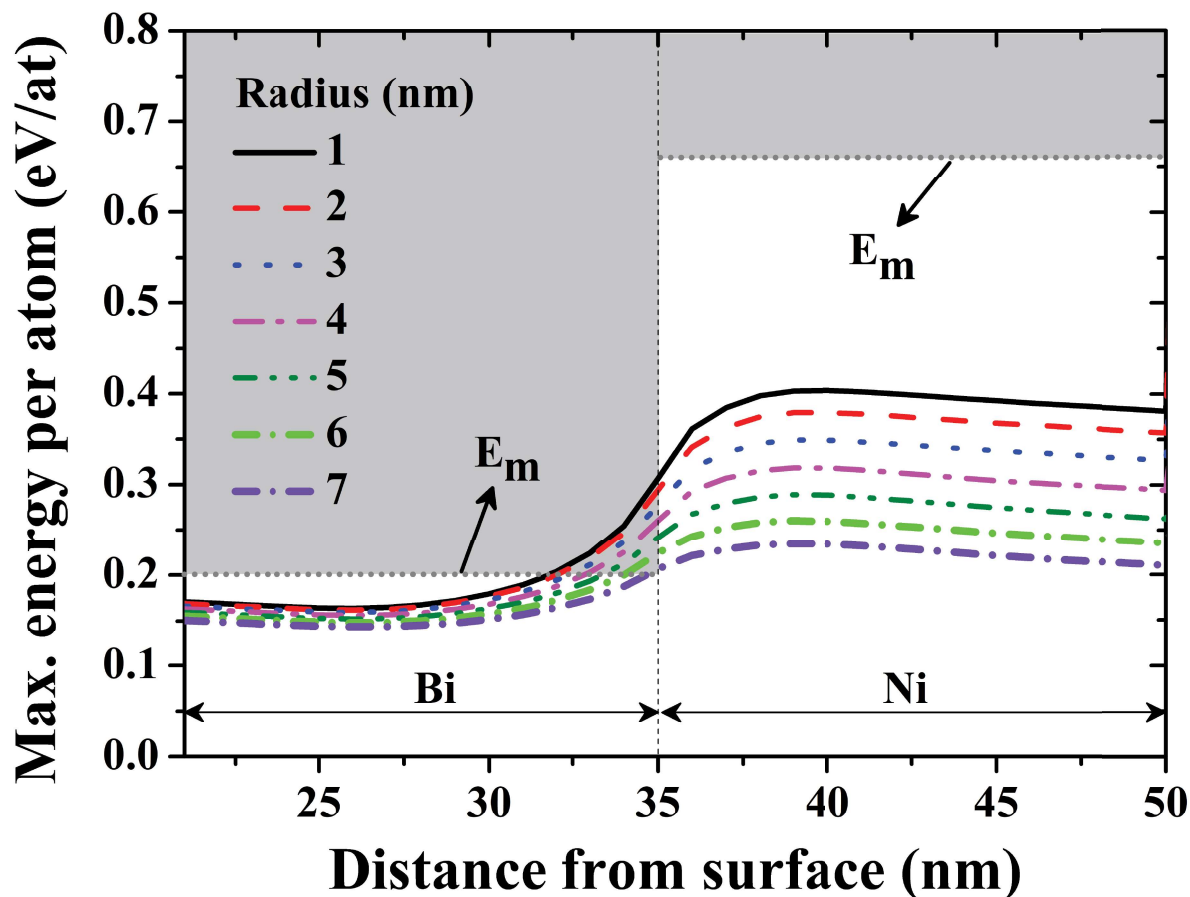
Figure 6.6: Maximum energy per atom due to 100 MeV Au ions as a function of distance from the surface in Ni/Bi bilayers.

and g for the substrate (Si) were as same as the values used in a report by Chettah *et al.* [21]. The estimated lattice temperatures due to 100 MeV Au ion irradiation on Ni/Bi five bilayers are shown in figure 6.7. To show clearly, the lattice temperature evolution at different radial distances from the ion path for the intermediate Bi/Ni/Bi layers are shown in this figure. The horizontal dashed lines at 544 K and 1726 K are drawn to emphasize the melting temperatures of Bi and Ni respectively. The vertical dashed lines represent two different interfaces of Ni and Bi. It is evident from the figure that the lattice temperatures corresponding to both the Bi layers reach more than the melting temperature of Bi with the radial distances of ≈9 nm. While in the case of Ni, the lattice temperatures reach around 1500 K, which is much lesser than the melting point of Ni. However, the temperatures are more than 1000 K with the radial distances of around 7 nm. However, the ion-induced mixing due to 100 MeV Au ion irradiation was observed experimentally in this case (as discussed in chapter 3). The evolution of such large
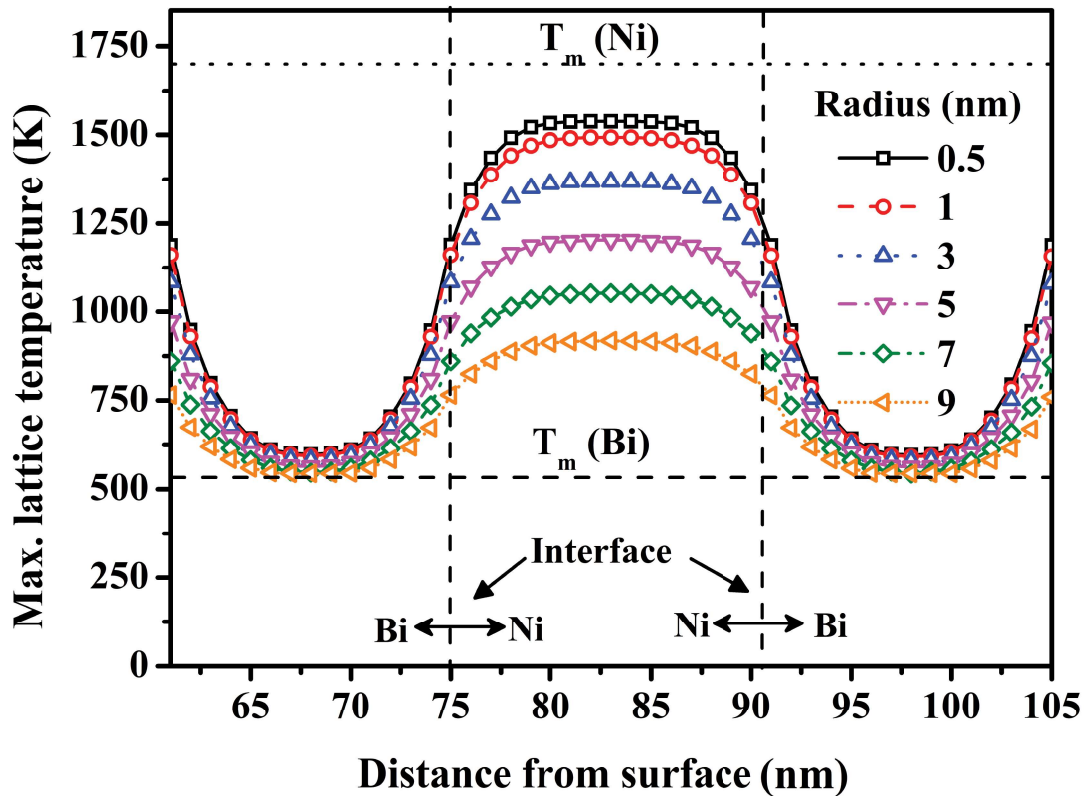
Figure 6.7: Maximum lattice temperatures as a function of distance from surface in five bilayer Ni/Bi films due to 100 MeV Au ion irradiation.

temperatures can play a role in the observed mixing from the depth profiles obtained from RBS spectra (in chapter 3). According to Gupta *et al.* [23], such mixing at the interface is expected to take place even if the lattice temperatures of one layer remain below its melting temperature in one side of the interface and the adjacent layer being in the melting temperature regime. This can be understood as the sufficiently higher temperatures above melting point on one side may contribute to the rise in lattice temperatures of the layer on the other side of the interface. Another possible reason, which cannot be ruled out, for the enhanced mixing is due to the S_n induced ballistic effects. However, the contribution of ballistic effects are believed to be less as the magnitude of S_n is small in this case. Furthermore, the lattice temperatures in both the layers are more than the melting points of Bi, $NiBi_3$ and NiBi phases. Since the observed temperatures are sufficiently higher than the melting temperatures of Bi, NiBi, and $NiBi_3$ phases. These phases above melting point are also expected to accelerate the diffusion-reaction process and hence lead to cause the observed mixing. Therefore, The observed enhancement in the mixing can be attributed to the above-mentioned possibilities.

Effect of 120 MeV Au ions on Ni/Bi five bilayer films:

Figure 6.8: Maximum lattice temperature evolution of the multilayers during the irradiation by 120 MeV Au ions as a function of depth from the surface for different radial distances. (a). Bi/Ni/Bi near the surface and (b). Bi/Ni/Bi intermediate. The horizontal solid lines show the T_m of Ni and Bi. The vertical dashed lines specify the interfaces between Bi and Ni.

The thermal spike model calculations were extended to multilayers [3,5–9] has been applied to the present system. The evolution of maximum lattice temperatures due to 120 MeV Au ions in the surface Bi/Ni/Bi layers and intermediate Bi/Ni/Bi layers corresponding to 5 bilayer Ni/Bi films are shown in figure 6.8(a) and (b) respectively. The parameters used in the calculations for both Ni and Bi were taken as mentioned in the table 6.2 [20]. It may be observed in figure 6.8(a) that the lattice temperatures of the Bi layers have reached more than the melting point

of Bi. There is a noticeable difference in the evolution of temperature in the top Bi layer and the next Bi layer from the surface. This is due to the top Bi layer (lower lattice temperatures) has only one interface with Ni layer (higher lattice temperatures) and the second Bi layer is being sandwiched between two Ni layers. While, the temperatures of Ni layer reaches almost its melting temperature, which is relatively high compared to the temperatures in the case of 100 MeV Au ions. This sandwiching effect of Bi layers between two Ni layers in the case of middle layers is much apparent from figure 6.8(b).

Figure 6.9: Maximum energy per atom evolution of the multilayer during the irradiation by 120 MeV Au ions as a function of distance from the surface for different radial distances. The horizontal solid lines show the E_m of Ni and Bi. The vertical dashed lines specify the interfaces between Bi and Ni. The calculation was performed with $g(Bi) = 1.35 \times 10^{11} \mathrm{Wcm^{-3}K^{-1}}$ and $D_e(300\ \mathrm{K}) = 38\ \mathrm{cm^2 s^{-1}}$.

The evolution of maximum energy per atom in the top three (Bi/Ni/Bi) layers out of 5 bilayers is shown in figure 6.9. The horizontal solid lines indicate the melting points of Ni and Bi in each layer. In the vicinity of both the interfaces, the temperature along the ion track in Bi layer goes beyond its melting point with the radius of around 10 nm. In the case of Ni, the observed value of maximum energy per atom is less than its melting point. However, this value

129

is more than twice compared to the ones observed in Bi layers. Due to the high gradient at the interface, the heat energy flows from Ni to Bi, which leads to the observed rise in temperature near the interface. Since the lattice temperature of Ni layer is below its melting point, the experimentally (RBS) observed enhancement in the mixing may not be interpreted as the ion beam mixing in the molten phases of Ni and Bi. Nevertheless, the mixing is believed to be enhanced due to the high temperature of Ni in contact with a large area of molten Bi ($\pi R^2 \approx$ 300 nm^2). Gupta *et al.* [23], have reported a similar case on mixing, where the mixing has been shown to be due to the much higher temperature of a layer above T_m on one side, which may enhance the temperature of the layer on the other side of the interface. In a previous study on the similar system [20], a spontaneous formation of the NiBi$_3$ compound during deposition and an enhancement in the thickness of NiBi$_3$ layer after 100 MeV Au ion irradiation was reported. In the case of 120 MeV Au ions, higher energy is deposited on electrons resulting in higher temperatures in both Ni and Bi at the interface. Though calculations did not include the existence of NiBi and NiBi$_3$ phases due to the lack of data, the high temperature generated along the ion path is expected to enhance the interdiffusion through the intermediate NiBi$_3$ phase resulting in the widening of the NiBi$_3$ thickness.

From figure 6.9, one may also notice that a thin layer of Bi ($\approx$ 8 nm thickness) at the surface of the multilayer does not undergo melting despite it reaching melting temperature. In this region, the energy transfer per atom ($\approx$0.17 eV/at) is slightly lower than E_m (0.2 eV/at). It is well known that the thermal behaviour of nanosized layers is different from the one observed in bulk material. It was shown that the nanometric layers or nanoparticles exhibit melting point depression. Such depression in the melting point of Bi was observed by Kusz *et al.* [24] from 544 to 387 K for nanosized Bi particles when these are embedded in silicate glass and to 502 K. In another work, Jiang *et al.* [25] have introduced a simple model supported by the experimental results to explain the melting behavior of low-dimensional crystals. They have shown that, in general, the melting temperature depression becomes significant when the layer thickness is lower than 20 nm. In our case, the thicknesses of Bi and Ni layers are of 15 nm each, therefore, one may expect melting to occur at lower temperatures. This means that the melting must be occurring at lesser values of E_m, i.e., $E_m < 0.2$ eV/at and $E_m < 0.66$ eV/at for Bi and Ni respectively. Based on this, it is safe to consider that the Bi is in molten phase locally at the surface of the multilayers after irradiation with 120 MeV Au ions, which can be noticed from the SEM images.
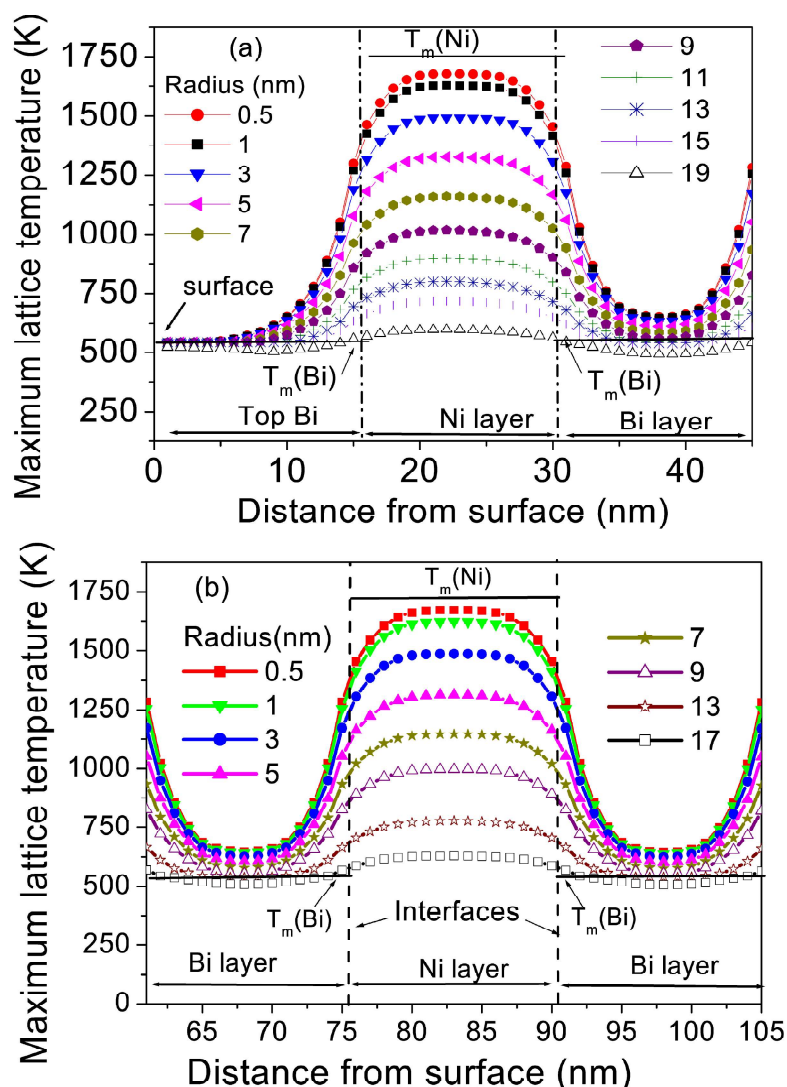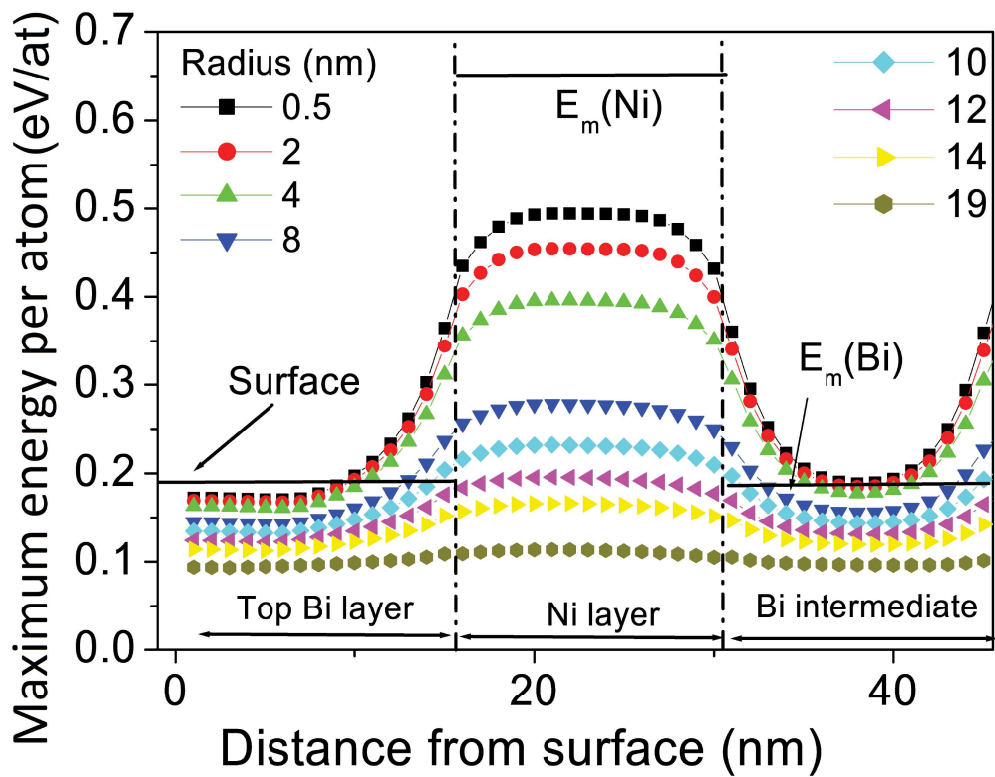
130
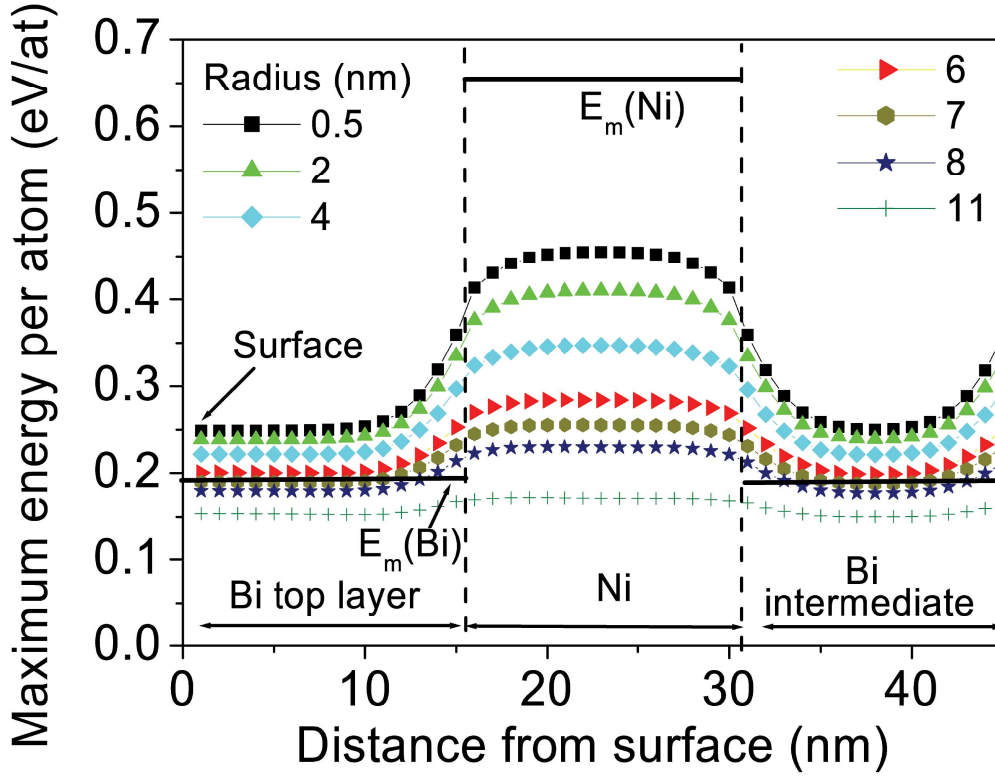
Figure 6.10: Maximum energy per atom evolution of the multilayer during the irradiation by 120 MeV Au ions as a function of distance from the surface for different radial distances. The horizontal solid lines show the E_m of Ni and Bi. The vertical dashed lines specify the interfaces between Bi and Ni. The calculation was performed with $g(\text{Bi}) = 4 \times 10^{11} \text{Wcm}^{-3}\text{K}^{-1}$ and $D_e(300 \text{ K}) = 150 \text{ cm}^2\text{s}^{-1}$.

The previous parameters for Bi target were proposed by Dufour *et al.* [10], which were further updated by the same group with a new set of variables [11]. The newly reported parameters were $g = 4 \times 10^{11} \text{ Wcm}^{-3}\text{K}^{-1}$ and $D_e = 150 \text{ cm}^2\text{s}^{-1}$. The values of maximum energy transfer(E_{am}) for Bi were found to reach higher values in the calculations using the updated parameters as shown in figure 6.10 compared to the previous ones (figure 6.9). In the present case, the value of E_{am} in the Bi throughout the layer, not only at the interface, reaches more than the melting point with the latent track radius $\approx$ 8 nm. Therefore, the cross-section of individual molten tracks in Bi is quite large and with increasing ion fluences there is a high possibility for these molten tracks to be overlapped. These features can be noticed in the SEM images that the samples irradiated at lower fluences have less molten regions while at higher fluences, such molten phase regions increase (Chapter-3). Furthermore, these melting features can be realized in the depth profiles obtained from RBS spectra. The enhancement in the mixing due to these
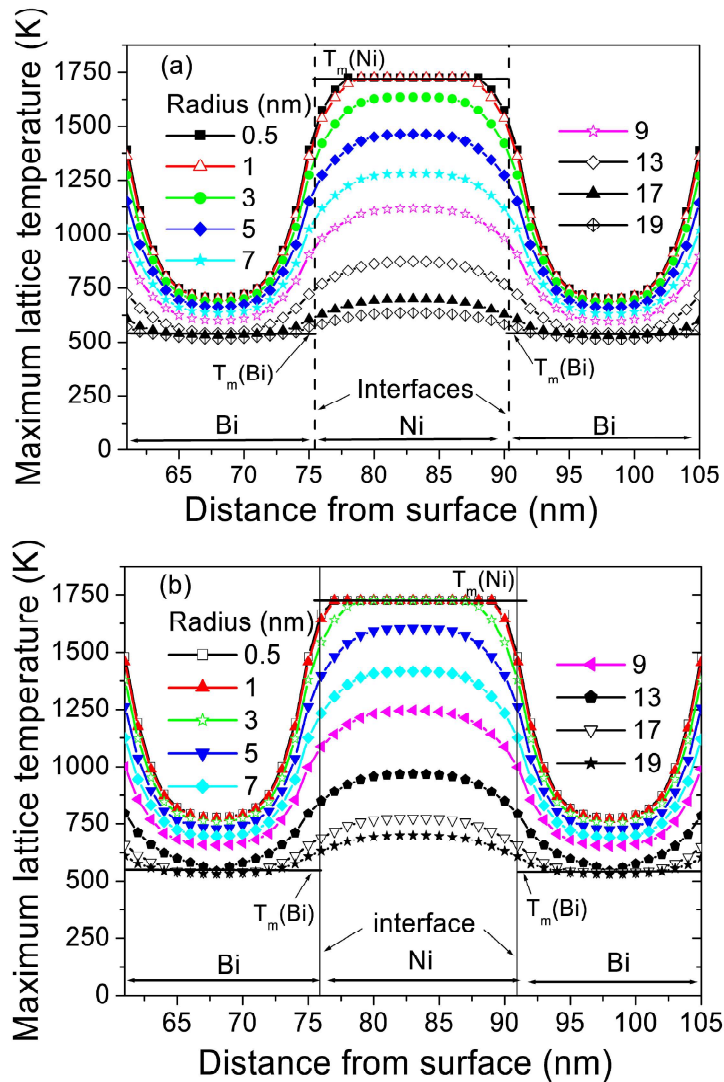
Figure 6.11: Maximum lattice temperature evolution of the multilayers during the irradiation by (a) 150 MeV and (b) 200 MeV Au ions as a function of depth from the surface for different radial distances. The horizontal solid lines show the T_m of Ni and Bi. The vertical dashed lines specify the interfaces between Bi and Ni.

120 MeV Au ions was found to be 88.6% of the total thickness of the films.

Effect of 150 and 200 MeV Au ions on Ni/Bi five bilayer films:

The calculations at higher energy regimes have been performed to predict the melting possibility of Ni and Bi layers, as the present energy was not sufficient to drive the Ni layer to melting phase. The calculations were performed at 150 MeV and 200 MeV Au ions for the same configuration of the samples. According to these calculations, higher mixing rates are expected for

these higher energies as shown in figure 6.11. It is interesting to note that the lattice tempera-
ture of Ni goes to its melting point, in the case of 150 MeV Au ions, till a track radius of 1 nm.
After increasing the ion energy to 200 MeV, the molten track radius increases to almost 3 nm.
Therefore, It can be inferred from these calculations that increasing the ion beam energy up to
200 MeV can lead to the melting of both Bi and Ni materials. Consequently, the mixing rates
in molten phases are expected to be more pronounced as compared to the observed mixing in
100 MeV [20] and 120 MeV Au ions. These experiments will be performed in near future, to
study the mixing features experimentally.

6.3.2   Effect of medium energy ions on Ni and Ni/Bi films
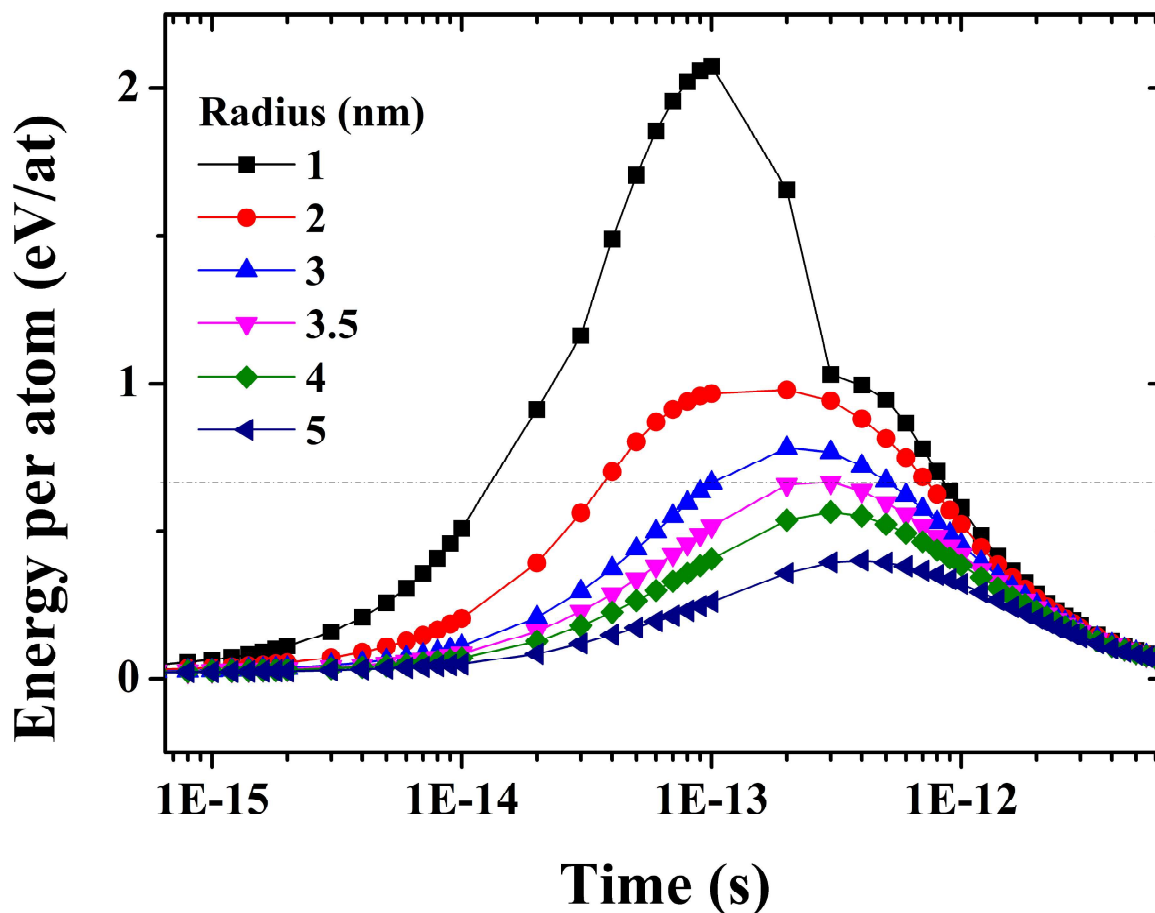
Figure 6.12: Maximum energy per atom as a function of time for different latent track radii in
Ni film irradiated using 2.2 MeV Au ions.

It can be inferred from the previous section that the Ni is insensitive to the ion beams in
the SHI regime below a threshold value (S_{eth}). Therefore, it is essential to confirm whether

the Ni is sensitive to the medium energy ions or not, before performing the ion beam mixing of Ni-Bi system. In chapter-4, the sensitivity study of Ni has been confirmed experimentally using medium energy ions [26]. The thermal spike model calculations corresponding to Ni at the interface using 2.2 MeV Au ions is shown in figure 6.12, where the energy per atom has been plotted against time for different latent track radii. A horizontal dashed line is drawn to emphasize the value of energy per atom required to drive the Ni into molten phase, which is 0.66 eV/at for Ni. It may be noticed that the Ni layer reaches molten phase with the latent track radii more than 3 nm. The latent track remains in molten phase within the duration of 1×10^{-14} to 1×10^{-12} seconds, depending on the track radii. This is the direct evidence that the Ni does reach molten phase and is sensitive to the present energy regime, which is also in good agreement with the experimental findings. Thus, the study of IBM of Ni-Bi system at the medium energy regime is expected to show the sufficient mixing (discussed below).
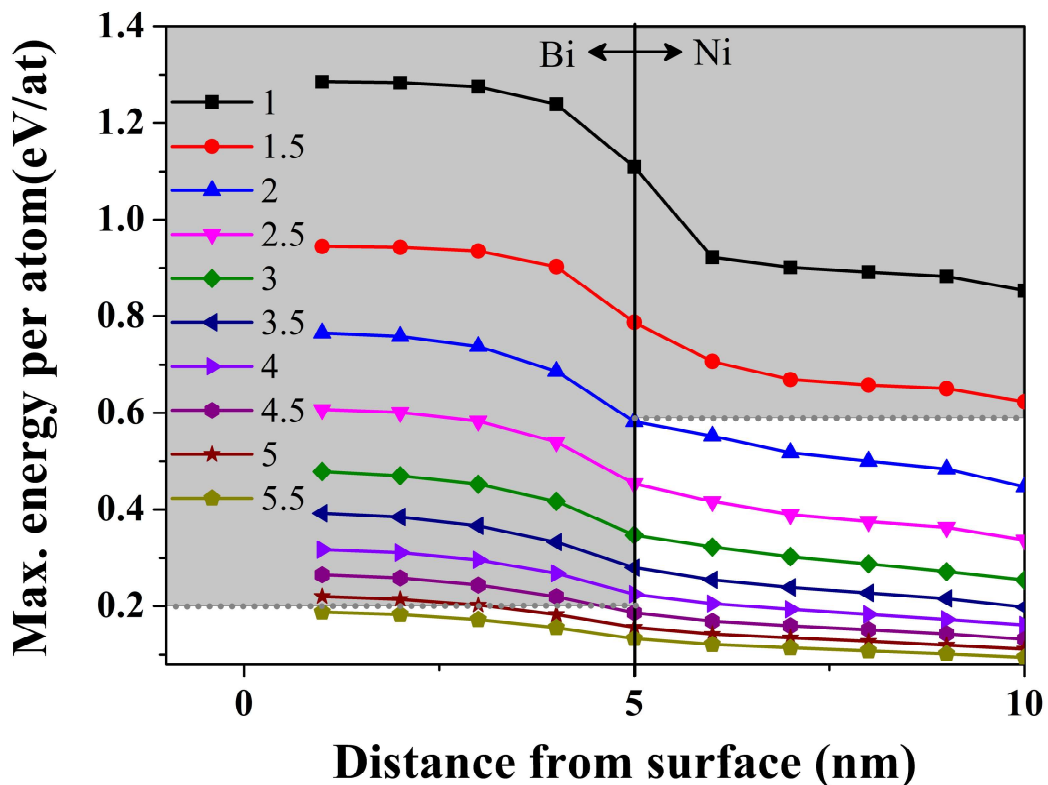
Figure 6.13: Evolution of the maximum energy per atom in Ni/Bi bilayers due to 1 MeV Ni ions.

In the case of 1 MeV Ni ions, the maximum energy transfer per atom for both Ni and Bi in Ni/Bi bilayer films are shown in figure 6.13. The molten phase of the layers are indicated

134

by the grey coloured back ground. Interestingly, both the layers of Ni and Bi are noticed to reach molten phase. It may be noticed that the Ni ions of 1 MeV energy are capable of driving the Bi layer into molten phase with the latent track radii of almost 4.5 nm around the ion path. The Ni layer was also seen to reach molten phase at this energy regime. However, the latent track radius, in this case, is approximately 1.2 nm. The experimentally observed mixing due to 1 MeV Ni ions is nearly 60% of total thickness of the films. Such enhancement in the mixing is due to the presence of both Ni and Bi in the molten phase at this regime. Since both the materials reached their melting temperatures, it becomes relatively easy for the Ni and Bi atoms to mix with each other at the interface. Therefore, the mixing in the present case can be attributed to the thermal spike effect in Ni and Bi driven by 1 MeV Ni ions.

6.3.3 Effect of low energy ions on Ni-Bi bilayers
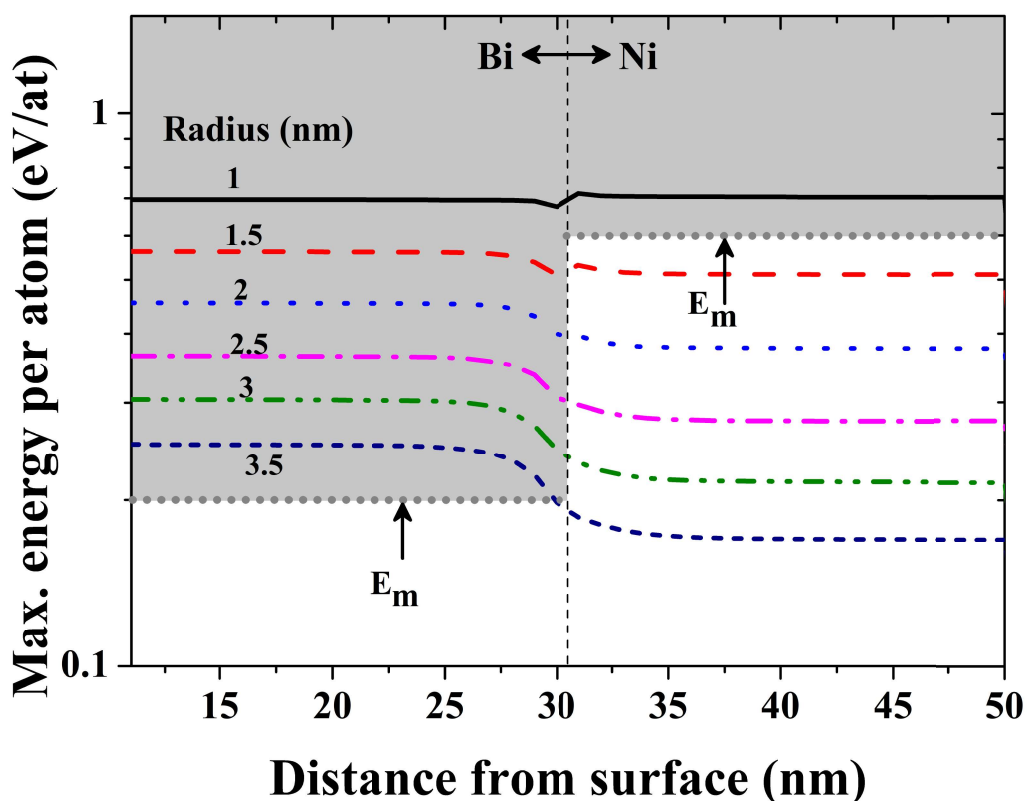
Figure 6.14: Evolution of maximum energy per atom in the case of 200 keV Ar irradiated Ni/Bi bilayers.

It was observed from the previous sections that the ion-induced mixing of Ni and Bi can be achieved by swift heavy ions and medium energy ions to certain extent. In this section, the

effect of low energy ions on Ni/Bi films is discussed. The evolution of maximum energy per atom as a function of distance from the surface in the case of 200 keV Ar ions are shown in figure 6.14. The grey colour back ground indicates the ion-induced molten phases of the layers. It may be observed that the Ar ions of 200 keV energy have driven the Bi into molten phase with > 3 nm latent track radii. Moreover, the Ni layer reaches molten phase along the latent track radii of ≈1 nm. The atoms at the interface of Ni and Bi along this molten track becomes mobile and mixing of the Ni and Bi atoms takes place. The observed mixing due to 200 keV Ar ions was almost 25% of total thickness of the films (as explained in chapter-5). The enhanced mixing in the present case can be attributed to the combination of low energy ion-induced thermal spike and ballistic effects [27]. The mixing in the present case is less compared to the mixing at medium energy regime (as explained above). This is due to relatively less radii of latent tracks in the case of both Ni and Bi layers.

6.4   Discussion

A schematic model has been shown in figure 6.15, based on the results of thermal spike model calculations. This figure describes the ion-induced latent track formation, which has been emphasized in red coloured cylinders at different energy regimes in both the Ni and Bi layers. In the case of swift heavy ions, these latent tracks are shown for 100, 120, 150 and 200 MeV Au ions. Whereas in the case of medium and low energy, the ion tracks are shown for 1 MeV Ni and 200 keV Ar ions. The radii of latent tracks in Ni are approximately 0 nm, 0 nm, 1 nm, and 3 nm for the case of 100, 120, 150, and 200 MeV Au ions respectively, while for the case of Bi, the radii were found approximately to be 9 nm, 13 nm, 17 nm, and 19 nm respectively. In the case of medium energy (1 MeV Ni ions), the radii of latent track in Ni and Bi were found to be approximately 1.7 nm and 4.5 nm respectively. The latent track radii for low energy (200 keV Ar) ions were observed to be ≈1.1 nm and ≈3.5 nm respectively.

The ion-induced enhanced mixing compared to the total thickness of the as-deposited films has been considered as the mixing percentages, which are shown in figure 6.16 for different energy regimes. These ion-induced mixing percentages in Ni/Bi single bilayers are ≈25%, ≈60%, and ≈15% for the 200 keV Ar ions, 1 MeV Ni ions, and 100 MeV Au ions respectively. The better mixing in the case of 1 MeV Ni ions compared to that of 100 MeV Au ions is due to the reaching of both Ni and Bi to molten phase instead of only one (Bi) layer reaching
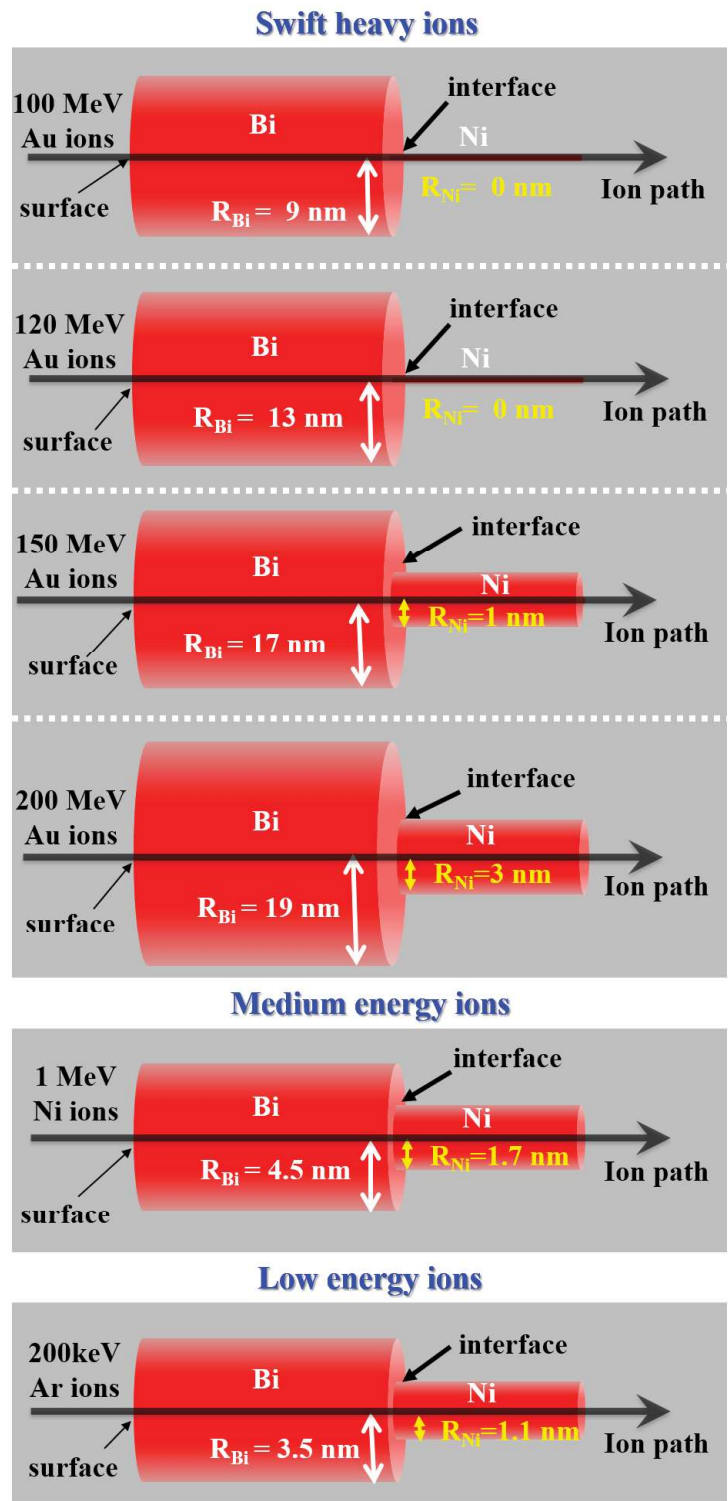
Figure 6.15: Schematic representation of formation of ion tracks at different energy regimes in both Ni and Bi layers.

molten phase. Both the layers across the interface reaching to molten phase is more effective for mixing as the atoms at the interface become more mobile compared to only one layer being in molten phase. Furthermore, the mixing percentage in the medium energy (1 MeV) regime is also more over the low energy (200 keV) regime. In fact, the mixing in the medium energy regime is more compared to the low and swift heavy ion energy regime, which is due to the fact that the latent track radii are more in both the Ni and Bi layers in the case of medium energy ions. Medium energy regime is the one, where both the electronic and nuclear energy losses are comparable in magnitude, whereas in the other cases one dominates over the other. Therefore, the observed more mixing at the medium energy regime can be attributed to the synergistic effects of both the electronic and nuclear energy losses.
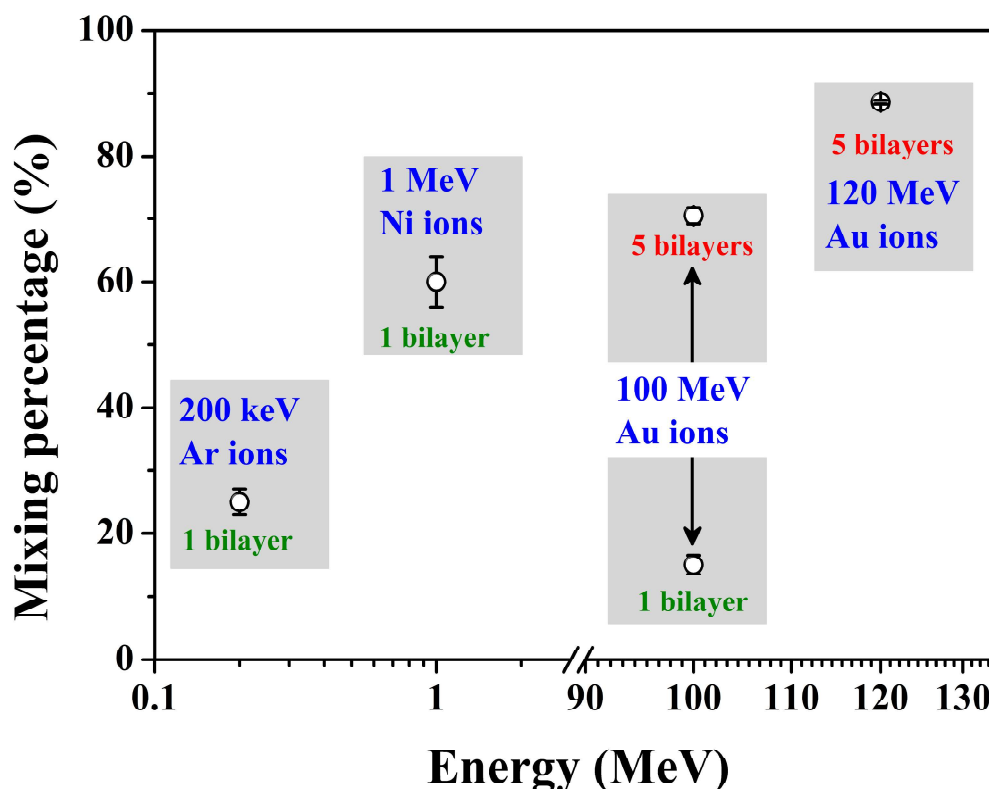
Figure 6.16: ion-induced mixing percentages compared to the total thickness of the films as a function of energy of ions.

Further, the experiments on ion beam mixing was carried out using 100 MeV Au ions, but by increasing the number of bilayers from one to five. In this case, the ion-induced mixing was found to be 69.7%, which is more than 4 times compared to single bilayer films. The more number of interfaces and thinner films of Ni and Bi, in this case, are the potential reasons

for such an enhancement. More interestingly, upon increasing the energy of Au ions to 120 MeV on the similar five bilayer samples, the mixing was found to be $\approx$88.6%. In the case of 120 MeV energy, both the energy per atom and the radius of ion track in Bi goes much higher compared to the other cases. These factors must have been the additional reasons to observe the highest mixing compared to the other cases.

6.5 Conclusion:

In this chapter, the details of the thermal spike model and importance of various parameters have been discussed. Thereafter, the experimentally observed ion-induced effects at different energy regimes have been explained on the basis of the TSM calculations. These calculation results were of sufficient help in understanding the experimental findings (discussed in chapter 3, 4, and 5). In the case of 100 MeV Au ions, it has been observed that the value of energy per atom of Bi reaches more than its melting point with almost 9 nm latent track radius, whereas the value that of Ni reach lesser value compared to its melting point. Therefore, the observed mixing has been assigned mostly to the athermal effects and partially to the ballistic effects. In the case of medium energy ions, both the Bi and Ni layers reach more than their melting temperatures with the latent tracks of radii 4.5 nm and 1.7 nm respectively. Hence, in this energy regime, the thermal spikes in Ni and Bi layers driven by 1 MeV Ni ions are believed to be responsible for the enhanced mixing. Similarly, in the case of low energy ions also, both the Bi and Ni layers were noticed to reach more than their melting temperatures with radii of latent tracks, 3.5 nm and 1.1 nm respectively. In addition to this, S_n induced ballistic effects are also expected to play sufficient role in the mixing. Therefore, the enhanced mixing at this energy regime has been attributed to the thermal spike effects as well as ballistic effects. While comparing the mixing features at different energy regimes, the medium energy ions have shown a maximum of 60% mixing due to irradiation. The higher mixing at the medium energy ions has been attributed the synergistic effects of both the electronic and nuclear energy losses as they are comparable at this energy regime. The lower mixing at the low and swift high ion regime has been attributed to dominant S_n over S_e and S_e over S_n respectively. Furthermore, the effect of increasing number of bilayers from one to five, by using 100 MeV Au ions has been studied. The mixing was observed to be almost 69.7%, which is a higher value compared to the previous cases, where the relatively more mixing has been attributed to more number

of interfaces and lesser thickness of the films. The effect of 120 MeV Au ions on five bilayer Ni/Bi films was further studied and the ion-induced mixing was turned out to be 88.6%. This is the highest mixing compared all the energy regimes and the additional factor for such an enhancement has been assigned to the increment in the ion track radii. Therefore, in order to have efficient mixing it is preferable to have more number of bilayers, lesser thick films at the appropriate energy regime. Further calculations of thermal spike model at higher energy regimes (150 and 200 MeV Au ions) suggest the chance of achieving more mixing of the Ni/Bi films.

Bibliography

[1] P. Sigmund and C. Claussen, J. Appl. Phys. 52, 990 (1981).

[2] A. Meftah, J. M. Costantini, N. Khalfaoui, S. Boudjadar, J. P. Stoquert, F. Studer, and M. Toulemonde, Nucl. Instrum. Methods Phys. Res. B 237, 563 (2005).

[3] Z. G. Wang, C. Dufour, E. Paumier, and M. Toulemonde, J. Phys.: Condens Matter 6, 6733 (1994).

[4] M. Toulemonde, W. J. Weber, G. Li, V. Shutthanandan, P. Kluth, T. Yang, Y. Wang, and Y. Zhang, Phys. Rev. B, 83, 054106 (2011).

[5] Z. G. Wang, C. Dufour, E. Paumier, and M. Toulemonde, J. Phys.: Condens. Matter, 7, 2525 (1995).

[6] C. Dufour, Z. G. Wang, E. Paumier, and M. Toulemonde, Bull. Mater. Sci., 22, 671 (1999).

[7] A. Chettah, Z. G. Wang, M. Kac, H. Kucal, A. Meftah, and M. Toulemonde, Nucl. Instrum. Methods Phys. Res., Sect. B, 245, 150 (2006).

[8] M. Toulemonde, C. Dufour, and E. Paumier, Phys. Rev. B, 46, 14362 (1992).

[9] M. Toulemonde, C. Dufour, Z. G. Wang, and E. Paumier, Nucl. Instrum. Methods Phys. Res., Sect. B, 112, 26 (1996).

[10] C. Dufour, A. Audouard, F. Beuneu, J. Dural, J. P. Girard, A. Hairie, M. Levalois, E. Paumier, and M. Toulemonde, J. Phys.: Condens. Matter, 5, 4573 (1993).

[11] C. Dufour, F. Beuneu, E. Paumier, and M. Toulemonde, Europhys. Lett., 45(5), 585 (1999).

[12] Z. G. Wang, C. Dufour, S. Euphrasie, and M. Toulemonde, Nucl. Instrum. Methods Phys. Res., Sect. B, 209, 194 (2003).

[13] C. Dufour, E. L. de chezelles, V. Delignon, M. Toulemonde, and E. Paumier, Modifications induced by irradiation in glasses ed. P Massoldi (Amsterdam: North-Holland) p. 61 (1992).

[14] M. P. R. Waligorski, R. N. Hamm, and R. Katz, Nucl. Tracks Radiat. Meas. 11, 309 (1986).

[15] H. D. Mieskes, W. Assmann, F. Grner, H. Kucal, Z. G. Wang, and M. Toulemonde, Phys. Rev. B 67, 155414 (2003).

[16] Z. Lin, L. V. Zhigilei, and V. Celli, Phys. Rev. B 77, 075133 (2008).

[17] M. I. Kaganov, I. M. Lifshitz, and L. V. Tanatarov, Zh. Eksp. Teor. Fiz. 31, 232 (1956) [Sov. Phys. JETP 4, 173 (1957)].

[18] S. Kraft, B. Schattat, W. Bolse, S. Klaumunzer, F. Harbsmeier, A. Kulinska, and A.Löffl, J. Appl. Phys. 91, 1129 (2002).

[19] B. Schattat and W. Bolse, Nucl. Instrum. Methods Phys. Res., Sect. B, 225, 105 (2004).

[20] V. Siva, A. Chettah, B. Satpati, S. Ojha, D. Kanjilal, and P. K. Sahoo, RSC Adv., 6, 58950 (2016).

[21] A. Chettah, H. Kucal, Z. G. Wang, M. Kac, A. Meftah, and M. Toulemonde, Nucl. Instrum. Methods B 267, 2719 (2009).

[22] D. K. Avasthi and G. K. Mehta, Springer Series in Material Science, 145, Springer Science and Business Media, (2011).

[23] A. Gupta, R. S. Chauhan, D. C. Agarwal, S. Kumar, S. A. Khan, S. Mohapatra, A. Tripathi, and T. Som, Rad. Eff. Def. Solids 166, 689 (2011).

[24] B. Kusz, K. Trzebiatowski, M. Gazda, and L. Murawski, J. Non-Crystal. Solids 328, 137 (2003).

[25] Q. Jiang , H. Y. Tong , D. T. Hsu , K. Okuyama, and F. G. Shi, Thin Solid Films, 312, 357 (1998).

[26] V. Siva, D. P. Datta, A. Singh, T. Som, and P. K. Sahoo, Appl. Surf. Sci. 360, 276 (2016).

[27] V. Siva, D. P. Datta, S. Chatterjee, S. Varma, D. Kanjilal, and P. K. Sahoo, Appl. Surf. Sci. 410, 519 (2017).

Chapter 7

Summary and future scope

7.1 Summary

In this thesis, the effect of ion beams on Ni/Bi films has been investigated in different energy regimes. Most importantly, the primary focus of the present thesis is to study the phase syntheses of Ni-Bi system using ion beam mixing (IBM) by playing with different parameters including energy of ions, number of bilayers, the thickness of the layers, and irradiation fluence etc. Ion beam mixing has experimentally been investigated, whose theoretical understanding was provided by the thermal spike model calculations. Initially, the ion beam mixing has been introduced along with the fundamentals of the ion-matter interaction. Moreover, different configurations for IBM study have been discussed. Different proposed models to explain the mixing phenomenon have been described along with their applicability depending on the energy of ion beam (low, medium and high energy regimes) and type of materials (like metals, semiconductors or insulators). The advantages of using the ion beam mixing over conventional techniques have also been discussed. In addition, an introduction to the Ni-Bi system has been provided along with its possible applications. The study of phase syntheses of Ni-Bi system by IBM includes the deposition of Ni/Bi films, ion irradiation, and their characterisation. Therefore, the details of these techniques have been discussed briefly. In a nut shell, the employed techniques in the present study such as thermal and e-beam evapourations for depositing the Ni/Bi films have been discussed. The details of various accelerator facilities that are used in irradiating the Ni/Bi films were also discussed. Furthermore, various characterisation and measurement tools have been discussed such as X-ray diffraction, Rutherford backscattering spectrometry, field emission scanning electron microscopy, transmission electron microscopy, atomic force microscopy and physical property measurement system.

144

7.1.1 High energy IBM

Firstly, the IBM study of Ni-Bi (single and five) bilayers using 100 and 120 MeV Au ions in the fluence range of 1×10^{12}-1×10^{14} ions/cm^2 has been performed. Prior to IBM study, a spontaneous formation of NiBi$_3$ grains has been observed in Ni/Bi bilayers during the deposition of the films, which has been explained on the basis of the reaction-diffusion mechanism. This thin NiBi$_3$ interfacial layer was found to play a role in enhancing the mixing after ion irradiation. After irradiation in single bilayer films, an evolution of porous like morphology has been noticed as a function of ion fluence. An enhancement in the mixing due to 100 MeV Au ions has been observed, which is almost 15% of the total thickness of as-deposited Ni/Bi single bilayer films. The enhanced mixing has been attributed to the molten (Bi and NiBi$_3$) phase induced athermal effects (mostly) as well as the ballistic effects (partly). Further, the same study has been performed by increasing the number of bilayers to five and reducing the thickness of the films from 35 nm to 15 nm, where the mixing enhancement was found to be 69.7%. Such an enhancement was attributed to the more number of Ni and Bi interfaces and less thickness of the films. Furthermore, the enhancement in the mixing was found to be 88.6% when the 120 MeV Au ions were used. Another possible reason for the enhancement can be attributed to the increased ion track radii and enhanced lattice temperatures compared to the 100 MeV case. However, the observed mixing in all these energy regimes is not complete, which is due to the insensitive nature of Ni below the threshold electronic energy loss in the swift heavy ion regime. The Ni/Bi bilayers were found to show ferromagnetic and superconducting properties and after 100 MeV Au ion irradiation there was hardly any change in their superconducting properties despite the enhanced irradiation damage. This non-deteriorating behaviour of NiBi$_3$ phase can be useful in heavy radiation conditions such as space.

7.1.2 Medium energy IBM

Prior to the medium energy ion beam mixing of Ni-Bi system, the behaviour of Ni films to the medium energy (2.2 MeV Au) ions has been investigated. After 2.2 MeV Au ion irradiation, the analysis of surface topography and power spectral density using atomic force microscopy has revealed that Ni is sensitive to this energy regime. After that the study of IBM of the Ni-Bi system has been performed using 1 MeV Ni ions as a function of ion fluence (1×10^{15}-1×10^{16} ions/cm^2). The ion-induced mixing was found to be almost 60% of the total thickness of the

as-deposited Ni/Bi single bilayer films, which is nearly 4 times more compared to the mixing in the case of 100 MeV Au ions. Such large mixing in the present case, compared to low and high energy regimes, is due to the collective effects of both nuclear and electronic energy losses (as their magnitudes are comparable at this energy). It is understood that the ion-induced mixing would be much pronouncing in such cases, where S_e and S_n are comparable, than in the case of low and high energy regimes (where one dominates the other), which is known as synergistic effects of electronic and nuclear energy losses.

7.1.3 Low energy IBM

In the case of low energy, the IBM has been investigated using 200 keV Ar ions as a function of ion fluence (5×10^{14}-1×10^{17} ions/cm^2). An evolution of sponge-like surface morphology has been observed upto a fluence of 5×10^{16} ions/cm^2, beyond which the surface becomes smoother. Such evolution of morphology has been ascribed to ion-induced sputtering and it is quite expected in this energy regime, which was confirmed using TRIDYN simulation. The RBS measurements and their analysis of all the samples have revealed the mixing after the irradiation along with the sputtering. The ion-induced mixing was observed to be 25% of the total thickness of the as-deposited samples, which has been attributed to the ion-induced thermal spikes and ballistic effects. In order to compare the IBM study with the conventional annealing process, a thermal annealing study has been performed on Ni/Bi bilayers. In this study, a formation of NiBi$_3$ and NiBi phases after thermal annealing has been observed above the eutectic temperature of Ni-Bi system. Above the peritectic temperature of Ni-Bi system, NiBi$_3$ phase was found to decompose into NiBi and Bi phases. Towards the end, the advantages of IBM over thermal annealing of Ni-Bi system has been discussed. In the case of 200 keV Ar ions at the lower fluences, the Ni/Bi films were found to be hydrophobic in nature, where NiBi$_3$ phase exists on the surface. Interestingly, these films become hydrophilic at the higher fluences as soon as the NiBi$_3$ phase disappears from the surface.

7.1.4 Theoretical understanding of IBM

All the aforementioned experimental facts at different energy regimes have been explained on the basis of thermal spike model calculations. The basic details of this model and various important parameters were also discussed. The TSM calculations were performed at all the energy regimes including high energy (100 MeV Au, 120 MeV Au) ions, medium energy (1

MeV Ni, 2.2 MeV Au) ions, and low energy (200 keV Ar) ions, in which the experiments were carried out. The observed experimental findings were validated using the TSM results. In addition, the TSM calculations were extended to 150 MeV and 200 MeV Au ions to predict the possibility of mixing at the higher energies. These calculations shows the formation of ion track of different radii in both Ni and Bi layers. The mixing features were quantified and explained on the basis of latent track formation around the ion path in all the energy regimes.

7.2 Future scope

The Ni-Bi system is interesting in the fundamental physics point of view, as discussed in previous chapters. For instance, the coexistence of superconductivity and ferromagnetism (CSF) in simple bilayer Ni/Bi films is one of the interesting aspects of this system. Moreover, the stable phases of Ni-Bi system, NiBi and $NiBi_3$, are also important for several reasons. Interestingly, both these phases are superconducting below a transition temperature of 4.25 K (NiBi) and 4.06 K ($NiBi_3$). Moreover, the $NiBi_3$ phase was also reported to exhibit the CSF property as suggested by several reports. On the other hand, the same compound was shown to be non-ferromagnetic by the other research groups. Therefore, the CSF nature of this compound is still under debate. Apart from these interesting fundamental aspects of Ni-Bi system, it also offers certain technological applications such as in galvanizing coatings, lead-free soldering technologies and large magneto-resistance applications. Since, the Ni-Bi system is a potential candidate for both science and technology, it is necessary to explore the phase synthesis using unconventional methods as well, which can offer several added advantages. Once, the complete mixing is accomplished, where the presence of Ni and Bi impurities can be completely avoided. These unconventionally prepared stable phases of Ni and Bi can be utilized in the study of coexistence of superconductivity and ferromagnetism, and also applied in the aforementioned technological applications.

We could accomplish a maximum mixing of 88.6% by using 120 MeV Au ions in Ni/Bi five bilayers through ion beam mixing. The observed mixing was more effective in the case of medium energy ions, which is $\approx 60\%$ in the single bilayer films itself. The mixing is expected to be considerably enhanced in the case of more number of bilayers at this energy regime. There are certain other aspects that one can look at, in order to achieve more mixing using the ion beam mixing.

- One of them could be supplying temperature to the films during ion irradiation. Through this process, the diffusion of atoms at the interface of Ni and Bi may get accelerated and thereby better mixing can be achieved.

- Another possibility of enhancing mixing is the post-annealing method, where the ex-situ thermal annealing is performed after the irradiation.

- As per the TSM calculations corresponding to 150 and 200 MeV Au ions, the ion track radius and lattice temperatures were found to reach sufficiently higher values. In such case, the complete mixing of Ni-Bi system can be anticipated, which needs to investigated experimentally.

- If both the Ni and Bi layers are thin enough, the spontaneously formed thin $NiBi_3$ layer (with thickness less than the coherence length) does not show the superconducting property. In such multilayer films, a masking based ion beam mixing can induce an array of superconducting (or CSF) and non-superconducting patterns. This is another interesting future scope of the present study, which can find their potential applications in spintronic devices.

Journal Publications and Conference Proceedings

[†]**1. V. Siva**, K. Senapati, B. Satpati, S. Prusty, D. K. Avasthi, D. Kanjilal, P. K. Sahoo, Spontaneous formation of superconducting $NiBi_3$ phase in Ni-Bi bilayer films, J. Appl. Phys. 117,083902 (2015).

[†]**2. V. Siva**, D. P. Datta, A. Singh, T. Som, P. K. Sahoo, Nanocomposite synthesis and photoluminescence properties of MeV Au-ion beam modified Ni thin films, Appl. Surf. Sci. 360, 276 (2016).

[†]**3. V. Siva**, P. C. Pradhan, G. S. Babu, M. Nayak, P. K. Sahoo, K. Senapati, Superconducting proximity effect in $NiBi_3$-Ni-$NiBi_3$ trilayer system with sharp superconductor-ferromagnet boundaries, J. Appl. Phys. 119, 063902 (2016).

[†]**4. V. Siva**, A. Chettah, B. Satpati, S. Ojha, D. Kanjilal and P. K. Sahoo, Enhanced surface and interface diffusion in NiBi bilayers by swift heavy ion irradiation, RSC Adv. 58950, 6 (2016).

[†]**5. V. Siva**, D. P. Datta, S. Chatterjee, S. Varma, D. Kanjilal and P. K. Sahoo, Synthesis of sponge-like hydrophobic $NiBi_3$ surface by 200 keV Ar ion implantation, Appl. Surf. Sci. 410, 519 (2017).

6. V. Siva, S. S. Sahu, D. P. Datta, P. C. Pradhan, M. Nayak, V. Solanki, D. Topwal, K. Senapati, P. K. Sahoo, Ion irradiation induced phase transition of Co in Co/Au thin films, J. Alloys Compd., 680, 722 (2016).

7. S. Prusty[‡], **V. Siva**[‡], N. Shukla, B. Satpati, K. Senapati and P. K. Sahoo, Unusual ferromagnetic behaviour of embedded non-functionalized Au nanoparticles in Bi/Au bilayer films, RSC Adv. 6, 106584(2016). [‡]equal contribution.

8. D. P. Datta, **V. Siva**, A. Singh, S. R. Joshi, D. Kanjilal and P. K. Sahoo, Ion-beam-induced nanodots formation from Au/Si thin films on quartz surface, Nucl. Instrum. Methods Phys. Res. Sect. B, 379, 48, (2016).

9. D. P. Datta, **V. Siva**, S. Varma, D. Kanjilal and P. K. Sahoo, Ion induced dewetting of Au-Si on SiO_2 surface- composite nanodot evolution and wettability transition, Phys.Chem. Chem. Phys. 18, 29955 (2016).

10. S. N. Sarangi, **V. Siva**, B. K. Padhi and P. K. Sahoo, Synthesis of Cu-doped ZnO nanorods for photosensitive UV detection application, Adv. Mater. Lett. 8, 524 (2017).

11. S. S. Sahu, **V. Siva**, P. C. Pradhan, M. Nayak, K. Senapati and P. K. Sahoo, Progressive magnetic softening of ferromagnetic layers in multilayer ferromagnet-nonmagnet systems and

the role of granularity, J. Appl. Phys. 121, 213905 (2017).

12. D. P. Datta, **V. Siva**, A. Singh, D. Kanjilal and P. K. Sahoo, Photoluminescent Au-Ge composite nanodots formation on SiO_2 surface by ion induced dewetting, Nucl. Instrum. Methods Phys. Res. Sect. B 407, 141 (2017).

[†]**13**. **V. Siva**, A. Chettah, A. Tripathi, D. Kanjilal and P. K. Sahoo, Interface mediated enhanced mixing of multilayered Ni-Bi thin films by swift heavy ion irradiation, Nucl. Instrum. Methods Phys. Res. Sect. B 409, 314 (2017)

[†]**14**. **V. Siva**, A. Chettah, A. Tripathi, D. Kanjilal and P. K. Sahoo, Enhanced mixing in Ni-Bi multilayers using swift heavy ion irradiation: Application of the inelastic thermal spike model, Intermetallics (Under review).

15. D. P. Datta, A. Chettah, **V. Siva**, D. Kanjilal, and P. K. Sahoo, Dewetting induced Au-Ge composite nanodot evolution in SiO_2, Appl. Surf. Sci. 428, 676 (2018).

16. D. Suri, **V. Siva**, S. Joshi, K. Senapati, P. K. Sahoo, S. Varma, R. S. Patel, A study of electron and thermal transport in layered titanium disulphide single crystals, J. Phys.: Cond. Matt. 29, 485708 (2017).

Conference Proceedings

[†]**1**. **V. Siva**, D. P. Datta, S. Prusty, and P. K. Sahoo, Solid state reaction induced phase evolution of Ni/Bi thin films, AIP conf. proc. 1832, 080021 (2017).

2. S. Prusty, **V. Siva**, S. Ojha, D. Kabiraj and P. K. Sahoo, Nanoscale Interfacial Mixing of Au/Bi Layers Using MeV Ion Beams, AIP Conf. Proc. 1832, 080026 (2017).

[†] Related to thesis.

Conferences and workshops presentations

1. Synthesis of chemically stable Phases in Ni/Bi Thin Film system by Ion Implantation and Thermal Annealing- **V. Siva**, S. Prusty, A. Behera, M. Kumar, T. Som, D. Kabiraj, S. Ojha, D. Kanjilal and P. K. Sahoo in an International Conference on Nanostructuring by Ion Beams (ICNIB 2013) at the Gold Palace and Resorts, Jaipur India, from 23-25, October, 2013.

2. Magnetic properties and phase synthesis of Ni/Bi thin film systems by swift heavy ions -**V. Siva**, K. Senapati, S. Prusty, S. Ojha, D. K. Avasthi, D. Kanjilal, and P. K. Sahoo in an International conference on Swift Heavy Ions in Materials Engineering and Characterisation (SHIMEC 2014) at Inter-University Accelerator Centre (IUAC), New Delhi, India from 14-17, October, 2014.

3. Structural modification of Ni/Bi bi-layer thin films by ion implantation and thermal annealing-**V. Siva**, S. Prusty, M. Kumar, T. Som and P. K. Sahoo in an International conference on Physics at surfaces and Interfaces, at Puri, Odisha, India from 24-28, February, 2014.

4. Modification of structural and magnetic properties of Ni/Bi systems by swift heavy ions -**V. Siva**, K. Senapati, B. Satpati, S. Prusty and P. K. Sahoo Indo-Japan Workshop on Magnetism at Nanoscale (IJWMN) at NISER Bhubaneswar, Odisha, India from 09-12, January, 2015.

5. Modifications of structural and magnetic properties of Au/Co multi layers by ion irradiation -**V. Siva**, K. Senapati, S. S. Sahu, A. Agrawal, P. C. Pradhan, M. Nayak, S. Mahana, D. Topwal and P. K. Sahoo Current trends on Condensed Matter Physics (CTCMP 2015) at NISER Bhubaneswar, Odisha, India from 19-22, February, 2015.

6. MeV Ion beam induced modification of bi-metallic system - **V. Siva**, P. C. Pradhan, M. Nayak, and P. K. Sahoo, in the Workshop on the Use of Low Energy Ion Beams at Institute of Physics, Bhubaneswar, Odisha, India from 7-9, November, 2015.

7. Interface mediated enhanced mixing of multilayered Ni-Bi thin films by swift heavy ion irradiation -**V. Siva**, E. Bhatia, K. Senapati, A. Tripathi, D. Kanjilal, P. K. Sahoo in an international conference Ion beam Modification of Materials (IBMM 2016) at Te Papa, Wellington, New Zealand from 30 October 04 November, 2016.

8. Solid state reaction induced phase evolution of Ni/Bi thin films **V. Siva**, D. P. Datta, S. Prusty and P. K. Sahoo in a national conference DAE Solid State Physics Symposium (DAE-SSPS 2016) at KIIT University, Bhubaneswar, Odisha, India from 26-30, 2016.